Simulation numérique des ondes de Faraday

Nicolas Périnet

THESE DE DOCTORAT DE
L'UNIVERSITE PARIS VI - PIERRE ET MARIE CURIE

Spécialité : Mécanique des fluides

Ecole doctorale de Sciences Mécaniques, Acoustique et Electronique de Paris

Présentée par

Nicolas Périnet

Pour obtenir le grade de

Docteur de L'Université Pierre et Marie Curie

Sujet de la thèse : Simulation numérique des ondes de Faraday

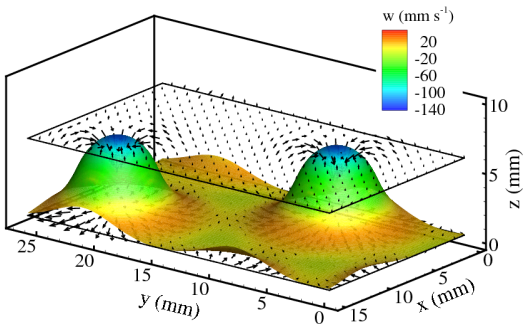

soutenue le 17 Décembre 2010

devant le jury composé de :

Mme. Laurette Tuckerman	Directeur de thèse	Directeur de recherche
M. Damir Juric	Directeur de thèse	Chargé de recherche
M. Edgar Knobloch	Rapporteur	Professeur
M. Christian Wagner	Rapporteur	Professeur
M. Stéphan Fauve	Examinateur	Professeur
M. Christophe Josserand	Examinateur	Chargé de recherche
M. Jean-Christophe Robinet	Examinateur	Maître de conférence

Le travail de cette thèse a été réalisé au PMMH (Physique et Mécanique des Milieux Hétérogènes) de l'ESPCI (Ecole Supérieure de Physique et de Chimie Industrielles de la ville de Paris) ainsi qu'au LIMSI (Laboratoire d'Informatique pour la Mécanique et les Sciences de l'Ingénieur)

PMMH - ESPCI
10, rue Vauquelin
75231 Paris Cedex 5
Téléphone : +33 1 40 79 45 22

LIMSI - CNRS
BP 133, Bât 508
F-91403 Orsay Cedex
Téléphone : +33 1 69 85 80 80

Remerciements

Mes remerciements s'adressent en tout premier lieu à mes deux directeurs de thèse, Laurette Tuckerman et Damir Juric. Je leur serai toujours redevable de leur disponibilité permanente, leur soutien pendant les périodes les plus difficiles et la qualité de l'aide qu'ils m'ont dispensée pendant ces trois années. J'espère que mon travail aura été à la hauteur de ce qu'ils ont pu m'apporter. Je remercie les rapporteurs de mon Jury, Edgar Knobloch et Christian Wagner d'avoir accepté de participer à ma soutenance, apporté autant d'attention à la lecture de mon mémoire ainsi que leur patience lors de nos collaborations et des nombreuses discussions si enrichissantes auxquelles ils m'ont convié à participer. Je suis pour les mêmes raisons extrêmement reconnaissant envers les autres membres du jury, Stéphan Fauve désigné volontaire pour être le président de mon jury, Christophe Josserand et Jean-Christophe Robinet. Jean-Christophe Robinet fut auparavant mon maître de stage de Master, lui et ses prédécesseurs, Jacques Léorat, Dr. Junaidah Osman et Eugène Bogomolny ont eux aussi grandement contribué à mon enrichissement scientifique et personnel, je leur dois bien toute ma gratitude. Je n'oublierai évidemment pas ma famille, tant il est vrai qu'ils m'ont apporté un soutien indéfectible et bien d'autres bénédictions avant et pendant cette période chaotique qu'est la thèse. Je me dois par ailleurs de remercier les autres doctorants des laboratoires que j'ai tant aimé fréquenter : Lyes, Benoît, Julie, Benjamin, Marx, Jérémie, Samia, Lan, Richard, Guillaume, Francky, Adolpho, Sébastien, Alberto, Christophe, et Li au LIMSI, Olivier, Romain, Nicolas, Bau, Nawal, Catherine, Hélène, Naïs, Rim, Guillaume, Thomas, Antoine, Lennaïc et Kévin au PMMH. Je leur souhaite aussi toute la réussite possible dans leur carrière. Enfin, je n'oublierai pas les directeurs, José-Eduardo Wesfreid et Patrick Le Quéré, et personnels de ces deux laboratoires, spécialement Jalel Chergui dont l'aide en informatique, toujours généreusement donnée, a été si précieuse, ainsi que les personnes avec qui j'ai eu la chance d'assurer des enseignements, tout particulièrement Catherine Weisman, Diana Baltean, Laurent Martin-Witkowski et Mouaouia Firdaouss. J'adresse aussi de sincères remerciements aux nombreuses personnes que j'ai rencontrées dans lors de mes périgrinations scientifiques qui ont participé à mon enrichissement intellectuel et personnel et se reconnaîtront si elles lisent un jour ma thèse. D'un point de vue moins professionnel, j'envoie à mes amis, qu'ils soient du lycée de l'université du roller ou d'autres activités un grand merci pour les bons moments passés ensemble.

Résumé

Quand deux couches fluides immiscibles sont soumises à des vibrations verticales, des ondes stationnaires apparaissent à l'interface si l'amplitude de ces oscillations est suffisamment grande. Des travaux récents ont mis en évidence que les motifs observés étaient étonnamment variés, ce qui a largement contribué à l'intérêt que revêt aujourd'hui le problème de Faraday. Nous avons réalisé la première simulation numérique complète tridimensionnelle des ondes de Faraday. Les algorithmes employés sont une méthode de projection dédiée à la résolution des équations de Navier-Stokes et une méthode de Front-Tracking consacrée au traitement de l'interface. Les courbes neutres et les modes propres temporels sont en accord avec la théorie de Floquet. Nous avons ensuite simulé le problème de Faraday dans des conditions d'apparition de motifs carrés et hexagonaux. Les spectres spatio-temporels des motifs simulés sont en accord avec l'expérience. Cependant, les hexagones se déstabilisent vers une alternance régulière de motifs de différentes symétries, suggérant la présence d'une orbite homocline. Nous avons élaboré un algorithme forçant la symétrie hexagonale pour déterminer le point fixe de cette orbite. Nous avons enfin réalisé une étude numérique de l'instabilité de dérive dans l'expérience de Faraday bidimensionnelle périodique. Un déplacement horizontal de motifs initialement immobiles avait été expérimentalement constaté lorsque les oscillations dépassaient un seuil secondaire. Les simulations ont confirmé ce résultat. Des diagrammes de bifurcation mettant en évidence des instabilités supplémentaires ont été tracés et complétés par une analyse spectrale spatio-temporelle.

Mots clés

Fluide, interface, instabilité, motif, symétrie, système dynamique.

Title

Numerical simulation of Faraday waves.

Summary

When two immiscible fluid layers are subjected to vertical vibration, standing waves appear at the interface if the oscillation amplitude is sufficiently large. Recent work has shown an astonishing variety of patterns, which has contributed to the current interest in the Faraday problem. We have carried out the first complete three-dimensional simulation of Faraday waves. The algorithm we use combines a projection method to solve the Navier-Stokes equations with a Front-Tracking method to treat the interface. The neutral curves and temporal modes agree with Floquet theory. We then simulated the Faraday problem under the conditions in which square and hexagonal patterns appear. The spatio-temporal spectra of the simulated patterns agree with experiment. Nevertheless, the hexagons destabilize in favor of a an alternating sequence of patterns with different symmetries, suggesting the presence of a homoclinic orbit. We have developed an algorithm which forces the hexagonal symmetry in order to calculate the fixed point of this orbit. Finally, we have carried out a numerical study of the drift instability in the Faraday experiment. A horizontal displacement of initially stationary patterns has been experimentally observed when the oscillation amplitude exceeds a secondary threshold. Our numerical simulations have confirmed this result. Bifurcation diagrams displaying additional instabilities have been constructed, as well as a complementary spatio-temporal spectral analysis.

Keywords

Fluid, interface, instability, pattern, symmetry, dynamical system.

Résumé

0.1 Introduction

L'expérience de Faraday consiste à agiter verticalement un récipient contenant deux fluides immiscibles (le plus léger pouvant être de l'air) générant des oscillations dans ces fluides ainsi que sur l'interface qui les sépare. Quand l'amplitude des vibrations dépasse un certain seuil, il se forme divers motifs qui peuvent être cristallins ou avoir d'autres formes plus complexes. Ce phénomène a été mis en évidence par Faraday (1831) qui remarqua que la fréquence de vibration de l'interface était le double de celle du forçage. Les résultats de Faraday furent confirmés par Rayleigh (1883a,b). Benjamin et Ursell (1954) réalisèrent la première analyse théorique des ondes de Faraday dans le régime linéaire, restreinte cependant à des fluides parfaits. Ils décomposèrent l'écoulement en modes normaux et montrèrent que l'équation de chaque mode pouvait être réduite à une équation de Mathieu dont le diagramme de stabilité avait déjà été calculé. A partir de 1990 fut découverte une profusion de nouvelles structures, comme des quasi-cristaux octogonaux observés par Christiansen et al. (1992) ou dodécagonaux vus par Edwards et Fauve (1993) qui imposèrent un forçage composé de deux sinusoïdales de fréquences commensurables. Müller (1993) généra des motifs périodiques triangulaires, encore jamais vus à l'époque, et Kudrolli et al. (1998) obtinrent des super-réseaux en utilisant un forçage périodique à deux fréquences. Kudrolli et Gollub (1996) effectuèrent une étude paramétrique des motifs (carrés, raies et hexagones) en fonction de la viscosité et de la fréquence du forçage. Ils étudièrent le chaos spatio-temporel dans les ondes de Faraday dont l'existence avait été signalée auparavant dans Ezerskii et al. (1986). Binks et al. (1997) mirent en évidence la dépendance en l'épaisseur de fluide des motifs rencontrés. Des ondes circulaires très localisées appelées oscillons furent pour la première fois vues expérimentalement par Lioubashevski et al. (1996). L'instabilité de Faraday constitue le premier système physique macroscopique où de telles structures ont été rencontrées, ce qui confère au problème de Faraday un grand intérêt pour qui veut comprendre les processus de formation de motifs.

De nombreuses études théoriques ont été inspirées de ces expériences. Kumar et Tuckerman (1994) généralisèrent l'étude de stabilité linéaire de Benjamin et Ursell (1954) aux fluides visqueux. Leurs résultats furent confirmés par les expériences de Bechhoefer et al. (1995) et utilisés par Kumar (1996) afin de prévoir les cas dans lesquels la réponse du fluide au forçage serait harmonique ou sous-harmonique. La méthode de Kumar et Tuckerman (1994) a ensuite été étendue par Besson et al. (1996) aux forçages à deux fréquences. Une formulation intégrale des équations de stabilité linéaire du problème visqueux fut dérivée par Beyer et Friedrich (1995). Cerda et Tirapegui (1998) se servirent de l'approximation de lubrification et de la méthode WKB pour étudier les couches minces visqueuses dont ils déduisirent une équation de Mathieu, utilisée par la suite par Huepe et al. (2006) afin de dériver des résultats analytiques concernant les forçages avec plusieurs fréquences.

L'analyse linéaire ne peut fournir d'information sur la forme des motifs attendus. D'autres méthodes sont alors nécessaires pour prédire l'occurrence d'un motif donné ou l'amplitude de stabilisation des ondes. Des approximations faiblement non linéaires ont été dérivées par Zhang et Viñals (1997), Chen et Viñals (1999) et plus récemment par Skeldon et Guidoboni (2007). L'analyse des différentes sortes de motifs utilisant la théorie des systèmes équivariants et des systèmes d'équations modèles pour la génération de motifs a, elle aussi, connu un certain succès (Porter et al., 2004). Une approximation de quasi-cristaux dans des domaines spatialement périodiques a été traitée par Rucklidge et Silber (2009).

D'autres phénomènes, comme la modulation spatiale de motifs, l'annihilation ou la nucléation d'une ou plusieurs longueurs d'onde d'un motif, ou encore l'instabilité de dérive (drift instability) ont été observés dans une configuration annulaire par Douady et al. (1989). L'instabilité de dérive consiste dans le déplacement des motifs autour de l'anneau. Ces phénomènes ont été traités par Fauve et al. (1991) à l'aide d'équations modèles. D'autres analyses de ce sujet ont été conduites ultérieurement par Vega et al. (2001) et Martín et al. (2002) à partir de développements faiblement non linéaires.

L'instabilité de Faraday en régime non linéaire nécessite un traitement numérique. Peu de simulations de ce problème ont été développées à ce jour; on peut cependant citer quelques travaux de Chen et Wu (2000), Chen (2002), Murakami et Chikano (2001), Valha et al. (2002), Ubal et al. (2003) ou encore O'Connor (2008). A l'exception de celle de O'Connor (2008), toutes les simulations numériques du problème de Faraday ont été conçues pour des domaines bidimensionnels. Le traitement numérique le plus complet a été celui de Chen et Wu (2000) et Chen (2002) qui s'appuie sur une résolution par des méthodes aux différences finies dans un système de coordonnées évoluant avec la forme de l'interface. A chaque pas de temps, l'interface est advectée et une nouvelle grille de points, adaptée à la forme de l'interface, est recalculée. L'amplitude des

ondes de Faraday 2D obtenues avec leur simulation s'est révélée en accord avec les prédictions faiblement non linéaires de Chen et Viñals (1999).

Murakami et Chikano (2001) utilisèrent une méthode similaire à celle de Chen et Wu (2000) et Chen (2002). Bien qu'ils reproduisirent certains comportements des expériences de Lioubashevski et al. (1996), leurs calculs étaient limités à des accélérations ne pouvant aller au-delà de 0.5% au-dessus du seuil d'instabilité. Ubal et al. (2003) se concentrèrent sur l'effet de l'épaisseur de la couche liquide dans un domaine en deux dimensions. A cette fin, ils mirent au point un code s'appuyant sur une méthode de Galerkine aux éléments finis. Ils comparèrent leurs prédictions sur la stabilité linéaire des ondes à celles de Benjamin et Ursell (1954) et de Kumar et Tuckerman (1994) et calculèrent les profils instantanés de l'interface ainsi que les champs de vitesse. Valha et al. (2002) étudièrent le comportement d'une couche liquide dans un récipient cylindrique d'axe vertical à l'aide d'une méthode MAC (Marker-and-Cell) due à Harlow et Welch (1965). La tension superficielle était traitée à l'aide d'un modèle de Brackbill et al. (1992). Enfin, O'Connor (2008) élabora un code spectral ALE (Arbitrary Lagrangian Eulerian) en deux et trois dimensions; il présenta une visualisation des motifs carrés.

Le travail de cette thèse consiste principalement à réaliser une simulation tridimensionnelle et non linéaire de l'instabilité de Faraday. Notre recherche est essentiellement motivée par l'obtention de motifs hexagonaux, quasi-cristallins ou encore d'oscillons qui sont des structures intrinsèquement tridimensionnelles et n'ont jamais encore été calculées à partir des équations complètes de la mécanique des fluides. La méthode numérique développée pendant cette période de thèse est élaborée à partir d'un algorithme de Front-Tracking dédié au traitement de l'interface et associé à des schémas aux différences finies. Cette méthode permet, de par sa structure, de résoudre les équations de Navier-Stokes dans deux milieux fluides quelconques. Les simulations précédentes étaient au contraire limitées par l'absence d'une couche supérieure et restreignaient ainsi le choix du fluide le moins dense à des gaz, très légers, dont la contribution à la dynamique est par conséquent négligeable. Ce dernier point revêt une importance considérable car la méthode que nous avons developpée permet des comparaisons avec certaines expériences utilisant deux couches de liquides, comme celle de Kityk et al. (2005) dans laquelle le fluide supérieur ne peut être négligé. Ces expériences ont été les premières à l'issue desquelles une mesure quantitative de la hauteur d'interface a été fournie, ainsi que des spectres spatio-temporels des motifs. Elles constituent donc un excellent moyen de validation de nos résultats numériques dans le régime non linéaire où les amplitudes sont finies (interfaces avec des pentes raides).

Le premier chapitre est consacré à la méthode numérique de simulation ; nous y expliquerons les algorithmes employés. Le second chapitre est dédié à la validation de la méthode. La première validation consiste à comparer les résultats de la simulation avec ceux issus de la théorie linéaire de Kumar et Tuckerman (1994), en particulier l'étude des seuils et des vecteurs propres dominants. La seconde vérification concerne le régime non linéaire ; nous opposerons les spectres spatio-temporels des motifs carrés et hexagonaux formés à l'interface avec ceux de l'expérience de Kityk et al. (2005). La troisième partie de ce document est consacrée à l'étude d'un comportement exotique des motifs hexagonaux obtenus dans les conditions d'expérimentation de Kityk et al. (2005). Enfin une dernière partie a été écrite au sujet de l'instabilité de dérive qui entraîne un déplacement des motifs à l'interface. Nous présentons les résultats d'une simulation de l'instabilité de Faraday dans un domaine bidimensionnel périodique, censé pouvoir modéliser un récipient annulaire.

0.2 Simulation numérique tridimensionnelle de l'expérience de Faraday

0.2.1 Equations du mouvement

Le problème de Faraday est mathématiquement modélisé par deux fluides non miscibles, incompressibles et visqueux dans un domaine tridimensionnel $\mathbf{x} = (x, y, z) \in \mathbb{R}^2 \times [0, h]$ délimité en $z = 0$ et $z = h$ par des murs imperméables. Les deux fluides sont de viscosités μ_1 et μ_2 et de masses volumiques ρ_1 et ρ_2 uniformes et sont initialement disposés en deux couches horizontales séparées par une interface. L'indice 1 est associé au fluide le plus lourd, l'indice 2 à celui de la couche supérieure. L'interface est définie par $\mathbf{x}' = (x, y, \zeta(x, y, t))$, elle sera monovaluée dans les plages d'accélérations considérées.

Le récipient est secoué verticalement. Dans le référentiel du récipient, les conditions aux bords s'appliquant

à la vitesse $\mathbf{u} = (u, v, w)$ sont

$$\mathbf{u}(x, y, 0, t) = 0, \tag{1}$$
$$\mathbf{u}(x, y, h, t) = 0. \tag{2}$$

En contrepartie, un terme périodique inertiel modélisant les vibrations est ajouté au terme gravitationnel

$$\mathbf{G} = (a\cos(\omega t) - g)\mathbf{e}_z, \tag{3}$$

où a est l'amplitude du forçage et ω sa fréquence. Les équations de Navier-Stokes pour des fluides incompressibles et newtoniens s'écrivent

$$\rho\frac{\mathrm{D}\mathbf{u}}{\mathrm{D}t} = -\boldsymbol{\nabla}p + \rho\mathbf{G} + \boldsymbol{\nabla}\cdot\mu\left(\boldsymbol{\nabla}\mathbf{u} + \boldsymbol{\nabla}\mathbf{u}^{\mathrm{T}}\right) + \mathbf{s}, \tag{4a}$$

$$\boldsymbol{\nabla}\cdot\mathbf{u} = 0. \tag{4b}$$

p étant la pression et $\mathbf{s}$ la force capillaire par unité de volume qui sera définie ultérieurement. Malgré la présence de discontinuités en ρ et μ à l'interface et la présence de $\mathbf{s}$ qui s'applique uniquement sur l'interface, les équations (4a) et (4b) sont définies dans tout le domaine si l'on exprime ρ et μ comme suit

$$\rho = \rho_1 + (\rho_2 - \rho_1)H, \tag{5a}$$
$$\mu = \mu_1 + (\mu_2 - \mu_1)H, \tag{5b}$$

à l'aide d'une fonction indicatrice H (ici, une fonction de Heaviside)

$$H\left(\mathbf{x} - \mathbf{x}'\right) = \begin{cases} 0 \text{ si } z < \zeta(x, y, t) \\ 1 \text{ si } z \geq \zeta(x, y, t) \end{cases}, \tag{6}$$

La force capillaire est

$$\mathbf{s} = \int_{S'(t)} \sigma\kappa\,\mathbf{n}\,\delta\left(\mathbf{x} - \mathbf{x}'\right)\mathrm{d}S, \tag{7}$$

où σ symbolise le coefficient de tension de surface supposé constant, $\mathbf{n}$ est la normale à l'interface dirigée vers la couche supérieure et κ sa courbure locale. $\delta(\mathbf{x} - \mathbf{x}')$ est une distribution de Dirac tridimensionnelle qui ne prend de valeur non nulle qu'en $\mathbf{x} = \mathbf{x}'$. $S'(t)$ est la surface déterminée par la position instantanée de l'interface. Pour fermer le système d'équations, il est nécessaire d'ajouter le mouvement de l'interface modélisé par

$$\mathrm{D}H/\mathrm{D}t = 0, \tag{8}$$

déduite de la condition d'incompressibilité $\mathrm{D}\rho/\mathrm{D}t = 0$. L'interface est donc implicitement représentée par H et advectée par le déplacement particulaire du fluide.

0.2.2 Méthodes numériques employées

Le domaine de calcul est un parallélépipède rectangle, périodique selon x et y, entouré de deux murs plans en $z = 0$ et $z = h$ sur lesquels est imposée une condition de non-glissement. Le domaine est discrétisé à l'aide d'un maillage aux différences finies eulérien, uniforme et tridimensionnel. Le maillage est décalé, de type MAC (Harlow et Welch, 1965) où les noeuds correspondant à u, v et w sont situés sur les faces des cellules alors que les variables scalaires sont situées en leur centre. Chaque cellule a pour dimension $\Delta x \times \Delta y \times \Delta z$. L'interface est modélisée sur un autre maillage. Ce maillage déformable est composé d'éléments triangulaires dont le déplacement est traité par une méthode de Front-Tracking aux frontières immergées (Peskin, 1977; Tryggvason et al., 2001). $\zeta(x, y, t)$ étant supposée monovaluée, les noeuds du maillage dédié à l'interface sont donc considérés comme mobiles uniquement selon la direction verticale z. Cette simplification évite les problèmes de réorganisation des noeuds, occasionnant des gains considérables en temps de programmation et de calcul en comparaison avec une méthode de Front-Tracking standard.

L'algorithme de résolution est décomposé en trois parties, répétées à chaque pas de temps. L'interface est advectée puis les viscosités et masses volumiques sont recalculées en fonction de la nouvelle position de l'interface. La force capillaire est calculée. Enfin, les champs de vitesse et de pression sont déterminés à l'aide d'une méthode de projection. Les trois étapes de résolution sont détaillées dans les paragraphes suivants.

Advection de l'interface

Les méthodes purement eulériennes telles que VOF (Volume of Fluid, Hirt et Nichols (1981)) ou alors Level Set (Osher et Sethian, 1988) utilisent une forme de (8) pour advecter un champ scalaire tel que H ou une fonction qui représente implicitement l'interface. Avec la méthode de Front-Tracking, l'advection se fait sur les points de l'interface qui sont les noeuds du maillage triangulaire. H est construite à partir de la position de l'interface et de sa géométrie. Partant de (8), nous déduisons l'équation d'advection de ζ dont les points sont modélisés comme étant immobiles selon les directions horizontales (Périnet et al., 2009)

$$\frac{\partial \zeta}{\partial t} = w - u\frac{\partial \zeta}{\partial x} - v\frac{\partial \zeta}{\partial y}, \tag{9}$$

dont la discrétisation au premier ordre est

$$\frac{\zeta^{n+1} - \zeta^n}{\Delta t} = w^n(\mathbf{x}'_e) - \frac{\partial \zeta^n}{\partial x}u^n(\mathbf{x}'_e) - \frac{\partial \zeta^n}{\partial y}v^n(\mathbf{x}'_e). \tag{10}$$

Les indices n et $n+1$ indiquent respectivement l'ancien et le nouveau pas de temps, $\mathbf{x}'_e$ symbolise la position d'un élément de l'interface. Cette discrétisation utilisant un schéma décentré amont est soumise à des conditions sur le nombre CFL (nombre de Courant-Friedrichs-Lewy).

Les vitesses au point $\mathbf{x}'_e$ qui ne fait pas partie du maillage fixe sont calculées par une interpolation typiquement utilisée dans les méthodes de frontières immergées (Peskin, 1977) ou de Front-Tracking (Tryggvason et al., 2001)

$$\mathbf{u}(\mathbf{x}'_e) = \sum_{ijk} \mathbf{u}(\mathbf{x}_{ijk})\delta_h(\mathbf{x}_{ijk} - \mathbf{x}'_e)\Delta x \Delta y \Delta z. \tag{11}$$

δ_h est une distribution de Dirac lissée dont le support s'étend sur les quatre noeuds du maillage fixe de position $\mathbf{x}_{ijk}$, voisins de $\mathbf{x}'_e$, et ceci dans chaque direction.

Enfin, la fonction indicatrice H est réactualisée en résolvant un problème de Poisson

$$\nabla^2 H = \boldsymbol{\nabla} \cdot \int_{S'(t)} \mathbf{n}\,\delta\left(\mathbf{x} - \mathbf{x}'\right) \mathrm{d}S, \tag{12a}$$

$$H(x, y, 0, t) = 0, \tag{12b}$$

$$H(x, y, h, t) = 1, \tag{12c}$$

dont la version discrétisée est

$$\nabla^2 H_{ijk} = \boldsymbol{\nabla} \cdot \sum_e \mathbf{n}_e \delta_h(\mathbf{x}_{ijk} - \mathbf{x}'_e)\Delta S_e. \tag{13}$$

Les opérateurs différentiels sont discrétisés avec des schémas centrés. La transition de 0 à 1 de cette version numérique de la fonction de Heaviside se retrouve lissée sur quatre points du maillage fixe. Les éléments du maillage étant triangulaires, ils possèdent un unique vecteur normal

$$\mathbf{n}_e = \frac{\mathbf{t}_2 \times \mathbf{t}_1}{||\mathbf{t}_2 \times \mathbf{t}_1||}. \tag{14}$$

$\mathbf{t}_1$ et $\mathbf{t}_2$ sont les vecteurs tangents à deux côtés de l'élément triangulaire (voir 1). Les champs scalaires ρ^{n+1} et μ^{n+1} sont calculés à l'aide de (5a) et (5b), connaissant la distribution H au temps $n+1$.

Force capillaire

D'après (7), le calcul des forces capillaires nécessite la connaissance de la courbure de l'interface et de son vecteur normal. Il est difficile d'évaluer numériquement la courbure et on préfère généralement traiter la force s'exerçant sur les côtés de chaque triangle et sommer les contributions de tous les éléments de l'interface. La force capillaire $\mathbf{s}_e$ exercée sur le périmètre d'un élément e de la surface, de périmètre δl et d'aire ΔS_e s'exprime comme suit

$$\mathbf{s}_e = \sigma \oint_{\delta l} \mathbf{t} \times \mathbf{n}\ \mathrm{d}l. \tag{15}$$

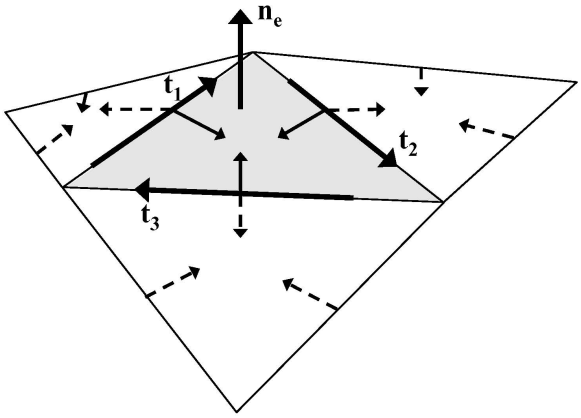

Figure 1: Elément triangulaire du maillage de l'interface illustrant l'action des forces capillaires d'après (15). Les forces agissant dans le triangle grisé s'exercent perpendiculairement à ses côtés (voir flèches continues non labélisées), les flèches pointillées sont les homologues de ces forces calculées dans les triangles voisins.

Cette force est dirigée dans le plan du triangle et orthogonalement au côté sur lequel elle s'applique, comme le montre Figure 1. La résultante des forces capillaires s'appliquant sur le côté commun à deux triangles est dirigée vers l'intérieur du fluide se situant dans la concavité de l'interface. Les forces capillaires sont redistribuées sur les mailles eulériennes en discrétisant (7) suivant la méthode des frontières immergées (Peskin, 1977)

$$\mathbf{s}_{ijk} = \sum_e \mathbf{s}_e \delta_h(\mathbf{x}_{ijk} - \mathbf{x}'_e). \tag{16}$$

Un noeud eulérien reçoit donc les contributions de forces exercées sur plusieurs éléments de l'interface.

Résolution des équations de Navier-Stokes

Les équations de Navier-Stokes sont résolues à l'aide d'une méthode de projection (Chorin, 1968; Temam, 1984) avec correction incrémentale de la pression (Goda, 1979) appliquée à un schéma aux différences finies d'ordre 1 en temps et d'ordre 2 en espace. En outre, un schéma semi-implicite a été choisi pour s'affranchir des conditions de stabilité sur le pas de temps dues à la diffusion visqueuse. Nous avons utilisé des schémas centrés classiques pour exprimer toutes les dérivées spatiales, sauf les termes non linéaires, évalués avec un schéma de type ENO (Essentially-Non-Oscillatory) d'ordre 2 (Shu et Osher, 1989; Sussman et al., 1998).

0.3 Validation

0.3.1 Régime linéaire

Nous avons comparé les résultats de nos simulations avec ceux obtenus par Kumar et Tuckerman (1994) dans les mêmes conditions physiques. Les paramètres physiques sont $\rho_1 = 519.933\,\mathrm{kg\,m^{-3}}$ et $\mu_1 = 3.908 \times 10^{-5}\,\mathrm{Pa\,s}$ pour le fluide inférieur, $\rho_2 = 415.667\,\mathrm{kg\,m^{-3}}$ et $\mu_2 = 3.124 \times 10^{-5}\,\mathrm{Pa\,s}$ pour le fluide supérieur. Les autres paramètres sont $\sigma = 2.181 \times 10^{-6}\,\mathrm{N\,m^{-1}}$ et $g = 9.8066\,\mathrm{m\,s^{-2}}$. La fréquence de forçage est $\omega/2\pi = 100$ Hz, d'où la période d'oscillation de $T = 0.01$s. La hauteur du container a été imposée à 0.231 mm et l'interface se situe à mi-hauteur quand elle est au repos. Nous avons considéré plusieurs nombres d'onde k et fixé la dimension en x de la boîte à une longueur d'onde $\lambda = 2\pi/k$, c'est à dire entre 0.074 et 0.224 mm.

Notions théoriques découlant de l'analyse de Kumar et Tuckerman (1994)

L'analyse de Kumar et Tuckerman (1994) prédit la forme suivante des solutions du problème linéarisé de Faraday dans un domaine de dimensions horizontales infinies. La hauteur d'interface $\zeta(x, y, t)$ par exemple,

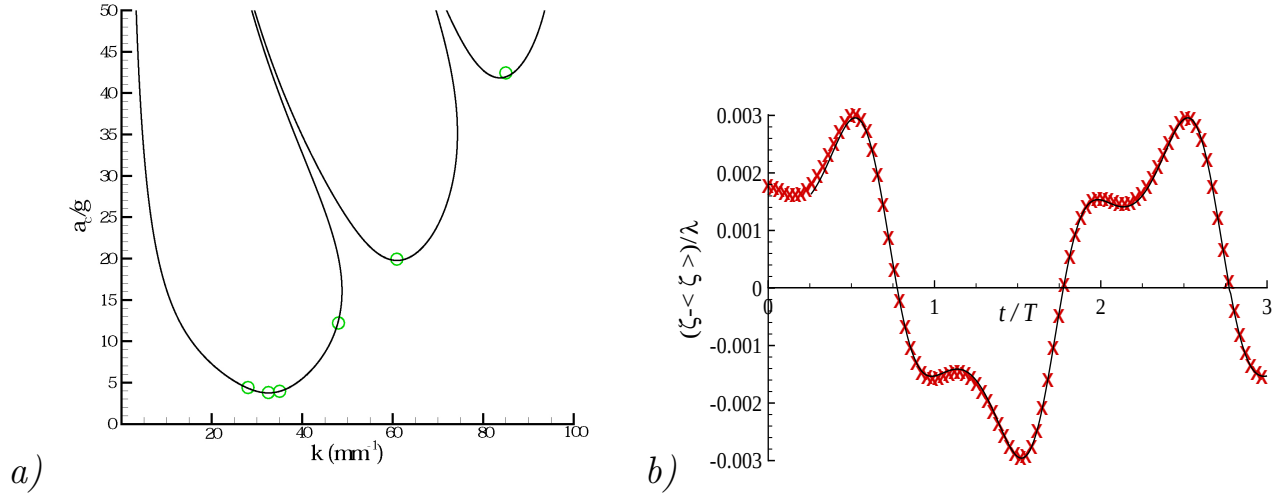

Figure 2: a) : accélération critique a_c/g en fonction du nombre d'onde k. Les lignes continues représentent les courbes neutres provenant de l'analyse théorique de Kumar et Tuckerman (1994). Les seuils a_c calculés avec nos simulations sont indiqués par des cercles. b) : évolution temporelle linéaire de la hauteur d'interface $\zeta(t) - \langle\zeta\rangle$ pour $k = 48$ mm^{-1}, sur la première langue d'instabilité. Les résultats de la simulation sont tracés avec des croix, ceux de la théorie sont symbolisés par la courbe continue. La hauteur et le temps sont respectivement adimensionnés par $\lambda = 2\pi/k$ et T.

se décompose en

$$\zeta(x,y,t) = \mathrm{e}^{\mathrm{i}\mathbf{k}\cdot\mathbf{x}}\mathrm{e}^{(\gamma+\mathrm{i}\alpha\omega)t}\sum_{n=-\infty}^{\infty} f_n(k)\mathrm{e}^{\mathrm{i}n\omega t}. \tag{17}$$

γ est le taux de croissance du mode propre ; le coefficient α ne peut prendre que les valeurs 0 et 1/2. Chaque mode propre est composé d'une somme de fonctions trigonométriques du temps $f_n(k)\mathrm{e}^{\mathrm{i}n\omega t}$. γ, α et $f_n(k)$ dépendent des paramètres physiques. En particulier, nous choisirons l'amplitude des secousses a comme paramètre de bifurcation. L'ensemble des $a(k)$ associé à un taux de croissance nul est appelé courbe neutre. D'après (17), le mode propre dominant s'exprime sur cette courbe neutre selon la valeur de α

$$\hat{\zeta}(x,y,t) = \mathrm{e}^{\mathrm{i}\mathbf{k}\cdot\mathbf{x}}\sum_{n=-\infty}^{\infty} f_n(k)\mathrm{e}^{\mathrm{i}\left(n+\frac{1}{2}\right)\omega t}, \qquad \alpha = 1/2, \text{ cas sous-harmonique,} \tag{18a}$$

$$\hat{\zeta}(x,y,t) = \mathrm{e}^{\mathrm{i}\mathbf{k}\cdot\mathbf{x}}\sum_{n=-\infty}^{\infty} f_n(k)\mathrm{e}^{\mathrm{i}n\omega t}, \qquad \alpha = 0, \text{ cas harmonique.} \tag{18b}$$

Résultats: seuils d'instabilités et modes propres

Nous avons calculé l'accélération critique $a_c(k)$ correspondant à chacun des nombres d'onde (Figure 2a). Initialement, la vitesse de l'écoulement est uniformément nulle, l'interface est une sinusoïde de vecteur d'onde $\mathbf{k}$ parallèle à l'axe $(\mathrm{O}x)$. L'amplitude de la sinusoïde est imposée très faible par rapport à λ de sorte que le comportement de l'écoulement ne soit pas parasité par des effets non linéaires. La résolution en x est d'environ 50 points par longueur d'onde, la résolution selon z varie entre 126 et 144 points selon le cas d'étude. L'écoulement étant homogène dans la direction y ($\mathbf{k}$ parallèle à $(\mathrm{O}x)$), le nombre de points pris en y est arbitraire et sera aussi petit que possible afin de réduire les temps de calculs.

L'écoulement subit une bifurcation fourche. Le taux de croissance se comporte donc comme une fonction linéaire de $a - a_c$ à proximité du seuil $a_c(k)$. La détermination de $a_c(k)$ nécessite donc deux calculs du taux de croissance résultant de nos simulations pour deux valeurs de a proches de la courbe neutre. Le seuil est

ensuite déterminé avec une interpolation linéaire entre ces deux points.

Les seuils numériques et théoriques de Figure 2a sont en très bon accord. En effet, les écarts relatifs sont échelonnés entre 0.1% et 2.4%. Figure 2b décrit le comportement du mode propre dominant. Il ne s'agit pas d'une fonction trigonométrique, mais d'une somme de plusieurs fonctions périodiques dont les fréquences sont toutes des multiples impairs de $\omega/2$ (17)-(18a). $\omega/2$ est d'ailleurs la fréquence exclusivement excitée même si les effets de la fréquence $3\omega/2$ sont significativement ressentis. D'après (18), le cas décrit est donc sous-harmonique. L'accord avec la théorie est presque parfait.

0.3.2 Régime non linéaire, motifs

Quand $a > a_c$, l'amplitude de la hauteur d'interface croît avec le temps jusqu'à ce que les termes non linéaires de (3)-(8) deviennent importants. Le mode qui avait le taux de croissance le plus fort génère, par des résonances non linéaires, une série de modes discrets, sélectionnés selon la norme et l'orientation de $\mathbf{k}$. Cette sélection non linéaire est responsable de la formation des motifs qui sera l'objet de nos futures validations.

Nous avons comparé les résultats de nos calculs avec ceux d'un article expérimental (Kityk et al., 2005, 2009) où des données quantitatives du spectre de Fourier $\hat{\zeta}(\mathbf{k}, t)$ ont été extraites des motifs carrés et hexagonaux. Les simulations ont été conduites dans les conditions expérimentales de Kityk et al. (2005): $\omega/2\pi = 12$ Hz ($T = 0.0833$ s), $\rho_1 = 1346\ \mathrm{kg\,m^{-3}}$, $\mu_1 = 7.2$ mPa s pour le fluide inférieur et $\rho_2 = 949\ \mathrm{kg\,m^{-3}}$, $\mu_2 = 20$ mPa s pour le fluide supérieur. La tension de surface vaut $\sigma = 35\ \mathrm{mN\,m^{-1}}$, la hauteur du récipient est 1.0 cm tandis que la hauteur moyenne de l'interface est $\langle\zeta\rangle = 1.6$ mm (avec des incertitudes de l'ordre du mm). L'analyse de Floquet de ce problème fournit une estimation de la longueur d'onde $\lambda_c = 2\pi/k_c = 13.2$ mm et de l'accélération critique $a_c = 25.8\ \mathrm{m\,s^{-2}}$.

Motifs carrés

Nous avons dans un premier temps pris comme élément de comparaison des motifs carrés que Kityk et al. (2005) avaient générés avec une amplitude de forçage $a = 30.0\ \mathrm{m\,s^{-2}}$. Les deux dimensions horizontales de notre boîte périodique sont fixées à $l_x = l_y = \lambda_c$. Un exemple de motif formé par l'interface à saturation apparaît Figure 3a. L'écoulement initial a été choisi uniformément immobile, l'interface initiale étant perturbée par un faible bruit blanc spatial.

Le motif montré Figure 3a possède exactement les symétries d'une structure cristalline carrée. Une comparaison quantitative de l'évolution des modes principaux du spectre spatial de ζ (Figure 3b) met en évidence un accord très satisfaisant entre les expériences de Kityk et al. (2005) et nos simulations. Les amplitudes, les périodes temporelles et les déphasages de chacun des modes sont bien reproduits. On remarquera la présence d'un décalage constant vers le haut du mode $2k_c$ tandis que les deux autres nombres d'ondes sont décrits par des courbes centrées en 0.

Motifs hexagonaux

En augmentant l'amplitude des vibrations, Kityk et al. (2005) constatent que s'opère une transition d'un régime à symétrie carrée vers un régime à symétrie hexagonale, correspondant à une réorganisation radicale du spectre spatial de l'écoulement. Pour simuler de tels hexagones, nous avons augmenté l'accélération similairement à Kityk et al. (2005) en prenant $a = 38.0\ \mathrm{m\,s^{-2}}$. En l'état actuel, la boîte qui est carrée et horizontalement périodique ne peut supporter les motifs hexagonaux composées de modes dont la longueur d'onde est λ_c. Les dimensions horizontales l_x et l_y de cette dernière ont été modifiées en conséquence : $l_x = 2\lambda_c/\sqrt{3}$ et $l_y = 2\lambda_c$. La résolution spatiale adoptée est $58 \times 100 \times 180$ dans les directions x, y, z. Les deux motifs tracés Figures 4a et 4b révèlent que le motif obtenu par le biais de nos simulations est hexagonal, ce que prévoyait aussi l'expérience de Kityk et al. (2005) dans ce régime de paramètres. L'étude spectrale réalisée pour les carrés est réitérée avec les motifs hexagonaux (voir Figure 5). Comme l'indique la légende de Figure 5, il existe une différence d'accélérations entre les deux cas. La comparaison quantitative perd alors une partie de sa valeur. Du fait de la différence faible et l'absence de seuil entre les deux accélérations,

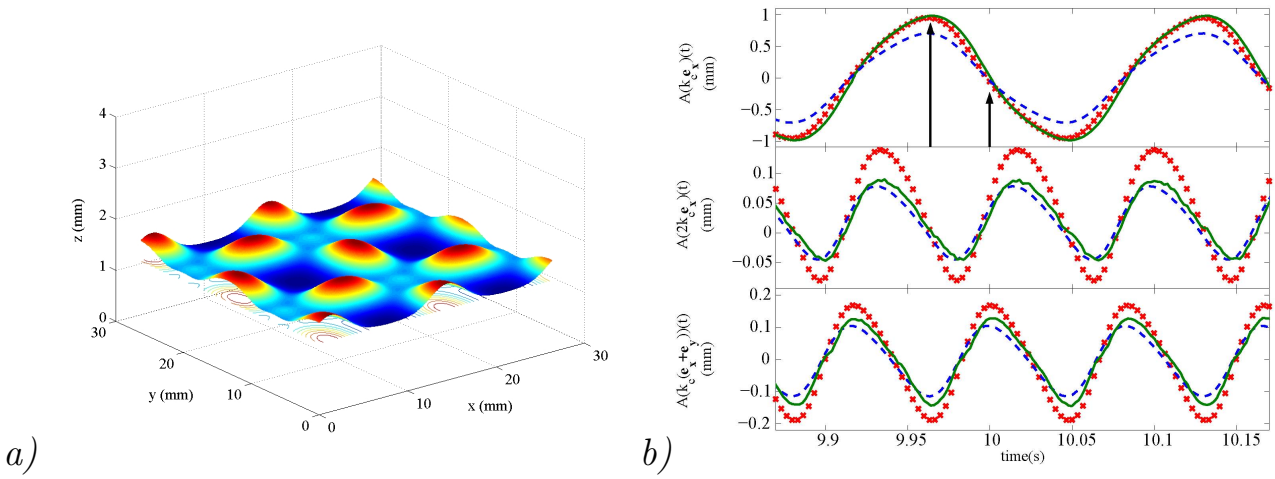

a) *b)*

Figure 3: a) : exemple de motif carré: hauteur d'interface en fonction de la position horizontale. Résolution en x, y, z: $80\times80\times160$. Les directions horizontales de la figure sont deux fois celles du domaine de calcul. b) : évolution temporelle des amplitudes des modes spatiaux k_c, $2k_c$ et $\sqrt{2}k_c$. Les courbes continues représentent les résultats expérimentaux de Kityk et al. (2009), les pointillés et les croix rendent respectivement compte des résultats numériques pour $\langle\zeta\rangle = 1.6$ mm et $\langle\zeta\rangle = 1.7$ mm.

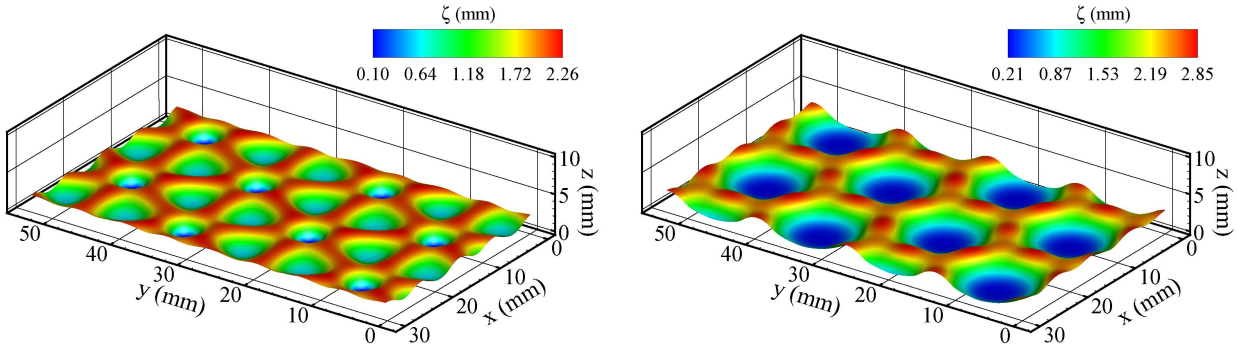

a) *b)*

Figure 4: Motifs hexagonaux : hauteur d'interface en fonction de la position horizontale à deux instants différents. Les directions horizontales des figures sont deux fois celles du domaine de calcul. Clichés pris a) $0.3\times 2T$ et b) $0.68\times 2T$ après que l'interface a atteint son maximum de hauteur. On peut constater en b) la dominance de modes dont la fréquence est plus élevée que k_c.

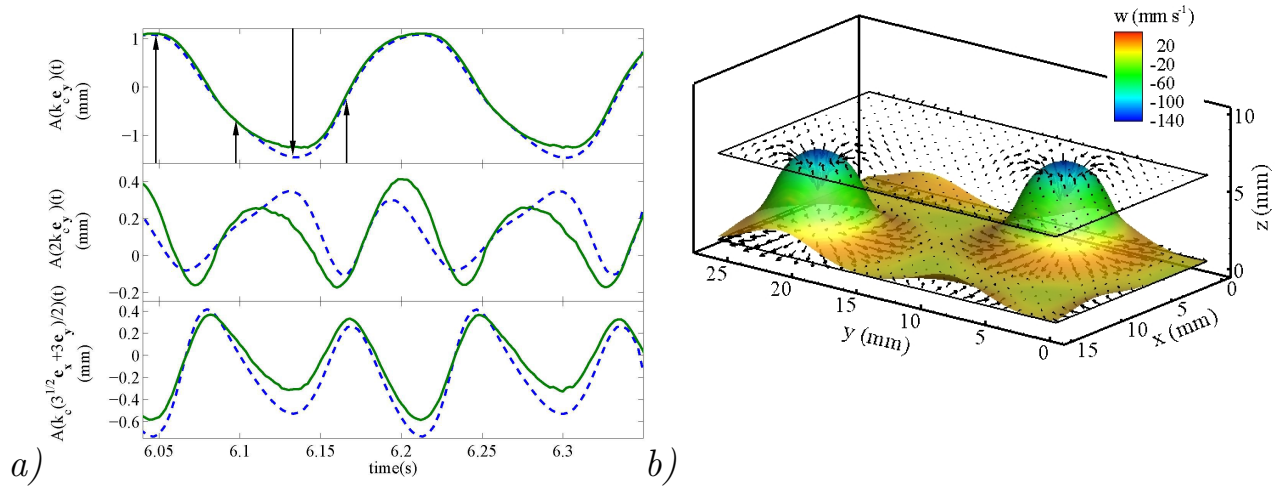

Figure 5: a) : évolution temporelle des modes de nombres d'onde k_c, $2k_c$ and $\sqrt{3}k_c$ du spectre spatial de l'interface. Les lignes continues représentent les résultats expérimentaux (Kityk & Wagner, communication privée) pour $a \approx 38.5\,\mathrm{m\,s^{-2}}$. les lignes pointillées symbolisent les résultats de notre simulation pour $a = 38.0\,\mathrm{m\,s^{-2}}$. b) : aperçu du motif hexagonal avec des champs de vitesses sur des plans horizontaux de part et d'autre de l'interface. La coloration varie avec la composante verticale w de la vitesse. Cliché pris $0.07 \times 2T$ après que l'interface a atteint son maximum d'amplitude. L'accélération a été diminuée à $36\,\mathrm{m\,s^{-2}}$.

on peut cependant s'attendre à ce que les courbes aient des comportements ressemblants et des amplitudes similaires, ce qui est le cas. Le décalage remarqué Figure 3b pour le mode $2k_c$ s'est transmis aux autres modes. Cette différence entre carrés et hexagones s'explique par la manière dont sont distribués les modes dans les deux configurations et par des considérations sur les interactions triadiques entre modes.

En plus de fournir les hauteurs d'interface, la simulation numérique procure aussi le champ complet des vecteurs vitesse, dispensant ainsi de précieux renseignements sur la dynamique des fluides dans le problème de Faraday actuellement inaccessibles à l'expérience. Nous montrons en Figures 5b et 6 une partie de ces champs de vitesse mesurés en des plans horizontaux. Les paramètres physiques sont restés inchangés excepté l'accélération qui a été abaissée à $a = 36.0\,\mathrm{m\,s^{-2}}$.

Avec l'appui de ces visualisations (Figures 5b et 6), nous donnons un bref aperçu de la dynamique des ondes de Faraday dans le cas hexagonal. Figure 5b a été prise juste après que l'interface a atteint sa hauteur maximale. Les pics de cette dernière commencent à s'effondrer. Le fluide supérieur converge alors vers ces pics tandis que le fluide situé sous ces bosses est très fortement entraîné vers le bas du domaine. Près de la paroi basse, le fluide diverge horizontalement vers la périphérie des pics. Dans les zones loin des pics, le fluide entame sa remontée. En Figure 6a, les pics se sont transformés en cratères plats et étendus ou subsiste entre l'interface et la paroi un film très mince (environ 0.1 mm). Le fluide continue de converger au-dessus de l'endroit où étaient situés les pics et de creuser les cratères qui y sont apparus. Le fluide inférieur est chassé de sous les cratères, alimentant la couronne en périphérie. Figure 6b montre que la couronne entourant les cratères s'est à son tour effondrée créant une vague circulaire qui remplit progressivement le cratère. Les fluides se mettent à converger par le dessous vers le centre des cratères et sont puissamment éjectés vers le haut du domaine (c'est à cet instant que les vitesses sont maximales). Le cratère redevient une bosse et la boucle est bouclée.

La formation du film mince en Figure 6a peut induire des difficultés numériques. L'épaisseur du film est comparable à la dimension verticale des mailles de notre domaine. En cet endroit où les vitesses peuvent être importantes, les événements qui s'y déroulent risquent d'être sous-résolus.

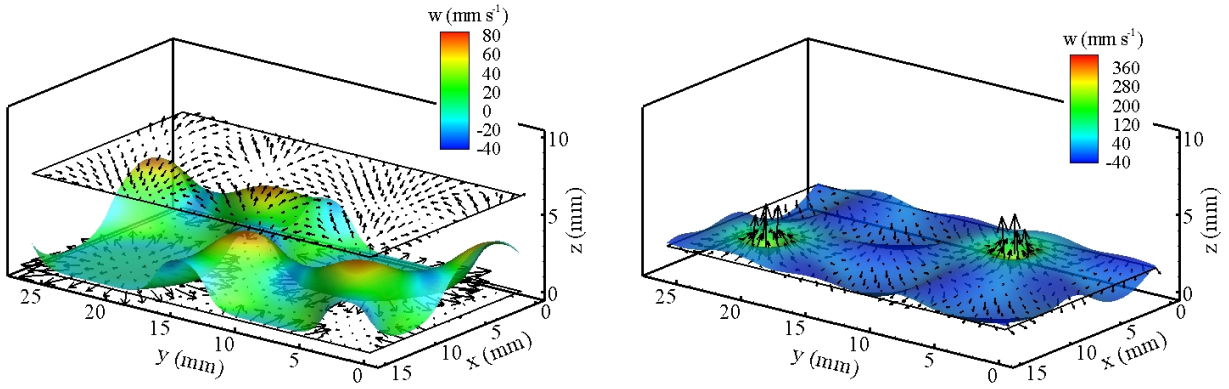

a) *b)*

Figure 6: Aperçus de motifs hexagonaux suivant les mêmes conventions qu'en Figure 5b. a) : cliché pris $0.41 \times 2T$ après que l'interface a atteint son maximum d'amplitude. b) : cliché pris $0.73 \times 2T$ après que l'interface a atteint son maximum d'amplitude.

0.4 Comportement des hexagones aux temps longs

0.4.1 Remarques d'ordre général

Les hexagones provenant des simulations sont apparemment transitoires. Ils ne durent que quelques secondes pendant lesquelles l'amplitude des modes spatiaux reste constante. C'est aussi ce qu'ont révélé les expériences (Kityk & Wagner, communication privée), la durée de vie du régime hexagonal étant cependant beaucoup plus longue. Après la disparition des hexagones, nos simulations ont décelé l'alternance de deux régimes: le premier (dont un exemple est donné Figure 8a), sans réelle symétrie, est associé à une baisse sensible de l'amplitude $\Delta\zeta$ de l'interface (voir Figure 7a). Le second, dont les propriétés sont celles d'un motif cristallin rectangulaire centré proche des hexagones (7b), se distingue par l'amplification de $\Delta\zeta$ vers le niveau atteint quand le régime était hexagonal. Une analyse spectrale du même type que celles des chapitres 0.3.2 et 0.3.2 a mis en évidence que la transition des hexagones vers le régime asymétrique était marquée par la disparition presque totale de certains modes spatiaux.

Nous basant sur les constats précédents, nous avons supposé que la solution obtenue est piégée par une orbite homocline dont le point fixe est le régime hexagonal. Nous nous sommes proposés d'étudier cette orbite dont les éléments accessibles sont le point fixe et le vecteur propre le plus instable. Si l'on parvient à simplifier suffisamment l'orbite à l'aide de considérations sur les fortes corrélations entre modes, comme le suggère l'analyse spectrale, Figure 8b, on pourra peut-être en calculer la trajectoire en tout point.

0.4.2 Détermination du point fixe

La méthode employée pour le calcul du point fixe consiste à forcer l'écoulement à avoir la symétrie hexagonale à des intervalles de temps réguliers. Ces pas de temps doivent être suffisamment petits pour que les effets de la direction instable du point fixe n'aient pas le temps de se manifester sensiblement. Dans ces conditions, la solution forcée devrait tendre vers un état proche du point fixe. La méthode de forçage d'un état s'appuie sur l'ensemble des invariances satisfaites par cet état. Elle est fondée sur des éléments de la théorie des symétries qui stipule en particulier que tout vecteur $\mathbf{q}(\mathbf{x}, t)$ est invariant sous l'application d'un opérateur $\mathbf{P}$ centré en $\mathbf{x}_0$ si

$$\mathbf{P}\mathbf{q}\left(\mathbf{x}-\mathbf{x}_0\right) = \mathbf{q}\left(\mathbf{P}\left(\mathbf{x}-\mathbf{x}_0\right)\right), \tag{19}$$

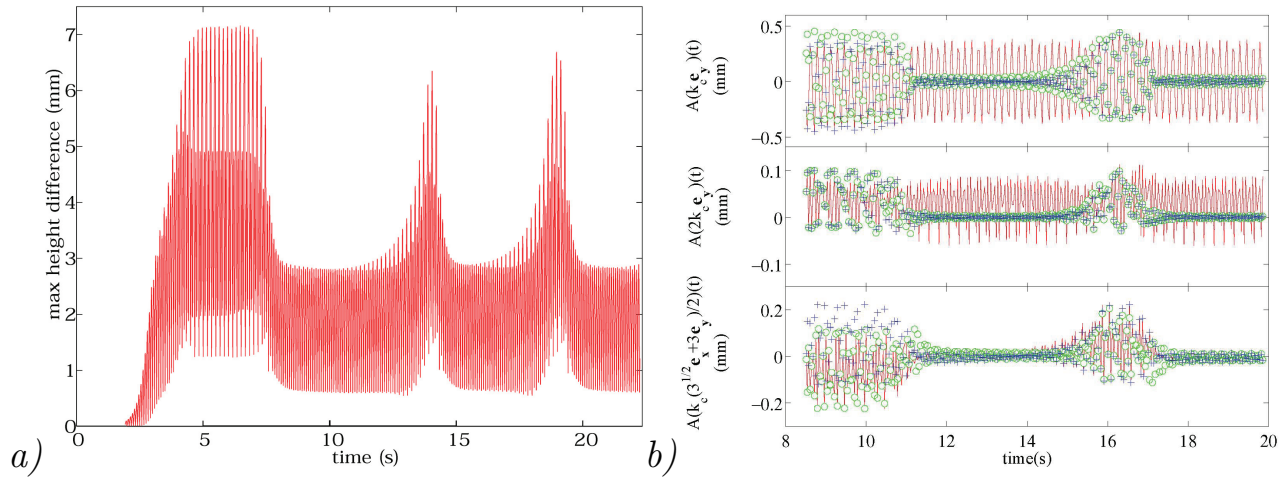

Figure 7: a) : évolution de $\Delta\zeta$ en fonction du temps. Résolution : 50 points par longueur d'onde en x et y, 180 points en z. b) : évolution temporelle des modes principaux. Pour chaque nombre d'onde sont tracées les évolutions de trois modes images les uns des autres par rotations successives de $2\pi/3$. La résolution est différente en a) et en b).

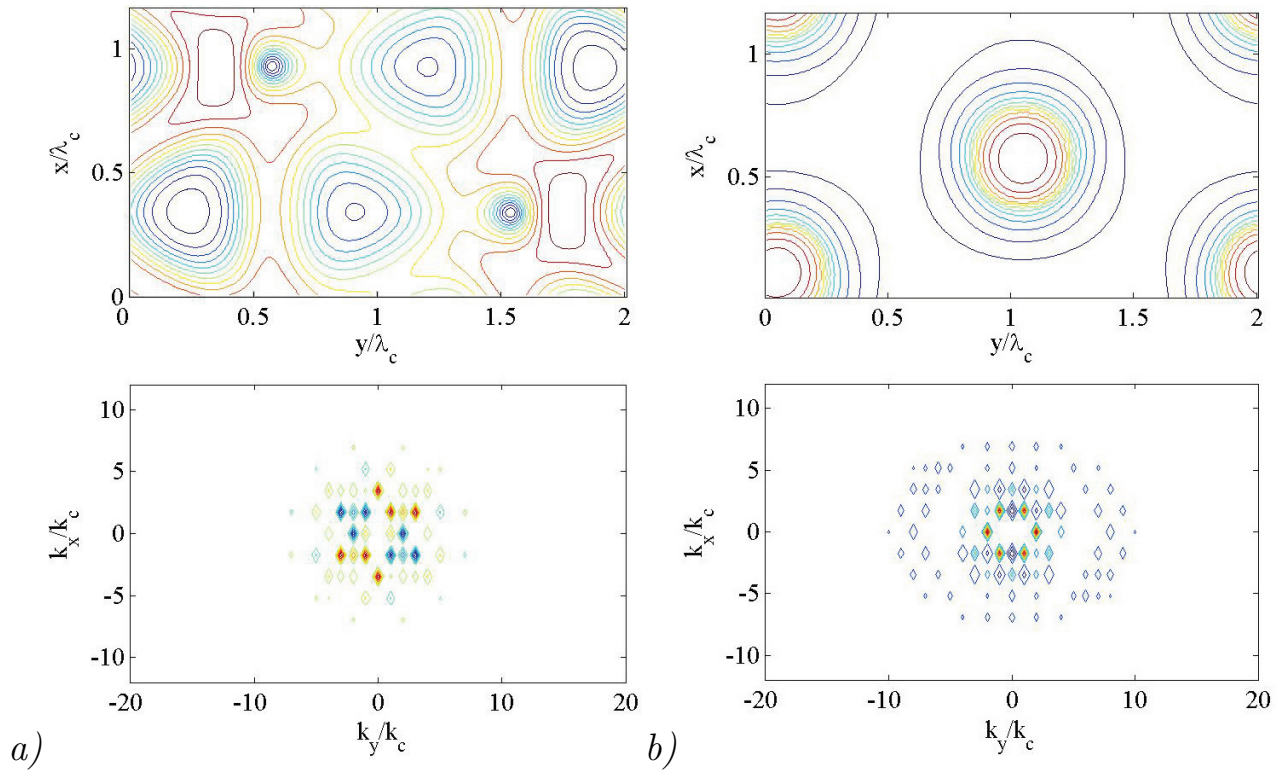

Figure 8: Exemples de motifs émergeant après la disparition des hexagones. a) : état sans symétrie particulière. b) : état à symétrie rectangulaire centrée. Haut : courbes de niveau de $\zeta(x, y, t)$. Bas : spectre spatial de ζ.

(19) se traduit dans l'espace spectral par

$$\mathbf{P}\left(\hat{\mathbf{q}}\left(\mathbf{k}\right)\right) - \hat{\mathbf{q}}\left(\mathbf{P}\left(\mathbf{k}\right)\right) = 0 \qquad \forall k \in \mathbb{R}^2 \tag{20}$$

où

$$\mathbf{q}(\mathbf{x}) = \int_{k_x} \int_{k_y} \hat{\mathbf{q}}(\mathbf{k}) \mathrm{e}^{\mathrm{i}\mathbf{k}\cdot(\mathbf{x})}\, dk_x\, dk_y \tag{21}$$

Il suffit ensuite d'appliquer (20) aux transformations qui laissent le champ considéré invariant. On obtient ainsi des contraintes sur les différentes composantes de $\hat{\mathbf{q}}$ et on en déduit la forme de $\hat{\mathbf{q}}$ ayant la symétrie exigée.

Dans le cas d'un motif hexagonal centré en O=(0,0) dont la droite (Ox) est un axe de symétrie, ces opérateurs sont:

- les rotations de $n\pi/3$, $n \in \mathbb{N}$,
- la réflexion d'axe (Ox) et de toutes ses images par rotations de $n\pi/3$.

L'application de (20) au motif hexagonal impose les conditions suivantes:

- Les composantes horizontales de tout vecteur de l'espace de Fourier sont des imaginaires purs,
- les composantes verticales de tout vecteur de l'espace de Fourier sont réelles,
- Pour tout vecteur d'onde $\mathbf{k}_{lm}$ dont les indices l et m indiquent ses composantes dans l'espace de Fourier (Figure 9a) et tout $\hat{\mathbf{q}}_{lm} = \hat{\mathbf{q}}(\mathbf{k}_{lm})$, $\hat{\mathbf{q}}_{lm_x} = \hat{\mathbf{q}}_{l-m_x}$, $\hat{\mathbf{q}}_{lm_y} = \hat{\mathbf{q}}_{-lm_y}$ et $\hat{\mathbf{q}}_{lm_z} = \hat{\mathbf{q}}_{-lm_z}$,
- $\hat{\mathbf{q}}_{lm_x}$ est parallèle à $\mathbf{k}_{lm}$.

Si les hexagones ne sont pas centrés en (0,0) mais en $\mathbf{x}_0$, cette méthode s'applique après avoir effectué le changement de variable $\mathbf{x} - \mathbf{x}_0 \to \mathbf{x}$. Une fois les coefficients calculés, il faut alors procéder au changement de variable inverse.

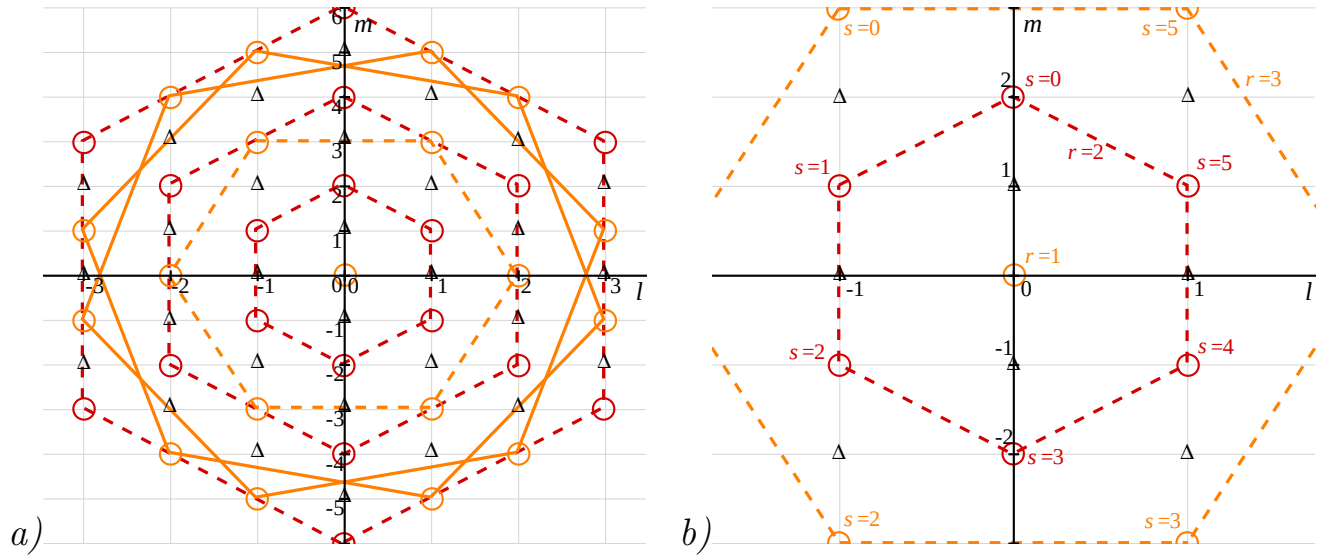

Figure 9: a) : premiers hexagones permis par le maillage dans l'espace de Fourier. Les Δ symbolisent les points qui ne font pas partie d'un hexagone complètement inclus dans le maillage. L'amplitude du mode correspondant doit alors être nulle, sans quoi on ajouterait à l'écoulement une composante qui ne vérifie pas les invariances des hexagones. Les cercles sont les modes appartenant à des hexagones complets du maillage. Les hexagones en pointillés ont les axes de symétrie (Ox) et (Oy), à l'inverse des hexagones en traits continus. Ces derniers doivent être traités spécialement. Le traitement des deux cas sera expliqué par la suite. b) : zoom de Figure 9a expliquant le passage du formalisme (l, m) vers (r, s), mêmes conventions que pour Figure 9a. Le vecteur $\mathbf{k}_{lm}$ joint le point (0,0) au point de coordonnées (l, m) de la grille. Le mode de Fourier $\mathbf{q}_{lm}$ est un vecteur quelconque dont l'origine est en (l, m).

Nous avons montré que certains modes $\hat{\mathbf{q}}_{lm}$ ne pouvaient contribuer à rendre la symétrie de l'écoulement hexagonale, comme indiqué Figure 9. Ils vérifient tous $l + m$ impair. L'amplitude de ces modes est fixée à 0. Les autres sont transformés comme suit :

- on fait une transformée de Fourier des différentes variables de champ en x et y,
- on calcule les coordonnées du centre $\mathbf{x}_0$ de l'hexagone principal formé de $\mathbf{k}_{02}$ et de ses images par rotations de $n\pi/3$ à partir de la phase de deux modes non colinéaires de cet hexagone,
- tous les modes $\hat{\mathbf{q}}_{lm}$ subissent un déphasage de $-\hat{\mathbf{k}}_{lm}\cdot\mathbf{x}_0$,
- les modes d'un même hexagone r sont notés $\hat{\mathbf{q}}_{rs}$, s variant de 0 à 5 (de même pour $\mathbf{k}_{rs}$). Le changement de formalisme est explicité Figure 9b,
- la composante verticale $\hat{q}_{rs_z}$ transformée selon le type d'hexagone auquel $\mathbf{k}_rs$ appartient: $\mathbf{S}_{10}$

$$\begin{aligned} \hat{\mathbf{q}}_{rs} &= \frac{1}{6}\sum_{s=0}^{5}\mathrm{Re}\left(\hat{\mathbf{q}}_{rs}\right) && \text{si l'hexagone admet (O}x\text{) comme axe de symétrie,} \\ \hat{\mathbf{q}}_{rs} &= \hat{\mathbf{q}}_{r's} = \frac{1}{12}\sum_{s=0}^{5}\left[\mathrm{Re}\left(\hat{\mathbf{q}}_{rs}\right)+\mathrm{Re}\left(\hat{\mathbf{q}}_{r's}\right)\right] && \text{sinon.} \end{aligned} \tag{22}$$

Pour la projection horizontale $\hat{\mathbf{q}}_{\mathrm{H}rs}$ de $\hat{\mathbf{q}}_{rs}$:

$$\begin{aligned} \hat{\mathbf{q}}_{\mathrm{H}rs} &= \frac{\mathrm{i}\mathbf{k}_{rs}}{6k_{rs}}\sum_{s'=0}^{5}\frac{\mathbf{k}_{rs'}}{k_{rs'}}\cdot\mathrm{Im}\left(\hat{\mathbf{q}}_{\mathrm{H}rs'}\right) && \text{si l'hexagone admet (O}x\text{) comme axe de symétrie,} \\ \hat{\mathbf{q}}_{\mathrm{H}rs} &= \hat{\mathbf{q}}_{\mathrm{H}r's} = \frac{\mathrm{i}\mathbf{k}_{rs}}{12k_{rs}}\sum_{s'=0}^{5}\left[\frac{\mathbf{k}_{rs'}}{k_{rs'}}\cdot\mathrm{Im}\left(\hat{\mathbf{q}}_{\mathrm{H}rs'}\right)+\frac{\mathbf{k}_{r's'}}{k_{r's'}}\cdot\mathrm{Im}\left(\hat{\mathbf{q}}_{\mathrm{H}rs'}\right)\right] && \text{sinon.} \end{aligned} \tag{23}$$

L'hexagone r' est le symétrique de r par rapport à (Ox). w, la composante verticale est transformée par (22) qui s'applique aussi aux variables scalaires telles que ζ ou la pression p. Le vecteur vitesse horizontal est transformé par (23),

- les nouveaux modes $\hat{\mathbf{q}}_{lm}$ subissent le déphasage inverse $\hat{\mathbf{k}}_{lm}\cdot\mathbf{x}_0$,
- On procède à la transformée de Fourier inverse des variables de champ.

On a testé cette méthode de symétrisation sur des cas statiques plus ou moins proches de motifs hexagonaux. Un exemple de forçage sur ζ est donné Figure 10. Ce test s'est révélé concluant. D'autres tests ont

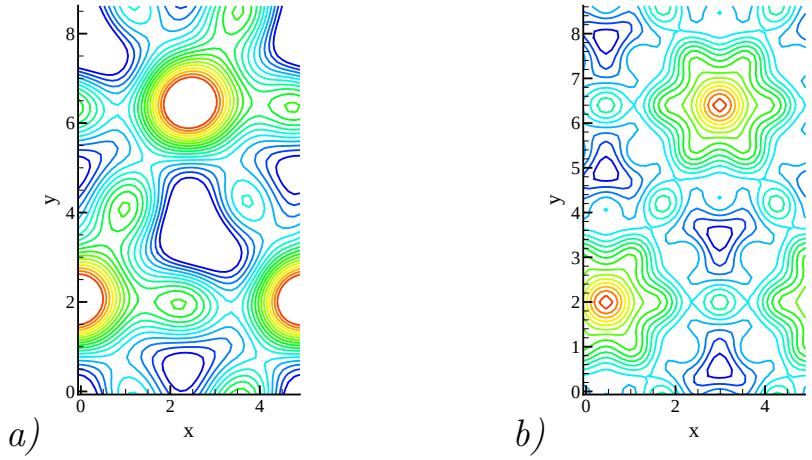

Figure 10: Test sur le forçage de la symétrie hexagonale de ζ. a) : état de l'interface avant le forçage . b) : interface après forçage.

été conduits sur ζ puis les vecteurs vitesses et se sont également avérés positifs.

0.4.3 Autres éléments de l'orbite

Le calcul du vecteur propre le plus instable est réalisé en prenant pour condition initiale l'état de l'écoulement sur le point fixe. Cet état est éventuellement légèrement perturbé et le forçage de la symétrie est désactivé. A des temps modérés, le vecteur propre le plus instable doit devenir dominant. Des caractéristiques singulières de l'orbite ont été mises en évidence Figure 7b ; particulièrement, des corrélations très fortes ont été repérées entre certains des modes principaux. En effectuant une analyse spectrale plus exhaustive, on devrait pouvoir comprendre plus en profondeur cette orbite.

0.5 Instabilité de dérive (drift instability)

L'instabilité de dérive a été observée depuis les années 1980 dans beaucoup de problèmes physiques. Douady et al. (1989) ont été les premiers à déceler ce phénomène dans l'expérience de Faraday réalisée dans un container annulaire étroit. Dans ces conditions, la dérive se traduit par un déplacement des motifs formés par l'interface dans la direction azimutale. La transition vers cette dérive se fait à une amplitude a supérieure à a_c au-dessus de laquelle persistent les ondes de Faraday. Fauve et al. (1991) ont élaboré une analyse basée sur un modèle phénoménologique dérivé des équations d'amplitude pour deux ondes se propageant vers la droite et la gauche. En conclusion de leur étude, l'instabilité de dérive serait la conséquence directe d'une brisure de symétrie entre ces deux ondes. De plus la vitesse de dérive des motifs serait constante.

Martín et al. (2002) ont développé un autre modèle théorique de cette instabilité à partir d'une analyse faiblement non linéaire dans un fluide visqueux avec surface libre. Ce modèle a lui-même pour base les résultats d'un papier de Martel et Knobloch (1997) donnant les modes propres solutions du problème d'ondes de surface sans forçage extérieur. Ces modes sont séparés en deux types de solutions: les ondes de surface non visqueuses et les ondes hydrodynamiques visqueuses, une solution jamais évoquée auparavant. L'une des hypothèses sous-jacentes au développement de Martín et al. (2002) est que la dérive serait conséquente au couplage d'un écoulement moyen dû aux modes hydrodynamiques avec le champ oscillant classique des ondes de Faraday. Cet écoulement moyen serait selon eux localisé près de la paroi basse. L'instabilité de dérive, d'après Martín et al. (2002), ne se traduirait pas par une dissymétrisation des ondes se déplaçant dans les deux directions, plus exactement, cette dissymétrisation existerait mais serait négligeable. Par ailleurs, la vitesse de dérive des motifs changerait au cours du temps.

0.5.1 Conditions physiques

Les simulations sont conduites dans un domaine périodique bidimensionnel, assimilable à un anneau de courbure très faible. Les modèles de Martín et al. (2002) et Vega et al. (2001) utilisent aussi cette approximation. Nous avons par ailleurs essayé de conformer au maximum les conditions physiques à celles de l'article de Martín et al. (2002) afin de nous placer dans l'espace de validité de leurs principales hypothèses:

$$hk = 2.37, \qquad C \lesssim 10^{-4}, \qquad |\omega - \omega_0| \ll 1. \tag{24}$$

à savoir, que la couche d'eau est peu profonde, la viscosité du fluide est faible et la fréquence du mode le plus amplifié est proche de celle de résonance avec le forçage périodique. Nous avons imposé $k = 2\pi/\lambda = 135\ \mathrm{m}^{-1}$, par conséquent la dimension horizontale de notre boîte est 46.54 mm et la hauteur moyenne de l'interface vaut $h_1 = 17.56$ mm. Le fluide inférieur a les propriétés physiques de l'eau, à savoir $\rho_1 = 1032\ \mathrm{kg\,m^{-3}}$ et $\nu_1 = 9.9205 \times 10^{-7}\ \mathrm{m^2\,s^{-1}}$, donc $C = 1.361 \times 10^{-4}$ remplit approximativement le critère (24-2). Martín et al. (2002) ont par ailleurs considéré l'écoulement d'une couche unique de fluide avec surface libre. Etant donnée la construction de la méthode numérique, seuls les écoulements avec deux fluides de masses volumiques et viscosités finies sont calculables. Nous avons opté pour que le fluide supérieur soit de l'air. Du fait de sa légèreté, il devrait influencer la dynamique de l'eau de manière presque insignifiante. Ses caractéristiques sont $\rho_2 = 1.205 \times 10^{-3}\ \mathrm{kg\,m^{-3}}$ et $\nu_2 = 1.511 \times 10^{-5}\ \mathrm{m^2\,s^{-1}}$. Nous avons aussi imposé à la couche d'air d'être importante pour minimiser l'effet des forces visqueuses dues notamment à la paroi supérieure, ce qui a été vérifié avec l'analyse linéaire de Kumar et Tuckerman (1994). La hauteur d'air a été fixée à 5 mm. La tension superficielle σ a été relaxée à 0, permettant un gain de temps de calcul substantiel.

La fréquence d'oscillation a été fixée à 11.6 Hz, à proximité de la fréquence critique 11.49 Hz de la première langue sous-harmonique respectant ainsi (24-3). La période d'oscillation du fluide est le double de la période

de vibration du container $T = 2\pi/\omega$. Pour la fréquence choisie, la transition vers les ondes de Faraday est de nature supercritique, une contrainte importante dictée par l'utilisation d'une théorie faiblement non linéaire. La résolution spatiale a été déterminée de façon à ce que les pas de temps numériques puissent être de l'ordre d'un centième de la période d'oscillation T. Une résolution de 100×125 respectant à peu près ce dernier critère a été choisie.

0.5.2 Resultats

Une étude préliminaire du taux de croissance γ en fonction de a montre que γ n'est pas une fonction affine de l'accélération. La détermination du seuil d'instabilité primaire résulte de l'étude précédente et de la méthode de recherche du seuil expliquée au chapitre 0.3.1. Une valeur de $a/g = 0.054185$ a été trouvée.

Premier aperçu des solutions observables

Au-dessus du seuil de Faraday, plusieurs types de solutions ont été obtenues à saturation : des solutions dont l'interface forme des motifs stationnaires et d'autres dont les motifs se déplacent horizontalement. Ces deux états sont systématiquement différenciés lors de visualisations des champs moyens (la période d'intégration pour le calcul des moyennes doit être un multiple de $2T$). En effet, quand les motifs ne bougent pas, les lignes de courant dessinent des boucles fermées ; de plus, l'écoulement possède des axes de réflexion verticaux. Au contraire, quand l'interface se déplace, les lignes de courant sont ouvertes et il n'existe plus d'axe de réflexion ; c'est sur cette base que Fauve et al. (1991) avaient établi leur modèle de naissance de la dérive. La dernière catégorie d'états rencontrée est elle-même scindée en deux sous-ensembles distingués par une propriété de symétrie très particulière : l'invariance par translation de $\lambda/2$ selon $(\mathrm{O}x)$ des champs moyennés en temps (tandis que la périodicité de tous les écoulements instantanés est λ).

Les solutions à motifs immobiles rencontrées vérifient toutes cette propriété d'invariance.

Un dernier type très singulier d'états a été remarqué. Les motifs semblent ne pas se déplacer, pourtant, l'écoulement n'admet pas d'axe vertical de réflexion. De plus, $\Delta\zeta = \zeta_{\max} - \zeta_{\min}$ semble très légèrement modulé en amplitude sur des temps longs devant T.

Les quatre catégories d'états sont présentées Figures 11 et 12. Ces états apparaissent spontanément et sont tous stables.

Les diagrammes des Figures 11 et 12 montrent entre autres que les champs moyens de vitesses et leur gradient sont maximaux, en terme d'amplitude, à proximité de l'interface, en conclusion de quoi il apparaît une divergence évidente entre nos simulations numériques et l'hypothèse sur laquelle repose en partie le développement de Martín et al. (2002): le couplage de l'écoulement oscillant avec l'écoulement moyen localisé près de la paroi.

Diagrammes de bifurcation

Nous avons tracé des diagrammes de bifurcation selon trois grandeurs qui semblent, à la vue des champs précédents, bien séparer les différents cas d'écoulements. La première de ces quantités est $\Delta\zeta$; elle caractérise généralement bien l'écoulement à proximité du seuil d'instabilité primaire. Les flux horizontaux moyennés en temps dans les couches fluides servent à quantifier la dérive. Ils sont exprimés de la manière suivante:

$$\begin{aligned} \phi_{eau} &= \frac{1}{4T\lambda} \int_0^{\lambda} \int_0^{<\zeta(x)>_t} \int_t^{t+4T} \mathbf{u}(x,y,t).\mathbf{e}_x \, dy \, dt \, dx. \\ \phi_{air} &= \frac{1}{8T\lambda} \int_0^{\lambda} \int_{<\zeta(x)>_t}^{h} \int_t^{t+8T} \mathbf{u}(x,y,t).\mathbf{e}_y \, dy \, dt \, dx \end{aligned} \tag{25}$$

Enfin, pour séparer les champs moyens qui satisfont ou non l'invariance par translation de $\lambda/2$ nous utilisons une norme basée sur la décomposition de Fourier en x et t (26) des vitesses,

$$\mathbf{u}(\mathbf{x},t) = \sum_m \sum_n \hat{\mathbf{u}}_{m,n}(y) \mathrm{e}^{\mathrm{i}\left(\frac{2\pi m x}{\lambda} + \frac{\pi n t}{T}\right)} \tag{26}$$

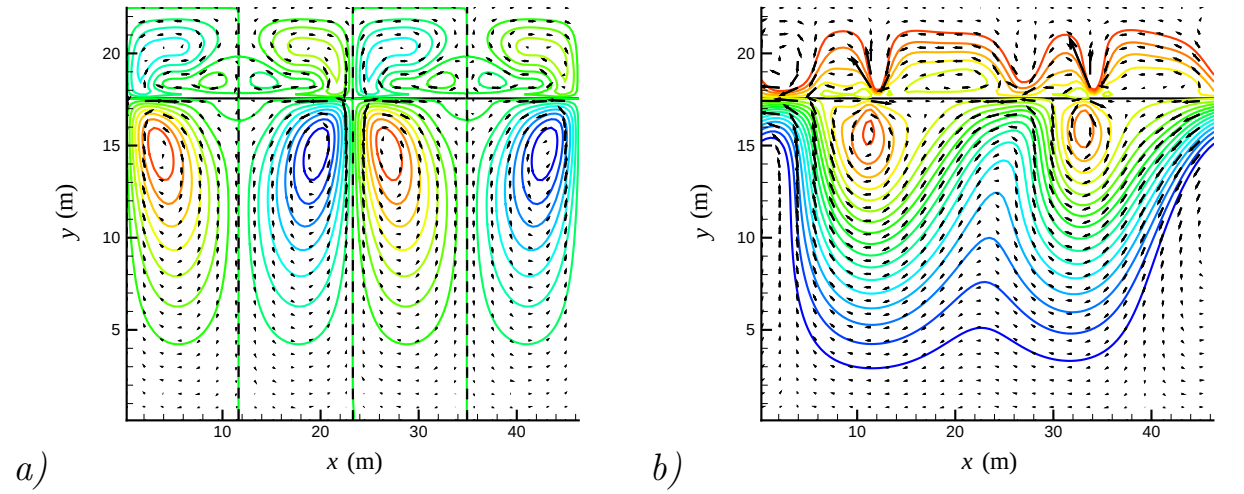

Figure 11: a) : aperçu de la moyenne sur $4T$ de la fonction de courant (couleurs) et de la hauteur d'interface ζ (ligne continue noire) pour une accélération de $a = 0.057g$. Les vecteurs représentent le champ de vitesses. Enfin, les lignes pointillées sont des axes de symétrie de l'écoulement moyen. Noter que dans le cas d'une symétrie axiale, la fonction de courant doit être impaire. b) : aperçu de la moyenne sur $4T$ de l'écoulement pour $a = 0.0548g$. Mêmes conventions qu'en Figure 11a. Figure 11a et Figure 11b correspondent respectivement aux solutions pointées par les flèches noire et orange sur le diagramme de bifurcation Figure 13.

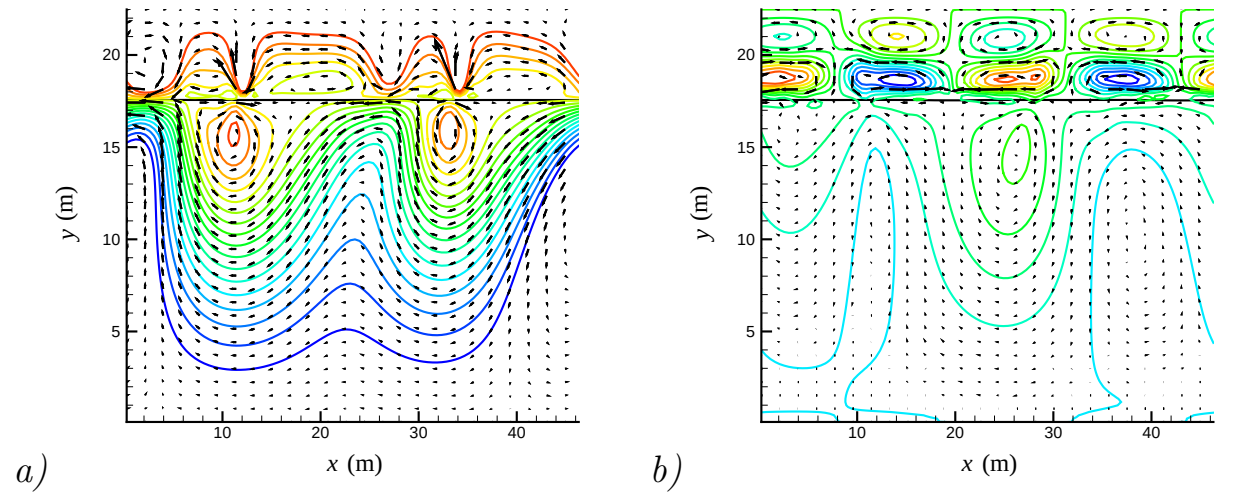

Figure 12: Ecoulement moyenné sur $4T$ pour a) $a = 0.0545g$, b) $a = 0.06g$. Mêmes conventions qu'en Figure 11a. 12a correspond à la solution pointée par la flèche rouge sur le diagramme de bifurcation Figure 13a. L'aperçu 12b ne correspond à aucun point du diagramme de bifurcation Figure 13a.

Nous définissons la mesure de $\lambda/2$-périodicité

$$\delta_{\lambda/2} = \frac{\overline{E}_{c_{odd}}}{\overline{E}_{c_{tot}}}, \tag{27}$$

où $\overline{E}_{c_{odd}}$ est l'énergie cinétique spectrale des modes $\hat{\mathbf{u}}_{2m+1,0}$ constants dans le temps et dont les nombres d'onde k sont des multiples impairs de k_c. $\overline{E}_{c_m}$ est l'énergie cinétique spectrale de tous les modes statiques $\hat{\mathbf{u}}_{m,0}$.

$$\overline{E}_{c_{odd}} = \sum_m \left(|\hat{u}_{2m+1,0}|^2 + |\hat{v}_{2m+1,0}|^2 \right) \qquad \overline{E}_{c_{tot}} = \sum_m \left(|\hat{u}_{m,0}|^2 + |\hat{v}_{m,0}|^2 \right). \tag{28}$$

La quantité $\delta_{\lambda/2}$ est comprise entre 0 et 1 et devient nulle quand l'écoulement est parfaitement invariant par translation de $\lambda/2$.

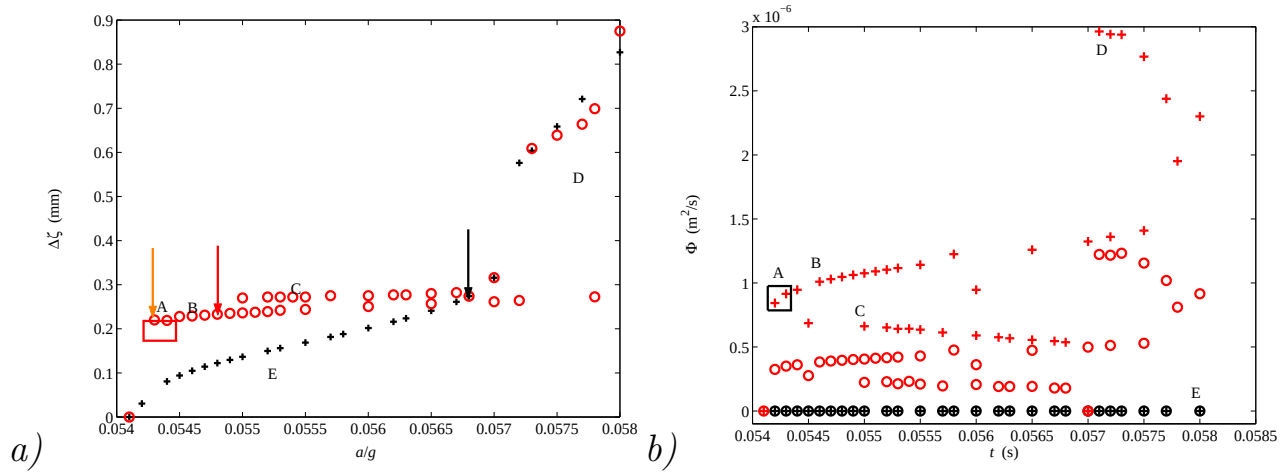

Figure 13: a) : évolution de $\Delta\zeta$ en fonction de a/g. Cercles : états apparaissant spontanément sans forçage de symétrie. croix : solutions observées lorsque la réflexion verticale est forcée. b) : évolution des flux ϕ en fonction de a/g. Rouge : quand on ne force pas la symétrie das l'écoulement. Noir : quand la réflexion verticale est forcée. Dans b) les cercles remplacent le flux d'eau ϕ_{eau}, les croix, ϕ_{air}. Les flèches noire, orange et rouge pointent respectivement vers les états décrits Figures 11a, 11b et 12a. Sur ces diagrammes, différentes branches correspondant soit à des écoulements aux symétries différentes, soit à des variations brutales des grandeurs $\Delta\zeta$, ϕ et $\delta_{\lambda/2}$ laissant présager la présence d'une bifurcation.

Il ressort des diagrammes de bifurcation (Figures 13 et 14) que l'instabilité de dérive est presque simultanée au seuil de Faraday. L'écoulement en $a = 0.0542g$, notre premier point de mesure au-dessus de a_c, a déjà un flux moyen non nul. L'instabilité de doublement de période sur l'écoulement moyen a lieu un peu plus tardivement, entre $0.0543g$ et $0.0544g$, l'écoulement $\lambda/2$-périodique se destabilise spontanément vers la branche B qui semble persister jusqu'à notre plus haut point de mesure $a = 0.058g$. Une autre branche possède manifestement les mêmes symétries mais se différencie de B par des valeurs distinctes des trois variables de bifurcation. Cette branche, nommée C, est stable sur une plage d'accélérations qui recoupe en partie celle sur laquelle B existe ($a/g \in [0.0545, 0.0568]$). Ce phénomène est appelé bistabilité ou hystéresis, La branche B ou C vers laquelle une solution tendra dépend de l'histoire de cette solution et entre autres de la condition initiale adoptée. La nouvelle branche, C, se démarque notamment par des valeurs très élevées de la grandeur $\delta_{\lambda/2}$. En $0.057g$, cette branche se déstabilise, la solution symétrique sans flux devenant l'attracteur principal ; l'écoulement moyen possède à nouveau une longueur d'onde de $\lambda/2$. Au-delà de $0.057g$, la solution sans flux se déstabilise au profit d'une solution avec flux mais conserve sa longueur d'onde moyenne $\lambda/2$. Sur cette nouvelle branche, nommée D, l'amplitude des oscillations d'interface se met à croître fortement.

La dernière branche figurant sur ces diagrammes provient d'écoulements dont l'invariance par réflexion a été forcée, elle sera appelée E. Le forçage de la réflexion s'inspire très largement de la méthode qui a été élaborée au chapitre 0.4.2. $\Delta\zeta$ semble sur une partie du diagramme être affecté par la symétrie de réflexion. Le flux est logiquement identiquement nul sur toute la branche, il en est de même de $\delta_{\lambda/2}$. Aux accélérations les plus faibles jusqu'à 0.057, cette branche enregistre des valeurs de $\Delta\zeta$ sensiblement inférieures à celles mesurées dans le cas sans forçage. En $0.057g$ les branches C et E se rejoignent sur les trois diagrammes, il s'agit donc très probablement de la même solution, que la symétrie de réflexion ait été forcée ou non.

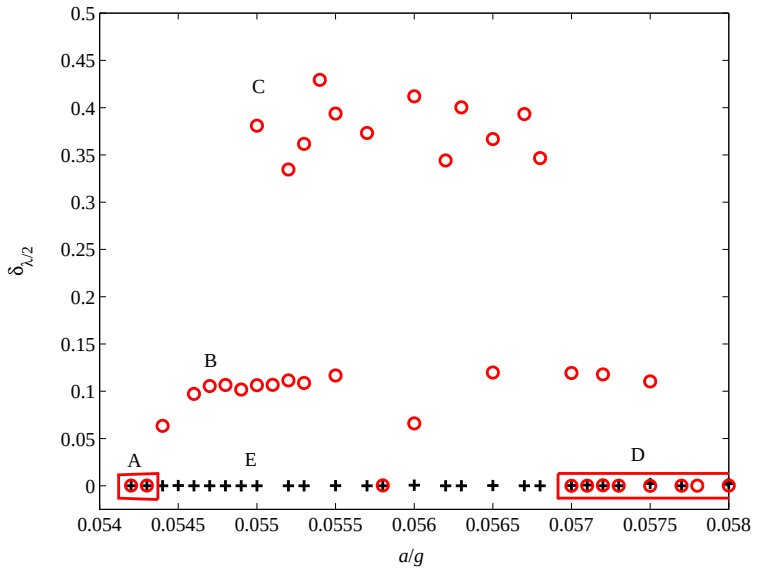

Figure 14: Coefficient d'apériodicité en $\lambda/2$ du champ moyen en fonction de a/g. Mêmes conventions que sur Figure 13a.

Au-dessus de $0.057g$, $\Delta\zeta$ subit une augmentation similaire à celle de la branche D.

Des diagrammes de stabilité détaillés ont été tracés pour des accélérations atteignant $0.058g$, soit 8% au-dessus de a_c. L'écart au seuil n'est pas grand, mais de nombreuses solutions aux symétries différentes ont été décelées.

Comparaison des spectres d'interface entre la branche forcée et la branche non forcée

La dérive naîtrait d'une déstabilisation de la symétrie droite-gauche de l'écoulement, comme le suggère l'article de Fauve et al. (1991) en conclusion d'une étude phénoménologique portant sur une équation d'amplitude des deux modes principaux. D'après la convention (26), ces deux modes seraient dans le cas de la hauteur d'interface $\hat{\zeta}_{1,1}$ et $\hat{\zeta}_{1,-1}$. Nous souhaitons voir si le déséquilibre entre ces deux modes contra-propagatifs est effectivement corrélé à l'émergence de la dérive. Nous procédons donc à la décomposition spectrale en k et ω de l'interface et sélectionnons $\hat{\zeta}_{1,1}$ et $\hat{\zeta}_{1,-1}$. L'écart relatif enregistré entre ces deux modes est de l'ordre de 0.01%. Nous concluons alors que les écoulements sans flux vérifient bien la symétrie gauche-droite, au moins à l'interface. Nous avons décidé de tracer $\hat{\zeta}_{1,1}$ en fonction d'un paramètre $\epsilon = (a - a_c)/a_c$ remplaçant l'accélération et rendant possibles les conversions en échelle logarithmique (Figure 15a), pour extraire d'éventuelles lois de puissance. En figure 15b sont représentés les autres modes les plus importants. Les deux graphiques Figure 15 révèlent que des lois de puissance existent bel et bien entre $\hat{\zeta}_{m,n}$ et ϵ, aux faibles accélérations (jusqu'à $0.57g$ environ, valeur précédant le saut d'amplitude remarqué sur le diagramme de bifurcation Figure 13a). Les analyses faiblement non linéaires prévoient une dépendance $\hat{\zeta}_{m,n}{=}\epsilon^{\frac{l}{2}}$ pour n inférieur à m. la loi $\hat{\zeta}_{1,1}(\epsilon)$ est caractérisée par un exposant de 0.40, sensiblement inférieur aux prévisions utilisant l'approche faiblement non linéaire. Les autres modes sont tous sous-évalués. On remarquera par ailleurs des ressemblances frappantes entre les comportements de certains modes, par exemple $\hat{\zeta}_{1,1}$ et $\hat{\zeta}_{1,3}$. Enfin, dans les régimes étudiés, le mode $\hat{\zeta}_{1,1}$ est complètement dominant, les autres modes sont à près de deux ordres de grandeur en dessous. Nous notons aussi que les modes tels que $m+n$ impair sont totalement absents de la dynamique lorsque la symétrie est forcée. Ils n'ont pas été dessinés car trop bas.

Nous traçons maintenant le graphe équivalent à Figure 15a sur l'ensemble des solutions pour lesquelles la symétrie droite-gauche n'est pas forcée (Figure 16a). Les tracés en log-log étant inintéressants, on a choisi l'échelle linéaire et de réutiliser a/g en abscisses par souci d'harmonisation. Figure 16b montre le coefficient

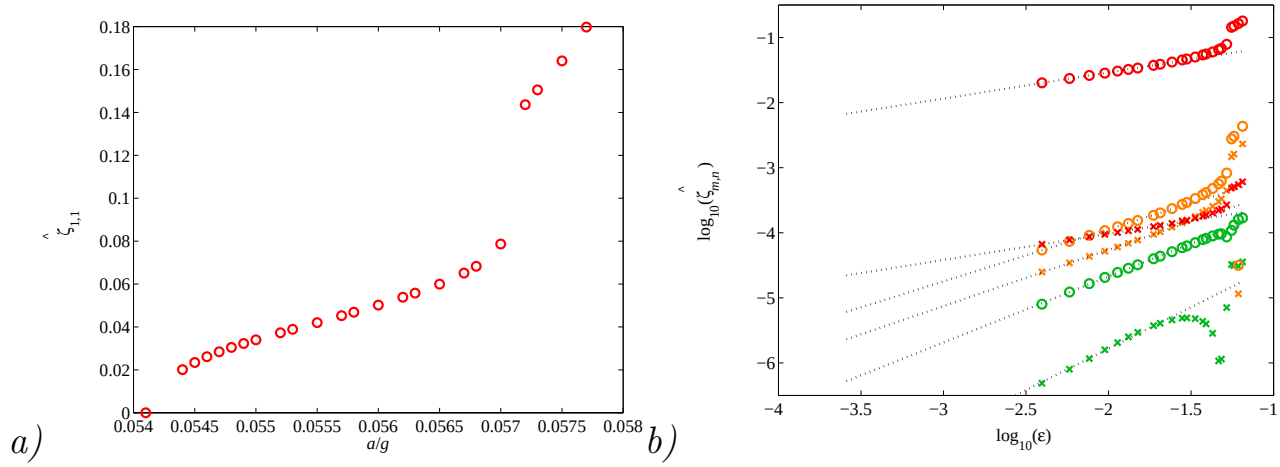

Figure 15: a) : évolution du mode $|\hat{\zeta}_{1,1}|$ quand l'invariance par réflexion est forcée (branche E) en fonction du paramètre ϵ. ϵ mesure la distance de l'accélération au seuil de Faraday dans un diagramme log-log. la ligne pointillée noire est une courbe de régression linéaire sur les dix premiers points .b) : comparaison avec les autres modes. Cercles rouges : $|\hat{\zeta}_{1,1}|$. Croix rouges : $|\hat{\zeta}_{1,3}|$. Cercles orange : $|\hat{\zeta}_{2,0}|$. Croix orange : $|\hat{\zeta}_{2,2}|$. Cercles verts : $|\hat{\zeta}_{3,1}|$. Croix vertes : $|\hat{\zeta}_{3,3}|$. Des courbes de régression linéaire sur les dix premiers points ont été ajoutées en pointillés noirs pour chaque mode.

R évoqué par Fauve et al. (1991) pour mesurer l'écart d'amplitude entre $\hat{\zeta}_{1,1}$ et $\hat{\zeta}_{1,-1}$. R est exprimé comme suit:

$$R = \frac{1}{2} \ln \left| \frac{\hat{\zeta}_{1,1}}{\hat{\zeta}_{1,-1}} \right| \tag{29}$$

A la différence de l'écoulement sans flux, les deux modes de mêmes fréquences se propageant dans des

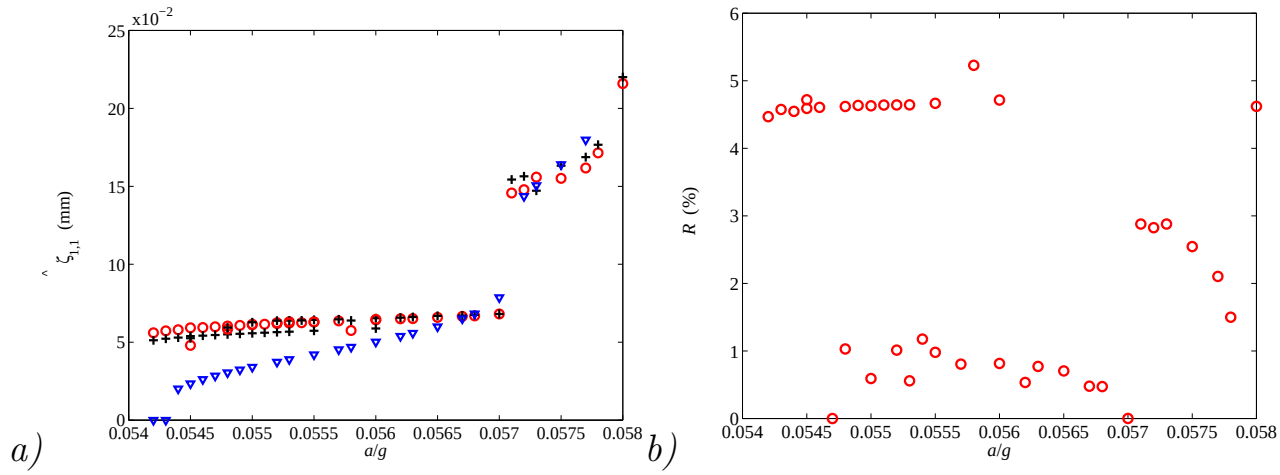

Figure 16: a) : évolution du mode $|\hat{\zeta}_{1,1}|$ en fonction de a/g sur une échelle linéaire. Cercles : $\hat{\zeta}_{1,-1}$, croix : $\hat{\zeta}_{1,1}$. b) : coefficient R en fonction de a/g.

directions oppsées ont des amplitudes différentes, ce qu'avaient prévu Fauve et al. (1991). Les transitions entre les différents états repérés sur les diagrammes de bifurcation (Figures 13 et 14) se répercutent sur le comportement de ces modes. On notera en particulier la symétrisation imparfaite entre $\hat{\zeta}_{1,1}$ et $\hat{\zeta}_{1,-1}$ sur

la branche C. Le coefficient R, quant à lui, est exclusivement corrélé au diagramme de flux Figure 13b, et confirme que symétrie gauche-droite et flux sont étroitement liés. D'autres modes ont été étudiés mais ne figurent pas ici. Les modes tels que $m+n$ est pair sont les seuls censés apparaître dans le problème de Faraday. Ils font partie d'un sous-espace invariant des solutions, sous-espace naturellement atteint près du seuil a_c, ce qui est démontrable à l'aide de l'analyse faiblement non linéaire et de la théorie de Floquet. Il a été remarqué que les modes vérifiant $m+n$ impair émergent dans certains cas, exclusivement dans le régime non forcé et sur les branches B et C, le support de $\delta_{\lambda/2}$. C'est le signe de la bifurcation de doublage de période (sur l'écoulement moyen) mentionnée au chapitre 0.5.2, la seule possibilité de sortie de ce sous-espace.

Nous avons enfin relié le coefficient R à la vitesse angulaire de déplacement du motif $\omega_{pattern}$. Nous avons observé que le motif à l'interface se déplace, pour toute branche caractérisée par un flux moyen non nul (branches A, B, C et D). Au contraire, en l'absence de flux (branche E) le motif reste immobile. De plus, la vitesse de déplacement de l'interface est constante ; nous l'avons tracée en fonction de l'accélération, Figure 17a.

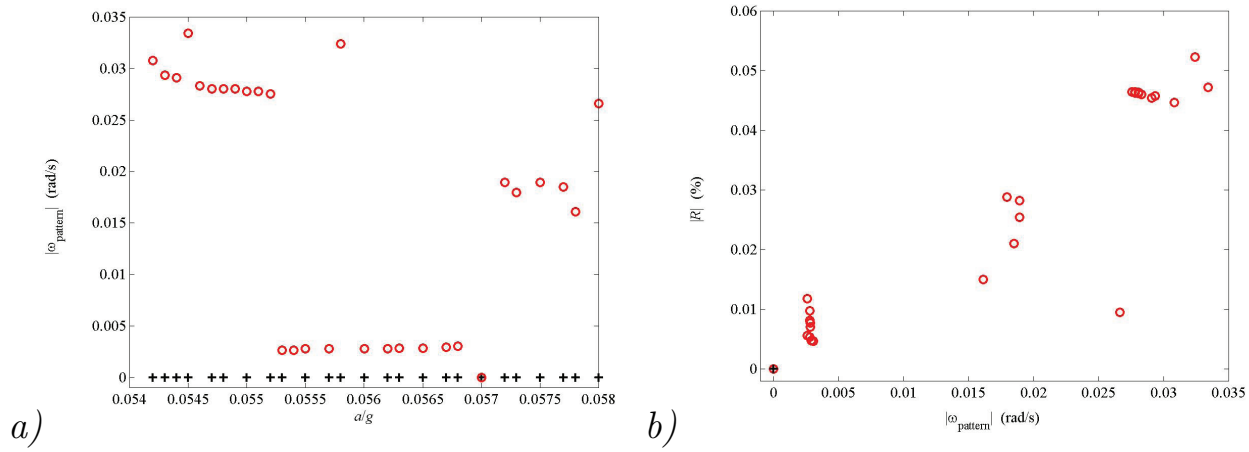

Figure 17: a) : évolution de la vitesse de déplacement de l'interface $\omega_{pattern}$ en fonction de a/g sur une échelle linéaire. Cercles : solutions asymétrique. Une partie seulement des résultats sans forçage a été traitée: branche A ($a/g \in [0.0542, 0.0543]$), branche B ($a/g \in [0.0544, 0.0552]$), branche C ($a/g \in [0.0553, 0.0568]$), branche D ($a/g \in [0.0572, 0.058]$). Croix : solutions dont la symétrie de réflexion a été forcée, branche E. Une corrélation forte avec le flux moyenné est à noter. b) : corrélation entre $\omega_{pattern}$ et R. Mêmes conventions qu'en Figure 17a. Tous les points corerspondant à la branche E sont confondus, d'où la présence d'une unique croix sur le graphique.

Les nuages de points représentés Figure 17b sont relativement peu diffus, montrant une corrélation évidente entre $\omega_{pattern}$ et R. De plus, la tendance de la fonction $\omega_{pattern}(R)$ apparaît comme monotone, à la diffusion des points près. Enfin, R culmine à une valeur d'environ 5%. Ces dernières remarques mettent en évidence que nos simulations seraient plus en accord avec la théorie de Fauve et al. (1991) que celle Martín et al. (2002). Une des causes du désaccord pourrait probablement être la différence constatée au niveau de la localisation du champ moyen.

0.6 Conclusion

Nous sommes les premiers à avoir realisé des simulations tridimensionnelles des ondes de Faraday fonctionnant dans des régimes pleinement non linéaires. Les validations ont montré un accord qualitatif et quantitatif impressionnant entre l'expérience et la simulation numérique. Une telle approche constitue une alternative intéressante aux expériences sur l'instabilité de Faraday, car tous les champs de variables sont calculables sans perturber aucunement l'écoulement. Il peut donc fournir une grande quantité d'informations intéressantes et

inaccessibles à l'expérience. De plus, il n'y a pas d'effets parasites induits par les perturbations extérieures. En contrepartie, le calcul est incomparablement plus coûteux en temps que l'expérimentation et doit se faire, pour l'instant, dans un domaine restreint.

La phase de validation a permis de mettre en évidence un phénomène exotique consistant en une alternance de deux types de motifs. Le scénario que nous avons envisagé est le piégeage de notre état dans une orbite homocline dont nous avons pensé et mis en oeuvre les moyens d'exploration à l'aide des outils tirés de la théorie des systèmes dynamiques et celle des symétries.

Enfin, nous avons exploré le phénomène d'instabilité de dérive dans un domaine annulaire, cas peu abordé jusqu'à maintenant. Nous avons établi un diagramme de bifurcation pour les accélérations proches du seuil. Ce diagramme, ainsi que l'analyse spectrale et d'autres moyens de visualisation ont permis de retirer certaines propriétés de l'écoulement et de découvrir une dynamique très riche. Ce problème qui semble au premier abord éloigné des motifs recèle pourtant des énigmes tout aussi intéressantes sur la théorie des symétries.

Le mécanisme d'apparition de la dérive a été exploré. Selon nos simulations, la dérive proviendrait de la dissymétrisation des modes principaux se déplaçant dans les directions horizontales opposées $\hat{\zeta}_{1,1}$ et $\hat{\zeta}_{1,-1}$, ce que prévoit l'étude menée par Fauve et al. (1991). Une cause envisageable de la différence observée avec le travail de Martín et al. (2002) réside dans la nature et la position du champ moyen couplé avec le champ oscillant, selon leur hypothèse. La localisation du champ moyen est elle-même liée à la viscosité. Quand C tend vers 0, le champ moyen est bien dominant à la paroi. Si C est fini, le champ moyen est plus fort à l'interface. Les disparités entre nos simulations et l'analyse de Martín et al. (2002) pourraient être la conséquence du fait qu'un C de l'ordre de 10^{-4} serait déjà au-dessus de la limite de validité de la théorie de Martín et al. (2002). Nous n'avons donc aucunement réfuté cette théorie mais pensons seulement que sa limite de validité sur la viscosité a été surévaluée. Ceci expliquerait pourquoi nos calculs s'ajustent bien avec le modèle de Fauve et al. (1991) et non avec celui de Martín et al. (2002).

Bibliography

Bechhoefer, J., Ego, V., Manneville, S., et Johnson, B. (1995). An experimental study of the onset of parametrically pumped surface waves in viscous fluids. *J. Fluid Mech.*, 288:325–350.

Benjamin, T. B. et Ursell, F. (1954). The stability of the plane free surface of a liquid in vertical periodic motion. *Proc. R. Soc. Lond.*, 225:505–515.

Besson, T., Edwards, W. S., et Tuckerman, L. S. (1996). Two-frequency parametric excitation of surface waves. *Phys. Rev. E*, 54:507–513.

Beyer, J. et Friedrich, R. (1995). Faraday instability: linear analysis for viscous fluids. *Phys. Rev. E*, 51:1162–1168.

Binks, D., Westra, M.-T., et van der Water, W. (1997). Effect of depth on the pattern formation of Faraday waves. *Phys. Rev. Lett.*, 79:5010–5013.

Brackbill, J. U., Kothe, D. B., et Zemach, C. (1992). A continuum method for modeling surface tension. *J. Comput. Phys.*, 100:335–354.

Cerda, E. A. et Tirapegui, E. L. (1998). Faraday's instability in viscous fluid. *J. Fluid Mech.*, 368:195–228.

Chen, P. (2002). Nonlinear wave dynamics in Faraday instabilities. *Phys. Rev. E*, 65:036308.

Chen, P. et Viñals, J. (1999). Amplitude equation and pattern selection in Faraday waves. *Phys. Rev. E*, 60:559–570.

Chen, P. et Wu, K.-A. (2000). Subcritical bifurcations and nonlinear balloons in Faraday waves. *Phys. Rev. Lett.*, 85:3813–3816.

Chorin, A. J. (1968). Numerical simulation of the Navier-Stokes equations. *Math. Comput.*, 22:745–762.

Christiansen, B., Alstrøm, P., et Levinsen, M. T. (1992). Ordered capillary-wave states: Quasicrystals, hexagons, and radial waves. *Phys. Rev. Lett.*, 68:2157–2161.

Douady, S., Fauve, S., et Thual, O. (1989). Oscillatory phase modulation of parametrically forced surface waves. *J. Phys. II*, 10:309–315.

Edwards, W. S. et Fauve, S. (1993). Parametrically excited quasicrystalline surface waves. *Phys. Rev. E*, 47:R788–R791.

Ezerskii, A. B., Rabinovich, M. I., Reutov, V. P., et Starobinets, I. M. (1986). Spatiotemporal chaos in the parametric excitation of a capillary ripple. *Sov. Phys., JETP*, 64:1228–1236.

Faraday, M. (1831). On a peculiar class of acoustical figures; and on certain forms assumed by groups of particles upon vibrating elastic surfaces. *Philos. Trans. R. Soc. London*, 121:299–340.

Fauve, S., Douady, S., et Thual, O. (1991). Drift instabilities of cellular patterns. *J. Phys. II*, 1:311–322.

Goda, K. (1979). A multistep technique with implicit difference schemes for calculating two- or three-dimensional cavity flows. *J. Comput. Phys.*, 30:76–95.

Harlow, F. H. et Welch, J. E. (1965). Numerical calculation of time dependent viscous incompressible flow of fluid with free surface. *Phys. Fluids*, 8:2182.

Hirt, C. W. et Nichols, B. D. (1981). Volume of fluid (VOF) method for the dynamics of free boundaries. *J. Comput. Phys.*, 39:201–225.

Huepe, C., Ding, Y., Umbanhowar, P., et Silber, M. (2006). Forcing function control of Faraday wave instabilities in viscous fluids. *Phys. Rev. E*, 73:16310.

Kityk, A. V., Embs, J., Mekhonoshin, V. V., et Wagner, C. (2005). Spatiotemporal characterization of interfacial Faraday waves by means of a light absorption technique. *Phys. Rev. E*, 72:036209.

Kityk, A. V., Embs, J., Mekhonoshin, V. V., et Wagner, C. (2009). Erratum: Spatiotemporal characterization of interfacial Faraday waves by means of a light absorption technique. *Phys. Rev. E*, 79:029902.

Kudrolli, A. et Gollub, J. P. (1996). Patterns and spatiotemporal chaos in parametrically forced surface waves: a systematic survey at large aspect ratio. *Physica D*, 97:133–154.

Kudrolli, A., Pier, B., et Gollub, J. P. (1998). Superlattice patterns in surface waves. *Physica D*, 123:99–111.

Kumar, K. (1996). Linear theory of Faraday instability in viscous fluids. *Proc. R. Soc. Lond.*, 452:1113–1126.

Kumar, K. et Tuckerman, L. S. (1994). Parametric instability of the interface between two fluids. *J. Fluid Mech.*, 279:49–68.

Lioubashevski, O., Arbell, H., et Fineberg, J. (1996). Dissipative solitary states in driven surface waves. *Phys. Rev. Lett.*, 76:3959–3962.

Martel, C. et Knobloch, E. (1997). Damping of nearly inviscid water waves. *Phys. Rev. E*, 56:5544–5548.

Martín, E., Martel, C., et Vega, J. M. (2002). Drift instability of standing Faraday waves. *J. Fluid Mech.*, 467:57–79.

Müller, H. W. (1993). Periodic triangular patterns in the Faraday experiment. *Phys. Rev. Lett.*, 71:3287–3290.

Murakami, Y. et Chikano, K. (2001). Two-dimensional direct numerical simulation of parametrically excited surface waves in viscous fluid. *Phys. Fluids*, 13:65–74.

O'Connor, N. L. (2008). *The complex spatiotemporal dynamics of a shallow fluid layer*. PhD thesis, Virginia Polytechnic Institute and State University, Blacksburg, VA.

Osher, S. et Sethian, J. (1988). Fronts propagating with curvature dependent speed: algorithms based on hamilton–jacobi formulations. *J. Comput. Phys.*, 79:12–49.

Périnet, N., Juric, D., et Tuckerman, L. S. (2009). Numerical simulation of Faraday waves. *J. Fluid Mech.*, 635:1–26.

Peskin, C. S. (1977). Numerical analysis of blood flow in the heart. *J. Comput. Phys.*, 25:220–252.

Porter, J., Topaz, C., et Silber, M. (2004). Pattern control via multi-frequency parametric forcing. *Phys. Rev. Lett.*, 93:034502.

Rayleigh, L. (1883a). On maintained vibrations. *Philos. Mag.*, 15:229–235.

Rayleigh, L. (1883b). On the crispations of fluid resting upon a vibrating support. *Philos. Mag.*, 16:50–58.

Rucklidge, A. M. et Silber, M. (2009). Design of parametrically forced patterns and quasipatterns. *SIAM J. Appl. Dyn. Syst.*, 8:298–347.

Shu, C. W. et Osher, S. (1989). Efficient implementation of essentially non-oscillatory shock capturing schemes, ii. *J. Comput. Phys.*, 83:32–78.

Skeldon, A. C. et Guidoboni, G. (2007). Pattern selection for Faraday waves in an incompressible viscous fluid. *SIAM J. Appl. Math.*, 67:1064–1100.

Sussman, M., Fatemi, E., Smereka, P., et Osher, S. (1998). An improved level set method for incompressible two-phase flows. *Computers & Fluids*, 27:663–680.

Temam, R. (1984). *Navier-Stokes Equations, Theory and Numerical Analysis*. North-Holland, Amsterdam.

Tryggvason, G., Bunner, B., Esmaeeli, A., Juric, D., Al-Rawahi, N., Tauber, W., Han, J., et Jan, Y.-J. (2001). A front-tracking method for the computations of multiphase flow. *J. Comput. Phys.*, 169:708–759.

Ubal, S., Giavedoni, M. D., et Saita, F. A. (2003). A numerical analysis of the influence of the liquid depth on two-dimensional Faraday waves. *Phys. Fluids*, 15:3099–3113.

Valha, J., Lewis, J. S., et Kubie, J. (2002). A numerical study of the behaviour of a gas–liquid interface subjected to periodic vertical motion. *Int. J. Numer. Methods Fluids*, 40:697–721.

Vega, J. M., Knobloch, E., et Martel, C. (2001). Nearly inviscid Faraday waves in annular containers of moderately large aspect ratio. *Physica D*, 154:313–336.

Zhang, W. et Viñals, J. (1997). Pattern formation in weakly damped parametric surface waves. *J. Fluid Mech.*, 336:301–330.

Contents

Part I

Introduction

In the appendix of a paper dedicated to the acoustics of elastic solid surfaces, Michael Faraday (1831) discovered that, above a certain threshold in the amplitude of vibration, the free surface of a fluid initially at rest over a vibrating plate will form waves whose shape and wavelength change with respect to the physical parameters. He performed experiments with numerous different fluids, also varying their depth. He observed the shape of the waves through the reflection of an inclined light at the surface of the fluids or by diluting ink in the water. The coloration of the resulting mixture changes with its depth. As a result, when the waves deform the interface, the crests are shown by darker coloration, while the troughs of the waves are located where the fluid is brighter. Faraday found that the waves could organize into concentric circles, squares or hexagons. In addition, he reported that the period of vibration of the fluid was twice the period of oscillation of the support. The latter result was confirmed by Rayleigh (1883a,b). Benjamin and Ursell (1954) performed the first linear analysis of the Faraday instability. The first part of their study concerned inviscid fluids in a horizontally bounded layer. It therefore involved potential flow and a decomposition into orthogonal eigenmodes conditioned by the shape of the container. They concluded that the dynamics of such a configuration were governed by a Mathieu equation. The curves that depict the stability of the Mathieu equation were already known. These tongues delimit the instability of an alternation of subharmonic waves (whose main frequency is an odd multiple of $\omega/2$, half the frequency of vibration of the container) and harmonic waves (whose main frequency multiplies ω). Benjamin and Ursell (1954) also derived the dispersion equation of the inviscid Faraday problem. They tried to extend their results to viscous flows by adding an empirical coefficient of energy dissipation that was supposed to account for the effect of viscosity, but the results of later experiments exhibited only poor agreement with the viscous generalization of the theory of Benjamin and Ursell (1954). The generalization to the case of viscous fluids was actually achieved much later by Kumar and Tuckerman (1994), for a horizontally infinite medium. To do this, they linearized the Navier-Stokes equations, including the viscous terms. They treated the exact Faraday viscous linear problem with a Floquet analysis, which is devoted to the study of non autonomous evolution equations whose explicit time-dependent terms are trigonometric functions. Afterwards, the solution of the Floquet problem was sought numerically. They also predicted the destabilization of waves which alternate between harmonic and subharmonic frequencies. The analysis of Kumar and Tuckerman (1994) was experimentally confirmed by Bechhoefer et al. (1995). The method was extended to two-frequency forcing by Besson et al. (1996). Integral equation formulations of the viscous linear stability problem were derived by Beyer and Friedrich (1995) and Müller et al. (1997), who studied the harmonic response case. Cerda and Tirapegui (1998) used the lubrication approximation and the WKB method to study shallow viscous layers, obtaining a Mathieu equation that was later used by Huepe et al. (2006) to derive analytic results about the response to multifrequency forcing.

During that time, a profusion of outstanding discoveries were made experimentally. Ezerskii et al. (1985) observed that square patterns bifurcated to spatially modulated square patterns if the vibration amplitude was increased beyond a secondary threshold. A further increase of this amplitude induced turbulence which led to a random interface. Christiansen et al. (1992) and Edwards and Fauve (1993) almost simultaneously created quasicrystalline patterns. These patterns satisfy some rotational invariances but are not periodic, in contrast with the classical crystalline patterns. The pattern of Christiansen et al. (1992) is an eight-fold quasipattern and was produced with a classical trigonometric forcing. According to Edwards and Fauve (1993), two forcing frequencies may result in critical modes of two different wavelengths. If the ratios between the frequencies and the amplitudes is well chosen, the two wavelengths can be of equal importance and moreover interact so as to produce an additional lattice of one of the two critical wavenumbers. The two lattices on the same circle have modes that are equally spaced in terms of orientation. Near the bicritical point, at which the two wavelegths become simultaneously unstable, Edwards and Fauve (1993) indeed observed a twelve-fold quasipattern, the result of two hexagonal lattices, orthogonal with each other and of the same wavenumber.

Using the same principle of forcing the waves with two frequencies Müller (1993) produced triangular patterns and Kudrolli et al. (1998), superlattices. The superlattices result from the same scenario as quasipatterns, but the two lattices which have the same wavenumber are oriented differently. The wavevectors of the two lattices must fulfill a condition of the following kind which determine a posteriori their relative orientation. This condition is of the form $a\mathbf{k}_1 + b\mathbf{k}_2 = c\mathbf{k}'_1$ where a, b and c are integers, $\mathbf{k}_1$ and $\mathbf{k}_2$ are two different wavevectors of the first lattice and $\mathbf{k}'_1$ belongs to the second lattice. This condition allows the

spatial periodicity of quasipatterns with higher wavenumbers ($c\|\mathbf{k}_1'\|$).

The existence of another kind of pattern, the oscillon, was reported by Lioubashevski et al. (1996). Oscillons are localized circular structures exhibiting very high peaks. They can appear on a flat interface as well as on interfaces which already contain patterns. Oscillons were previously observed in Faraday waves with granular media (Umbanhowar et al., 1996).

The recent discoveries of the astounding variety of new patterns and the inexpensive apparatus required by the Faraday experiment make this problem one of the most popular hydrodynamical pattern-forming systems. These patterns also motivate the improvement of theoretical models, the ultimate goal being the prediction of patterns.

In infinite domains and for homogeneous fluids (conditions which are approximately satisfied in the experimental investigations), the linear tools provide only the most unstable wavenumber. They are incapable of forecasting the nature of patterns from the set of physical parameters. The prediction of patterns is only possible through nonlinear analysis, which takes into account the interactions between waves. These interactions explain the selection of a discrete subset of modes. Nonlinear interactions are generally destructive, because of viscous nonlinear effects. They can be more or less destructive according to the angle between the two waves considered. Zhang and Viñals (1997) were the first to our knowledge to give predictions of the shape of the pattern, by calculating the angles which minimize these interactions. Towards this end, they used weakly nonlinear expansions. Although their work is based on several approximations (quasipotential equations and terms in boundary conditions), they were able to explain phenomena such as the spatial modulation of patterns (Ezerskii et al., 1985) and to verify theoretically the occurrence of the quasipatterns reported by Christiansen et al. (1992) and Edwards and Fauve (1993). The analysis of Zhang and Viñals (1997) was enhanced by Chen and Viñals (1999) who removed some of the approximations on the boundary conditions. A more recent article (Skeldon and Guidoboni, 2007) removed all of these approximations by carrying out a perturbation expansion of the Navier–Stokes equations and the related boundary conditions, without any assumption except the restriction to a single fluid in an unbounded domain.

The Faraday instability has been studied in frameworks other than that of classical pattern formation. Douady et al. (1989) investigated the Faraday instability in an annular container. The resulting patterns consist in this case of regularly spaced azimuthal waves. Douady et al. (1989) observed new phenomena such as spatiotemporal modulations of patterns, the collapsing or birth of one or several wavelengths and the displacement of the patterns around the annulus, i.e. the drift instability. These phenomena are the consequences of secondary bifurcations, like, for example, the spatial modulation reported by Ezerskii et al. (1985). These phenomena have been explained heuristically (Fauve et al., 1991), using stability analyses of model equations. Other investigations have been conducted on the same subject by Vega et al. (2001) and Martín et al. (2002), based on the hypothesis of a coupling between the oscillating motion and a streaming flow which undergoes only slow time variations.

As stated above, theoretical analysis has made great progress during the last few decades, especially due to the development of equivariant dynamical systems theory and the elaboration of patterns with model equations (Porter et al., 2004). The approximation of quasipatterns in spatially periodic domains has also been addressed in Rucklidge and Silber (2009). Experimental measurements have also progressed. The experiment of Kityk et al. (2005), conducted with two layers of liquid encapsulated in a closed transparent vessel, was the first to provide precise quantitative measurements of the interface height and the first spatiotemporal spectrum of patterns (applied to squares and hexagons). They dyed one of the two fluids, illuminated the vessel from above and filmed the vessel from below. The rate of transmitted light, measured by the camera, is related to the height of the interface and provides direct measurements of the interface height. Another method, using the deformation of a grid drawn at the bottom of a vessel containing a transparent fluid, has been recently developed (Moisy et al., 1984) and supplies very accurate measurements. There has been a great deal of analysis of lattices, superlattices and quasipatterns using equivariant dynamical systems theory, as well as model equations designed to produce specific patterns, e.g. Porter et al. (2004).

Numerical simulation represents a very interesting alternative to explore the Faraday instability but has up to now only been employed to a small extent. In addition, no previous investigation simulated the complete non-linear Faraday problem. Only one simulation (O'Connor, 2008) was designed for the three-

dimensional problem, for which the question of pattern formation can be raised. Chen and Wu (2000), Chen (2002), Murakami and Chikano (2001), Valha et al. (2002) and Ubal et al. (2003) designed two-dimensional simulations. The most extensive simulation thus far has been that of Chen and Wu (2000) and Chen (2002), who used a finite-difference method applied to a boundary-fitted time-dependent coordinate system. At each timestep, the surface is advected and a new 2D grid, adapted to the surface, is recomputed. The amplitude of their numerically computed Faraday waves confirmed the weakly nonlinear analysis of Chen and Viñals (1999), including their prediction of a range of subcriticality. Their calculations also predicted qualitatively new phenomena, such as disconnected solution branches and slow modulated dynamics.

Murakami and Chikano (2001) used a method similar to that of Chen and Wu (2000) and Chen (2002). Although they reproduced some features of the experiments by Lioubashevski et al. (1996), their calculations were limited to accelerations only 0.5 % above critical. The investigation by Ubal *et al.* (2003) focused on the influence of liquid depth in two-dimensional simulations using a Galerkin finite-element method in transformed coordinates. In addition to comparing their linear stability predictions with those of Benjamin and Ursell (1954) and Kumar and Tuckerman (1994), they calculated instantaneous surface profiles and velocity fields, as well as the temporal evolution and spectrum. Valha *et al.* (2002) examined the response of a liquid layer in a vertical cylindrical vessel using the MAC (Marker-and-Cell) method of Harlow and Welch (1965). Surface tension was treated by the continuum surface force model of Brackbill et al. (1992). O'Connor (2008) conducted numerical simulations using an ALE (Arbitrary Lagrangian-Eulerian) spectral-element code in both two and three dimensions; a visualization of a square pattern was presented.

We have undertaken the simulation of the Faraday instability in three dimensions. The first part of this document is devoted to describing the simulation algorithm. It is first tested in the linear regime by comparison with the neutral curves and the most unstable eigenmode on the threshold, provided in Kumar and Tuckerman (1994). A further comparison was made in the nonlinear regime with the experimental quantitative measurements of Kityk et al. (2005) for square and hexagonal patterns. The instantaneous spatial and spatiotemporal spectra were calculated.

However, it was seen that in the conditions used by Kityk et al. (2005) to obtain hexagons, the hexagonal regime is only transient and undergoes drastic changes in its structure. Among these changes, the hexagonal symmetry disappears and leads to patterns with other invariances, then reappears partially after a few seconds. This alternation is very visible through the spatial study we peformed. We hypothesized that this singular behaviour was the signature of a homoclinic orbit whose hexagonal regime was a fixed point. We proposed an exploration of this hypothesis, in three parts: the calculation of the fixed point, the computation of the most unstable eigenvector and the exploration of the orbit far from the fixed point.

Finally, we studied in detail the drift instability (Douady et al., 1989) in a two-dimensional periodic domain. The study was initially dedicated to the description of the mechanisms which lead to the drift instability, but we also discovered additional branches. These imply the existence of further instabilities, whose properties are under investigation.

Part II

Three-dimensional numerical simulation of the Faraday experiment

Périnet, N., Juric, D. and Tuckerman, L. S. (2009). Numerical simulation of Faraday waves. J. Fluid Mech., 635:1–26.

2.1 Historical introduction

The Faraday experiment consists of shaking vertically a container holding two immiscible fluids (the lighter of which can be air) thereby inducing oscillations of the fluids and the interface between them. Beyond a certain threshold, the interface can form many kinds of standing wave patterns, including crystalline patterns and others which are more complex. This phenomenon was first studied by Faraday (1831) who noticed that the vibration frequency of the interface was half that of the forcing. The latter result was confirmed theoretically Rayleigh (1883a,b). Benjamin and Ursell (1954) carried out the first theoretical linear analysis of the Faraday waves, restricted to inviscid fluids. They decomposed the fluid motion into normal modes of the container and showed that the evolution equation of each mode reduced to a Mathieu equation whose stability diagram is well known.

In the 1990s, new behaviours of the interface were discovered, such as quasi-crystalline eight-fold patterns seen by Christiansen et al. (1992). By introducing a forcing which is the sum of two periodic functions with commensurable frequencies, Edwards and Fauve (1993) were able to produce twelve-fold quasi-patterns. Triangular patterns were observed by Müller (1993) and superlattice patterns by Kudrolli et al. (1998), also using two-frequency forcing. Spatio-temporal chaos was studied by Kudrolli and Gollub (1996), who also surveyed the occurrence of lattice patterns – stripes, squares or hexagons – as a function of viscosity and frequency. Binks et al. (1997) demonstrated the dependence of the pattern on the depth of the layer. In addition to patterns or quasi-patterns, very localized circular waves called oscillons may occur, as seen by Lioubashevski et al. (1996). The Faraday instability is the first macroscopic system in which such structures have been observed. These discoveries endow the Faraday instability with a very great fundamental interest for understanding the natural formation of patterns.

A number of theoretical or semi-numerical analyses were inspired by these experiments. Kumar and Tuckerman (1994) extended the linear stability analysis of Benjamin and Ursell (1954) to viscous fluids. This analysis was experimentally confirmed by Bechhoefer et al. (1995) and used by Kumar (1996) to predict cases in which the response would be harmonic rather than subharmonic. The method was extended by Besson et al. (1996) to calculate the stability tongues in the case of two-frequency forcing. Integral equation formulations of the viscous linear stability problem were derived by Beyer and Friedrich (1995) and Müller et al. (1997), who also studied the harmonic response case. Cerda and Tirapegui (1998) used the lubrication approximation and the WKB method to study shallow viscous layers, obtaining a Mathieu equation that was later used by Huepe et al. (2006) to derive analytic results about the response to multifrequency forcing.

Linear analysis provides no information about the shape of the patterns which appear; other means are necessary to understand the occurence of a given pattern or the amplitude of stabilization. Weakly nonlinear approximations have been derived from the Navier–Stokes equations by Viñals and co-workers, e.g. Zhang and Viñals (1997), Chen and Viñals (1999) and by Skeldon and Guidoboni (2007), focusing on the competition between different patterns. Vega et al. (2001) derived equations governing the interaction between Faraday waves and the mean flow. There has been a great deal of analysis of lattices, superlattices and quasi-patterns using equivariant dynamical systems theory, as well as model equations designed to produce specific patterns, e.g. Porter et al. (2004). The approximation of quasipatterns in spatially periodic domains has also been addressed in Rucklidge and Silber (2009).

Investigation of the full nonlinear viscous problem, however, requires numerical simulations, of which there have been very few up to now, specifically those of Chen and Wu (2000), Chen (2002), Murakami and Chikano (2001), Valha et al. (2002), Ubal et al. (2003) and O'Connor (2008). With the exception of O'Connor (2008), all previous simulations have been two-dimensional. The most extensive simulation thus far has been that of Chen and Wu (2000) and Chen (2002), who used a finite-difference method applied to a boundary-fitted time-dependent coordinate system. At each timestep, the surface is advected and a new 2D grid, adapted to the surface, is recomputed. The amplitude of their numerically computed Faraday waves confirmed the weakly nonlinear analysis of Chen and Viñals (1999), including their prediction of a range of subcriticality. Their calculations also predicted qualitatively new phenomena, such as disconnected solution branches and slow modulated dynamics.

Murakami and Chikano (2001) used a method similar to that of Chen and Wu (2000) and Chen (2002). Although they reproduced some features of the experiments by Lioubashevski et al. (1996), their calculations were limited to accelerations only 0.5 % above critical. The investigation by Ubal *et al.* (2003) focused on the influence of liquid depth in two-dimensional simulations using a Galerkin finite-element method in

transformed coordinates. In addition to comparing their linear stability predictions with those of Benjamin and Ursell (1954) and Kumar and Tuckerman (1994), they calculated instantaneous surface profiles and velocity fields, as well as the temporal evolution and spectrum. Valha *et al.* (2002) examined the response of a liquid layer in a vertical cylindrical vessel using the MAC (Marker-and-Cell) method of Harlow and Welch (1965). Surface tension was treated by the continuum surface force model of Brackbill et al. (1992). O'Connor (2008) conducted numerical simulations using an ALE (Arbitrary Lagrangian-Eulerian) spectral-element code in both two and three dimensions; a visualization of a square pattern was presented.

The hexagonal patterns, quasi-patterns and oscillons which motivate our investigation are intrinsically three-dimensional, and have never been calculated numerically from the fluid-dynamical equations. Here we report on the results of fully nonlinear, three-dimensional simulations of Faraday waves using a finite-difference front-tracking method. In the classic Faraday problem the lighter fluid is usually taken to be air whose effects can be neglected. However, in contrast to the previously cited investigations, the numerical method described here solves the Navier–Stokes equations for the general case of two distinct superposed fluids. The capability of the method to simulate the motion of both fluids is important in that it permits comparison of numerical results with those of certain experimental configurations, namely those of Kityk et al. (2005) where the lighter fluid cannot be ignored. These experiments were the first to provide quantitative measurements of the complete spatio-temporal Fourier spectrum of Faraday waves and thus form an excellent basis for quantitative comparison with our numerical results in the nonlinear finite amplitude regime, i.e. interfaces with steep slopes.

In the next two sections of this article, we present the hydrodynamic equations that govern the Faraday instability and then describe the computational method. The two sections following these are dedicated to the comparison of our results with the linear theory of Kumar and Tuckerman (1994) and with the experiments of Kityk *et al.* (2005, 2009). After comparing numerical and experimental spatio-temporal spectra for squares and hexagons, we present the three-dimensional velocity field for the hexagonal pattern.

2.2 Equations of motion

The mathematical model of the Faraday experiment consists of two incompressible and immiscible viscous fluids in a three-dimensional domain $\mathbf{x} = (x, y, z) \in \Re^2 \times [0, h]$, bounded at $z = 0$ and $z = h$ by flat walls. The two fluids, each uniform and of densities ρ_1, ρ_2 and viscosities μ_1 and μ_2, initially form two superposed horizontal layers with an interface between them. This two-dimensional interface is defined by $\mathbf{x}' = (x, y, \zeta(x, y, t))$. Within the parameter range we wish to simulate, the height ζ remains a single-valued function of (x, y, t).

The container is shaken vertically in z. In the reference frame of the container the boundary conditions for the fluid velocities $\mathbf{u} = (u, v, w)$ are

$$\mathbf{u}(x, y, 0, t) = 0, \tag{2.1a}$$

$$\mathbf{u}(x, y, h, t) = 0. \tag{2.1b}$$

The gravitational acceleration g is augmented by a temporally periodic inertial acceleration

$$\mathbf{G} = (a\cos(\omega t) - g)\mathbf{e}_z, \tag{2.2}$$

where a is the amplitude of the forcing and ω is its frequency.

The Navier–Stokes equations for incompressible, Newtonian fluids are

$$\rho\frac{\mathrm{D}\mathbf{u}}{\mathrm{D}t} = -\boldsymbol{\nabla}p + \rho\mathbf{G} + \boldsymbol{\nabla}\cdot\mu\left(\boldsymbol{\nabla}\mathbf{u} + \boldsymbol{\nabla}\mathbf{u}^{\mathrm{T}}\right) + \mathbf{s}, \tag{2.3a}$$

$$\boldsymbol{\nabla}\cdot\mathbf{u} = 0. \tag{2.3b}$$

Here p is the pressure and $\mathbf{s}$ is the capillary force (per unit volume) and is defined below. Equations (2.3a) and (2.3b) are valid for the entire domain, including the interface, in spite of the fact that the density and viscosity change discontinuously and the surface tension acts only at the interface. In this single-fluid

formulation, the density and viscosity fields are defined in terms of the densities and viscosities of the two fluids

$$\rho = \rho_1 + (\rho_2 - \rho_1)H, \tag{2.4a}$$
$$\mu = \mu_1 + (\mu_2 - \mu_1)H, \tag{2.4b}$$

with the aid of a Heaviside function,

$$H(\mathbf{x} - \mathbf{x}') = \begin{cases} 0 \text{ if } z < \zeta(x, y, t) \\ 1 \text{ if } z \geq \zeta(x, y, t) \end{cases}, \tag{2.5}$$

where we recall that $\mathbf{x} = (x, y, z)$ is a point anywhere in the three-dimensional volume and $\mathbf{x}' = (x, y, \zeta(x, y, t))$ is the vertical projection of $\mathbf{x}$ onto the interface. The capillary force is

$$\mathbf{s} = \int_{S'(t)} \sigma\kappa\,\mathbf{n}\,\delta(\mathbf{x} - \mathbf{x}')\,\mathrm{d}S, \tag{2.6}$$

where σ is the surface tension coefficient, assumed to be constant, $\mathbf{n}$ is the unit normal to the interface (directed into the upper fluid) and κ its curvature. $\delta(\mathbf{x} - \mathbf{x}')$ is a three-dimensional Dirac distribution that is nonzero only where $\mathbf{x} = \mathbf{x}'$. $S'(t)$ is the surface defined by the instantaneous position of the interface.

To complete the system of equations we need an expression for the motion of the interface. One such expression can be easily derived by noting that mass conservation in an incompressible flow requires $\mathrm{D}\rho/\mathrm{D}t = 0$, which in view of the discontinuous density field (2.4a), is equivalent to

$$\mathrm{D}H/\mathrm{D}t = 0. \tag{2.7}$$

Thus the interface is represented implicitly by H and advected by material motion of the fluid.

2.3 Computational methods

The computational domain is a rectangular parallelepiped, horizontally periodic in x and y and bounded in z by flat walls for which we impose no-slip boundary conditions. The entire domain is discretized by a uniform fixed three-dimensional finite-difference mesh. This mesh has a standard staggered MAC cell arrangement (Harlow and Welch, 1965) where the u, v and w velocity nodes are located on the corresponding cell faces and scalar variables are located at the cell centres. Each cell is of dimension $\Delta x \times \Delta y \times \Delta z$.

Within the domain, the two distinct immiscible fluids are separated by a two-dimensional interface which is discretized by a second mesh as sketched in figure 2.1. This moving and deformable mesh is composed of triangular elements whose motion is treated by a front-tracking/immersed-boundary method (Peskin, 1977; Tryggvason et al., 2001). Because we have assumed that $\zeta(x, y, t)$ is single valued, the nodes of the mesh can be fixed in x and y and only their vertical displacements need to be calculated, which is a considerable simplification to the general front-tracking method.

After setting appropriate initial and boundary conditions, the computational solution algorithm for each timestep is composed of three main phases. First, the interface is advected and the density and viscosity fields updated according to the new interface position. The capillary force $\mathbf{s}$ is then calculated. Finally, the velocity and pressure are found by means of a standard projection method. Each of these steps is described below.

2.3.1 Advection of the interface

Purely Eulerian interface methods such as Volume of Fluid (Hirt & Nichols 1981) or Level Set (Osher & Sethian 1988) use a form of (2.7) to advect a scalar field such as H, or a level-set function that implicitly represents the interface. However, in the front-tracking approach that we use here, the interface markers themselves (the nodes of the triangular mesh) are advected. H is then constructed from the position and geometry of the interface. Taking (2.7) as a starting point, we develop an equivalent expression for the vertical displacement of the triangular interface mesh.

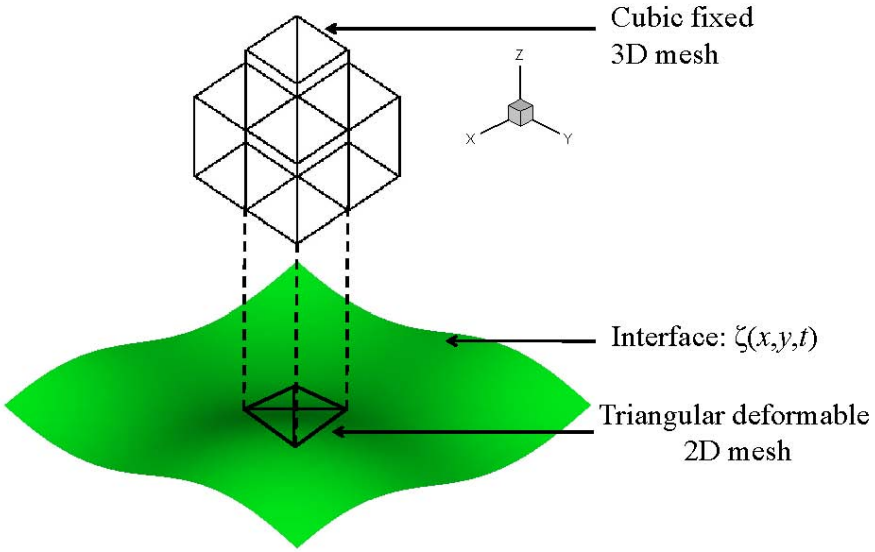

Figure 2.1: Spatial discretization of the domain.

The material derivative of (2.5) gives:

$$\frac{\mathrm{D}H}{\mathrm{D}t} = \boldsymbol{\nabla} H \cdot \frac{\mathrm{D}\mathbf{x}}{\mathrm{D}t} + \boldsymbol{\nabla}' H \cdot \frac{\mathrm{D}\mathbf{x}'}{\mathrm{D}t}, \tag{2.8}$$

where $\boldsymbol{\nabla}' = \partial_{\mathbf{x}'}$ and

$$\boldsymbol{\nabla} H = -\boldsymbol{\nabla}' H = \int_{S'(t)} \mathbf{n}\delta(\mathbf{x} - \mathbf{x}')\mathrm{d}S. \tag{2.9}$$

(For a derivation of (2.9) see Tryggvason *et al.* 2001.) Factoring (2.8) by $\boldsymbol{\nabla} H$

$$\frac{\mathrm{D}H}{\mathrm{D}t} = \boldsymbol{\nabla} H \cdot \left(\mathbf{u} - \frac{\mathrm{D}\mathbf{x}'}{\mathrm{D}t} \right). \tag{2.10}$$

The right-hand side of (2.10) can only be zero everywhere, including on the surface, $\mathbf{x} = \mathbf{x}'$, if

$$\frac{\mathrm{D}\mathbf{x}'}{\mathrm{D}t} = \mathbf{u}(\mathbf{x}', t), \tag{2.11}$$

which establishes the material motion of the explicit interface representation $\mathbf{x}'$. Furthermore

$$\frac{\partial \mathbf{x}'}{\partial t} = (\mathbf{I} - \boldsymbol{\nabla}\mathbf{x}') \cdot \mathbf{u}(\mathbf{x}', t), \tag{2.12}$$

where $\mathbf{I}$ is the identity tensor. The specific choice of $\mathbf{x}' = (x, y, \zeta(x, y, t))$ made here gives for $\boldsymbol{\nabla}\mathbf{x}'$

$$\begin{bmatrix} 1 & 0 & 0 \\ 0 & 1 & 0 \\ \dfrac{\partial \zeta}{\partial x} & \dfrac{\partial \zeta}{\partial y} & 0 \end{bmatrix}. \tag{2.13}$$

With this, (2.12) leads to the specific displacement relations:

$$\partial x/\partial t = 0, \tag{2.14a}$$

$$\partial y/\partial t = 0, \tag{2.14b}$$

$$\frac{\partial \zeta}{\partial t} = w - u\frac{\partial \zeta}{\partial x} - v\frac{\partial \zeta}{\partial y}. \tag{2.14c}$$

The application of this advection to the triangular mesh we use for tracking the interface is straightforward. At each vertex the horizontal displacement is zero and for the vertical displacement we compute a first-order approximation to (2.14c):

$$\frac{\zeta^{n+1} - \zeta^n}{\Delta t} = w^n(\mathbf{x}'_e) - \frac{\partial \zeta^n}{\partial x}u^n(\mathbf{x}'_e) - \frac{\partial \zeta^n}{\partial y}v^n(\mathbf{x}'_e). \tag{2.15}$$

The superscripts n and $n+1$ denote, respectively, the old and new time levels. The derivatives on the right-hand side are evaluated using a simple upwind scheme which requires the usual CFL (Courant-Friedrichs-Lewy) time step restriction. The vertical displacement of the interface mesh requires knowledge of the velocities at the element nodes $\mathbf{x}'_e$. These in general do not coincide with the Eulerian grid nodes $\mathbf{x}_{ijk}$, whose indices correspond to discretized coordinates along the respective directions x, y and z. The problem of communicating Eulerian grid velocities to the element nodes is overcome by interpolation between the two grids as is typically done in front-tracking and immersed-boundary methods. Here we use the particular interpolation

$$\mathbf{u}(\mathbf{x}'_e) = \sum_{ijk} \mathbf{u}(\mathbf{x}_{ijk})\delta_h(\mathbf{x}_{ijk} - \mathbf{x}'_e)\Delta x \Delta y \Delta z. \tag{2.16}$$

The kernel δ_h is a smoothed version of the three-dimensional Dirac delta function with compact support of four grid nodes in each direction (for details of the front-tracking method, see Tryggvason *et al.*, 2001, and for the immersed-boundary method, see Peskin, 1977). In (2.16) the weighted information collected from nearby Eulerian grid nodes is interpolated to a given element node.

We now seek to update the density and viscosity fields needed in (2.4), which require H. The equation for H, based on the updated values of $\mathbf{x}'$ and $\mathbf{n}$, is formulated by taking the divergence of (2.9):

$$\nabla^2 H = \boldsymbol{\nabla} \cdot \int_{S'(t)} \mathbf{n}\,\delta\left(\mathbf{x} - \mathbf{x}'\right) \mathrm{d}S, \tag{2.17a}$$

$$H(x, y, 0, t) = 0, \tag{2.17b}$$

$$H(x, y, h, t) = 1. \tag{2.17c}$$

The discretized version of the Poisson problem (2.17a) is

$$\nabla^2 H_{ijk} = \boldsymbol{\nabla} \cdot \sum_e \mathbf{n}_e \delta_h(\mathbf{x}_{ijk} - \mathbf{x}'_e)\Delta S_e, \tag{2.18}$$

where standard central differencing is used for the gradient and divergence operators. This numerically calculated Heaviside function is a smoothed transition from 0 to 1 across a distance of 4 grid cells in the direction normal to the interface. In contrast to (2.16), the summation above serves to distribute weighted information from an element node to nearby Eulerian grid nodes. Since an element is triangular, its vertices lie in the same plane, its normal vector is unique and the three tangent vectors are simple to calculate:

$$\mathbf{n}_e = \frac{\mathbf{t}_2 \times \mathbf{t}_1}{||\mathbf{t}_2 \times \mathbf{t}_1||} \tag{2.19}$$

where $\mathbf{t}_1$ and $\mathbf{t}_2$ are the tangents on two distinct edges of the triangle (see the sketch in figure 2.2). We solve (2.18) by fast Fourier transform. Finally, ρ^{n+1} and μ^{n+1} are updated using (2.4a) and (2.4b).

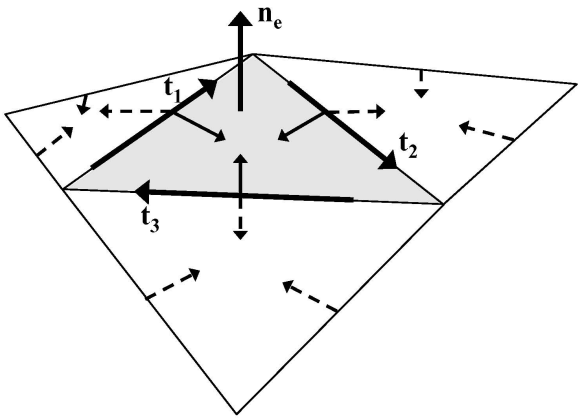

Figure 2.2: A triangular element of the interface mesh illustrating the action of the capillary forces according to (2.20). For the shaded triangle the forces act perpendicular to the triangle's edges (unlabelled solid arrows), the dashed arrows are the corresponding forces on the edges of neighboring triangles. The net capillary force at the shared edge between any two triangles (the sum of the solid and dashed vectors) is directed into the fluid on the concave side of the interface.

2.3.2 Capillary force

From (2.6), the capillary force involves the curvature of the interface and its normal vector. However, from a computational point of view, curvature is a difficult quantity to compute accurately. It is more accurate and physically appealing to calculate the force pulling on the edge of each individual triangular surface element and then sum the contributions for all the elements over the surface. For a given surface element e of surface area ΔS_e and perimeter δl, we can write:

$$\begin{aligned} \mathbf{s}_e &= \sigma \int_{\Delta S_e} \kappa \mathbf{n} \, \mathrm{d}A, \\ &= \sigma \int_{\Delta S_e} (\mathbf{n} \times \boldsymbol{\nabla}) \times \mathbf{n} \, \mathrm{d}A, \\ &= \sigma \oint_{\delta l} \mathbf{t} \times \mathbf{n} \, \mathrm{d}l, \end{aligned} \tag{2.20}$$

where the last integral represents the sum of the capillary forces exerted around the element perimeter. As sketched in figure 2.2, the directions of these forces are oriented along the surface and normal to the element's edges. The net force at the shared edge between any two triangles (the sum of the solid and dashed vectors) is directed into the fluid on the concave side of the interface. Following Peskin's immersed boundary method (Peskin, 1977), the discrete version of (2.6) becomes

$$\mathbf{s}_{ijk} = \sum_e \mathbf{s}_e \delta_h(\mathbf{x}_{ijk} - \mathbf{x}'_e), \tag{2.21}$$

where we use the same smoothed δ_h as in (2.16) and (2.18). Thereby, several interfacial elements contribute to the calculation of the force applied to a single Eulerian node, and a single element influences more than one Eulerian node.

2.3.3 Solution of the Navier–Stokes equations

The Navier–Stokes equations are solved by a projection method (Chorin, 1968; Temam, 1984) with incremental pressure correction (Goda, 1979) applied to a finite-difference scheme which is first order in time and second order in space. In addition a semi-implicit scheme is chosen for the velocities to relax the stability

restriction on the time step due to viscous diffusion. All spatial derivative operators are evaluated using standard centred differences, except in the nonlinear term where we use a second-order ENO (Essentially-Non-Oscillatory) scheme (Shu and Osher, 1989; Sussman et al., 1998). (For an overview of projection methods for the incompressible Navier–Stokes equations, see Guermond et al. (2006).) The time stepping algorithm is thus

$$\begin{aligned}\frac{\mathbf{u}^{n+1}-\mathbf{u}^n}{\Delta t} = &-\mathbf{u}^n\cdot\boldsymbol{\nabla}\mathbf{u}^n + \frac{1}{\rho^{n+1}}\boldsymbol{\nabla}\cdot\mu^{n+1}\left(\boldsymbol{\nabla}\mathbf{u}+\boldsymbol{\nabla}\mathbf{u}^{\mathrm{T}}\right)^{n+1}\\ &-\frac{1}{\rho^{n+1}}\boldsymbol{\nabla}p^{n+1}+\frac{\mathbf{s}^{n+1}}{\rho^{n+1}}+\mathbf{G}^{\ n+1},\end{aligned} \tag{2.22}$$

with the boundary conditions on the top and bottom walls

$$\mathbf{u}^{n+1}\big|_\Gamma = 0. \tag{2.23}$$

In (2.22), ρ, μ and $\mathbf{s}$ depend on $\mathbf{x}$ via (2.4–2.6) and have already been updated by (2.15). We decompose the solution of (2.22) in three steps. The first step is a semi-implicit calculation of an intermediate unprojected velocity $\tilde{\mathbf{u}}$, involving only velocities and their gradients:

$$\frac{\tilde{\mathbf{u}}-\mathbf{u}^n}{\Delta t} = -\mathbf{u}^n\cdot\boldsymbol{\nabla}\mathbf{u}^n+\frac{1}{\rho^{n+1}}\boldsymbol{\nabla}\cdot\mu^{n+1}\left(\boldsymbol{\nabla}\tilde{\mathbf{u}}+\boldsymbol{\nabla}\tilde{\mathbf{u}}^{\mathrm{T}}\right) \tag{2.24a}$$

$$\tilde{\mathbf{u}}\big|_\Gamma = 0 \tag{2.24b}$$

In the second step, we include the capillary, acceleration and old pressure gradient terms to calculate the unprojected velocity $\mathbf{u}^*$:

$$\frac{\mathbf{u}^*-\tilde{\mathbf{u}}}{\Delta t} = \mathbf{G}^{n+1}+\frac{\mathbf{s}^{n+1}}{\rho^{n+1}}-\frac{1}{\rho^{n+1}}\boldsymbol{\nabla}p^n. \tag{2.25}$$

Finally we perform a projection step to find the divergence free velocity $\mathbf{u}^{n+1}$:

$$\frac{\mathbf{u}^{n+1}-\mathbf{u}^*}{\Delta t} = -\frac{1}{\rho^{n+1}}\boldsymbol{\nabla}\left(p^{n+1}-p^n\right), \tag{2.26a}$$

$$\boldsymbol{\nabla}\cdot\mathbf{u}^{n+1} = 0, \tag{2.26b}$$

$$\mathbf{u}^{n+1}\cdot\mathbf{n}\big|_\Gamma = 0. \tag{2.26c}$$

Equations (2.26) imply the following elliptic problem for the pressure increment

$$\frac{\boldsymbol{\nabla}\cdot\mathbf{u}^*}{\Delta t} = \boldsymbol{\nabla}\cdot\frac{1}{\rho^{n+1}}\boldsymbol{\nabla}\left(p^{n+1}-p^n\right), \tag{2.27a}$$

$$\left.\frac{\partial\left(p^{n+1}-p^n\right)}{\partial\mathbf{n}}\right|_\Gamma = 0, \tag{2.27b}$$

which we solve with an iterative biconjugate gradient stabilized algorithm (Saad, 1996). In the horizontal directions, periodic boundary conditions are imposed on the velocity and pressure, thus excluding a net horizontal pressure gradient. For the simulations we will present here, this choice is consistent with the requirement of no mean horizontal flux in a large but bounded container.

We note that in the implicit solution of (2.24), we apply the same biconjugate gradient stabilized solver used for the pressure to each component of $\tilde{\mathbf{u}} = (\tilde{u},\tilde{v},\tilde{w})$ separately. Thus only the diagonal terms of the diffusion operator are treated fully implicitly. The off-diagonal terms are treated quasi-implicitly in that the newest available values of $(\tilde{u},\tilde{v},\tilde{w})$ are used in the evaluation of the cross derivatives. To ensure symmetry, we permute the order of solution for each component.

2.4 Results: linear analysis

2.4.1 Floquet analysis

In the absence of lateral boundaries, the equations are homogeneous in the horizontal coordinates and the solutions can be represented by a spatial Fourier transform:

$$\zeta(x,y,t) = \sum_{\mathbf{k}} \hat{\zeta}(\mathbf{k},t)\mathrm{e}^{\mathrm{i}\mathbf{k}\cdot\mathbf{x}} \tag{2.28}$$

The linear instability of the interface between two fluids is described by (2.2)–(2.7) linearized about a zero velocity field and flat interface $\zeta = \langle\zeta\rangle$. The linearized equations depend only on the wavenumber $k \equiv ||\mathbf{k}||$ of each wave and not on its orientation and hence the coefficient of $\mathrm{e}^{\mathrm{i}\mathbf{k}\cdot\mathbf{x}}$ can be written as $\hat{\zeta}(k,t)$; additionally the dynamics of each $\hat{\zeta}(k,t)$ is decoupled from the others. Linear partial differential equations with constant coefficients have solutions which are exponential or trigonometric in time. For the Faraday instability $\hat{\zeta}(k,t)$ is instead governed by a system of linear partial differential equations with time-periodic coefficients, i.e. a Floquet problem, whose solutions are of the form

$$\hat{\zeta}(k,t) = \mathrm{e}^{(\gamma+\mathrm{i}\alpha\omega)t} f(k, t \bmod T), \tag{2.29}$$

where $T = 2\pi/\omega$, γ is real and $\alpha \in [0,1[$. The Floquet modes,

$$f(k, t \bmod T) = \sum_{n=-\infty}^{\infty} f_n(k)\mathrm{e}^{\mathrm{i}n\omega t}, \tag{2.30}$$

are not trigonometric, but remain periodic with fundamental frequency ω. Thus, the linearized behavior for a single mode is

$$\zeta(x,y,t) = \mathrm{e}^{\mathrm{i}\mathbf{k}\cdot\mathbf{x}}\mathrm{e}^{(\gamma+\mathrm{i}\alpha\omega)t} \sum_{n=-\infty}^{\infty} f_n(k)\mathrm{e}^{\mathrm{i}n\omega t}. \tag{2.31}$$

Analogous expressions hold for the velocity $\mathbf{u}$.

Equation (2.29) shows that if γ is non-zero or α is irrational, the evolution of the interface motion is not periodic. A non-zero γ indicates that the motion grows or decays according to the sign of γ. An irrational α yields a quasi-periodic evolution function. For the Faraday instability, it can be shown that α can only take two values: 0 and 1/2. As the imposed acceleration a is increased, one encounters regions in the (k,a) plane in which $\gamma > 0$ for one dominant temporal frequency, $j\omega/2$, where $j = 1,2,3,...$ (see figure 2.3). Within each instability tongue, the amplitude of the mode grows exponentially. These tongues are called harmonic if $\alpha = 0$ and subharmonic if $\alpha = 1/2$. As k is increased, one encounters an alternating sequence of subharmonic and harmonic tongues, which are bounded by neutral curves $(k, a_c(k))$ on which $\gamma = 0$. On the neutral curves, the solutions are periodic:

$$\hat{\zeta}(k,t) = \sum_{n=-\infty}^{\infty} f_n(k)\mathrm{e}^{\mathrm{i}\left(n+\frac{1}{2}\right)\omega t}, \qquad \text{subharmonic case,} \tag{2.32a}$$

$$\hat{\zeta}(k,t) = \sum_{n=-\infty}^{\infty} f_n(k)\mathrm{e}^{\mathrm{i}n\omega t}, \qquad \text{harmonic case.} \tag{2.32b}$$

2.4.2 Computation of the neutral curves

We first compare our numerically calculated instability thresholds with those found by Kumar and Tuckerman (1994) for the same parameter values. The physical parameters are $\rho_1 = 519.933\,\mathrm{kg\,m^{-3}}$ and $\mu_1 = 3.908 \times 10^{-5}\,\mathrm{Pa\,s}$ for the lower fluid and $\rho_2 = 415.667\,\mathrm{kg\,m^{-3}}$ and $\mu_2 = 3.124 \times 10^{-5}\,\mathrm{Pa\,s}$ for the upper fluid. The other parameters are $\sigma = 2.181 \times 10^{-6}\,\mathrm{N\,m^{-1}}$ and $g = 9.8066\,\mathrm{m\,s^{-2}}$. The frequency of the forcing is $\omega/2\pi = 100\,\mathrm{Hz}$ and thus its period is $T = 0.01\mathrm{s}$. The capillary length is defined as $l_c = \sqrt{\sigma/(|\rho_1 - \rho_2|g)}$. The container height is taken to be $5l_c = 0.231\,\mathrm{mm}$, and the interface, when unperturbed, is equidistant from the top and bottom boundaries. We consider several wavenumbers k and set the x dimension of the box in

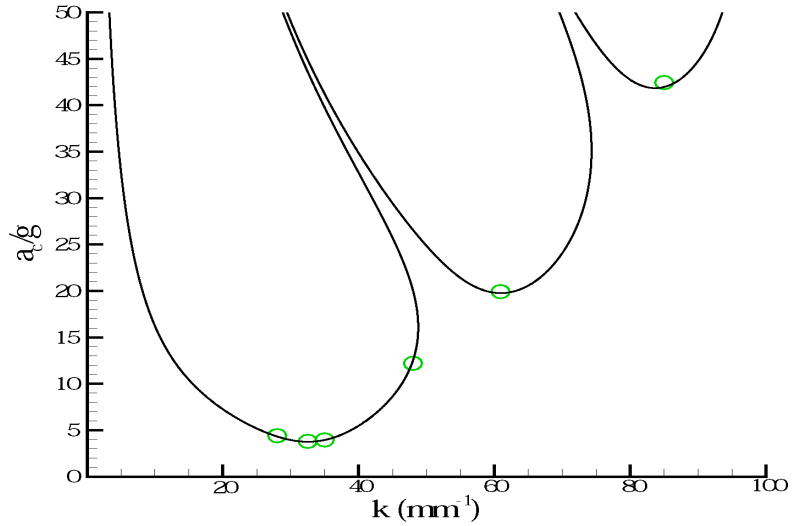

Figure 2.3: Critical acceleration a_c/g as a function of the wavenumber k. The solid curves represent the neutral curves obtained by Kumar and Tuckerman (1994). The a_c found with the simulation are indicated by the circles.

each case to one expected wavelength $\lambda = 2\pi/k$, i.e. to between 0.074 and 0.224 mm, as listed in Table 2.1. We can estimate the importance of various physical effects for these parameters by defining dimensionless quantities with length k^{-1} and forcing period T. The Bond number $Bo = (kl_c)^{-2} = |\rho_1 - \rho_2|\, g/(\sigma k^2)$ measures the relative importance of gravitational to capillary effects and ranges between 0.0649 and 0.598. The Reynolds number $Re = \rho/(\mu k^2 T)$ is a nondimensional measure of viscous damping and ranges between 0.184 and 1.70 for both fluids.

We have computed the critical acceleration from our fluid-dynamical simulation for the wavenumbers listed in Table 2.1. Initially, the interface is sinusoidal with wavevector $\mathbf{k}$ parallel to the x-axis and the velocity is zero. Moreover, to ensure that the solution corresponds initially to the linear solution, we require the amplitude of the interface displacement to be small compared to λ. In order to maintain a roughly cubic mesh and a minimum x-resolution of about 50 grid cells per wavelength, we vary the resolution in the z direction between 126 and 144 points. Since $\mathbf{k}$ points along the x direction, ζ does not depend on y (neither do the velocity nor the pressure) and so the size of the domain and resolution in y are arbitrary. The acceleration a is taken near $a_c(k)$, the expected critical acceleration corresponding to each wavenumber. At the threshold, the flow undergoes a pitchfork bifurcation. Since the growth rate is proportional to $a - a_c$ close to the neutral curve, it is sufficient to find the growth rates for two values of a and to interpolate linearly between these points.

In figure 2.3, we plot the values of a_c obtained from our fluid-dynamical simulation for several values of k, along with the curves $(k, a_c(k))$ obtained from the method of Kumar and Tuckerman (1994). Figure 2.3 shows that these thresholds are in good agreement, despite whatever inaccuracies in a_c are introduced by spatial discretization and linear interpolation. The relative error in the critical acceleration at the conditions previously stated is of the order of a few per cent as shown in Table 2.1.

The results suggest that there is a k below which calculation of the growth rates is not possible. Some zones of the diagram are not accessible because a domain of width $2\pi/k$ necessarily accommodates all wavenumbers which are integer multiples of k up to the resolution limit $\pi/k\Delta x$. The coefficients of the Fourier expansion of the initial condition differ slightly from zero due to finite-difference spatial approximations and if the growth rate of one of these is greater than that of k itself, then it will quickly come to dominate k. This difficulty is exacerbated by the fact that several forcing periods are required for γ to stabilize.

k(mm^{-1})	λ(mm)	No. of gridpoints in x/z	a_c/g (Theor.)	a_c/g (Comp.)	Error(%)
28	0.224	124/128	4.375	4.407	0.7
32.5	0.193	96/128	3.777	3.800	0.6
35	0.180	100/128	3.960	3.954	-0.1
48	0.131	72/126	12.506	12.207	-2.4
60.9	0.103	56/126	19.760	19.922	0.8
85	0.074	48/144	41.953	42.358	1.0

Table 2.1: Comparison of the computed a_c with Floquet theory for various wavenumbers k.

Then the amplitude, whose evolution was expected to be almost periodic, starts to rise before the precise determination of γ is possible, for example in the range of k between 0 and roughly 15 mm^{-1}. As we see in figure 2.3, the critical forcing is substantially lower for one of its multiples closer to 32.5 mm^{-1}. The amplitude corresponding to this wavelength, although initially negligible, increases and rapidly dominates the mode we wish to study, making the calculation of γ unfeasible. In contrast, for $k = 48$ mm^{-1}, the growth rate did not vary significantly after having reached a value near zero (relative fluctuations of about 0.1% of the growth rate's limit value were recorded after the stabilization).

2.4.3 Temporal profile of a mode

We recall from section 2.4.1 that the time dependence of a Floquet mode is not sinusoidal. As a further validation, we can compare the results of our fluid-dynamical simulations to the entire temporal behavior over a period. This is a stronger validation than merely predicting the threshold since it provides a comparison at every time instead of once per period.

In figures 2.4–2.6, we plot the deviation $\zeta - \langle\zeta\rangle$ from the flat interface as a function of time at a fixed spatial location from our fluid-dynamical simulation, for values $k = 48$, 60.9 and 85 mm^{-1} belonging to the first three tongues. On the same figures, we plot the behavior of (2.32), where the temporal coefficients $f_n(k)$ of the Floquet modes have been calculated by the method in Kumar and Tuckerman (1994). The value of a is set to the interpolated critical acceleration $a_c(k)$, so the oscillations approximately retain their initial amplitude as long as they remain small. The comparisons in figures 2.4–2.6 show a nearly perfect agreement. The differences observed initially, due to the phase difference between the initial conditions and acceleration, vanish remarkably quickly, in well under one period of oscillation of the container.

Figures 2.4–2.6 correspond to tongues $j\omega/2$, with j =1, 2, 3, respectively, which show j zero crossings per forcing period T. Odd (even) values of j correspond to subharmonic (harmonic) oscillations, with period $2T$ (T). The temporal spectrum $f_n(k)$ becomes richer as k increases, leading to increasingly more complex modes, as can be observed by comparing figures 2.4–2.6. This strong anharmonicity of the curves is due to the increasing contribution of higher frequency trigonometric functions to the Floquet modes as a increases. The Floquet mode corresponding to $k_c = 32.5$ mm^{-1}, with the smallest value of $a = a_c$, should be closer to trigonometric, with a fundamental frequency of $\omega/2$.

2.5 Results: nonlinear analysis

In the full nonlinear evolution of the interface for $a > a_c$, the amplitude of the interface height grows in time until nonlinear terms in (2.2)–(2.7) become important. After that, the mode whose linear growth rate is maximal gives rise, via nonlinear resonances, to a series of other discrete modes, selected according to the magnitudes and orientations of their wavevector $\mathbf{k}$. This selection is responsible for the formation of patterns that will be the object of our further validations. We seek to compare our calculations with the experimental results of Kityk *et al.* (2005, 2009) where quantitative data concerning the Fourier spectrum $\hat{\zeta}(\mathbf{k}, t)$ are available for squares and hexagons.

We run our numerical simulations with the same experimental parameters as Kityk et al. (2005): $\omega/2\pi =$ 12 Hz ($T = 0.0833$ s), $\rho_1 = 1346$ kg m^{-3}, $\mu_1 = 7.2$ mPa s for the lower fluid and $\rho_2 = 949$ kg m^{-3}, $\mu_2 =$ 20 mPa s for the upper fluid. The surface tension at the interface is $\sigma = 35$ mN m^{-1}, the total height of the

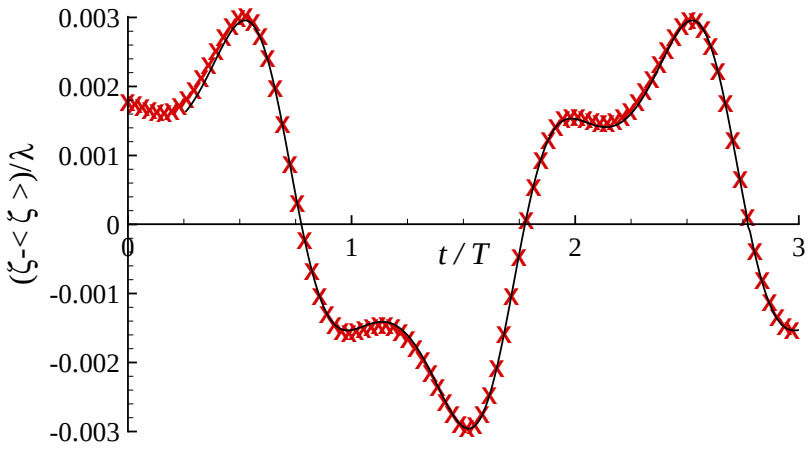

Figure 2.4: Linear evolution of the surface height deviation $\zeta(t) - \langle\zeta\rangle$ for $k = 48$ mm^{-1}, in the first instability tongue. Our simulation results are plotted with symbols and those derived from a Floquet analysis with the solid line. The height and time are nondimensionalized by the wavelength $\lambda = 2\pi/k$ and forcing period T, respectively.

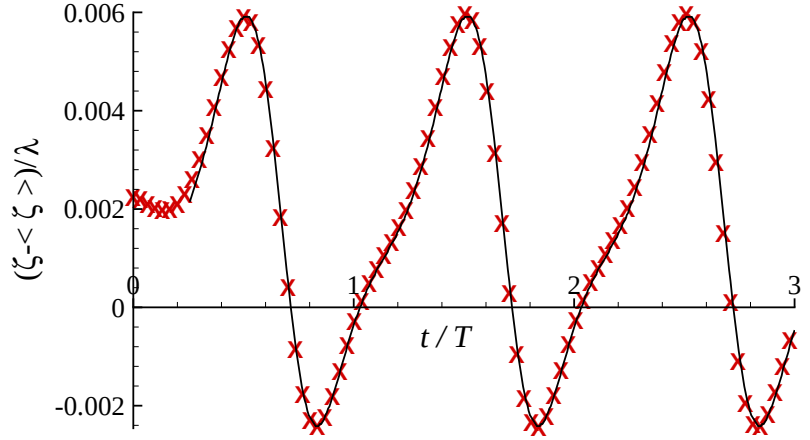

Figure 2.5: Linear evolution of the surface height deviation $\zeta(t) - \langle\zeta\rangle$ for $k = 60.9$ mm^{-1}, in the second instability tongue. Same conventions used as figure 2.4.

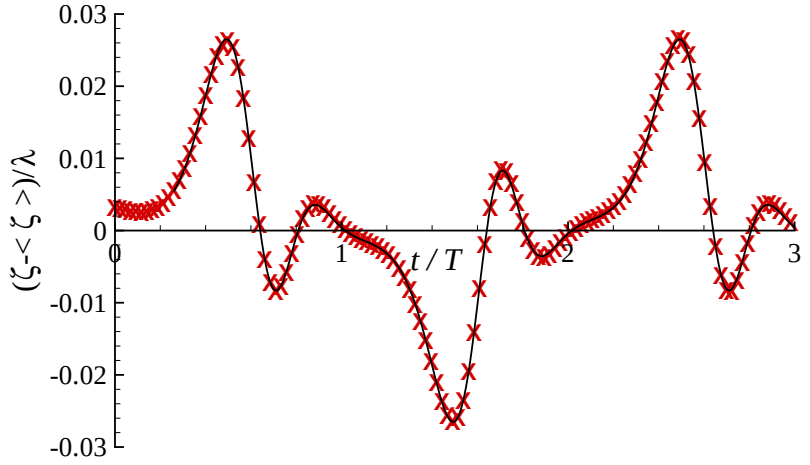

Figure 2.6: Linear evolution of the surface height deviation $\zeta(t) - \langle\zeta\rangle$ for $k = 85$ mm^{-1}, in the third instability tongue. Same conventions used as figure 2.4.

vessel is 1.0 cm and the mean height of the interface, the initial fill height of the heavy fluid, is $\langle\zeta\rangle = 1.6$ mm (with some uncertainty; see below). The Floquet analysis for these parameters yields a critical wavelength of $\lambda_c = 2\pi/k_c = 13.2$ mm and a critical acceleration of $a_c = 25.8\,\mathrm{m\,s^{-2}}$. Here, the Bond number defined in section 2.4.2 is $Bo = |\rho_1 - \rho_2|\, g/(\sigma k_c^2) = 0.49$. The Reynolds number $Re = \rho/(\mu k_c^2 T)$ is $Re_1 = 9.9$ and $Re_2 = 2.52$ for the lower and upper fluid, respectively.

Rather than starting from a sinusoidal interface, we chose to add two-dimensional white noise of small amplitude to $\langle\zeta\rangle$ to define the initial interface height $\zeta(x, y, t = 0)$ in order to excite every mode allowed by the box's horizontal dimensions and number of cells. It is thus possible to check that the correct critical mode (that whose growth rate is maximal) emerges from the linear dynamics. In order to reproduce the experimental results in a computational domain of a minimal size, the dimensions in x and y of the box must correspond to the periodicity and symmetries of the expected pattern. The minimal required resolution along these directions has been found to be between 40 and 50 cells per wavelength. The number of triangles used to represent the interface is 16 times the total number of horizontal gridpoints. The number of cells in the z direction is taken so that $\min_{S'} \zeta(x, y, t)$ is greater than about the height of 3–5 cells. The required vertical resolution thus varies with the forcing amplitude. The initial velocity is taken to be zero.

2.5.1 Square patterns

To compare with the experiment of Kityk et al. (2005) for their square patterns, we choose the same forcing acceleration, $a = 30.0\,\mathrm{m\,s^{-2}}$. Our box has horizontal dimensions which we take both equal to $2\pi/k_c$. The timestep is $\Delta t = 2.78 \times 10^{-4}$ s. Figures 2.7 and 2.8 represent examples of the patterns obtained at saturation under these conditions and are taken from the same simulation at the two instants shown by the two arrows in figure 2.10. The symmetries characterizing the squares (reflections and $\pi/2$ rotation invariance) are clear, showing a first qualitative agreement with Kityk et al. (2005) where both structures were observed. The pattern oscillates subharmonically, at $2T$, where T is the forcing period. Figure 2.7 is taken when the interface attains its maximum height, while figure 2.8 is taken at a time $0.24 \times 2T$ later. At this later time, we observe the dominance of a higher wavenumber, which will be discussed below.

Further quantitative investigations of the patterns involve the spatial Fourier transform of the interface height. In the case of square patterns, the distribution of the spatial modes is shown in figure 2.9. The modes with non-negligible amplitude are $\pm k_c \mathbf{e}_x$ and $\pm k_c \mathbf{e}_y$, with $|\mathbf{k}| = k_c$ and amplitude $A(k_c)$; $\pm 2k_c \mathbf{e}_x$ and $\pm 2k_c \mathbf{e}_y$, with $|\mathbf{k}| = 2k_c$ and amplitude $A(2k_c)$; and $k_c(\pm\mathbf{e}_x \pm \mathbf{e}_y)$, with $|\mathbf{k}| = \sqrt{2}k_c$ and amplitude $A(\sqrt{2}k_c)$. (For a square pattern, the amplitude of each mode is identical to that of each of its images through rotation by any integer multiple of $\pi/2$.) The interface height is written as:

$$\begin{aligned}\zeta(\mathbf{x}, t) = \langle\zeta\rangle \quad &+ \quad A(k_c, t) \sum_{j=1}^{4} \mathrm{e}^{\mathrm{i}k_c \mathbf{e}_j \cdot \mathbf{x}} + A(2k_c, t) \sum_{j=1}^{4} \mathrm{e}^{\mathrm{i}2k_c \mathbf{e}_j \cdot \mathbf{x}} \\ &+ \quad A(\sqrt{2}k_c, t) \sum_{j=1}^{4} \mathrm{e}^{\mathrm{i}\sqrt{2}k_c \mathbf{e}'_j \cdot \mathbf{x}} + \text{higher order terms}, \end{aligned} \tag{2.33}$$

where $\mathbf{e}_j \equiv \mathbf{e}_x \cos(\pi j/2) + \mathbf{e}_y \sin(\pi j/2)$ and $\mathbf{e}'_j \equiv \mathbf{e}_x \cos(\pi/4 + \pi j/2) + \mathbf{e}_y \sin(\pi/4 + \pi j/2)$ for $j = 1, \ldots 4$. We have chosen this notation, rather than $\hat{\zeta}(k, t)$ as used in equation (2.28), to facilitate comparison with Kityk *et al.* (2005, 2009).

We have compared the evolution of the three principal spatial modes (figure 2.10) and their temporal Fourier transform (figure 2.11) with the experimental results (Kityk *et al.* 2005). Here we turn the reader's attention to the recent erratum by Kityk et al. (2009) for correct quantitative comparisons of the spectra.

Figure 2.10 compares the experimental evolution of each spatial wavenumber to numerical calculations for two different mean heights $\langle\zeta\rangle = 1.6$ mm and $\langle\zeta\rangle = 1.7$ mm. Our calculations show that the results depend strongly on $\langle\zeta\rangle$, which is the initial fill height of the heavy fluid. Our discussions with Kityk and Wagner (Kityk & Wagner, private communication) indicate that this is true as well in the experiments, and also that 0.1 mm is within the experimental uncertainty for their mean height. Thus we chose to vary $\langle\zeta\rangle$, in preference to other parameters, in order to check whether the range of amplitudes caused by experimental uncertainties includes those obtained numerically.

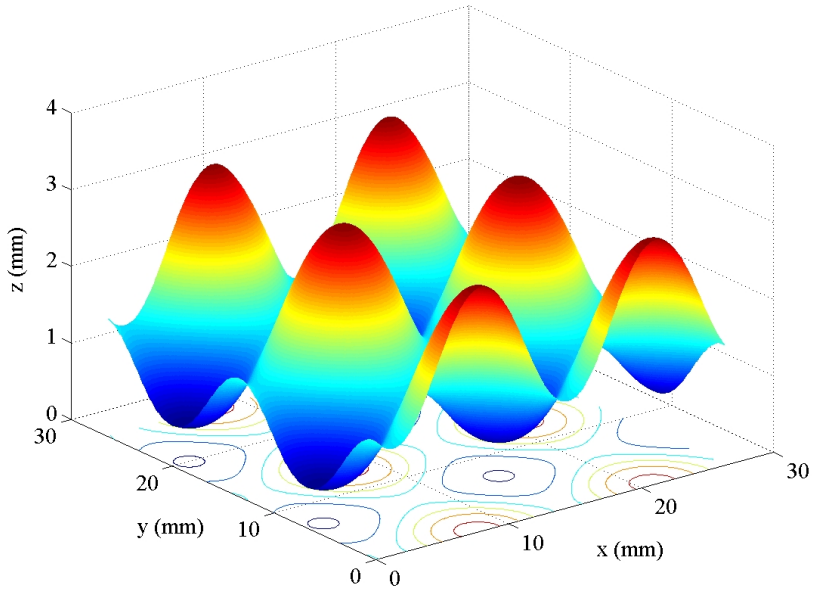

Figure 2.7: Example of square pattern. Height of interface as a function of the horizontal coordinates, at the instant corresponding to first arrow of figure 2.10, when height is maximal. Resolution in x, y, z directions: $80 \times 80 \times 160$. Note that the vertical scale is stretched with respect to the horizontal scale. Each horizontal direction in the figure is twice that of the calculation domain.

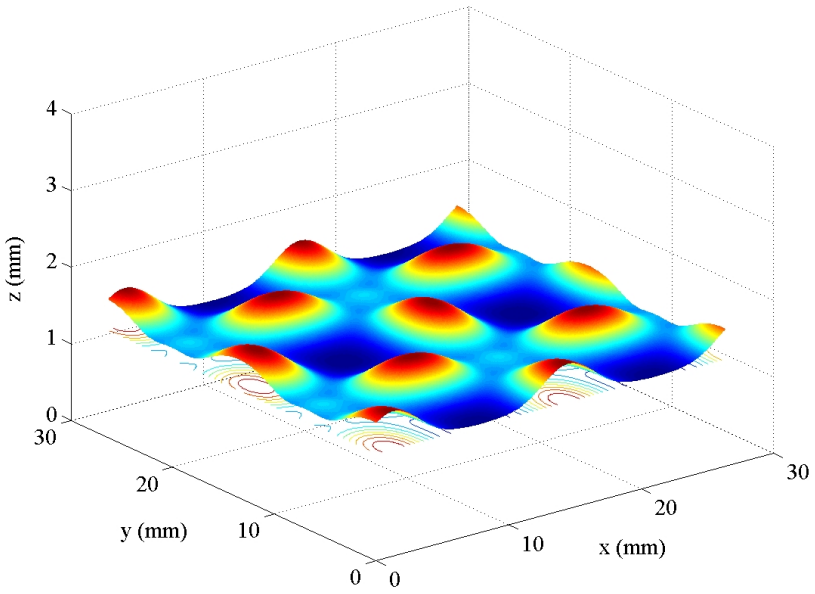

Figure 2.8: Example of square pattern, at the instant corresponding to second arrow of figure 2.10, time $0.24 \times 2T$ after figure 2.7.

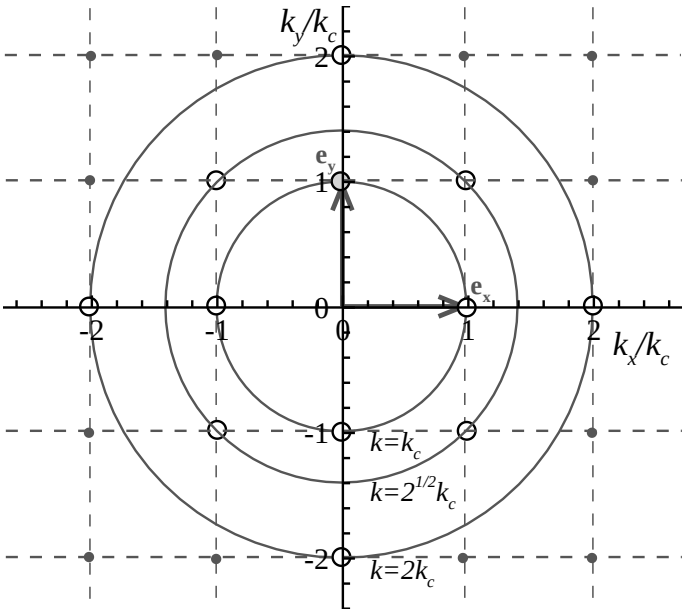

Figure 2.9: Lattice formed by the spatial modes comprising a square pattern. The principal modes, with wavenumbers k_c, $2k_c$ and $\sqrt{2}\,k_c$, whose evolution will be studied in figures 2.10 and 2.11 are indicated by hollow black circles.

The main features found in Kityk et al. (2009) are recognized in figure 2.10. In particular, both the fundamental periodicity of each mode (harmonic or subharmonic) and the form of each numerical curve in figure 2.10 are very similar to the experimental data. The amplitudes and the phases are also quite close. Most of the experimental amplitudes are bracketed by the numerical ones. Thus, they lie in the interval of amplitudes allowed by the range of uncertainties which is surely underestimated since only the uncertainty in $\langle\zeta\rangle$ has been taken into account. $A(k_c)$ crosses zero at times different from the two higher wavenumbers, $A(2k_c)$ and $A(\sqrt{2}k_c)$. At these instants, the higher wavenumbers dominate the pattern. In particular, the pattern of figure 2.8, taken near the second arrow in figure 2.10, when $A(k_c)$ is low, contains more peaks than that of figure 2.7, taken when $A(k_c)$ is high. The large ratio between the amplitude of k_c and the others makes this phenomenon very short-lived.

Figure 2.11 shows the temporal Fourier decomposition of the curves in figure 2.10. These spectra for the experiment Kityk et al. (2009) and for the computation are quite similar too. All of the square patterns that we have observed, once saturation is attained, remain so for the entire duration of the calculation.

We present a brief numerical grid convergence study in figure 2.12. All qualitative features, such as the square symmetry, were observed with each of the three resolutions chosen, despite the coarseness of the $20 \times 20 \times 40$ and $40 \times 40 \times 80$ grids. With increasing resolution, the principal spatial modes converge to the experimental curves shown in figure 2.10, with only a small difference between the curves with the two highest resolutions. The order of numerical convergence of the maximum and minimum of the amplitudes of each of the three modes in figure 2.12 shows that the convergence is between first and second order, which is expected to be the case with the immersed-boundary method. In particular, we would expect that a further doubling of the resolution would change the results by at most 4 % for the principal k_c mode.

2.5.2 Hexagonal patterns

When the amplitude of the forcing acceleration a is further increased, the modes can reorganize. The symmetries change and, in the experiments of Kityk et al. (2005), the initial square pattern becomes hexagonal. Though k_c remains constant, the horizontal dimensions of the minimal computational box necessary to support the periodic pattern must change too. These dimensions become $4\pi/k_c$ in y and $4\pi/(\sqrt{3}k_c)$ in x, as shown in figure 2.13. The wavevector lattice for hexagonal patterns is shown in figure 2.14. The principal

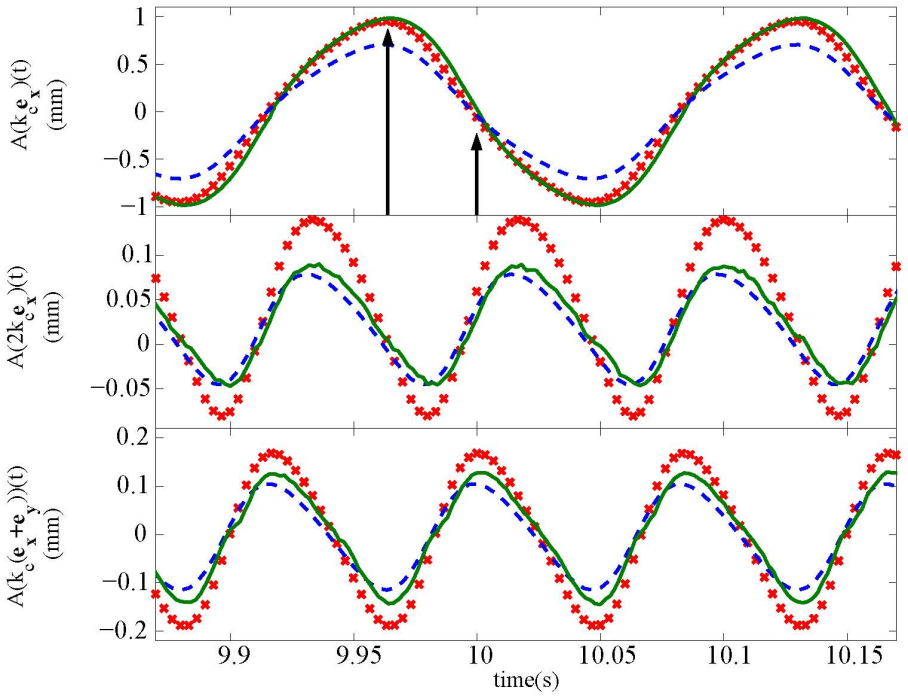

Figure 2.10: Temporal evolution of the amplitudes of the spatial modes with wavenumbers k_c, $2k_c$ and $\sqrt{2}k_c$. Solid curves represent the experimental results of Kityk et al. (2009), dashed curves and crosses represent numerical results for $\langle\zeta\rangle = 1.6$ mm and $\langle\zeta\rangle = 1.7$ mm, respectively. Resolution in x, y, z directions: $80 \times 80 \times 160$. Arrows, from left to right, show the time at which figures 2.7 and 2.8 have been plotted.

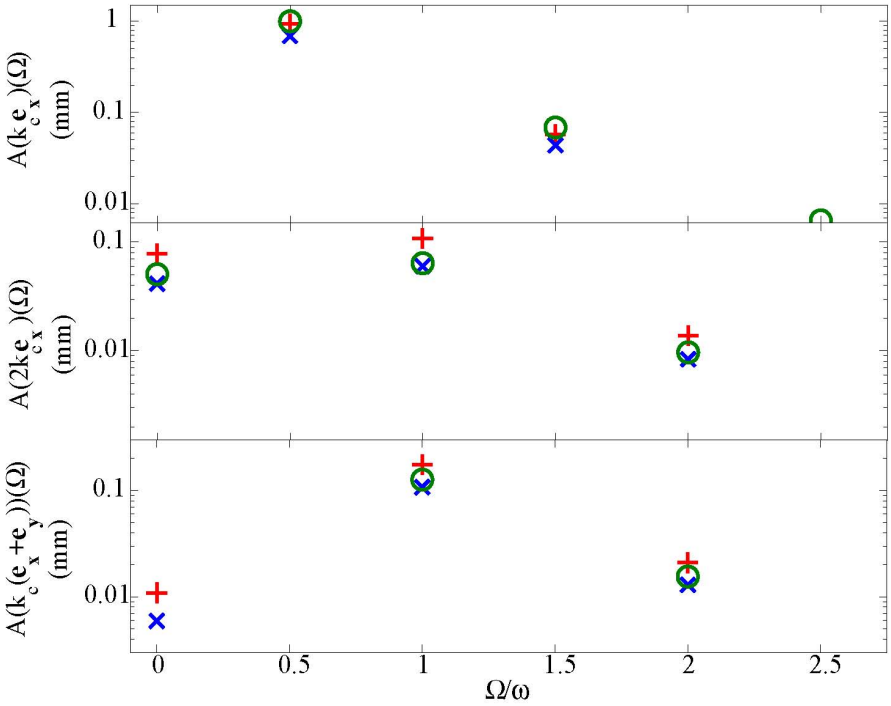

Figure 2.11: Temporal Fourier transform of the amplitudes in figure 2.10. Circles indicate experimental results of Kityk et al. (2009), while crosses and plus signs indicate numerical data with $\langle\zeta\rangle = 1.6$ mm and $\langle\zeta\rangle = 1.7$ mm respectively.

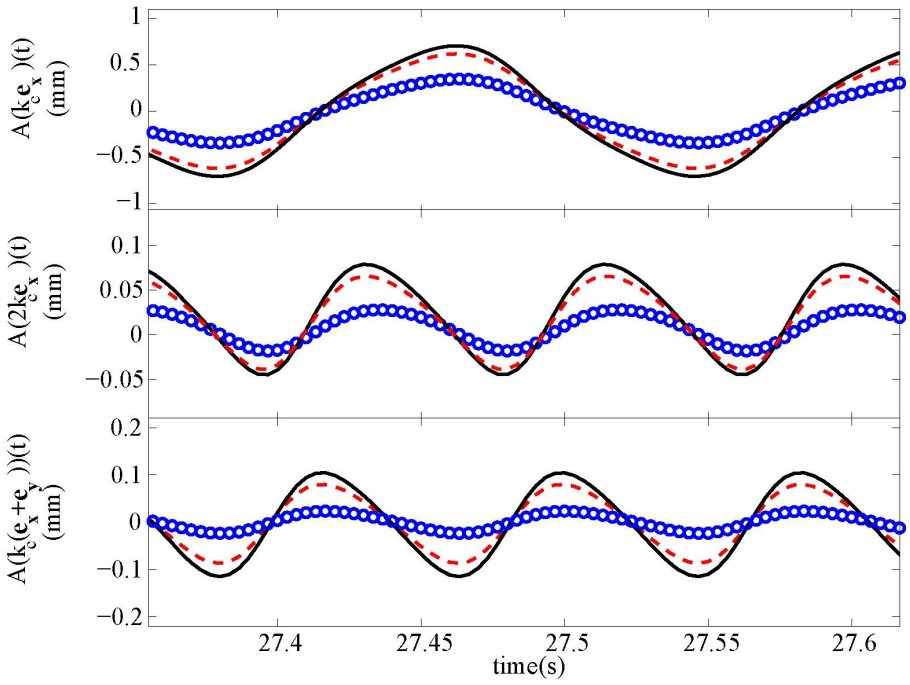

Figure 2.12: Temporal evolution of the amplitudes of the spatial modes with wavenumbers k_c, $2k_c$ and $\sqrt{2}k_c$ for square patterns. Study of the convergence with three different spatial resolutions. Circles indicate a resolution (in x, y, z directions) of $20\times20\times40$, dashed curves $40\times40\times80$ and continuous curves $80\times80\times160$. The timestep is the same, $\Delta t = 2.78\times10^{-4}$ s, for all curves shown.

modes are again of three amplitudes: k_c, $2k_c$ and $\sqrt{3}k_c$. When a pattern is hexagonal, a mode will have the same amplitude and temporal behaviour as each of its images through rotations by any integer multiple of $\pi/3$. The interface height is thus

$$\begin{aligned}\zeta(\mathbf{x},t) = \langle\zeta\rangle \quad &+ \quad A(k_c,t)\sum_{j=1}^{6} \mathrm{e}^{\mathrm{i}k_c\mathbf{e}_j\cdot\mathbf{x}} + A(2k_c,t)\sum_{j=1}^{6}\mathrm{e}^{\mathrm{i}2k_c\mathbf{e}_j\cdot\mathbf{x}} \\ &+ \quad A(\sqrt{3}k_c,t)\sum_{j=1}^{6}\mathrm{e}^{\mathrm{i}\sqrt{3}k_c\mathbf{e}'_j\cdot\mathbf{x}} + \text{higher order terms,} \end{aligned} \tag{2.34}$$

where $\mathbf{e}_j \equiv \mathbf{e}_x\cos(\pi j/3) + \mathbf{e}_y\sin(\pi j/3)$ and $\mathbf{e}'_j \equiv \mathbf{e}_x\cos(\pi/6+\pi j/3) + \mathbf{e}_y\sin(\pi/6+\pi j/3)$. for $j = 1,\ldots,6$.

Our simulations are carried out at acceleration $a = 38.0\,\mathrm{m\,s^{-2}}$ and mean height $\langle\zeta\rangle = 1.6$ mm. We have used two different initial conditions: a rectangular pattern, and also white noise, as in our previous simulations of the square patterns. In both cases, hexagons emerge and saturate. The results shown below are those that emerge from the white noise. The time step varies during the calculation, depending on the viscous diffusion limit and the CFL condition. The spatial resolution is 58x100x180 in the x, y, z directions, respectively.

In figures 2.15–2.18, we show visualizations of the patterns at four instances in time. A movie of the temporal evolution of the hexagon pattern over one subharmonic oscillation is available in the online version of this article. The $\pi/3$ rotational symmetry confirms that the rectangular numerical grid does not forbid the formation of hexagonal patterns, which are not aligned with this grid. The patterns reproduce several prominent features from the visual observations of hexagons in the experiments. For example, one can observe in figures 2.15 and 2.17 the up and down hexagons shown in the experimental snapshots (figure 10 of Kityk *et al.* 2005). The pattern in figure 2.18, when the surface elevation is minimal, is dominated by wavenumbers higher than k_c, as is also the case in figure 10 of Kityk et al. (2005). This is reflected by the disappearance of $A(k_c)$ and the resulting dominance of $A(2k_c)$ and $A(\sqrt{3}k_c)$ at the corresponding instant in

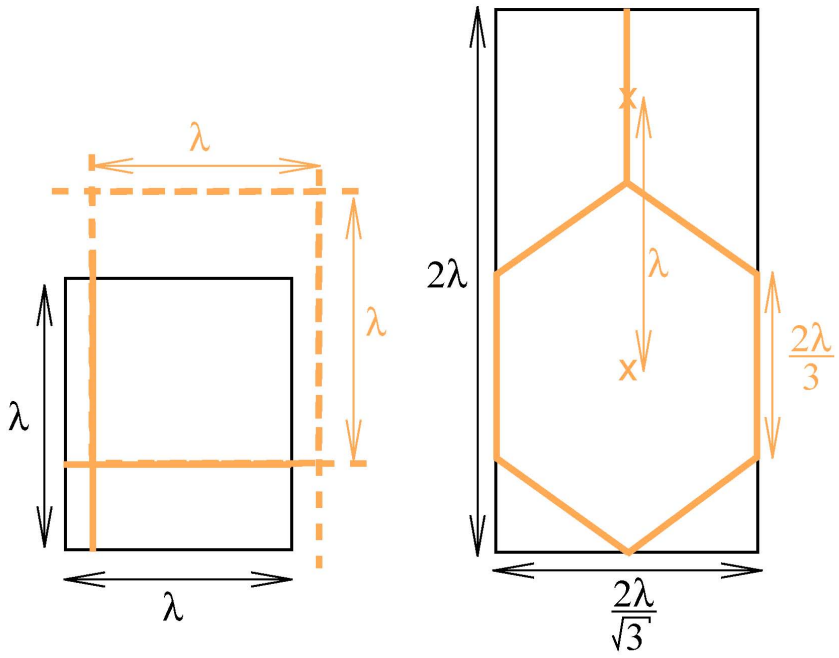

Figure 2.13: Boxes supporting the periodic patterns in the square and hexagonal cases. In black, the borders of the box. Light lines, pattern contained by each box; $\lambda = 2\pi/k_c$.

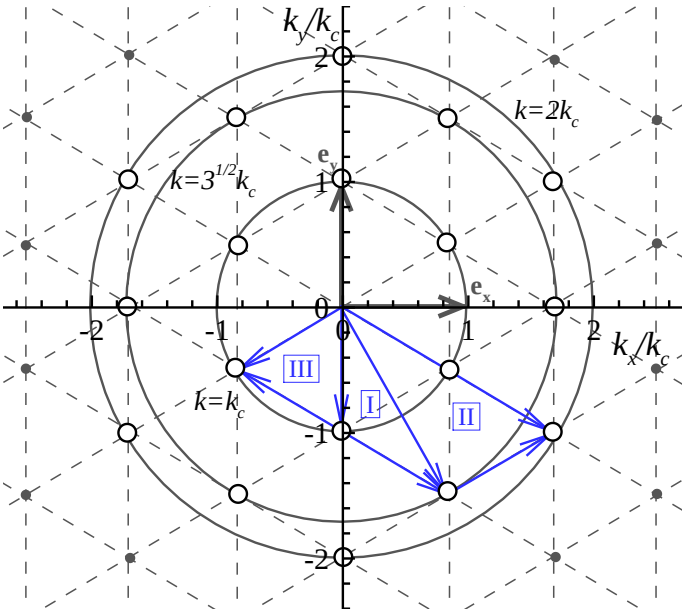

Figure 2.14: Lattice formed by the spatial modes comprising a hexagonal pattern. The principal modes, with wavenumbers k_c, $2k_c$ and $\sqrt{3}\,k_c$, involved in later quantitative investigations are indicated by hollow black circles. The labelled triangles illustrate resonance mechanisms leading to harmonic contributions to higher wavenumbers.

the spectral timeseries of figure 2.19. This apparent wavenumber increase is analogous to that which occurs for the squares, shown in figures 2.8 and 2.10.

The spectra from experiments and simulations are represented in figures 2.19 and 2.20. Given that experimental uncertainties concerning the hexagons are greater than for the squares (Kityk & Wagner, private communication), the agreement is remarkable. The principal mode is well reproduced while the other two modes show rough agreement. It is striking that, in contrast to square patterns, every wavevector is a superposition of harmonic and subharmonic temporal modes, so that each has temporal period $2T$. This phenomenon was explained by Kityk et al. (2005) as a spatio-temporal resonance as follows. In the case of the square lattice, two critical subharmonic modes (e.g. $k_c\mathbf{e}_x$ and $k_c\mathbf{e}_y$) interact to yield a higher wavenumber harmonic mode (e.g. $k_c(\mathbf{e}_x+\mathbf{e}_y)$). In the hexagonal case, two critical subharmonic modes (e.g. $-k_c\mathbf{e}_y$ and $k_c(\sqrt{3}\mathbf{e}_x-\mathbf{e}_y)/2$) interact to yield a higher wavenumber harmonic mode ($k_c(\sqrt{3}\mathbf{e}_x-3\mathbf{e}_y)/2$), as in triangle I of figure 2.14. Further interaction of this mode with a critical subharmonic mode ($k_c(\sqrt{3}\mathbf{e}_x+\mathbf{e}_y)/2$) yields subharmonic contributions to the higher spatial wavenumber mode ($k_c(\sqrt{3}\mathbf{e}_x-\mathbf{e}_y)$), as shown in triangle II. Other quadratic interactions between critical subharmonic modes can contribute to a third harmonic mode of wavenumber k_c (triangle III).

In addition to the interface height, our simulations also produce the entire velocity field, which is the focus of figures 2.21–2.23. These figures show the velocity fields on horizontal planes at three instants spanning the oscillation period of a hexagonal pattern, as well as the vertical velocity on the interface. Figures 2.21, 2.22 and 2.23 correspond approximately to the visualizations of figures 2.15, 2.16 and 2.18, where the structures are more visible since the interface has been repeated periodically in the horizontal directions for clarity. The parameters are the same as those given previously, except that the acceleration a has been decreased to $36.0\,\mathrm{m\,s^{-2}}$, and the number of triangles used to represent the interface has been increased to 64 times the total number of horizontal gridpoints.

Figure 2.21 is taken at $t=0.07\times(2T)$, just after the interface reaches its maximum height (at $t=0$), when the peaks are beginning to descend. Consequently, the fluid converges horizontally towards the interface peaks, then descends dramatically below them. The fluid then diverges horizontally outwards near the bottom and moves upwards in the large regions between the peaks. The motion shown in figure 2.22, at

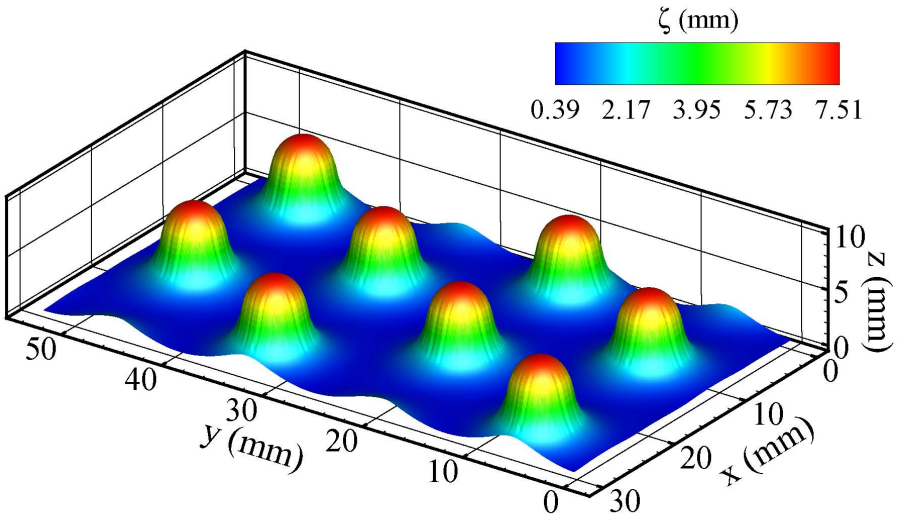

Figure 2.15: Snapshot of hexagonal pattern, taken when height of the interface peaks is maximal. Each horizontal direction s twice that of the calculation domain.

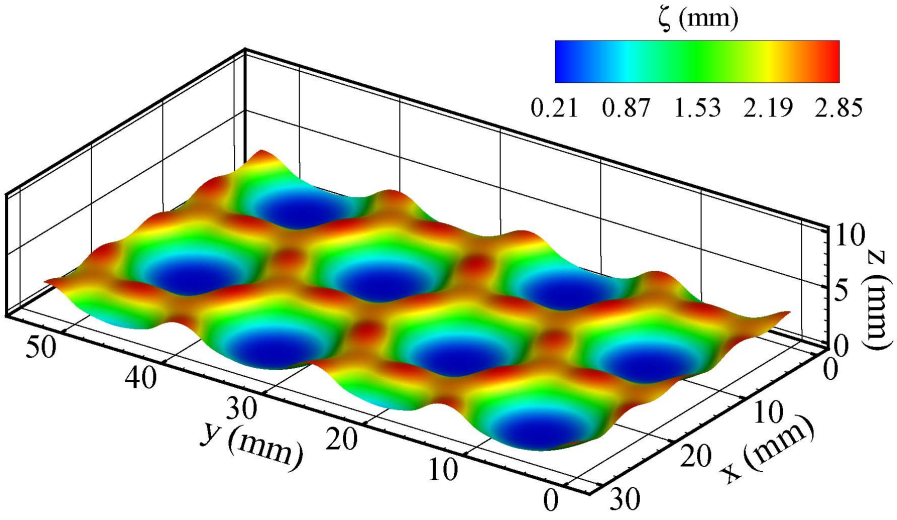

Figure 2.16: Snapshot of hexagonal pattern taken $t = 0.3 \times 2T$ after instant of maximal interface height.

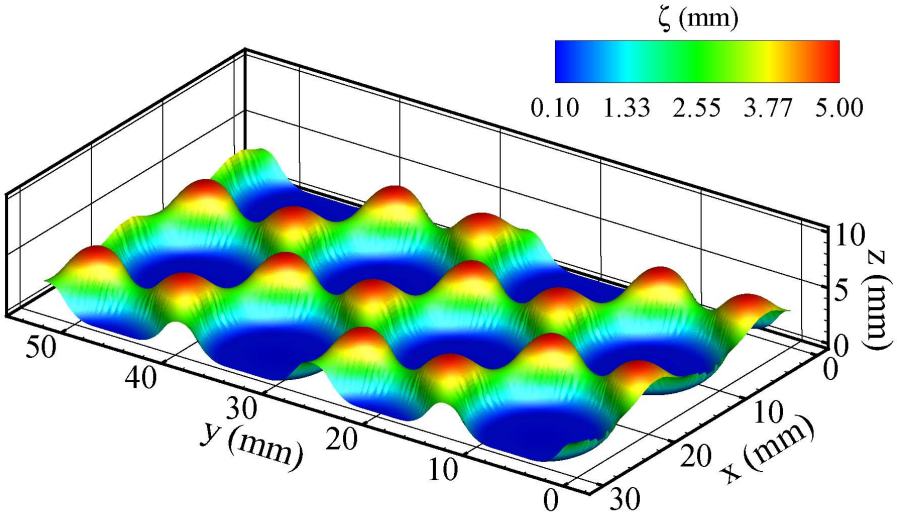

Figure 2.17: Snapshot of hexagonal pattern taken $t = 0.48 \times 2T$ after instant of maximal interface height.

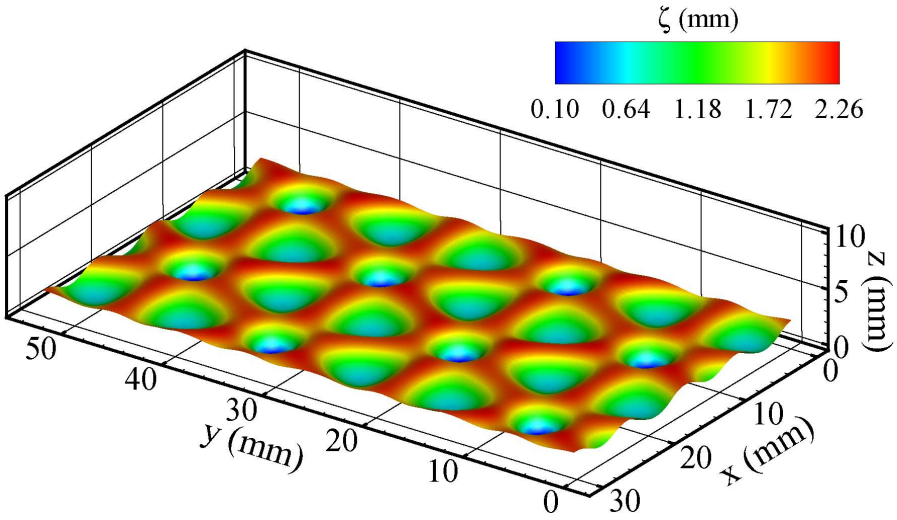

Figure 2.18: Snapshot of hexagonal pattern taken $t = 0.68 \times 2T$ after instant of maximal interface height.

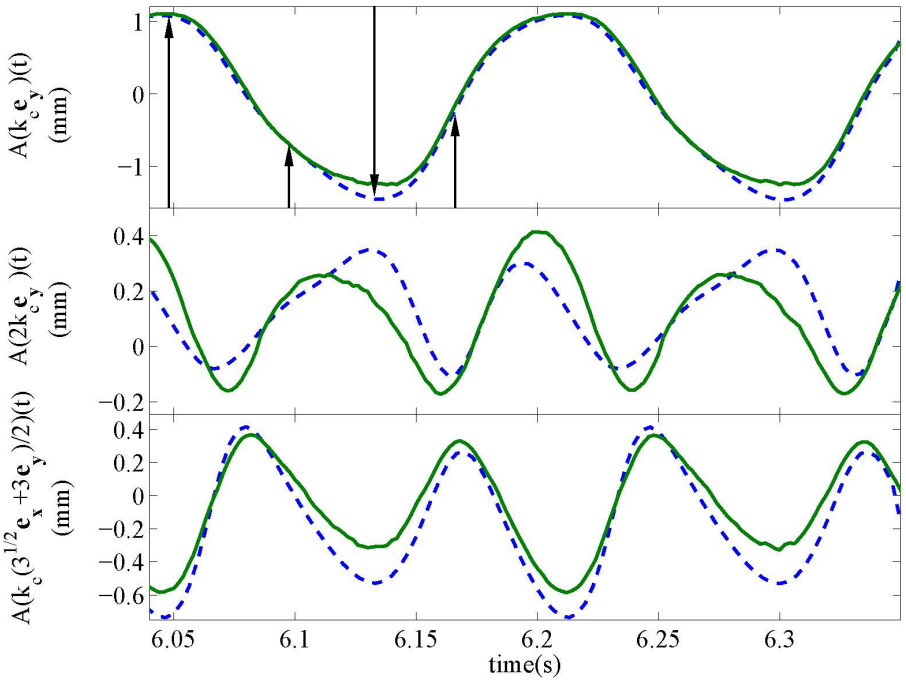

Figure 2.19: Temporal evolution of the amplitudes of the spatial modes with wavenumbers k_c, $2k_c$ and $\sqrt{3}k_c$. Solid curves represent experimental results (Kityk & Wagner, private communication) at $a \approx 38.5\,\mathrm{m\,s^{-2}}$. dashed curves represent the simulation for $a = 38.0\,\mathrm{m\,s^{-2}}$ at resolution (in x, y, z directions) of $58 \times 100 \times 180$. Arrows indicate times corresponding to figures 2.15–2.18.

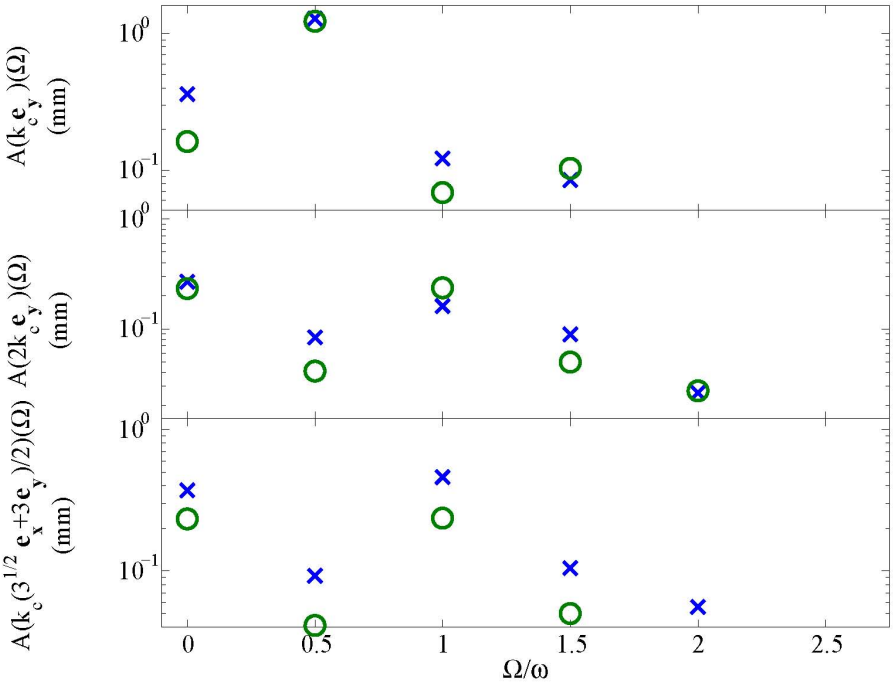

Figure 2.20: Temporal Fourier transform of the amplitudes in figure 2.19. Circles represent experimental results (Kityk & Wagner, private communication) for $a \approx 38.5\,\mathrm{m\,s^{-2}}$. Crosses represent numerical results for $a = 38.0\,\mathrm{m\,s^{-2}}$ at resolution $58 \times 100 \times 180$.

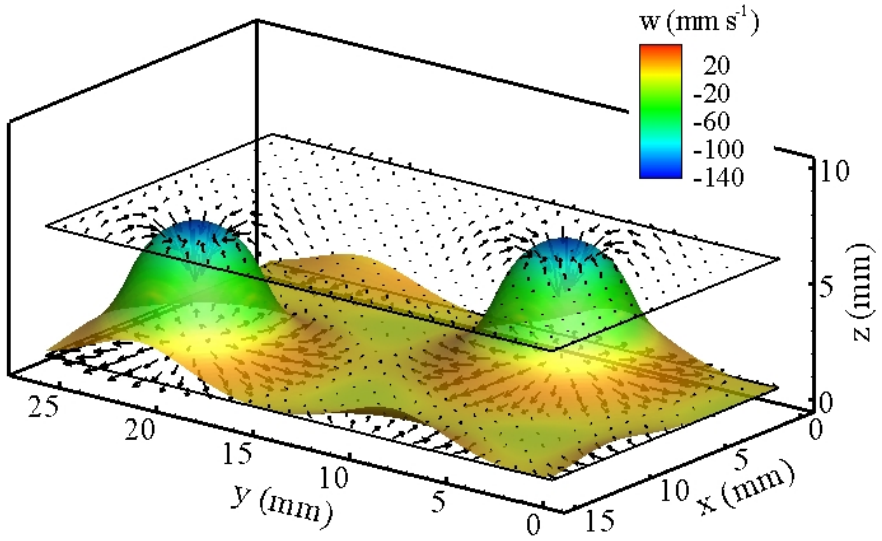

Figure 2.21: Velocity field at time $t = 0.07 \times (2T)$ after the instant of maximum height. Interface is colored according to the vertical velocity w. Arrows show velocity field at $z = 0.53$ mm and $z = 6.08$ mm. (Total height is 10 mm, average interface height is 1.6 mm.) For clarity, velocity vectors are plotted only at every fourth gridpoint in each direction. Note that the vertical and horizontal scales are different. One computational domain is shown.

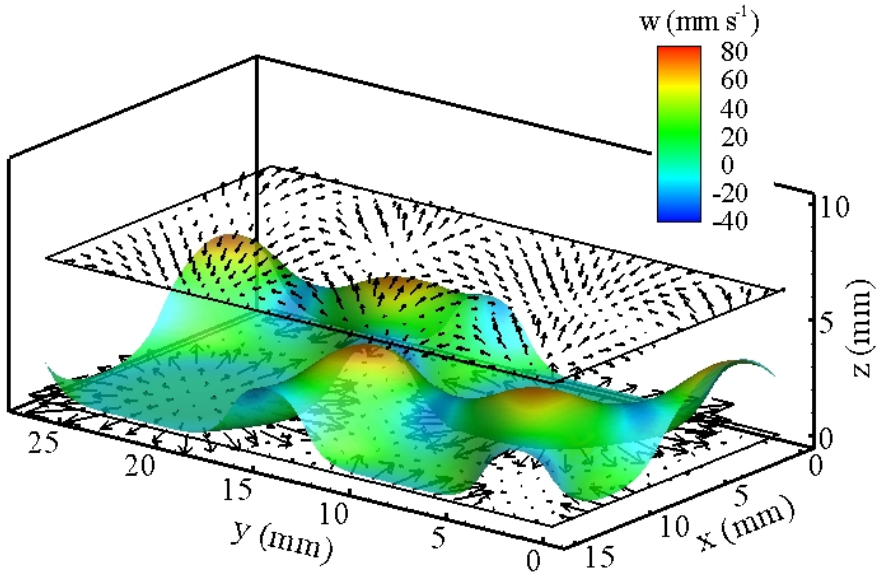

Figure 2.22: Velocity field at time $t = 0.41 \times (2T)$ after the instant of maximum height. Vectors shown at $z = 0.083$ mm and $z = 6.25$ mm. Vector and color scales differ from those of figure 2.21.

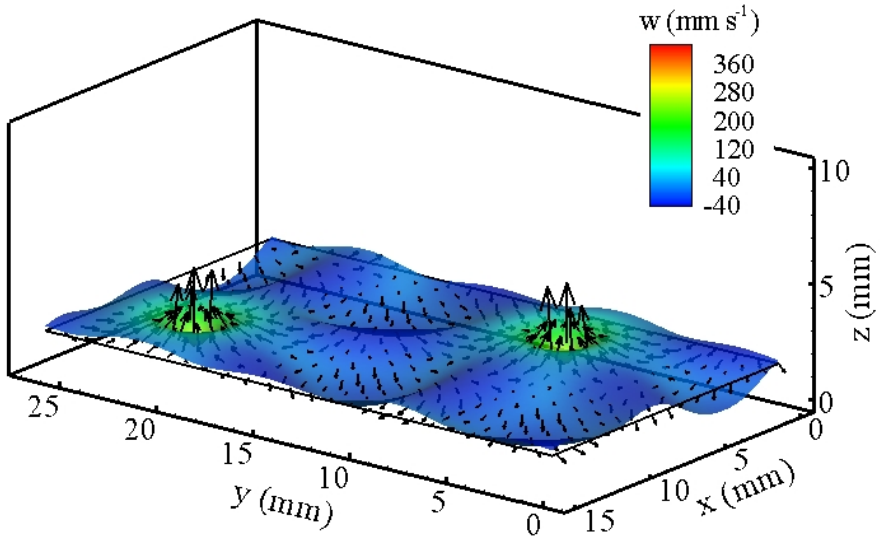

Figure 2.23: Velocity field at time $t = 0.73 \times (2T)$ after the instant of maximum height. Arrows show velocity field at $z = 1.58$ mm. Vector and color scales differ from those of figures 2.21 and 2.22.

$t = 0.41 \times (2T)$, is quite different from that in figure 2.21. The peaks of figure 2.21 have collapsed into wide flat craters. The fluid converges inwards horizontally above the peaks, then descends into the craters and diverges outwards horizontally just below them. Figure 2.23, at $t = 0.73 \times (2T)$, shows that the rims of the wide flat craters seen in figure 2.22 have in turn collapsed inwards, forming circular waves which invade the craters, whose remnants are visible as dimples. The velocity field of figure 2.23 shows fluid converging horizontally below these dimples. These are erupting at velocities which are the largest in the cycle, and will eventually reconstitute the high peaks seen in figure 2.21.

Figures 2.21–2.23, as well as figures 2.15–2.18, show that these cases pose great computational difficulties. The interface periodically forms a very thin film (approximately 0.1 mm; see wide crater in figures 2.17 and 2.22) over large portions of the lower boundary, within which the velocity may be significant. These features make it difficult to adequately resolve the flow in this layer. For the time being we use a uniform grid spacing; however, in this case an adaptive grid would be more efficient and is under development. We have also simulated hexagons with resolutions of $70 \times 120 \times 100$ and $70 \times 120 \times 50$. Although we do not show these, the two highest resolutions lead to very similar spatial spectra with a maximum difference in amplitudes of the principal modes of about 5% between the $70 \times 120 \times 100$ and $58 \times 100 \times 180$ resolutions. The case resolved by only 50 cells in the z direction shows differences mainly in the $2k_c$ mode where the difference between the $70 \times 120 \times 50$ and $58 \times 100 \times 180$ resolution is about 25%; for the two other modes the difference is about 10%. Hexagonal motifs were observed for all of the resolutions.

The calculation for the hexagon case, for the resolution of $58 \times 100 \times 180$ takes about 7 h per subharmonic oscillation on a 2.16 GHz Intel processor. This corresponds to 42 h of calculation time for 1 s of physical time.

In contrast to the square patterns, all of the hexagonal patterns that we have observed are transient. In our calculations, they last for several seconds, i.e. about 15–20 subharmonic oscillation periods, over which time the amplitudes and periods of the principal modes remain constant. This is also the case for the experimental observations (Kityk & Wagner, private communication), although the experimental lifetimes are longer. In our simulations, hexagonal patterns alternated with patterns with other symmetries, whose lifetimes were long (on the order of several seconds) but irregular. This behaviour suggests that the hexagonal state may belong to a heteroclinic orbit. A more extensive examination of the hexagonal regime will be the subject of a future investigation.

2.6 Conclusion

We have carried out full nonlinear three-dimensional simulations of Faraday waves. The incompressible Navier–Stokes equations for two fluid layers of different densities and viscosities are solved using a finite-difference method. The interface motion and surface tension are treated using a front-tracking/immersed-boundary technique. The simulations are validated in several ways. First, for small oscillation amplitudes, our computations match the solution of Kumar and Tuckerman (1994) to the Floquet problem which results from the linearized evolution equations. The boundaries of the instability tongues, i.e. the critical amplitude as a function of horizontal wavenumber are calculated for several wavenumbers on several tongues and are in good agreement with the theoretical values. The temporal dependence of the Floquet modes is also well reproduced by our numerical results, an even more quantitatively significant validation.

For finite oscillation amplitude, our computations reproduce the square and hexagonal patterns observed by Kityk *et al.* (2005, 2009) at moderate and high-oscillation amplitudes, respectively. Although the domains shown in figure 2.13 were chosen to accommodate square and hexagonal patterns respectively, we consider the emergence of these patterns at the appropriate parameter values a non-trivial test of our program, since these domains can also accommodate rectangles and stripes. Quantitative comparisons were made between experiment and simulation of the spatio-temporal spectra. Our numerical results lie well within the experimental uncertainty. The hexagonal patterns are long-lived transients and show intriguing dynamical behavior. Our direct numerical simulations provide velocity fields and pressure throughout the entire domain of calculation. Thus, we have been able to ascertain precisely the fluid motion for the Faraday waves, both above and below the interface between the two fluids.

Our future studies of Faraday waves will include a more detailed investigation of the dynamics of the hexagonal patterns, and the simulation and interpretation of oscillons.

Acknowledgments

The authors acknowledge J. Fineberg, E. Knobloch and A. Rucklidge for insights on theoretical aspects of the Faraday phenomenon, J. Chergui, M. Firdaouss and K. Borońska for advice regarding implementation of certain numerical algorithms and, especially, A. Kityk and C. Wagner for extensive discussions and for sharing their experimental data. This work was supported by computer resources of the Institut du Développement et des Ressources en Informatique Scientifique (IDRIS) of the CNRS, France.

Part III

Time dependent hexagons

3.1 Long time behavior of hexagons

The hexagonal patterns which appear in our simulation of the experiment of Kityk et al. (2005) are transient. The hexagons vanish after a few seconds and are replaced by patterns with other symmetries. The experimental observations confirm this but the lifetimes of the hexagonal regime do not coincide with those in our simulations (Kityk & Wagner, private communication).

We recall the parameters used here and in the experiments of Kityk et al. (2005): $\omega/2\pi = 12$ Hz ($T = 0.0833$ s), $\rho_1 = 1346\ \mathrm{kg\,m^{-3}}$, $\mu_1 = 7.2$ mPa s for the lower fluid and $\rho_2 = 949\ \mathrm{kg\,m^{-3}}$, $\mu_2 = 20$ mPa s for the upper fluid. The surface tension is $\sigma = 35\ \mathrm{mN\,m^{-1}}$, the total height is 1.0 cm and the mean height of the interface, i.e. the initial fill height of the heavy fluid, is $\langle\zeta\rangle = 1.6$ mm. The acceleration is $a = 38.0\ \mathrm{m\,s^{-2}}$, yielding a value of $\epsilon = (a - a_c)/a_c$ of 0.47, where the critical acceleration $a_c = 25.8\ \mathrm{m\,s^{-2}}$ is found by means of a Floquet analysis. The starting condition is a motionless pattern with $\zeta(x, y, t = 0)$ initialized by a white noise of low amplitude in x and y. The dimensions of a box designed to contain the hexagonal patterns are shown in Figure 3.1a.

The symmetry breaking is closely linked to the amplitude $\Delta\zeta$. We notice in Figure 3.1b that the amplitude saturates but only for a short while, the same as the duration of the hexagons. The hexagons only persist

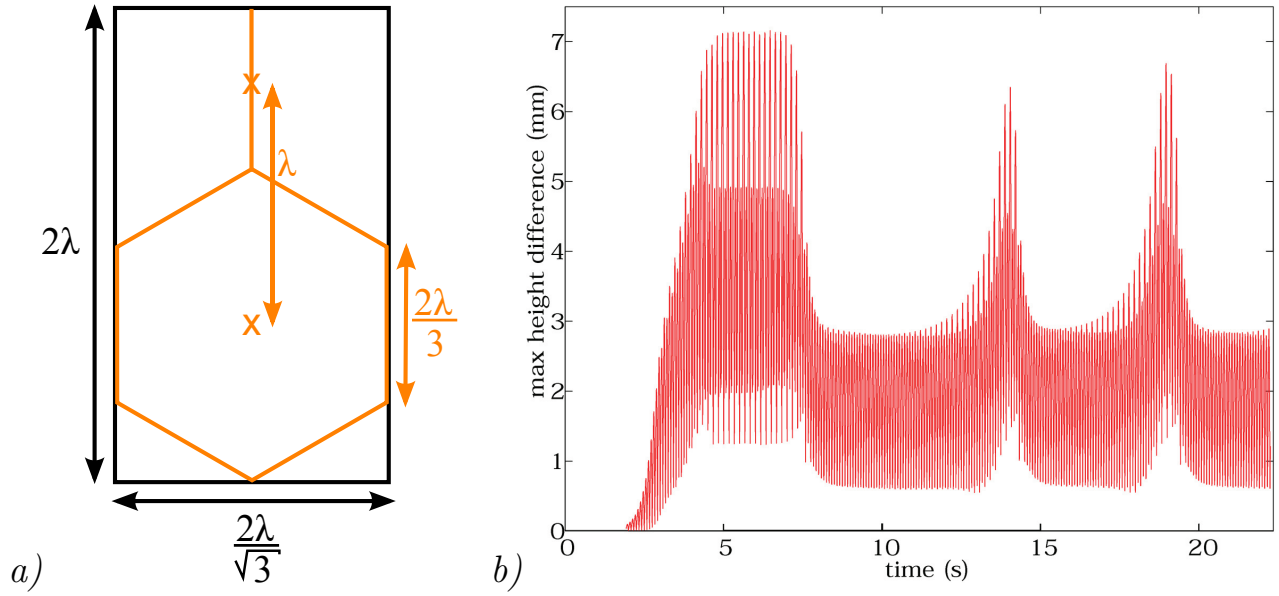

Figure 3.1: a) : Horizontal dimensions of the periodic box that includes one hexagon. Orange : hexagonal pattern. Black : borders of the box. b) : Evolution of $\Delta\zeta(t)$ in the nonlinear saturated regime. Resolution: 180 points in z, 50 points per wavelength in x and y. The hexagonal state is reached when the height amplitude is maximum.

while this saturation amplitude is maintained, after which $\Delta\zeta$ decreases and the hexagons disappear due to symmetry breaking (see Figures 3.1b and 3.2).

$\Delta\zeta$ then remains at a lower level for a few seconds but this state is punctuated by jumps in amplitude correlated with the partial reappearance of the hexagonal invariance. The pattern observed during such amplitude peaks is shown in Figure 3.3 where it can be noticed that the rotational invariance of the state is $2\pi/3$ instead of $\pi/3$. The contour lines of ζ in Figure 3.3 form some kinds of head-to-tail eggs whose direction alternates when the coordinate y changes. This last feature and the presence of the two blue peaks near the origin of the spectrum suggest that the pattern is centered-rectangular instead of triangular. We perform a spectral decomposition by which we can track the modes of wavenumber k_c and the modes they generate through nonlinear interactions (Figure 3.4). The modes associated with the same wavenumber but different orientations have different behaviors. Some spatial modes are significantly damped, coinciding with the decay of the amplitude $\Delta\zeta$. Their angular distribution is responsible for the changes in the symmetry of the pattern.

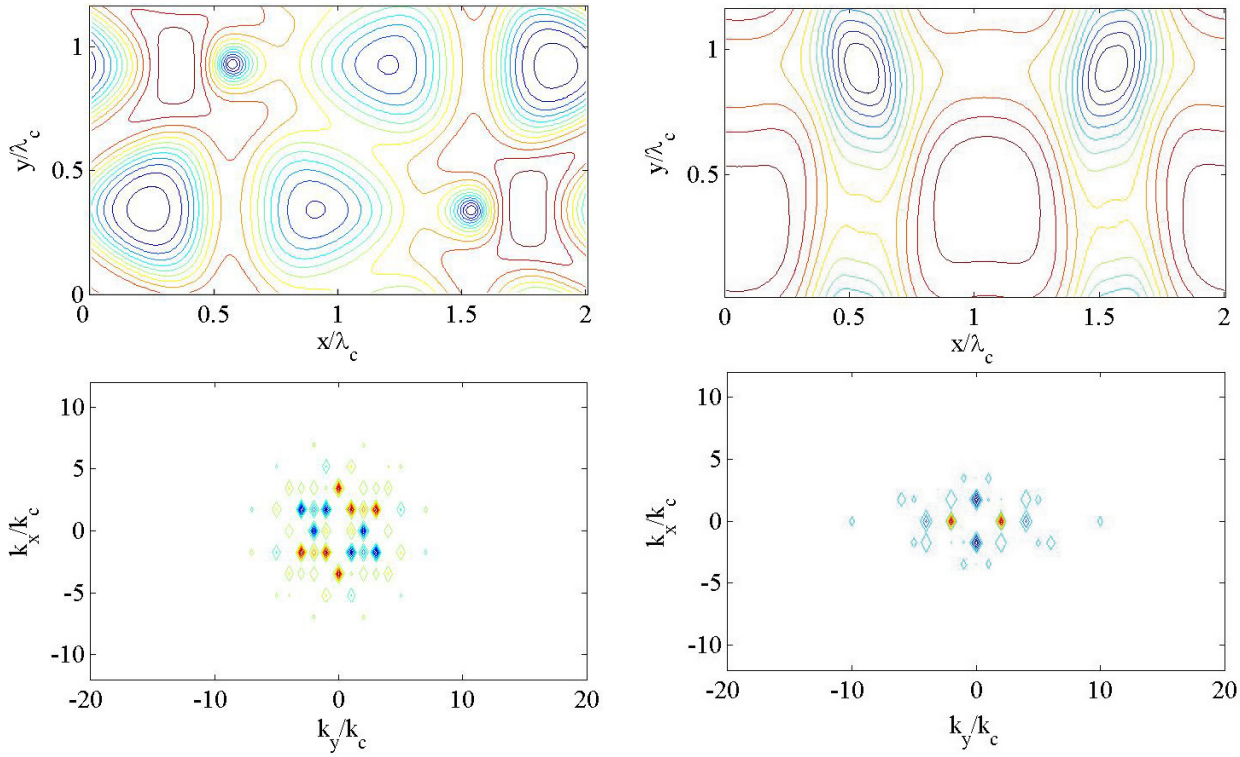

Figure 3.2: Examples of patterns occurring after the hexagons have vanished. Top: contour lines of $\zeta(x, y, t)$. bottom: spatial spectrum of ζ.

The successive approaches to the hexagonal regime suggest that this state is the fixed point of a homoclinic orbit. Considering the elements provided by Figures 3.1b to 3.4, we imagine the scenario which is described in Figure 3.5.

The fixed point has a hexagonal symmetry. The flow is initially quite far from the hexagonal regime. The hexagonal symmetry conditions are satisfied only in part, leading to centered rectangles. The first passage near the fixed point yields a pattern very resembling hexagons, the next passages produce patterns whose differences to hexagons are more marked, the ones displayed in Figure 3.3.

We propose in this chapter to study the hexagonal regime, with the purpose of determining whether it belongs to a homoclinic orbit. Some important elements that characterize this orbit are:

- The location of the fixed point in phase space.
- The most unstable eigenvector.
- The general appearance of the orbit far from the fixed point.

3.2 Imposing hexagonal symmetry

The first step is to identify the exact location of the fixed point in phase space, e.g. the amplitude of every spatiotemporal mode in the case of perfect hexagonal symmetry. To achieve this, the hexagonal symmetry of the interface is forced at regular time intervals. The field variables before and after the forcing should also be as close as possible to each other. Assuming that the unstable direction at the fixed point is responsible for the hexagonal symmetry breaking, we foresee that forcing the hexagonal regime will avoid the unstable eigenvector and project the solution onto the stable eigenspace at the vicinity of the fixed point, leading the dynamics to converge towards this point. The group D_6 of hexagonal symmetry consists of:

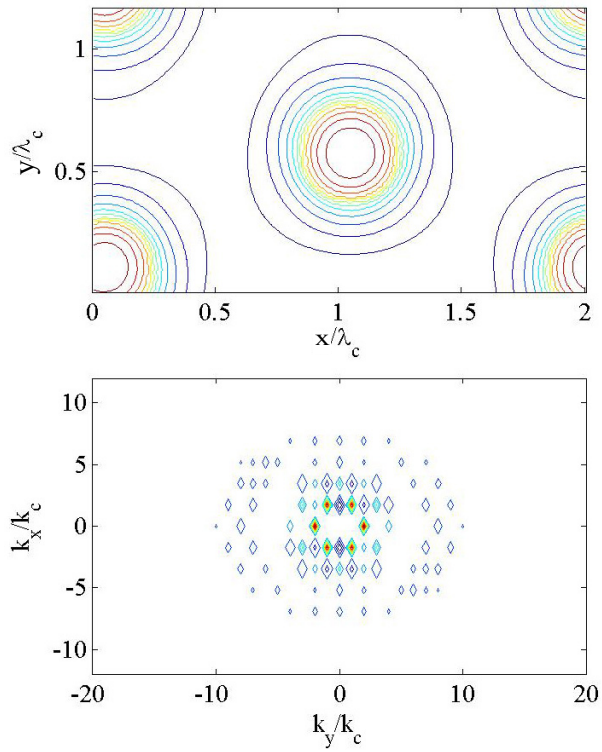

Figure 3.3: Centered-rectangular pattern observed during a jump of amplitude. Top: contour lines of $\zeta(x, y, t)$. bottom: spatial spectrum of ζ.

- $n\pi/3$ rotational invariance ($\in \mathbb{N} \cap [0, 5]$), associated with the operator $\mathbf{R}_{n\pi/3}$,
- reflection through the three vertical planes containing an axis joining opposite vertices of the hexagon or the three perpendicular bisectors of the hexagon edges denoted by $\mathbf{S}$. The orientation of the axes is fixed by the ratio between the size of the box and the wavelength of the mode that is considered (see Figure 3.6a).

Let $\mathbf{f}$ be an affine isometry operator, hence a linear operator, represented by the matrix $\mathbf{P}$ and centered at the point $\mathbf{x} = \mathbf{x}_0$. Hence $\mathbf{f}$ is a bijection of $\mathbb{R}^2$ on $\mathbb{R}^2$. According to the theory of symmetries, the vector field $\mathbf{q}(\mathbf{x})$ is invariant under the action of $\mathbf{f}$ if

$$\mathbf{f}(\mathbf{q}(\mathbf{x} - \mathbf{x}_0)) = \mathbf{q}(\mathbf{f}(\mathbf{x} - \mathbf{x}_0)) \tag{3.1}$$

Suppose first that $\mathbf{q} \in L^2(\mathbb{R}^2)$. Then Plancherel's theorem states that $\mathbf{q}$ can be Fourier-transformed as

$$\mathbf{q}(\mathbf{x}) = \int_{k_x} \int_{k_y} \hat{\mathbf{q}}(\mathbf{k}) \mathrm{e}^{\mathrm{i}\mathbf{k}\cdot(\mathbf{x})} dk_x dk_y \tag{3.2}$$

The use of (3.1) in (3.2) leads to

$$\mathbf{f}\left[\int_{k_x} \int_{k_y} \hat{\mathbf{q}}(\mathbf{k}) \, \mathrm{e}^{\mathrm{i}\mathbf{k}\cdot(\mathbf{x}-\mathbf{x}_0)} dk_x dk_y\right] = \int_{k_x} \int_{k_y} \hat{\mathbf{q}}(\mathbf{k}) \, \mathrm{e}^{\mathrm{i}\mathbf{k}\cdot\mathbf{f}(\mathbf{x}-\mathbf{x}_0)} dk_x dk_y \tag{3.3}$$

We perform on the right hand side of (3.3) the change of variable $\mathbf{k} = \mathbf{f}(\mathbf{k}') = \mathbf{P}\mathbf{k}'$. The formula for integrating a multivariable function with a change of variable states that

$$\int_{k_x} \int_{k_y} \hat{\mathbf{q}}(\mathbf{k}) \, \mathrm{e}^{\mathrm{i}\mathbf{k}\cdot\mathbf{f}(\mathbf{x}-\mathbf{x}_0)} dk_x dk_y = \int_{k'_x} \int_{k'_y} \hat{\mathbf{q}}(\mathbf{f}(\mathbf{k}')) \, \mathrm{e}^{\mathrm{i}\mathbf{f}(\mathbf{k}')\cdot\mathbf{f}(\mathbf{x}-\mathbf{x}_0)} |\mathrm{Det}(\mathbf{P})| dk'_x dk'_y \tag{3.4}$$

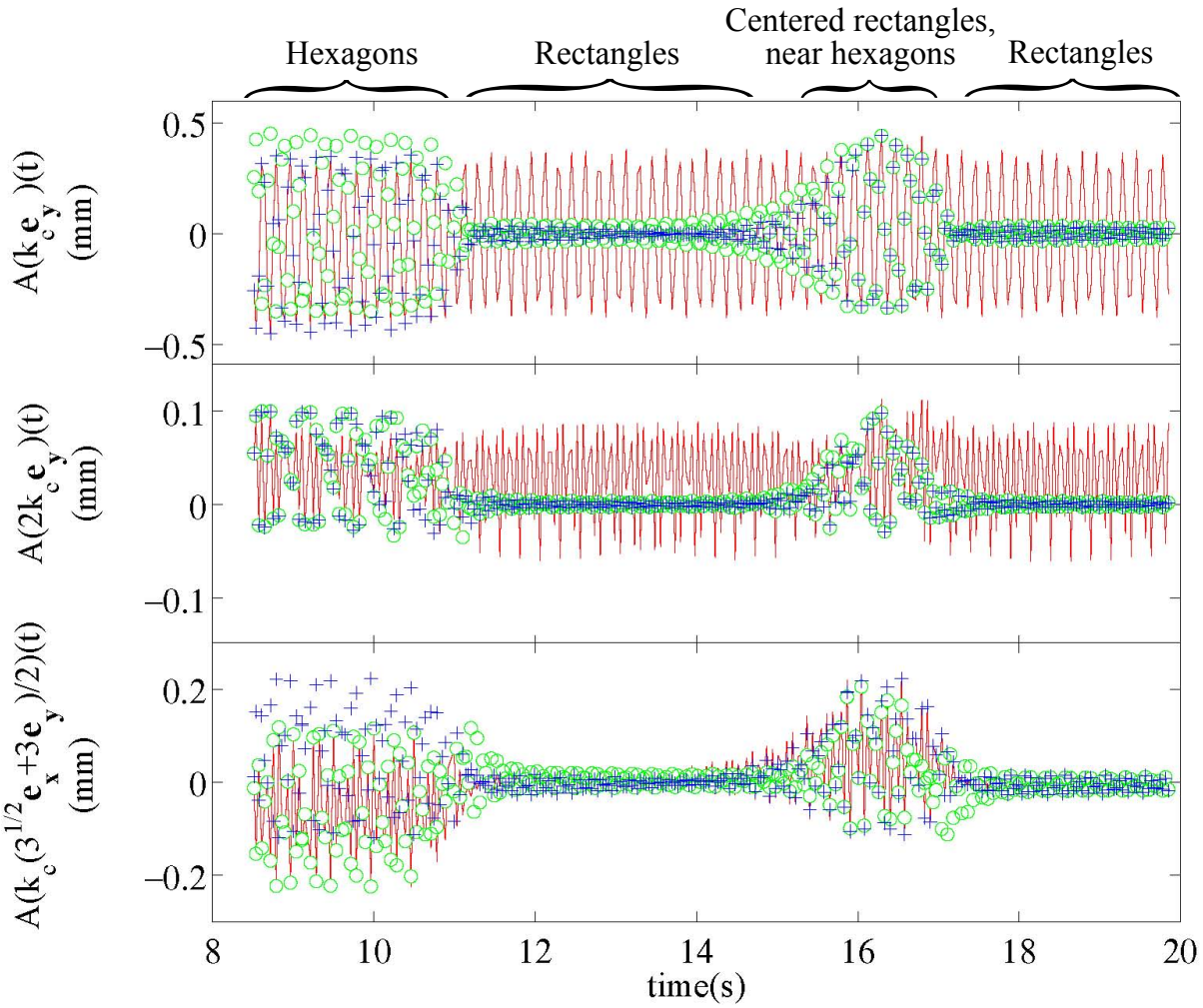

Figure 3.4: Evolution of the main horizontal modes of the interface: the three modes $k_c\mathbf{e}_y$, $2k_c\mathbf{e}_y$, $(\sqrt{3}k_c\mathbf{e}_x + 3k_c\mathbf{e}_y)/2$ (solid lines) and their images under rotations of $\pi/3$ (circles) and $2\pi/3$ (crosses). Hexagons are observed until $t \approx 10.5$ s. When the amplitude of the modes is lower, patterns obviously different from the original hexagons are found (Figures 3.2 and 3.3). The centered-rectangular patterns are observed at the amplitude peaks which occur periodically after the disappearance of the hexagons.

Note that $\mathbf{P}$ is the Jacobian matrix of $\mathbf{f}$. After using (3.4) and rewriting $\mathbf{f}$ in its matrix representation $\mathbf{P}$, (3.3) becomes,

$$\mathbf{P}\left[\int_{k_x}\int_{k_y}\hat{\mathbf{q}}\left(\mathbf{k}\right)\mathrm{e}^{\mathrm{i}\mathbf{k}\cdot\left(\mathbf{x}-\mathbf{x}_0\right)}dk_xdk_y\right] = \int_{k'_x}\int_{k'_y}\hat{\mathbf{q}}\left(\mathbf{P}\mathbf{k}'\right)\mathrm{e}^{\mathrm{i}\mathbf{P}\mathbf{k}'\cdot\mathbf{P}\left(\mathbf{x}-\mathbf{x}_0\right)}|\mathrm{Det}\mathbf{P}|dk'_xdk'_y \tag{3.5}$$

The dot product $\mathbf{P}\mathbf{k}'\cdot\mathbf{P}\left(\mathbf{x}-\mathbf{x}_0\right)$ is transformed with the help of the properties of isometries; in particular the adjoint of $\mathbf{P}$ satisfies $\mathbf{P}^\dagger = \mathbf{P}^{-1}$. Then

$$\mathbf{P}\mathbf{k}'\cdot\mathbf{P}\left(\mathbf{x}-\mathbf{x}_0\right) = \mathbf{P}^\dagger\mathbf{P}\mathbf{k}'\cdot\left(\mathbf{x}-\mathbf{x}_0\right) = \mathbf{k}'\cdot\left(\mathbf{x}-\mathbf{x}_0\right) \tag{3.6}$$

Furthermore, the determinant of an isometry matrix is ± 1, so (3.5) becomes:

$$\mathbf{P}\left[\int_{k_x}\int_{k_y}\hat{\mathbf{q}}\left(\mathbf{k}\right)\mathrm{e}^{\mathrm{i}\mathbf{k}\cdot\left(\mathbf{x}-\mathbf{x}_0\right)}dk_xdk_y\right] = \int_{k'_x}\int_{k'_y}\hat{\mathbf{q}}\left(\mathbf{P}\mathbf{k}'\right)\mathrm{e}^{\mathrm{i}\mathbf{k}'\cdot\left(\mathbf{x}-\mathbf{x}_0\right)}dk'_xdk'_y \tag{3.7}$$

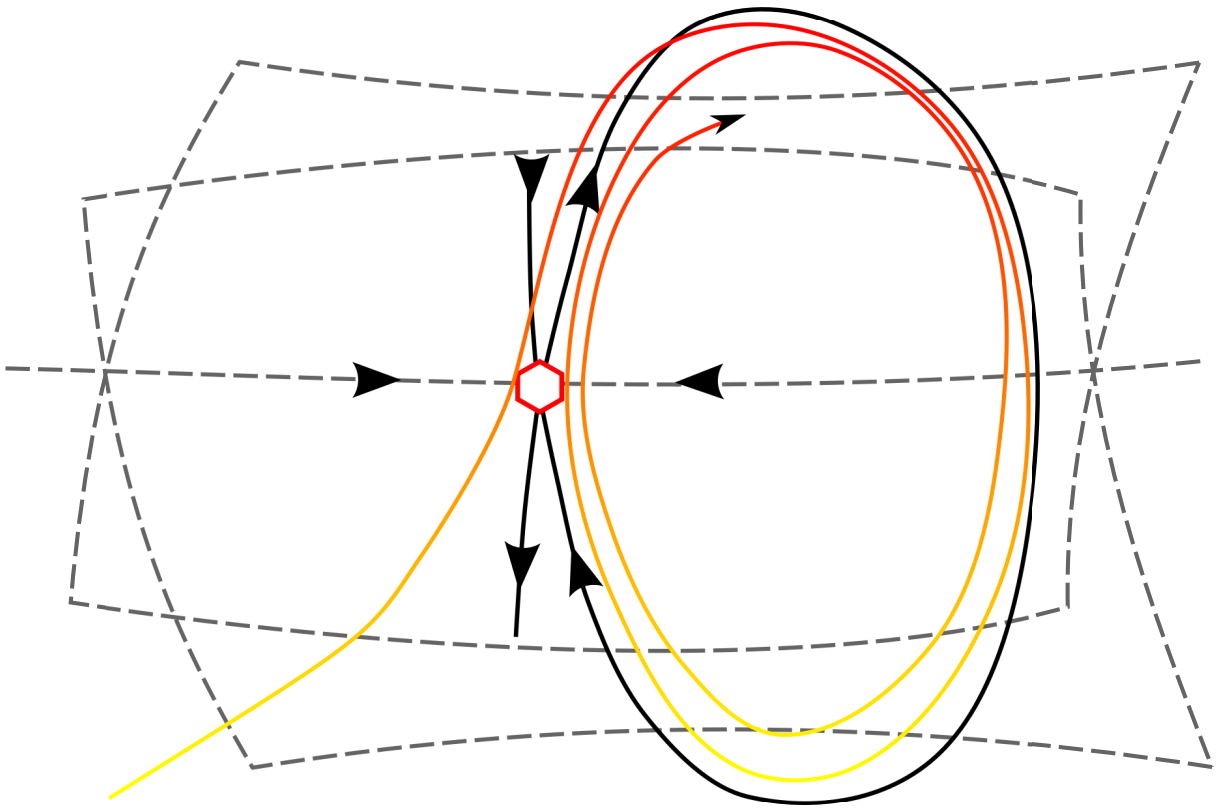

Figure 3.5: Scenario of evolution of the Faraday waves near the hexagonal regime in the phase space. One fixed point is of importance, the hexagonal symmetry which is the departure of the orbit. The red hexagon designates the fixed point and represents the symmmetry of the corresponding flow at this point. The black solid curve is the homoclinic orbit, a limit cycle for the trajectory in colors. The arrows represent the eigenvectors and their stability at the vicinity of the fixed point.

Since $\mathbf{k}'$ and $\mathbf{k}$ are dummy variables, $\mathbf{k}'$ can be changed into $\mathbf{k}$ in the right hand side of (3.7) so that

$$\mathbf{P}\left[\int_{k_x}\int_{k_y}\hat{\mathbf{q}}\left(\mathbf{k}\right)\mathrm{e}^{\mathrm{i}\mathbf{k}\cdot\left(\mathbf{x}-\mathbf{x}_0\right)}dk_xdk_y\right]=\int_{k_x}\int_{k_y}\hat{\mathbf{q}}\left(\mathbf{Pk}\right)\mathrm{e}^{\mathrm{i}\mathbf{k}\cdot\left(\mathbf{x}-\mathbf{x}_0\right)}dk_xdk_y \tag{3.8}$$

$$\Rightarrow\int_{k_x}\int_{k_y}\left[\mathbf{P}\left(\hat{\mathbf{q}}\left(\mathbf{k}\right)\right)-\hat{\mathbf{q}}\left(\mathbf{P}\left(\mathbf{k}\right)\right)\right]\mathrm{e}^{\mathrm{i}\mathbf{k}\cdot\left(\mathbf{x}-\mathbf{x}_0\right)}dk_xdk_y=0 \tag{3.9}$$

A spatial phase change $\mathbf{x}-\mathbf{x}_0\rightarrow\mathbf{x}$, eliminates $\mathbf{x}_0$ in the complex exponential. Since the complex exponential functions are a basis of the functions of L^2, then the integral is zero for all $\mathbf{x}$ if and only if

$$\mathbf{P}\left(\hat{\mathbf{q}}\left(\mathbf{k}\right)\right)-\hat{\mathbf{q}}\left(\mathbf{P}\left(\mathbf{k}\right)\right)=0\qquad\forall k\in\mathbb{R}^2 \tag{3.10}$$

3.2.1 Effect of rotational invariance on the Fourier coefficients

To find the conditions on the coefficients $\hat{\mathbf{q}}$ that correspond to rotational invariance of the vector field $\mathbf{q}$, (3.10) must be solved by identifying $\mathbf{P}$ with $\mathbf{R}_{n\pi/3}$. This leads to the condition that

$$\mathbf{R}_{n\pi/3}\left(\hat{\mathbf{q}}\left(\mathbf{k}\right)\right)=\hat{\mathbf{q}}\left(\mathbf{R}_{n\pi/3}\left(\mathbf{k}\right)\right)\qquad\forall n\in\mathbb{N}\cap\left[1,5\right] \tag{3.11}$$

(3.11) has an important consequence for our simulations. Indeed, when a rectangular Cartesian periodic box is used, the set of available wavenumbers is restricted to a finite and discrete collection in $\mathbb{R}^2$ which we shall

call G and whose basis vectors are

$$\begin{cases} \mathbf{k}_{10} = \dfrac{2\pi}{\lambda_x}\mathbf{e}_x \\ \mathbf{k}_{01} = \dfrac{2\pi}{\lambda_y}\mathbf{e}_y \end{cases} \tag{3.12}$$

where λ_x and λ_y are the horizontal dimensions of the periodic box. Recall that these dimensions are related to the critical wavelength λ_c.

$$\begin{cases} \lambda_x = 2\lambda_c \\ \lambda_y = \dfrac{2\sqrt{3}}{3}\lambda_c \end{cases} \tag{3.13}$$

The simulation can only excite the modes associated with

$$\mathbf{k}_{lm} = l\mathbf{k}_{10} + m\mathbf{k}_{01} \tag{3.14}$$

where l and m are integer coefficients limited by the number of gridpoints in each direction. The set of $\mathbf{k}_{lm}$ permitted by the periodic box dimensions and the discrete mesh is denoted G. Suppose that the critical wavenumber is k_{02}. The only modes on the circle of radius k_{02} are $\mathbf{k}_{20}$ and its images under the rotations $\mathbf{R}_{n\pi/3}$, since the shape of the box prevents the excitation of other critical modes. Now let $\hat{\mathbf{q}}_{lm}$ be the Fourier coefficient associated with the wavevector $\mathbf{k}_{lm}$. It results from (3.11) that:

- If there exists n in $\mathbb{N} \cap [1,5]$ such that $\mathbf{R}_{n\pi/3}(\mathbf{k}_{lm}) \notin G$ then $\hat{\mathbf{q}}_{lm}(\mathbf{k}_{lm}) = \hat{\mathbf{q}}_{lm}\left(\mathbf{R}_{n\pi/3}(\mathbf{k}_{lm})\right) = 0$,
- Otherwise $\hat{\mathbf{q}}_{lm}\left(\mathbf{R}_{n\pi/3}(\mathbf{k}_{lm})\right) = \mathbf{R}_{n\pi/3}\left[\hat{\mathbf{q}}_{lm}(\mathbf{k}_{lm})\right]$ $\forall n \in \mathbb{N} \cap [1,5]$.

The first condition allows us to track easily every mode whose amplitude is strictly zero if the hexagonal symmetry is forced. It also makes it possible to reorganize the indices in a more practical way for computer algorithms:

$$\mathbf{q}(\mathbf{x}) = \sum_r \sum_{s=0}^{5} \hat{\mathbf{q}}_{rs} \mathrm{e}^{\mathrm{i}\mathbf{k}_{rs}\cdot\mathbf{x}} \tag{3.15}$$

where the index r represents the number of the hexagons entirely contained in the discrete set G and $\mathbf{R}_{\pi/3}(\mathbf{k}_{rs}) = \mathbf{k}_{r(s+1)\bmod 6}$ (the same convention will be used for $\hat{\mathbf{q}}_{rs}$). In this formalism, the first hexagon ($r = 1$) is composed of the homogeneous mode and the second one ($r = 2$), of the critical eigenmodes. The correspondence between the two formalisms is shown in Figure 3.6. Hence, the second condition is equivalent to $\hat{\mathbf{q}}_{r(s+1)\bmod 6} = \mathbf{R}_{\pi/3}(\hat{\mathbf{q}}_{rs})$. Here, as well as below for the lm notation, we have omitted commas between two indices in the interest of lightening the notation; r and $(s+1)\bmod 6$ should be interpreted as the first and second subscipt of $\hat{\mathbf{q}}$.

3.2.2 Action of the reflections on the Fourier coefficients

As stated in section 3.2, the orientation of the hexagons varies with the indices l and m, or equivalently with r and s. So do the reflections $\mathbf{S}$. The indexing convention that will be adopted here is the convention lm of subsection 3.2.1 (see equations (3.11) to (3.13)).

Let us begin with the reflection symmetry $\mathbf{S}_{10}$ whose axis is generated by $\mathbf{k}_{10}$. $\mathbf{S}_{10}$, applied to (3.10) in the discrete Fourier space and after the change of variable $\mathbf{x} - \mathbf{x}_0 \to \mathbf{x}$, becomes

$$\sum_l \sum_m \left[\mathbf{S}_{10}\left(\hat{\mathbf{q}}_{lm}\right)\mathrm{e}^{\mathrm{i}\mathbf{k}_{lm}\cdot\mathbf{x}} - \hat{\mathbf{q}}_{lm}\mathrm{e}^{\mathrm{i}\mathbf{S}_{10}^{-1}(\mathbf{k}_{lm})\cdot\mathbf{x}}\right] = 0 \tag{3.16}$$

Since $\mathbf{S}_{10}^{-1} = \mathbf{S}_{10}$, we have

$$\Rightarrow \sum_l \sum_m \left[\mathbf{S}_{10}\left(\hat{\mathbf{q}}_{lm}\right)\mathrm{e}^{\mathrm{i}\mathbf{k}_{lm}\cdot\mathbf{x}} - \hat{\mathbf{q}}_{lm}\mathrm{e}^{\mathrm{i}\mathbf{S}_{10}(\mathbf{k}_{lm})\cdot\mathbf{x}}\right] = 0 \tag{3.17}$$

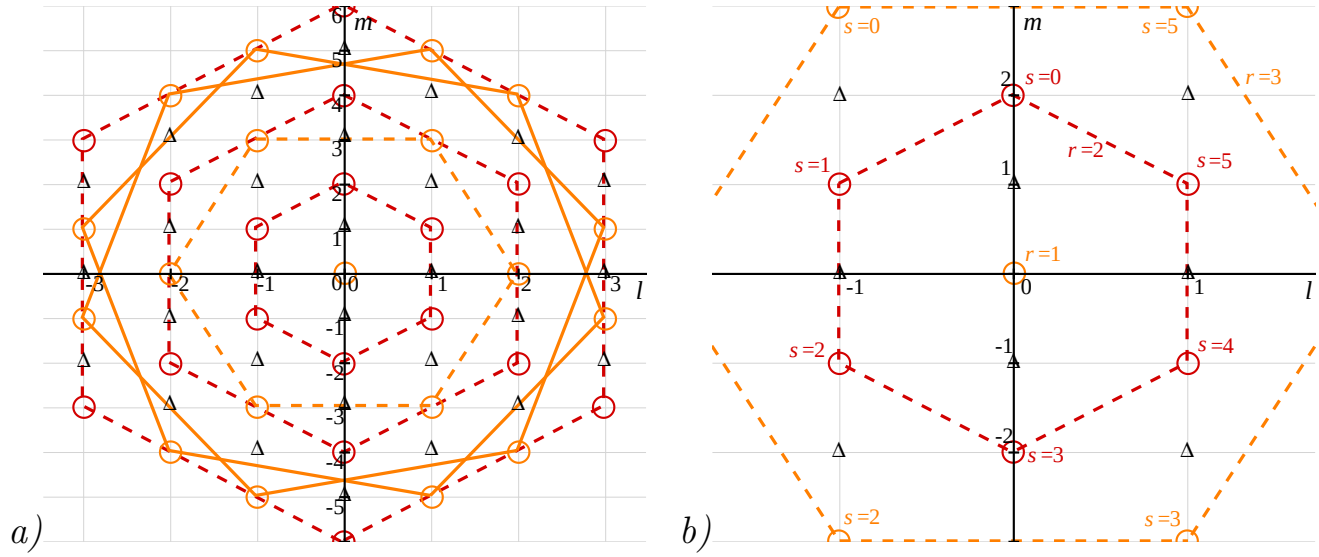

Figure 3.6: a): First hexagons permitted by the mesh in the Fourier space. Δ represent modes which do not belong to a complete hexagon and whose amplitude must then vanish when hexagonal symmetry is forced. Circles are modes which belong to a complete hexagon. Dashed hexagons possess (Ox) and (Oy) as symmetry axes whereas continuous hexagons do not possess these symmetry axes and must be treated in a particular way explained in the text. b): Enlargement of the image on the left and correspondence between the formalisms (l, m) and (r, s), same conventions as for a).

The decomposition of the Fourier coefficients into $\hat{\mathbf{q}}_{lm_\perp}$ and $\hat{\mathbf{q}}_{lm_{//}}$, the components orthogonal and parallel respectively to the vertical plane containing $\mathbf{k}_{10}$, ($\mathbf{k}_{lm_\perp}$ and $\mathbf{k}_{lm_{//}}$ follow the same rule, see Figure 3.7) leads to

$$\sum_l \sum_m \left[\left(\hat{\mathbf{q}}_{lm_{//}} - \hat{\mathbf{q}}_{lm_\perp} \right) \mathrm{e}^{\mathrm{i}\left(\mathbf{k}_{lm_{//}} + \mathbf{k}_{lm_\perp}\right)\cdot\mathbf{x}} - \left(\hat{\mathbf{q}}_{lm_{//}} + \hat{\mathbf{q}}_{lm_\perp} \right) \mathrm{e}^{\mathrm{i}\left(\mathbf{k}_{lm_{//}} - \mathbf{k}_{lm_\perp}\right)\cdot\mathbf{x}} \right] = 0 \tag{3.18}$$

In fact, by following the convention lm, we have in the case of symmetry $\mathbf{S}_{10}$ as represented in Figure 3.7:

$$\begin{cases} \mathbf{k}_{lm_\perp} = \mathbf{k}_{0m} \\ \mathbf{k}_{lm_{//}} = \mathbf{k}_{l0} \end{cases} \tag{3.19}$$

but

$$\begin{cases} \hat{\mathbf{q}}_{lm_\perp} = \hat{\mathbf{q}}_{lm_y} \mathbf{e}_y \\ \hat{\mathbf{q}}_{lm_{//}} = \hat{\mathbf{q}}_{lm_x} \mathbf{e}_x + \hat{\mathbf{q}}_{lm_z} \mathbf{e}_z \end{cases} \tag{3.20}$$

Then (3.18) becomes

$$\sum_l \sum_m \left(\hat{\mathbf{q}}_{lm_{//}} - \hat{\mathbf{q}}_{lm_\perp} \right) \mathrm{e}^{\mathrm{i}(\mathbf{k}_{l0} + \mathbf{k}_{0m})\cdot\mathbf{x}} - \sum_l \sum_m \left(\hat{\mathbf{q}}_{lm_{//}} + \hat{\mathbf{q}}_{lm_\perp} \right) \mathrm{e}^{\mathrm{i}(\mathbf{k}_{l0} - \mathbf{k}_{0m})\cdot\mathbf{x}} = 0 \tag{3.21}$$

We then perform a change of variable in the second sum of (3.21) in order to obtain only one wavevector in each term

$$\sum_l \sum_m \left(\hat{\mathbf{q}}_{lm_{//}} - \hat{\mathbf{q}}_{l-m_{//}} - \hat{\mathbf{q}}_{lm_\perp} - \hat{\mathbf{q}}_{l-m_\perp} \right) \mathrm{e}^{\mathrm{i}\mathbf{k}_{lm}\cdot\mathbf{x}} = 0 \tag{3.22}$$

Because the complex exponentials represent a basis of the periodic functions, (3.22) implies

$$\hat{\mathbf{q}}_{lm_{//}} - \hat{\mathbf{q}}_{l-m_{//}} - \hat{\mathbf{q}}_{lm_\perp} - \hat{\mathbf{q}}_{l-m_\perp} = 0 \tag{3.23}$$

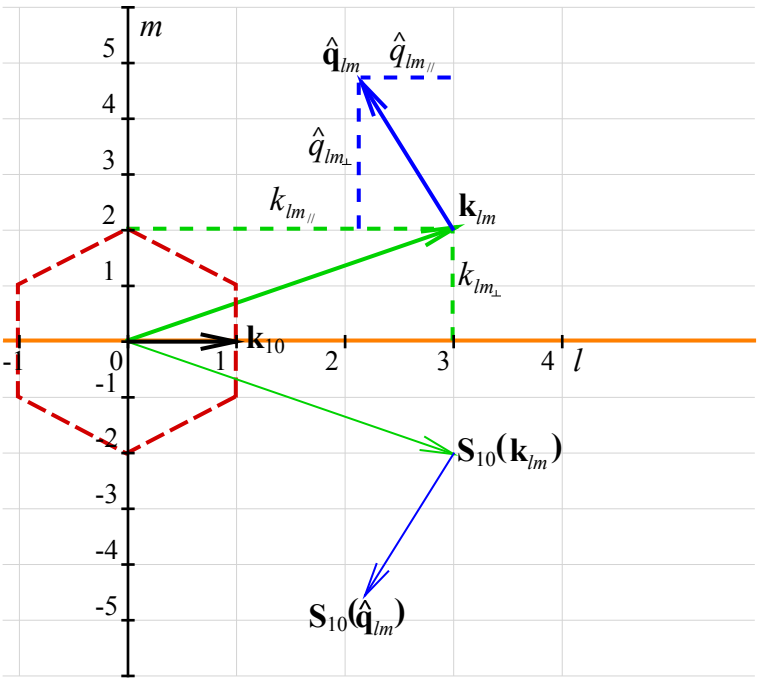

Figure 3.7: Construction of $\hat{q}_{lm_{//}}$ and $\hat{q}_{lm_{\perp}}$, resp. $k_{lm_{//}}$ and $k_{lm_{\perp}}$ the components of $\hat{\mathbf{q}}_{lm}$, resp. $\mathbf{k}_{lm}$ parallel and orthogonal to the reflection axis of $\mathbf{S}_{10}$ generated by the wave vector $\mathbf{k}_{10}$. This axis is plotted in orange. $\mathbf{k}_{lm}$ is represented by the green thick arrow while $\hat{\mathbf{q}}_{lm}$ by the blue one. $\mathbf{k}_{lm}$ joins the origin to a point of the grid whereas $\hat{\mathbf{q}}_{lm}$ is not constrained by the discretization. Images of $\hat{\mathbf{q}}_{lm}$ and $\mathbf{k}_{lm}$ are drawn with thin arrows. Vectors $\hat{q}_{lm_{//}}$ and $\hat{q}_{lm_{\perp}}$ change when the direction of the reflection axis changes.

The expansion of (3.23) into each component of $\hat{\mathbf{q}}$ in the Cartesian frame, with the help of (3.20), leads to the system

$$\begin{cases} \hat{\mathbf{q}}_{lm_x} - \hat{\mathbf{q}}_{l-m_x} = 0 & \hat{\mathbf{q}}_{-lm_x} - \hat{\mathbf{q}}_{-l-m_x} = 0 \\ \hat{\mathbf{q}}_{lm_y} + \hat{\mathbf{q}}_{l-m_y} = 0 & \hat{\mathbf{q}}_{-lm_y} + \hat{\mathbf{q}}_{-l-m_y} = 0 \\ \hat{\mathbf{q}}_{lm_z} - \hat{\mathbf{q}}_{l-m_z} = 0 & \hat{\mathbf{q}}_{-lm_z} - \hat{\mathbf{q}}_{-l-m_z} = 0 \end{cases} \tag{3.24}$$

which is valid for every permitted pair (l,m).

The first hexagon is also invariant under the reflection $\mathbf{S}_{01}$ whose axis is generated by $\mathbf{k}_{01}$. From this consideration is deduced a new system

$$\begin{cases} \hat{\mathbf{q}}_{lm_x} + \hat{\mathbf{q}}_{-lm_x} = 0 & \hat{\mathbf{q}}_{l-m_x} + \hat{\mathbf{q}}_{-l-m_x} = 0 \\ \hat{\mathbf{q}}_{lm_y} - \hat{\mathbf{q}}_{-lm_y} = 0 & \hat{\mathbf{q}}_{l-m_y} - \hat{\mathbf{q}}_{-l-m_y} = 0 \\ \hat{\mathbf{q}}_{lm_z} - \hat{\mathbf{q}}_{-lm_z} = 0 & \hat{\mathbf{q}}_{l-m_z} - \hat{\mathbf{q}}_{-l-m_z} = 0 \end{cases} \tag{3.25}$$

that must be solved simultaneously with (3.24). Gathering, for example, all the equations which involve the x component gives

$$\begin{bmatrix} 1 & -1 & 0 & 0 \\ 0 & 0 & 1 & -1 \\ 1 & 0 & 1 & 0 \\ 0 & 1 & 0 & 1 \end{bmatrix} \begin{bmatrix} \hat{\mathbf{q}}_{lm_x} \\ \hat{\mathbf{q}}_{l-m_x} \\ \hat{\mathbf{q}}_{-lm_x} \\ \hat{\mathbf{q}}_{-l-m_x} \end{bmatrix} = 0 \tag{3.26}$$

from which is deduced the solution for the x component:

$$\hat{\mathbf{q}}_{lm_x} = -\hat{\mathbf{q}}_{-l-m_x} = \hat{\mathbf{q}}_{l-m_x} = -\hat{\mathbf{q}}_{-lm_x} \tag{3.27}$$

Applying the same methods for both components y and z, we find that

$$\hat{\mathbf{q}}_{lm_y} = -\hat{\mathbf{q}}_{-l-m_y} = -\hat{\mathbf{q}}_{l-m_y} = \hat{\mathbf{q}}_{-lm_y} \tag{3.28}$$

and

$$\hat{\mathbf{q}}_{lm_z} = \hat{\mathbf{q}}_{-l-m_z} = \hat{\mathbf{q}}_{l-m_z} = \hat{\mathbf{q}}_{-lm_z} \tag{3.29}$$

Finally, we recall that the vector $\mathbf{q}$ must be real, hence $\hat{\mathbf{q}}_{lm}$ and $\hat{\mathbf{q}}_{-l-m}$ must be complex conjugate, so both $\hat{\mathbf{q}}_{lm_x}$ and $\hat{\mathbf{q}}_{lm_y}$ are in $\mathrm{i}\mathbb{R}$ (see (3.27) and (3.28)) and $\mathbf{q}_{lm_z}$ belongs to $\mathbb{R}$ according to (3.29).

In addition, any Fourier coefficient $\hat{\mathbf{q}}_{lm}$ must be symmetric under reflections in $\mathbf{k}_{lm}$. (3.18) is reused but the symmetry plane now contains the wavevector $\mathbf{k}_{lm}$. Then $\mathbf{k}_{lm_{//}}$ becomes $\mathbf{k}_{lm}$ and $\mathbf{k}_{lm_\perp} = 0$.

$$\sum_l \sum_m \hat{\mathbf{q}}_{lm_\perp} \mathrm{e}^{\mathrm{i}\mathbf{k}_{lm}\cdot\mathbf{x}} = 0 \tag{3.30}$$

It is deduced that for all (l, m) $\hat{\mathbf{q}}_{lm_\perp} = 0$. In other words, the horizontal component $\hat{\mathbf{q}}_{lm}$ is parallel to $\mathbf{k}_{lm}$.

To summarize, the important results of this paragraph are that hexagonal symmetry is possible if:

- both horizontal components of all Fourier coefficients are pure imaginary (3.27)–(3.28),
- the vertical component of every Fourier coefficient is real (3.29),
- $\hat{\mathbf{q}}_{lm_x} = \hat{\mathbf{q}}_{l-m_x}$, $\hat{\mathbf{q}}_{lm_y} = \hat{\mathbf{q}}_{-lm_y}$ and $\hat{\mathbf{q}}_{lm_z} = \hat{\mathbf{q}}_{-lm_z}$ for all Fourier coefficients (3.27)–(3.29),
- $\hat{\mathbf{q}}_{lm}$ is parallel to $\mathbf{k}_{lm}$.

The first two constraints always provide supplementary information about the Fourier coefficients. For the third constraint, there are two cases, depending on the hexagon which is treated and more precisely whether this hexagon is symmetric or not through the (Ox) or the (Oy) axes. If it is symmetric in the Ox or Oz axes, then the third condition does not further constrain the Fourier coefficients associated with this hexagon. If not, let us assume that the r^{th} hexagon is not symmetric though (Ox). Then there exists a hexagon r' which is the image of r under reflection in (Ox) and for which the third condition must necessarily be applied so as to relate the Fourier coefficients $\hat{\mathbf{q}}_{rs}$ and $\hat{\mathbf{q}}_{r's}$ with each other.

The velocity vector will be treated in this way. The interface height will be treated as a vertical vector and consequently governed by the laws found for $\hat{\mathbf{q}}_{lm_z}$.

3.2.3 Algorithm used to force hexagonal symmetry

We restart the simulations at a time when the regime is near the fixed point, *i.e.* the fluid is close to its hexagonal regime, with the regular symmetry forced at regular time intervals. These intervals must not be so short as to drastically increase the calculation time but must be sufficiently short to provide efficient convergence to the fixed point.

Selection of the modes on the mesh involved in the dynamics

We now describe our treatment of hexagons. We show that $\mathbf{k}_{lm}$ belongs to a hexagon if l and m have the same parity (dashed and solid lines in Figure 3.6). According to (3.11), we wish to select the modes involved in the hexagonal symmetry in a rectangular discrete mesh: these are the only nonzero modes. To do this, all the Fourier modes $\mathbf{k}_{lm}$ are sought in the sector $m > 0$ and $l \in [0, m[$ delimited by the two axes that form an angle of $\pi/3$ (3.13). The upper limit is excluded to avoid possible redundancies. Points not belonging to the sector are either images of the aforementioned modes through $\mathbf{R}_{\pi/3}$ or do not belong to regular hexagons. The operator $\mathbf{R}_{\pi/3}$ is applied to each $\mathbf{k}_{lm}$ in the sector. We act on the vectors of indices $\begin{bmatrix} l \\ m \end{bmatrix}$ through the operator $\mathbf{Q} = \mathbf{M}^{-1}\mathbf{R}_{\pi/3}\mathbf{M}$ instead of $\mathbf{R}_{\pi/3}$, where

$$\mathbf{M} = \frac{2\pi}{\lambda_z} \begin{bmatrix} \sqrt{3} & 0 \\ 0 & 1 \end{bmatrix} \tag{3.31}$$

is a distortion matrix that is used to transform $\begin{bmatrix} l \\ m \end{bmatrix}$ into $\mathbf{k}_{lm}$. The vectors $\begin{bmatrix} l \\ m \end{bmatrix}$ are more convenient than $\mathbf{k}_{lm}$ since they are composed of pairs of integers. The condition for a pair (l, m) to be in a hexagon is that $\mathbf{Q}\begin{bmatrix} l \\ m \end{bmatrix}$ and $\mathbf{Q}^2\begin{bmatrix} l \\ m \end{bmatrix}$ both be in $\mathbb{N}^2$ (the three remaining vertices of the hexagon are found by acting on the pair $(-l, -m)$ which also belongs to the mesh). In fact,

$$\mathbf{Q} = \frac{1}{2}\begin{bmatrix} 1 & -1 \\ 3 & 1 \end{bmatrix} \tag{3.32}$$

has a form which projects out of the mesh all pairs (l, m) whose sum is odd. We set to zero the amplitude of all modes which do not satisfy this condition. For wave vectors $\mathbf{k}_{lm}$ satisfying (3.11), *i.e.* belonging to the hexagons, the formalism rs is adopted:

- $\mathbf{k}_{lm} \to \mathbf{k}_{r0}$ for $m > 0$ and $l \in [0, m[$
- $\mathbf{R}^s_{\pi/3}(\mathbf{k}_{lm}) \to \mathbf{k}_{rs},\ s \in [1, 5]$.

Afterwards the relationship between (l, m) and (r, s) is stored in an array of dimensions $r_{\max} \times 6$. The image of the r^{th} hexagon under $\mathbf{S}_{10}$ is simultaneously sought and the correspondence between r and its image is stored in a $r_{\max} \times 2$ array. This procedure is performed only once at the beginning of the simulation because the horizontal structure of the meshes is never altered.

Transformations applied to obtain the hexagonal symmetry

The following steps are performed at regular time intervals.
First, 2D-Fourier transforms (the *jmfft* package) are applied to the interface height ζ and to each velocity component (one Fourier transform per plane of constant height z). The structure of the 2D-Fourier transform library compels us to use only indices s between 1 and 4 if the hexagon r has one point on (Oz), and between 1 and 3 otherwise.

The change of variable $\mathbf{x} - \mathbf{x}_0 \to \mathbf{x}$ is performed as in the passage from (3.9) to (3.10) in order to displace the symmetry center onto the origin by multiplying the Fourier coefficients $\hat{\mathbf{q}}_{rs}$ by $\mathrm{e}^{-\mathrm{i}\mathbf{k}_{rs}\cdot\mathbf{x}_0}$. The calculation of $\mathbf{x}_0$ involves the phases Φ_{rs} of two modes that are chosen arbitrarily (the modes $\mathbf{k}_{20}$ and $\mathbf{k}_{25}$ in the rs formalism which lie on the critical circle have been retained).

$$\begin{aligned} \Phi_{rs} &= \mathbf{k}_{rs} \cdot \mathbf{x}_0 \\ &= \tan^{-1}\left(\frac{\mathrm{Im}(\hat{\mathbf{q}}_{rs})}{\mathrm{Re}(\hat{\mathbf{q}}_{rs})}\right) \end{aligned} \tag{3.33}$$

The following intermediate quantities are then used

$$\varphi_{rs} = \mathbf{e}_{rs} \cdot \mathbf{x}_0 = \frac{\Phi_{rs}}{k_{rs}} \tag{3.34}$$

and with the indications displayed on Figure 3.8, the coordinates x_0 and y_0 of the symmetry center are deduced:

$$\begin{cases} x_0 = \dfrac{\lambda_x}{4\pi}(2\Phi_{25} - \Phi_{20}) \\ y_0 = \dfrac{\lambda_y}{4\pi}\Phi_{20} \end{cases} \tag{3.35}$$

-The interface height ζ or the vertical velocity, w, are treated as follows. Using the conditions gathered in subsections 3.2.1 and 3.2.2, if the hexagon is invariant through $\mathbf{S}_{10}$, then we set

$$\hat{\zeta}_{rs} \leftarrow \frac{1}{6}\sum_{s=0}^{5} \mathrm{Re}\left(\hat{\zeta}_{rs}\right) \tag{3.36}$$

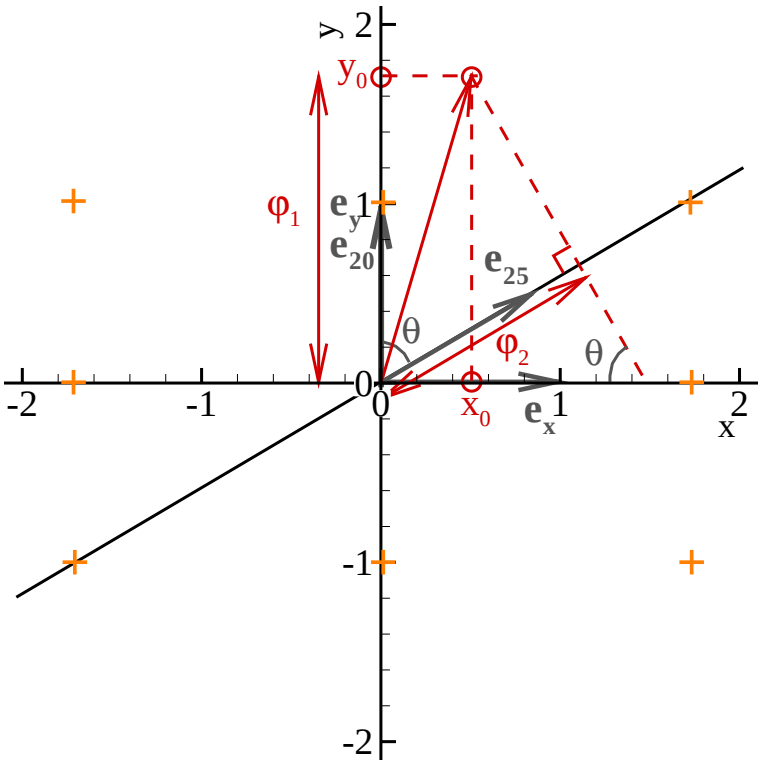

Figure 3.8: Calculation of the symmetry center's coordinates (the red circles) in the orthogonal frame $(O, \mathbf{e}_x, \mathbf{e}_y)$ starting from the phase of two waves $\mathbf{k}_{20}$ and $\mathbf{k}_{25}$ expressed in the system of coordinates $(O, \mathbf{e}_{20}, \mathbf{e}_{25})$. (3.33) and (3.34). The + signs represent the nodes in the discrete mesh.

Otherwise, we set

$$\hat{\zeta}_{rs} = \hat{\zeta}_{r's} \leftarrow \frac{1}{12} \sum_{s=0}^{5} \left[\mathrm{Re}\left(\hat{\zeta}_{rs}\right) + \mathrm{Re}\left(\hat{\zeta}_{r's}\right) \right] \tag{3.37}$$

where r' denotes the image of the hexagon r under $\mathbf{S}_{10}$. Note that, after the transformation, $\hat{\zeta}_{rs}$ are real quantities. The vertical velocity w is handled in the same manner as ζ.

-The horizontal components of the velocity, $\mathbf{u}_{\mathrm{H}} = \begin{bmatrix} u \\ v \end{bmatrix}$, are treated as follows. When the hexagon is symmetric through $\mathbf{S}_{10}$ they are calculated via

$$\hat{\mathbf{u}}_{\mathrm{H}rs} \leftarrow \frac{\mathrm{i}\mathbf{k}_{rs}}{6k_{rs}} \sum_{s'=0}^{5} \frac{\mathbf{k}_{rs'}}{k_{rs'}} \cdot \mathrm{Im}\left(\hat{\mathbf{u}}_{\mathrm{H}rs'}\right) \tag{3.38}$$

Otherwise,

$$\hat{\mathbf{u}}_{\mathrm{H}rs} = \hat{\mathbf{u}}_{\mathrm{H}r's} \leftarrow \frac{\mathrm{i}\mathbf{k}_{rs}}{12k_{rs}} \sum_{s'=0}^{5} \left[\frac{\mathbf{k}_{rs'}}{k_{rs'}} \cdot \mathrm{Im}\left(\hat{\mathbf{u}}_{\mathrm{H}rs'}\right) + \frac{\mathbf{k}_{r's'}}{k_{r's'}} \cdot \mathrm{Im}\left(\hat{\mathbf{u}}_{\mathrm{H}rs'}\right) \right] \tag{3.39}$$

where r' and r are hexagons related by reflection under $\mathbf{S}_{10}$.

The final operations consist of forming hexagons centered at the origin. To move back the center of symmetry of the field to its original position, we perform the reciprocal variable change $\mathbf{x} \to \mathbf{x} - \mathbf{x}_0$, by multiplying each Fourier coefficient by $\mathrm{e}^{\mathrm{i}\mathbf{k}_{rs}\cdot\mathbf{x}_0}$. The inverse 2D-Fourier transforms of each variable are then applied, using the same strategy, *i.e.* one inverse 2D-FT per horizontal plane for the velocity.

Additional remarks

The interface, ζ, is calculated on a triangular mesh, more precisely centered-rectangular. The vertices of the rectangles and the centers are treated separately. Our current algorithm yields an unexplained phase shift between the points at the centers of the squares and their counterparts located at the edges. We eliminate this shift by interpolating ζ at a center from its values at the neighboring corners as shown in Figure 3.9. The interpolation scheme is of order 4.

$$\begin{aligned} \zeta^{\,c}_{i,j} = & \quad \frac{1}{40}\left[\zeta^{\,v}_{i-1,j-1} + 9\zeta^{\,v}_{i,j} + 9\zeta^{\,v}_{i+1,j+1} + \zeta^{\,v}_{i+2,j+2}\right] \\ + & \quad \frac{1}{40}\left[\zeta^{\,v}_{i-1,j+2} + 9\zeta^{\,v}_{i,j+1} + 9\zeta^{\,v}_{i+1,j} + \zeta^{\,v}_{i+2,j-1}\right] \end{aligned} \tag{3.40}$$

Problems related to the phase shift may also appear when the horizontal components of the velocity are

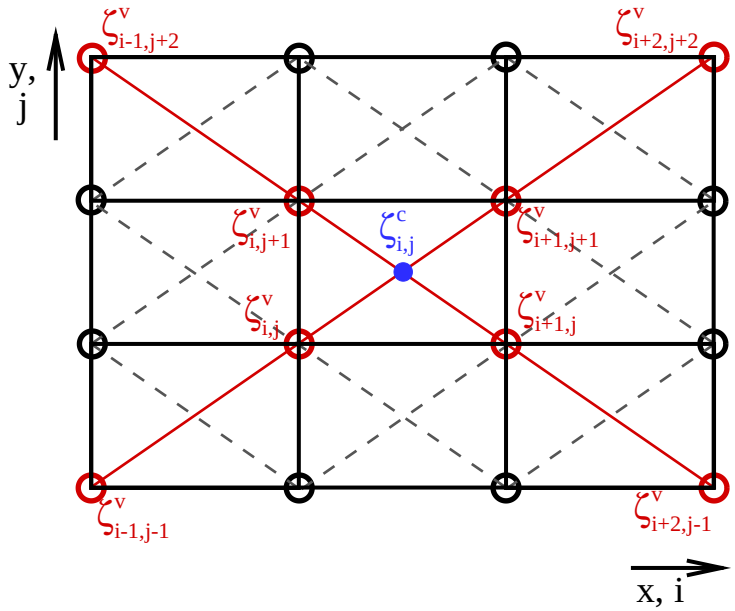

Figure 3.9: Interpolation scheme for the interface height ζ at the centers of the squares based on the values of ζ at the corners in the triangular mesh (black and gray lines). Red circles indicate points used in the interpolation, while the blue point is that for which ζ is sought.

calculated, because of the use of a staggered Eulerian mesh. Special care must be taken in the calculations of the coordinates (x_0,y_0) of the center of the hexagon for the velocity components.

The density and viscosity at each point of the domain are deduced from the interface height. These need not be explicitly symmetrized, but the indicator function that determines in which fluid each point of the Eulerian mesh is located must be calculated from the interface height by solving a Poisson equation. The new pressure is given by an additional solution of a Poisson equation after having forced the hexagonal symmetries on the velocity.

Test cases

Subsections 3.2.1 and 3.2.2 highlighted that there are three mechanisms that can cause departure from hexagonal symmetry. The first is the variation in amplitude of one mode with respect to its images under a transformation of D_6. The second is the generation of a spatial phase difference between a mode and one of its counterparts. The third is the generation of additional modes which are not included in hexagons (the modes whose sum of indices $l + m$ is odd). The following tests are carried out in order to check that

the hexagonal symmetry is well restored after the action of these three mechanisms. We first check the case of amplitudes with the six available modes of wavenumber k_c. These modes have various amplitudes comprised within the interval $[0.8, 1.2]$ arbitrary units, but with the same phase. Patterns close to hexagons are therefore expected. The initial configuration and the pattern after symmetrization are shown in Figure 3.10.

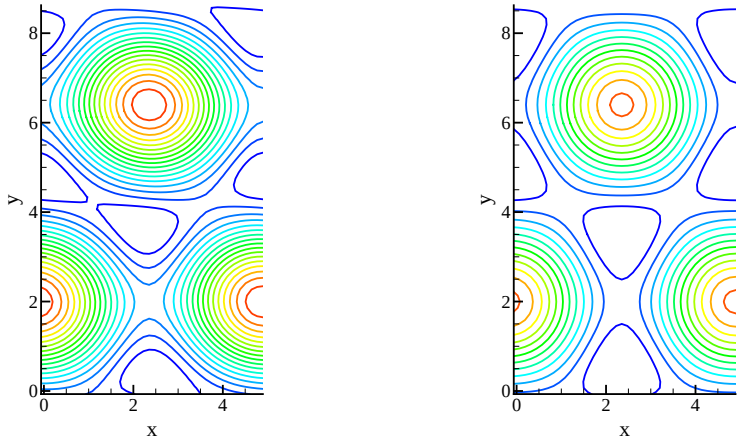

Figure 3.10: Test on the amplitude for the interface ζ (colors). Resolution: 80 points in x, 128 points in y. Left: initial pattern, right: symmetrized pattern.

The symmetrization after a phase difference is now tested. This time, the modes chosen are distributed over the two hexagons of wavenumbers of k_c and $2k_c$. Their amplitudes are 1 and 0.5 arbitrary units, respectively. All the modes have the same phase except $\hat{\zeta}_{11}$ which is shifted by $\pi/2$. This generates a symmetry breaking in the direction of $\hat{k}_{11}$ and induces the breaking of the invariance through rotations of $\pi/3$. The results of the test are displayed in Figure 3.11.

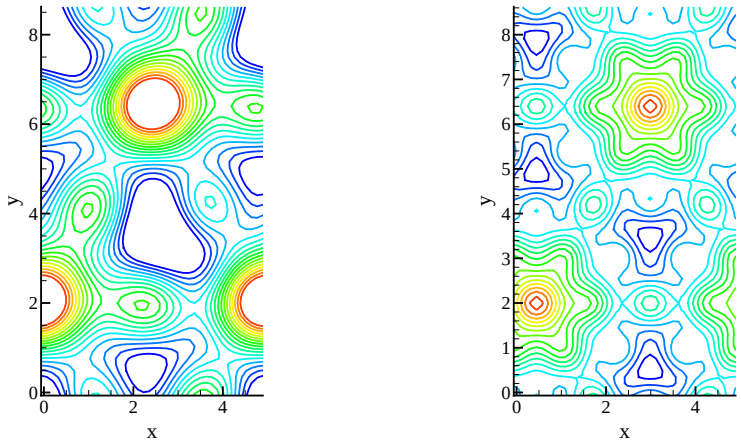

Figure 3.11: Test on the phase for the interface ζ. Same resolution and convention as in Figure 3.10.

Finally, we carry out a global test to see whether every situation has been accounted for, *i.e.* whether modes that do not belong to hexagons vanish, and whether the pair-by-pair treatment of hexagons which do not exhibit symmetry under $\mathbf{S}_{10}$ is effective. The initial surface height ζ is generated randomly for the 20×20 first modes in x and y. With random initial modes, there may be drastic transformations of ζ between its initial state and the symmetrized one (see Figure 3.12). All three graphs, Figure 3.10 to Figure

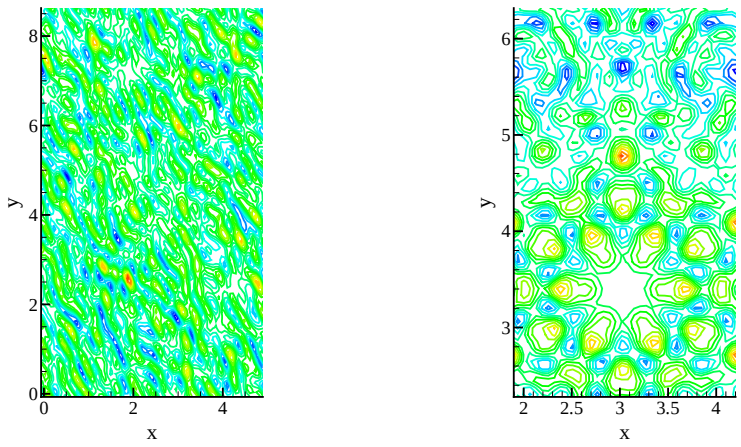

Figure 3.12: Test on random initial modes ζ. Resolution and conventions as in Figure 3.10.

3.12, highlight that the process of symmetrization works qualitatively well. The superposition of the centers of symmetry of both the velocity field and ζ has also been monitored.

3.3 Calculation of the most unstable eigenvector and behavior of the orbit far from the fixed point

The most unstable eigenvector is naturally computed by the code without forcing the symmetry, because the unstable components of the solution near the fixed point will always be generated by the various approximations due to the discretization. (The introduction of a perturbation can, however, speed up the computation.) Let us assume that $\mathbf{V}_F = (\mathbf{u}_F, \zeta_F, p_F)$ is the solution after convergence of the algorithm described in section 3.2, assumed to be sufficiently close to the fixed point sought. If $\mathbf{V}(t)$ is the state after having run the code without forcing the symmetry and starting from $\mathbf{V}_F$, then the eigenvector is nearly $\mathbf{V}(t) - \mathbf{V}_F$ after a time large enough to have converged to the most unstable eigenvector but not so long as to make nonlinear interactions significant.

The basic spectral analysis of section 3.1 (see Figure 3.4) suggests that even though the pattern of the interface undergoes drastic changes, the underlying dynamics are simpler than they may appear. Indeed, some subsets of modes seem to be strongly correlated since they decay and rise at the same time. The justification of such group dynamics is most likely provided by the triadic interactions. Taking into account this behavior, we could greatly simplify the homoclinic orbit study, or equivalently reduce the dimension of the orbit. We could use results of a deeper spectral analysis involving more modes and classifying the modes that have similar evolution.

3.4 Conclusion

An exotic regime of Faraday waves has been discovered: a state of the flow with intermittent appearance and disappearance of an hexagonal symmetry.

We have proposed that the behavior might be due to the presence of a homoclinic orbit. We have formulated a method of investigation to determine the fixed point, the most unstable eigenvector and the trajectory far from the fixed point. We have described above a method that should lead to the convergence of the solution to the fixed point by forcing a set of symmetries while maintaining the flow as close as possible to its asymmetric counterpart. Static tests on the method have been performed and have shown its validity.

The homoclinic orbit might be related to the size of our box, which was designed to contain only one hexagonal unit cell composed of wave vectors whose length is λ_c, the critical wavelength. Although periodic boundary conditions have been implemented across the vertical walls, a box of such a small extent has

consequences on the dynamics because it bans a large number of solutions, in particular squares of dimension λ_c. It was noticed in Kityk et al. (2005) that there was a transition from squares to hexagons over a finite range of accelerations. Our value of a was chosen to be above these intermediate accelerations, but because of the uncertainties in the experimental parameters, a may actually belong to the transition range; if a were increased hexagons might be permanent. We tested this issue by increasing a to $41\,\mathrm{m\,s^{-2}}$, or ϵ to 0.59. As a result, the flow approached the fixed point more than previously, $\Delta\zeta$ reached its highest value at each passage near the fixed point, the peaks displayed in Figure 3.1b mutated into plateaus whose lifetime became approximately half the period of an alternation. Our intuition seems hence to be confirmed and after amplifying the vibration of the container we should observe a state that always keeps the hexagonal symmetry.

The experiment conducted in a large domain showed that the transition was marked by the coexistence of hexagons and squares. The homoclinic orbit could be the temporal analog of this spatial coexistence.

Part IV

Drift instability

4.1 Introduction

In numerous hydrodynamical problems, a medium originally free of global motion can undergo changes in its structure that lead to the creation of currents. This phenomenon is called drift instability. The drift instability was discovered recently and almost simultaneously in many physical problems. In 1984, Malomed and Tribelsky predicted theoretically that stationary patterns could destabilize in favor of traveling structures through a secondary bifurcation. The drift instability was first observed experimentally in 1985 in Rayleigh-Bénard convection in mixtures of water and alcohol (Walden et al., 1985). Experiments in a partially filled Taylor-Couette column (Mutabazi et al., 1988) showed that the basic laminar state could destabilize in favor of shifted traveling rolls in the fluid bulk, in contrast to the motionless patterns always found in the fully filled Taylor-Couette experiment. Traveling patterns were observed in digitation experiments (Rabaud et al., 1990). Simon et al. (1988) reported another kind of drift instability observed at the surface of separation of the nematic and isotropic phases of a liquid crystal. Traveling asymmetric waves that stretch and then compress the initially periodic and symmetric patterns formed at the interface were noticed.

In the framework of Faraday waves, the drift instability consists of the horizontal displacement of patterns at the interface and was reported for the first time in 1989 by Douady et al.. The same authors, Fauve et al. (1991), supplied a phenomenological explanation of the transition from motionless patterns to a regularly moving state with a simple model coupling amplitudes of slowly varying periodic patterns. Under the hypotheses of saturating nonlinear terms and weak detuning, a drift arises when the amplitude of the forcing is increased. A symmetry-breaking bifurcation occurs in which the standing wave solution, or equivalently, the superposition of two counter-propagating waves of equal amplitudes, wave number and temporal frequencies, destabilizes. When the forcing becomes strong enough, the amplitudes of the two waves, deviate from one another and generate a drift. Fauve et al. (1991) showed that the drift velocity was slaved to the asymmetry variable and, in particular, that the patterns move in the propagation direction of the wave with the higher amplitude.

Martín et al. (2002) and Vega et al. (2001) conducted a weakly nonlinear analysis of Navier–Stokes equations in a free-surface flow subjected to vertical oscillations when the viscosity is small. They modeled the annular container by a rectangular domain of finite height which was periodic along the horizontal direction. The linear analysis leads to two kinds of coexisting modes: the surface modes and the viscous modes (see, for example, Lamb (1930) or Martel and Knobloch (1997)). In the early work on drift, only the effect of the surface modes was taken into account. However, it has been demonstrated by Martel and Knobloch (1997) that, especially for low viscosity, the viscous modes play a non-negligible role in the dynamics of free-surface flows and therefore of Faraday waves. These modes are singular in the sense that they do not produce deformations of the free surface and they should be responsible for the appearance of the streaming flow, according to Martín et al. (2002). The effect of the coupling of the streaming flow with the oscillating flow that results from the classical studies of Faraday waves may generate a drift of the patterns at the interface. Martín et al. (2002) constructed bifurcation diagrams to characterize the flows they obtained in terms of two properties: the phase velocity of the patterns and the $\lambda/2$-aperiodicity of the mean flow.

We study numerically the drift instability of Faraday waves in a case close to that of Martín et al. (2002). Our study is based on simulations of the Navier-Stokes equations in two viscous and incompressible fluids separated by an interface. The details of the numerical algorithms are given in Périnet et al. (2009). No further approximations are performed. The first section will be dedicated to the presentation of the theories of Fauve et al. (1991), Martel and Knobloch (1997) and Martín et al. (2002) which are complementary since the former displays the two kinds of waves that stem from the linear analysis and that are the starting point of the latter theory. This theoretical overview is supplemented by the description of the modeling of Vega et al. (2001). In the second section, we describe the physical conditions chosen for our simulations. The results of our computations are presented and discussed in the third part, which is followed by a conclusion.

4.2 The theory of nearly inviscid waves

4.2.1 First phenomenological approach

Fauve et al. (1991) proposed the following model to describe the drift instability near the primary Faraday

instability threshold, where the interface has the form

$$\zeta(x,t) = A(t)\mathrm{e}^{\mathrm{i}(-kx+\omega t)} + B(t)\mathrm{e}^{\mathrm{i}(kx+\omega t)} + c.c. \tag{4.1}$$

at leading order, where ω is half the forcing frequency and A, B are assumed to vary slowly in t only. The amplitude equations they obey are

$$\begin{aligned} A_t &= (-\delta + \mathrm{i}d)A + \left(\alpha_1|A|^2 + \alpha_2|B|^2\right)A + \alpha_3\overline{B} \\ B_t &= (-\delta + \mathrm{i}d)B + \left(\alpha_1|B|^2 + \alpha_2|A|^2\right)B + \alpha_3\overline{A} \end{aligned} \tag{4.2}$$

where $\delta > 0$ denotes a dissipation coefficient, d a detuning coefficient, α_1 and α_2 are complex coefficients measuring the strength of the nonlinear terms. The coefficient α_3 represents the forcing; if $\alpha_3 \leq 0$, a standing wave regime is observed. The stability of this regime is studied by writing A and B as:

$$\begin{aligned} A &= \mathrm{e}^{R+S}\mathrm{e}^{\mathrm{i}(\Theta+\Phi)} \\ B &= \mathrm{e}^{S-R}\mathrm{e}^{\mathrm{i}(\Theta-\Phi)} \end{aligned} \tag{4.3}$$

S is a measure of the mean of both waves, R measures the asymmetry, Θ is the spatial phase of the pattern and Φ is its temporal phase. (4.2) and (4.3) imply

$$\begin{aligned} S_t &= -\delta + \cosh(2R)\left[\alpha_3\cos(2\Theta) + \mathrm{Re}(\alpha_1+\alpha_2)\mathrm{e}^{2S}\right] \\ R_t &= \sinh(2R)\left[-\alpha_3\cos(2\Theta) + \mathrm{Re}(\alpha_1-\alpha_2)\mathrm{e}^{2S}\right] \\ \Theta_t &= d + \cosh(2R)\left[-\alpha_3\sin(2\Theta) + \mathrm{Im}(\alpha_1+\alpha_2)\mathrm{e}^{2S}\right] \\ \Phi_t &= \sinh(2R)\left[\alpha_3\sin(2\Theta) + \mathrm{Im}(\alpha_1-\alpha_2)\mathrm{e}^{2S}\right] \end{aligned} \tag{4.4}$$

The stationary solution ($S_t = R_t = \Theta_t = \Phi_t = 0$), is given by $(S_0, 0, \Theta_0, \Phi)$ where Φ is an arbitrary value; for a standing wave solution, S_0 and Θ_0 are related through

$$\begin{aligned} \cos(2\Theta_0) &= \frac{\delta - \mathrm{Re}(\alpha_1+\alpha_2)\mathrm{e}^{2S_0}}{\alpha_3} \\ \sin(2\Theta_0) &= \frac{d + \mathrm{Im}(\alpha_1+\alpha_2)\mathrm{e}^{2S_0}}{\alpha_3} \end{aligned} \tag{4.5}$$

The linear stability analysis around the standing wave solution yields

$$\begin{aligned} S_t &= \left[\Theta(-d - \mathrm{Im}(\alpha_1+\alpha_2)\mathrm{e}^{2S_0}) + S\mathrm{Re}(\alpha_1+\alpha_2)\mathrm{e}^{2S_0}\right] \\ R_t &= 2R\left[-\delta + 2\mathrm{Re}(\alpha_1)\mathrm{e}^{2S_0}\right] \\ \Theta_t &= \left[\Theta(-\delta + \mathrm{Re}(\alpha_1+\alpha_2)\mathrm{e}^{2S_0}) + S\mathrm{Im}(\alpha_1+\alpha_2)\mathrm{e}^{2S_0}\right] \\ \Phi_t &= 2R\left[d + 2\mathrm{Im}(\alpha_1)\mathrm{e}^{2S_0}\right] \end{aligned} \tag{4.6}$$

The system (4.6) is decoupled into two subsets of two equations involving S and Θ on the one hand, R and Φ on the other, since R_t and Φ_t depend only on R. Fauve et al. (1991) assumed that $\mathrm{Re}(\alpha_1+\alpha_2) < 0$, and that $|d| < \delta\,|\mathrm{Re}(\alpha_1)/\mathrm{Im}(\alpha_1)|$. Under these conditions, the perturbations in S and Φ then decrease and the destabilization would come from the other pair of variables. If S_0 is small enough, $S_0 < \log(\delta/2\mathrm{Re}(\alpha_1))/2$, then the perturbations R and Φ decay; otherwise, the solutions tend to a finite value of R and Φ_t. If R is nonzero, the $x \to -x$ symmetry breaks, and since Φ_t also becomes nonzero, the standing wave solution is replaced by drifting waves.

4.2.2 Linear analysis, surface waves and viscous waves

Modeling

We consider a two-dimensional domain (x, y) of infinite horizontal dimension x but bounded from below in its vertical dimension y by an impermeable wall. The domain is partially filled by a fluid layer. The upper

boundary of the fluid is the free surface whose position is denoted by $\zeta(x,t)$ and which moves according to the forces exerted on it. The fluid is incompressible, isothermal and viscous, characterized by its density ρ and its viscosity ν. The velocity field is $\mathbf{u} = (u, v)$. The forces exerted on the fluid are pressure, gravity and surface tension; there is at present no oscillation of the domain. The fluid satisfies the Navier-Stokes equations, no-slip boundary conditions at the bottom wall and continuity conditions at the free surface. These equations are nondimensionalized using the distance h of the flat interface to the bottom wall as the characteristic length and $\sqrt{h/g}$, with g the gravitational acceleration, as the characteristic time. The equations in the bulk are

$$\begin{aligned} u_t + uu_x + vu_y &= -p_x + C\left(u_{xx} + u_{yy}\right) \\ v_t + uv_x + vv_y &= -p_y + C\left(v_{xx} + v_{yy}\right) \\ u_x + v_y &= 0 \end{aligned} \tag{4.7}$$

and the boundary conditions are

$$\begin{aligned} &u = v = 0 && \text{at } y = -1 \\ &\zeta_t + u\zeta_x = v && \text{at } y = \zeta(x,t) \\ &2C\frac{u_x\zeta_x^2 - \zeta_x\left(u_y + v_x\right) + v_y}{1+\zeta_x^2} = p - \zeta + T\frac{\partial}{\partial x}\left(\frac{\zeta_x}{\sqrt{1+\zeta_x^2}}\right) && \text{at } y = \zeta(x,t) \\ &\left(u_y + v_x\right)\left(1-\zeta_x^2\right) + 2\zeta_x\left(v_y - u_x\right) = 0 && \text{at } y = \zeta(x,t) \end{aligned} \tag{4.8}$$

The nondimensional constant $C = \nu/\sqrt{gh^3}$ in (4.7) can be seen as an inverse Reynolds number whereas $T = \sigma/(\rho g h^2)$ in (4.8) is the ratio between surface tension, measured by σ, and gravity, and is the inverse of the Bond number.

Linearization of the equations and boundary conditions

The Navier-Stokes equations linearized around the trivial solution of a quiescent flow under a flat interface $(u, v, p, \zeta) = (0, 0, 0, 0)$, have as their general solution $(u, v, p, \zeta) = \left(\hat{u}(k,y), \hat{v}(k,y), \hat{p}(k,y), \hat{\zeta}(k,y)\right) \mathrm{e}^{\mathrm{i}kx+\gamma t}$. The wavenumber, k, is assumed real and such that $k \simeq O(1)$. The growth rate, γ, can be complex, in which case an oscillation is added to the growth or decay.

$$\begin{aligned} \gamma\hat{u} &= -\mathrm{i}k\hat{p} + C\left(\hat{u}_{yy} - k^2\hat{u}\right) \\ \gamma\hat{v} &= -\hat{p}_y + C\left(\hat{v}_{yy} - k^2\hat{v}\right) \\ \hat{u}_x + \hat{v}_y &= 0 \end{aligned} \tag{4.9}$$

The linearized boundary conditions are

$$\begin{aligned} &\hat{u} = \hat{v} = 0 && \text{at } y = -1 \\ &\gamma\hat{\zeta} = \hat{v} && \text{at } y = 0 \\ &2C\hat{v}_y = \hat{p} - \left(1 + Tk^2\right)\hat{\zeta} && \text{at } y = 0 \\ &\hat{u}_y + \mathrm{i}k\hat{v} = 0 && \text{at } y = 0 \end{aligned} \tag{4.10}$$

Solution of the linearized system

The solution of the system (4.9) has the general form

$$\begin{aligned} \hat{u} &= \mathrm{i}a\sinh(ky) + \mathrm{i}b\cosh(ky) + \mathrm{i}\frac{\kappa}{k}c\sinh(\kappa y) + \mathrm{i}\frac{\kappa}{k}d\cosh(\kappa y) \\ \hat{v} &= a\cosh(ky) + b\sinh(ky) + c\cosh(\kappa y) + d\sinh(\kappa y) \\ \hat{p} &= -\frac{1}{k}\left[s\left[a\sinh(ky) + b\cosh(ky)\right] + \left(Ck^2 - C\kappa^2 + s\right)\frac{\kappa}{k}\left[c\sinh(\kappa y) + d\cosh(\kappa y)\right]\right] \\ \hat{\zeta} &= \frac{a+c}{\gamma} \end{aligned} \tag{4.11}$$

where a, b, c, d are coefficients to be determined by (4.10) and

$$\kappa^2 = k^2 + \gamma/C \tag{4.12}$$

The boundary conditions express κ as a function of k through the dispersion relation.

$$\begin{aligned} k\left(1+Tk^2\right)\left[\kappa\cosh(\kappa)\sinh(k) - k\cosh(k)\sinh(\kappa)\right] = C^2\left[\left(k^4+6k^2\kappa^2+\kappa^4\right)k\sinh(k)\sinh(\kappa)\right. \\ \left.-5\left(k^4+2k^2\kappa^2+\kappa^4\right)\kappa\cosh(k)\cosh(\kappa) + 4k^2\kappa\left(k^2+\kappa^2\right)\right] \end{aligned} \tag{4.13}$$

We now focus on the moderate wavelength case, where k is of the order of unity (the wavelength and the depth of the fluid layer are of the same order of magnitude). The dispersion relation (4.13) admits two kinds of solutions, whose nature depends on the magnitude of κ.

The surface modes

Let us focus on the surface modes, which are characterized by $\kappa_s \simeq C^{-\frac{1}{2}}$. Equations (4.11)-(4.13) and κ are then expanded in powers of $C^{\frac{1}{2}}$:

$$\kappa_s = \kappa_0 C^{-\frac{1}{2}} + \kappa_1 + \kappa_2 C^{\frac{1}{2}} + \dots \tag{4.14}$$

with all coefficients κ_i of order one. In the same way, (4.13) is expanded in powers of $C^{\frac{1}{2}}$ and only the three lowest orders of the expansion are conserved. Since $\kappa_s \gg 1$, $\cosh(\kappa_s) \simeq \sinh(\kappa_s) \simeq \mathrm{e}^{\kappa_s}/2 \gg \kappa_s$. The terms that do not contain hyperbolic functions of q are then negligible in comparison with the other ones. The powers of $C^{\frac{1}{2}}$ are then separated from one other:

$$\begin{aligned} &\kappa_0 k\left(1+Tk^2\right)\sinh(k) = -\kappa_0^5\cosh(k) \\ &\kappa_1\left[5\kappa_0^4\cosh(k) + k\left(1+Tk^2\right)\sinh(k)\right] = k\kappa_0^4\sinh(k) - k^2(1+Tk^2)\cosh(k) \\ &\kappa_2\left[5\kappa_0^4\cosh(k) + k\left(1+Tk^2\right)\sinh(k)\right] = 4k\kappa_0^3\kappa_1\sinh(k) - \left[2k^2\kappa_0^3 + 10\kappa_0^3\kappa_1^2\right]\cosh(k) \end{aligned} \tag{4.15}$$

whose solutions are

$$\begin{aligned} \kappa_0 &= \pm\frac{1\pm\mathrm{i}}{\sqrt{2}}\sqrt[4]{k\left(1+Tk^2\right)\tanh(k)} \\ \kappa_1 &= -\frac{k}{2\sinh(2k)} \\ \kappa_2 &= \left(\pm\frac{1\pm\mathrm{i}}{\sqrt{2}}\right)^3 \frac{k^2\sqrt[4]{\tanh^3(k)}}{32\sqrt[4]{k\left(1+Tk^2\right)}^3\sinh^3(k)\cosh(k)}\left(8\sinh^2(k) + 16\sinh^2(k)\cosh^2(k) + 5\right) \end{aligned} \tag{4.16}$$

The associated growth rate is deduced from (4.12) and also expanded in the three leading powers of $C^{\frac{1}{2}}$.

$$\gamma_s = \gamma_0 + \gamma_1 C^{\frac{1}{2}} + \gamma_2 C \tag{4.17}$$

where

$$\gamma_0 = \pm\mathrm{i}\sqrt{k\left(1+Tk^2\right)\tanh(k)} \tag{4.18a}$$

$$\gamma_1 = \mp\frac{1\pm\mathrm{i}}{\sqrt{2}}\cdot\frac{k\sqrt[4]{k\left(1+Tk^2\right)\tanh(k)}}{\sinh(2k)} \tag{4.18b}$$

$$\gamma_2 = -k^2\left(2 + \frac{\tanh^2(k)+2}{4\sinh^2(k)}\right) \tag{4.18c}$$

The effective growth rate of the surface modes corresponds to the real part of γ_s while the imaginary part of γ_s represents an oscillating contribution. Equations (4.17) and (4.18a) show that when the fluid is inviscid, namely $C = 0$, the temporal coefficient $\gamma_s = \gamma_0$ becomes a pure imaginary number that represents the eigenfrequency of a capillary-gravity wave in an inviscid fluid. The coefficient γ_0 is the same as the frequency calculated in the first stability analysis performed on Faraday waves (Benjamin and Ursell, 1954).

As a result, the surface modes in inviscid fluids are purely oscillating and persist in time in the absence of any forcing. When the fluid is weakly viscous, the term of order $C^{\frac{1}{2}}$ has a negative real part that weakly damps these surface modes. The imaginary part of this term consists of a departure of the waves from their inviscid frequency γ_0, called detuning.

The same expression for the surface modes was computed in several previous works. Among other things, we mention the studies conducted by Wehausen and Laitone (1960) and Kakutani and Matsuuchi (1975). Wehausen and Laitone (1960) studied the case of surface waves in infinite and finite media. Using a decomposition of the linearized velocity into a potential and a vortical field, they obtained a dispersion relation in both cases. For finite depth, they expanded the dispersion relation to second order in $\sqrt{\nu}$, assuming the viscosity ν small. The resulting temporal frequency was also expanded to order ν^1. Kakutani and Matsuuchi (1975) derived an exact dispersion relation from the Navier-Stokes equations but for gravity waves, they afterwards expanded the solution of their dispersion relation up to the same order in the viscosity, considered small, and found the same solution up to order $\nu^{\frac{1}{2}}$. For this, they made the additional assumptions that $k \simeq k \simeq O(1)$ and $\kappa \gg 1$, the same as in Martel and Knobloch (1997). The great novelty in the work of Martel and Knobloch (1997) is that they calculated another kind of solution which had not been previously reported and is, according to Martín et al. (2002), of considerable importance for the occurrence of the drift instability.

The viscous modes

The other kind of solution, called the viscous modes, are such that $\kappa_v \simeq k \simeq O(1)$. These modes cannot exist when $C = 0$, in contrast with the surface modes, thus their name. Here, the right hand side of (4.13) is negligible due to the factor C^2, hence κ is a solution of

$$\kappa_v \tanh(k) = k \tanh(\kappa_v) \tag{4.19}$$

Except for the trivial solution $\kappa_v = \pm k$, κ_v is not analytically expressible as a function of k. Nevertheless, some general features of $\kappa_v(k)$ can be extracted from the relation (4.19).

- κ_v is imaginary, $\kappa_v(k) = \mathrm{i}\xi_n(k)$ where n distinguishes the various accessible solutions and every $\xi_n(k)$ therefore satisfies
$$\frac{\xi_n}{\tan(\xi_n)} = \frac{k}{\tanh(k)} \tag{4.20}$$

- $\lim\limits_{k\to 0} \dfrac{k}{\tanh k} = 1$ thus
$$\lim_{k\to 0} \xi_n(k) = \xi_n(0) \quad \text{with } \xi_n(0) = \tan \xi_n(0) \tag{4.21}$$

- $\lim\limits_{k\to \infty} \dfrac{k}{\tanh k} = 0$ thus
$$\lim_{k\to \infty} \xi_n(k) = 0 + n\pi, \quad n \in \mathbb{N} \tag{4.22}$$

The associated growth rate (cf (4.12)) becomes, at leading order in $C^{\frac{1}{2}}$,

$$\gamma_v = -C(k^2 + \xi_n^2) \tag{4.23}$$

Since γ_v is negative and real, the viscous modes do not oscillate, but only decay. In addition, the viscous modes should decrease much more slowly than the surface modes whose growth rate satisfies $\Re(\gamma_s) \simeq O(C^{\frac{1}{2}})$, so they must generally be considered in the dynamics of fluid layers with interface. Finally, a study based on the orders of magnitude of (u, v, p, ζ) shows that $\zeta_v \simeq O(C)$ in comparison with the other fields; the viscous modes thus generate a surface elevation which is negligible. The boundary conditions show that the relative amplitudes of the coefficients of (4.11) satisfy $a \simeq c \simeq C^2 d \simeq C^2 b$ and it is deduced that $\zeta \simeq Cv \simeq Cu \simeq Cp$.

4.2.3 Weakly nonlinear analysis

Modeling of the problem

We now consider the effect of vertical oscillation on surface waves at the free surface of a single fluid. Martín et al. (2002) took as a basis for their weakly nonlinear study the linear analysis of Martel and Knobloch (1997), where both surface and viscous modes are considered. The formalism they adopted differs slightly from that in Martel and Knobloch (1997), and consists of the following equations

$$\begin{aligned} &u_t + v(u_y - v_x) = -p'_x + C\left(u_{xx} + u_{yy}\right) \\ &v_t + u(u_y - v_x) = -p'_y + C\left(v_{xx} + v_{yy}\right) \\ &u_x + v_y = 0 \end{aligned} \tag{4.24}$$

where p' is a modified pressure term supplemented by the gravity and the inertial force due to the vibration of the container,

$$p' = p + \frac{u^2 + v^2}{2} + y - 4\omega^2 \epsilon y \cos(2\omega t) \tag{4.25}$$

and 2ω and ϵ are the frequency of the forcing and its amplitude, respectively. The boundary conditions also change because of the addition of the vibration and the formalism that involves p' instead of p:

$$\begin{aligned} &u = v = 0 && \text{at } y = -1 \\ &\zeta_t + u\zeta_x = v && \text{at } y = \zeta(x,t) \\ &2C\frac{u_x\zeta_x^2 - \zeta_x\left(u_y + v_x\right) + v_y}{1 + \zeta_x^2} = p' - \frac{u^2 + v^2}{2} - \zeta + 4\omega^2\epsilon\zeta\cos(2\omega t) + T\frac{\zeta_{xx}}{\sqrt{1 + \zeta_x^2}^3} && \text{at } y = \zeta(x,t) \\ &\left(u_y + v_x\right)\left(1 - \zeta_x^2\right) + 2\zeta_x\left(v_y - u_x\right) = 0 && \text{at } y = \zeta(x,t) \end{aligned} \tag{4.26}$$

with periodic boundary conditions at their vertical walls. Further restrictions concerning the periodic forcing are:

$$\epsilon \ll 1 \qquad\qquad |\omega - \gamma_0| \ll 1 \tag{4.27}$$

where we recall that γ_0 is the natural frequency of the inviscid waves and is given by (4.18a). The second condition of (4.27) means, among other things, that the interfacial waves are close to resonant with the forcing. In the following paragraphs, the symbol $'$ will be omitted.

Amplitude equations for the fast oscillating terms

Due to the weakness of the forcing ϵ, Martín et al. (2002) expanded the variables and the equations of the problem into powers of $\mu \ll 1$, where the quantities ϵ and C are of order of magnitude μ^2.

$$\begin{aligned} u(x,y,t) &= \sum_{n=0}^{\infty} \mu^n u_n(x,y,t), \\ v(x,y,t) &= \sum_{n=0}^{\infty} \mu^n v_n(x,y,t)... \end{aligned} \tag{4.28}$$

The solution at order μ^0 is the trivial state: the motionless fluid under a plane interface. The solutions of the equations at order μ^1 are the surface modes of Martel and Knobloch (1997) (see (4.29) and (4.30)). At higher order, the solutions are combinations of the viscous modes and of other components that arise from the interaction of the surface modes with themselves. Here Martín et al. (2002) have assumed that the viscous modes are much weaker than the surface modes.

$$\begin{cases} u(x,y,t) = \mu U_0(y)\mathrm{e}^{\mathrm{i}\omega_0 t}\left[A(t)\mathrm{e}^{\mathrm{i}kx} - B(t)\mathrm{e}^{-\mathrm{i}kx}\right] + \text{ c.c. } + \mu^2 u_2(x,y,t) + \mu^3 u_3(x,y,t) \\ v(x,y,t) = \mu V_0(y)\mathrm{e}^{\mathrm{i}\omega_0 t}\left[A(t)\mathrm{e}^{\mathrm{i}kx} + B(t)\mathrm{e}^{-\mathrm{i}kx}\right] + \text{ c.c. } + \mu^2 v_2(x,y,t) + \mu^3 v_3(x,y,t) \\ p(x,y,t) = \mu P_0(y)\mathrm{e}^{\mathrm{i}\omega_0 t}\left[A(t)\mathrm{e}^{\mathrm{i}kx} + B(t)\mathrm{e}^{-\mathrm{i}kx}\right] + \text{ c.c. } + \mu^2 p_2(x,y,t) + \mu^3 p_3(x,y,t) \\ \zeta(x,t) = \mu\mathrm{e}^{\mathrm{i}\omega_0 t}\left[A(t)\mathrm{e}^{\mathrm{i}kx} + B(t)\mathrm{e}^{-\mathrm{i}kx}\right] + \text{ c.c. } + \mu^2\zeta_2(x,y,t) + \mu^3\zeta_3(x,y,t) \end{cases} \tag{4.29}$$

$$P_0 = \omega_0^2 \frac{\cosh[k(y+1)]}{k\sinh(k)}, \qquad U_0 = -\frac{kP_0}{\omega_0}, \qquad V_0 = \frac{iP_{0y}}{\omega_0} \tag{4.30}$$

The slowly varying amplitudes A and B remain to be determined. Their equations at order μ^2 are

$$u_{2x} + v_{2y} = 0 \tag{4.31a}$$

$$u_{2t} + p_{2x} = -v_1(u_{1y} - v_{1x}) \tag{4.31b}$$

$$v_{2t} + p_{2y} = u_1(u_{1y} - v_{1x}) \tag{4.31c}$$

while the boundary conditions become

$$\begin{aligned} &v_2 = 0 && \text{at } y = -1 \\ &v_2 - f_{2t} = v_{1y}f_1 + u_1 f_{1x} && \text{at } y = 0 \\ &p_2 - f_2 + Tf_{2xx} = \frac{u_1^2 + v_1^2}{2} - p_{1y}f_1 && \text{at } y = 0 \end{aligned} \tag{4.32}$$

The height of the interface has been taken constant. The same process was followed for the establishment of the boundary conditions at order μ^1 (4.10) from (4.8). This allows the y-dependent functions to be expanded near $y = 0$ in powers of ζ, for example $u(x,\zeta,t) = u(x,0,t) + \zeta u_y(x,0,t) + \frac{\zeta^2}{2}u_{yy}(x,0,t) + ...$ The terms of (4.32) that have no equivalent in (4.8) arise in this way. The homogeneous problem is first solved, leading to a set of solutions that have the same form as the viscous modes. Afterwards, a particular solution of the inhomogeneous equations (4.31) and (4.32) is sought. Resonant terms of the right-hand-side, i.e. those which oscillate with the frequency $\pm\omega_0$, must vanish in order to eliminate nonperiodic solutions. (They are in fact absent from the equations (4.31) and (4.32)). The nonresonant terms compel the solution to have the form

$$(u_2, v_2, p_2, \zeta_2) = \sum_{l,m=(-2,0,2)} (U_{lm}, V_{lm}, P_{lm}, Z_{lm})\mathrm{e}^{\mathrm{i}lkx}\mathrm{e}^{\mathrm{i}m\omega_0 t} + c.c. \tag{4.33}$$

where we can differentiate two kinds of contributions: those which vibrate with the frequency $\pm 2\omega_0$ and the constant ones which are related to the streaming. The variables U_{20} and V_{20} cannot be determined because the equations of motion do not involve them at order μ^2. The expansion is carried out to order μ^3.

This leads to the amplitude equations that govern the evolution of the slowly varying coefficients A and B.

$$\begin{aligned} A_t &= \left[-\gamma_s + \mathrm{i}\alpha_1|A|^2 - \mathrm{i}\alpha_2|B|^2 - \mathrm{i}\alpha_4 L^{-1}\textstyle\int_{-1}^{0}\int_0^L g(y)u^s \mathrm{d}x\mathrm{d}y\right] A + \mathrm{i}\epsilon\alpha_3\bar{B} \\ B_t &= \left[-\gamma_s + \mathrm{i}\alpha_1|B|^2 - \mathrm{i}\alpha_2|A|^2 - \mathrm{i}\alpha_4 L^{-1}\textstyle\int_{-1}^{0}\int_0^L g(y)u^s \mathrm{d}x\mathrm{d}y\right] B + \mathrm{i}\epsilon\alpha_3\bar{A} \end{aligned} \tag{4.34}$$

where γ_s comes from the relations (4.17) and (4.18). The other coefficients are provided below,

$$\begin{aligned} \alpha_1 &= 2\omega_0 k^2 + \frac{\omega_0 k^2}{4\sigma^2}\frac{(9-\sigma^2)(1-\sigma^2) + (7-\sigma^2)(3-\sigma^2)Tk^2}{\sigma^2 + (\sigma^2-3)Tk^2} - \frac{3T\omega_0 k}{4(1+Tk^2} \\ \alpha_2 &= \frac{\omega_0 k^2}{2}\left[\frac{(\sigma^2+1)^2}{\sigma^2}\frac{1+Tk^2}{1+4Tk^2} + \frac{4+7Tk^2}{1+Tk^2}\right] \\ \alpha_3 = \omega_0 k\sigma \qquad \alpha_4 &= \frac{k\sigma}{2\omega_0} \qquad g(y) = \frac{2\omega_0 k\cosh[2k(y+1)]}{\sinh^2 k} \qquad \sigma = \tanh k \end{aligned} \tag{4.35}$$

Note from (4.30) that the streaming terms in u^s are of the same order as the cubic coefficients, according to the approximations performed. Neglecting them is consequently illegitimate. The set of amplitude equations (4.34) are different from those given by Fauve et al. (1991) (4.2) in two respects: the presence of the integral term in (4.34) that accounts for the coupling with a streaming flow and the fact that the coefficients associated with the nonlinear interactions α_1 and α_2 are real numbers. Hence, the nonlinear interactions will only produce a nonlinear detuning. The equations for the streaming flow are deduced from the same perturbation analysis but taken to a higher order of perturbation.

4.2.4 Coupled spatial phase-streaming flow equations

Martín et al. (2002) decoupled the amplitude equations (4.30) using the substitution $A = A_0 e^{-ik\psi}$, $B = B_0 e^{ik\psi}$ where ψ is the phase of the waves. The evolution equations for ψ, A and B become

$$\psi_t = \left[\frac{\alpha_4}{kL}\right] \int_{-1}^{0} \int_{0}^{L} g(y) u^s(x, y, t)\, dx\, dy \tag{4.36a}$$

$$A_0' = \left[-\delta - iD + i\alpha_1 |A_0|^2 - i\alpha_2 |B_0|^2\right] A_0 + i\epsilon\alpha_3 \overline{B}_0 \tag{4.36b}$$

$$B_0' = \left[-\delta - iD + i\alpha_1 |B_0|^2 - i\alpha_2 |A_0|^2\right] B_0 + i\epsilon\alpha_3 \overline{A}_0 \tag{4.36c}$$

where γ_s (4.34) has been decomposed into its real part δ, the linear damping, and its imaginary part D, the linear detuning (4.17) and (4.18). L is the length of the periodic domain and is a multiple of the wavelength $2\pi/k$. The state $A_0 = B_0 = 0$ becomes unstable through the set of equations (4.36) if the forcing ϵ is greater than $\epsilon_c = \sqrt{\delta^2 + D^2}/\alpha_3$, which is the threshold for the Faraday instability. In the set of equations (4.36), the evolution of A and B is not coupled to ψ and stationary values of A_0 and B_0 are deduced from (4.36b) and (4.36c) with $A_0' = B_0' = 0$. Indeed, it is found that for $\epsilon > \epsilon_c$, if $\alpha_1 - \alpha_2 \neq 0$, the fixed points have the form:

$$A_0 = B_0 = R_0 e^{i\phi_0} \tag{4.37}$$

with R_0 the amplitude of Faraday waves, given by

$$R_0 = \frac{D \pm \sqrt{\alpha_3^2 \epsilon^2 - \delta^2}}{\alpha_1 - \alpha_2} \tag{4.38}$$

The theoretical occurrence of a drift results from (4.36c) which states that the interfacial pattern will move only if the streaming flow denoted by u^s is not zero nor orthogonal to $g(y)$ where u^s is computed after transient variation from the Coupled Spatial Phase-Streaming Flow (CSPSF) equations, which are:

$$\tilde{u}_x + \tilde{v}_y = 0 \tag{4.39a}$$

$$\frac{d\tilde{u}}{d\tau} + \tilde{v}(\tilde{u}_y - \tilde{v}_x) = -\tilde{q}_x + \frac{1}{Re}(\tilde{u}_{xx} + \tilde{u}_{yy}) \tag{4.39b}$$

$$\frac{d\tilde{v}}{d\tau} - \tilde{u}(\tilde{u}_y - \tilde{v}_x) = -\tilde{q}_y + \frac{1}{Re}(\tilde{v}_{xx} + \tilde{v}_{yy}) \tag{4.39c}$$

$$\tilde{u}(x, -1, \tau) = -\sin[2k(x - \psi)], \qquad \tilde{v}(x, -1, \tau) = 0 \tag{4.39d}$$

$$\frac{d\tilde{u}(x, 0, \tau)}{dy} = \tilde{v}(x, 0, \tau) = 0 \tag{4.39e}$$

$$\tilde{u}(x + 2m\pi/k, y, \tau) = \tilde{u}(x, y, \tau), \qquad \tilde{v}(x + 2m\pi/k, y, \tau) = \tilde{v}(x, y, \tau), \qquad \tilde{q}(x + 2m\pi/k, y, \tau) = \tilde{q}(x, y, \tau) \tag{4.39f}$$

$$\frac{d\psi}{d\tau} = \frac{1}{L} \int_{-1}^{0} \int_{0}^{L} G(y) \tilde{u}(x, y, \tau) dx dy \tag{4.39g}$$

where the variables are rescaled as

$$\tau = ReCt, \quad \tilde{u} = \frac{u^s}{ReC}, \quad \tilde{v} = \frac{v^s}{ReC}, \quad \tilde{q} = \frac{q^s}{ReC^2}, \quad m \geq 1 \tag{4.40}$$

with

$$G(y) = 2k \frac{\cosh[2k(y + 1)]}{\sinh 2k}, \quad Re = \frac{6R_0^2 \omega_0 k}{C \sinh^2 k} \tag{4.41}$$

The system (4.39) is solved numerically. Particularly, the stability of the various solution is sought and a bifurcation diagram is constructed. Equation (4.37) implies that, at this order of perturbation, the drift is not associated with an asymmetry between the two counter-propagating modes whose amplitudes are A and B. A difference between A and B may occur at higher order. Hence, a nonzero R associated with a drifting flow does not invalidate the theory of Martín et al. (2002). The theory of Martín et al. (2002) can indeed

be differentiated from the analysis of Fauve et al. (1991) by comparing the order of magnitude of R from (4.3) with that of the distance to the threshold. Second, $\tilde{u}$ depends a priori on time, hence the drift velocity ψ_t may not be constant in time; Martín et al. (2002) showed that with such a coupling, the standing wave solution bifurcates to a drifting flow through a Hopf bifurcation, leading to a horizontally oscillating flow instead of a purely translating motion. This is the other noticeable difference with the analysis of Fauve et al. (1991).

4.3 Physical conditions

We attempt to keep the physical conditions close to those in Martín et al. (2002) and to be in the range of validity of their analysis

$$hk = 2.37, \tag{4.42a}$$

$$C \lesssim 10^{-4}, \tag{4.42b}$$

$$|\omega - \omega_0| \ll 1 \tag{4.42c}$$

Equation (4.42a) is the classic condition delimiting shallow water waves, for which $\tanh(hk) > 0.99$ and so can be approximated as 1. We impose the value of k to be 135 m^{-1}, thus $h_1 = 17.56$ mm. The lower fluid has the density and viscosity of water, namely, $\rho_1 = 1032\,\mathrm{kg\,m^{-3}}$ and $\nu_1 = 9.9205 \times 10^{-7}\,\mathrm{m^2\,s^{-1}}$; hence $C = 1.361 \times 10^{-4}$ fulfills the requirement stated in (4.42b). Martín et al. (2002) consider only the dynamics of one fluid. However, our numerical method requires the presence of two layers of fluid: the boundaries of the domain of calculation must be motionless and ρ and μ must be positive. We endow the upper fluid with the physical characteristics of air: $\rho_2 = 1.205 \times 10^{-3}\,\mathrm{kg\,m^{-3}}$ and $\nu_2 = 1.511 \times 10^{-5}\,\mathrm{m^2\,s^{-1}}$. We require that the air layer be thick enough (ideally infinite) so that the viscous forces within the air bulk are minimal and their impact on the dynamics of the lower layer is weak. The minimum thickness that provides results close to those supplied by the Faraday problem with an infinite layer is first determined approximately with measurements of linear thresholds and growth rates. Afterwards, tests on nonlinear properties of the flow are conducted to confirm or to refine the former assessments, more specifically the saturation amplitude of the interface height and the criticality of the bifurcation to Faraday waves, leading to a height of $h_2 = 5$cm. The excitation frequency must satisfy two conditions: the bifurcation must be supercritical and the detuning must be weak, as specified by (4.42c). The frequency of oscillation of the vessel has been set to 11.6 Hz. We have set the surface tension to zero in order to simplify and speed up the numerical calculation. This choice of pure gravity waves is within the scope of the treatment of Martín et al. (2002). Once the physical conditions are set, additional criteria that stem from numerical considerations come into play:

- the resolution along the horizontal directions has been fixed at 100 points per spatial period in order to capture accurately the lower multiples of k that may play an important role in the dynamics of Faraday waves if the acceleration becomes much larger than the primary threshold.
- The resolution along the vertical direction was calculated so that the viscous time step

$$\Delta t_{visc} = \frac{1}{4}\min\left(\frac{1}{\nu_1}, \frac{1}{\nu_2}\right)\min(\Delta x, \Delta y)^2 \tag{4.43}$$

  would be of the same order of magnitude as (ideally greater than) $T/100$, where T is the oscillation period of the container. Equation (4.43) highlights that the viscous time step is only a function of ν_2, the viscosity of the upper fluid, since the kinematic viscosity of air is higher than that of water.

4.4 Results

4.4.1 Primary threshold and first linear results

The critical acceleration a_c (or primary threshold) is first sought. The initial condition for the computation is

$$(u, v, p, \zeta)\,|_{t=0} = (0, 0, 0, \epsilon \sin(kx)) \tag{4.44}$$

Above the threshold, ϵ must be small; otherwise the nonlinear contributions would alter the growth rate. In contrast, below a_c, a higher ϵ would be more appropriate since if the eigenvalue is complex with a small imaginary part, the resulting long-time oscillations might not be captured before the amplitude decays to computer precision limits. The method for seeking the threshold is based on the fact that, near the threshold a_c, the growth rate γ_r, should increase linearly with a . Two accelerations close to a_c are then sufficient to determine the threshold by linear interpolation. Due to the ω-periodic forcing, the eigenvectors are time-periodic functions of the fundamental frequency $\omega/2$. The calculation of the growth rate at a fixed a requires two flow states separated by any time interval $2nT = 4n\pi/\omega$ where $n \in \mathbb{N}$:

$$\gamma_r = \frac{1}{2nT} \ln \left[\frac{q(t+2nT)}{q(t)} \right] \tag{4.45}$$

However, the behavior of the growth rate γ_r as a function of a turns out to be far from linear as shown in Figure 4.1a. Figure 4.1b displays an enlargement of the dependence of γ on a near the threshold. Both the

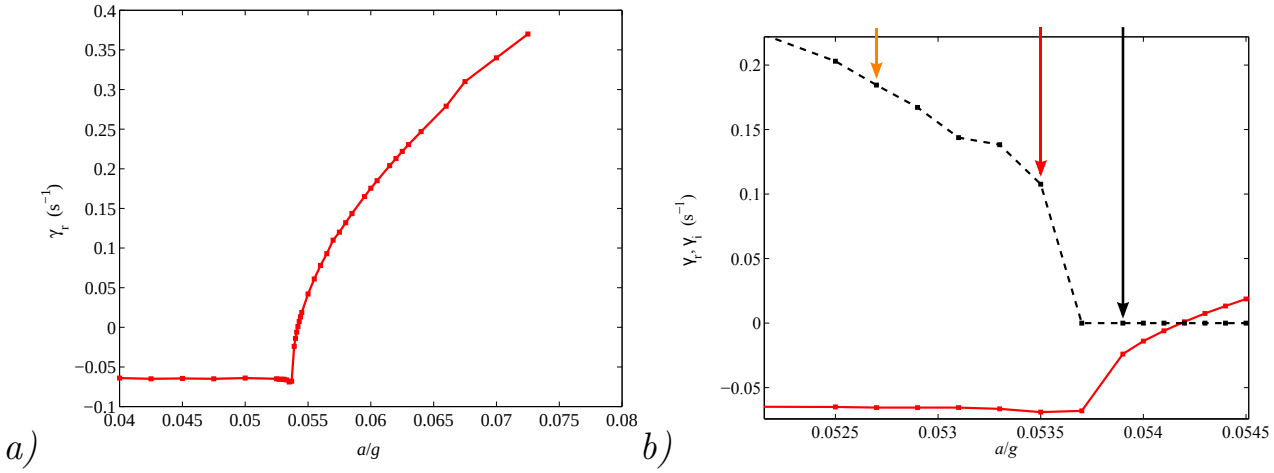

Figure 4.1: a) Growth rate or real part of the most unstable eigenvalue as a function of a/g. b) Enlargement of the evolution of the most unstable eigenvalue near the threshold. Solid lines: γ_r, dashed lines: γ_i. Arrows correspond to temporal evolution curves shown in figure 4.2.

real and imaginary parts are represented. It is observed on Figure 4.1b that γ_r reaches a plateau at the lowest a. This plateau is correlated with the transition from real γ to complex γ. The fact that γ becomes complex adds an oscillatory contribution to the decay. The method for the determination of γ_r must then be supplemented by a further step that requires the calculation of γ_i, π times the time interval between two maxima of the envelope of $q(t)$. Then (4.45) is reused, replacing $2nT$ by $2\pi/\gamma_i$ and $q(t)$ by its envelope.

The growth rate, γ, acquires real values at $a = 0.0536g \pm 0.0001g$ while the threshold is determined by linear interpolation to be $a_c = 0.054186g$. The linear analysis of the same problem (Kumar and Tuckerman, 1994) yields threshold $a_{c_{th}} = 0.051$, a variation of around 6% between the theory and our simulation. One possible cause of this deviation is the large discontinuity in density and viscosity at the interface. An increase in the resolution could provide better results, but the calculation time would then be prohibitive. We also give the approximate value of γ_r when it becomes constant: when $a < 0.0536g$, $\gamma_r \simeq -0.065\,\mathrm{s}^{-1}$. As a decreases below $0.0536\,g$, $|\gamma_i|$ increases and so the envelope oscillations become faster.

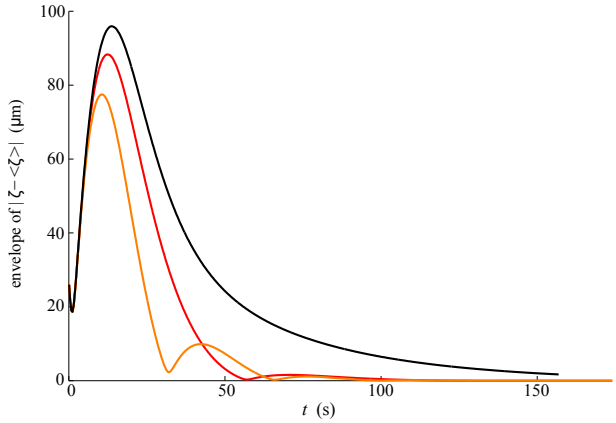

Figure 4.2: Envelope of the height of one point at the interface as a function of time for the values of a indicated in figure 4.1b. Black: $a = 0.0539g$, red: $a = 0.0535g$, orange: $a = 0.0527g$. The first hump is due to transient growth. Afterwards, the least stable eigenvector dominates and the decrease of the solution is exponential, and oscillatory for values of $a/g < 0.0536$. In that case, the growth rate must be calculated starting from the second hump to avoid the parasitic effects caused by the additional eigenvectors that may not yet be negligible at the first crest.

4.4.2 Bifurcation diagrams

Criticality of the bifurcation

The weakly nonlinear theory is applies to waves of infinitesimal amplitude. If the flat flow destabilizes to Faraday waves through a subcritical bifurcation, the standing-wave solutions form a stable branch of finite amplitude and the drifting solutions which arise from the standing-wave branch through a secondary bifurcation cannot be computed. Hence, to compare our simulations with the calculations of Martín et al. (2002), it is important to check that the primary transition is clearly supercritical. The bifurcation is supercritical when $k > k_c$, where k_c is the critical wave number and subcritical otherwise. We have chosen $k > k_c$ and should therefore bifurcate to Faraday waves supercritically. To check that numerics and theory agree, we use the method of Henderson and Barkley (1996) which is valid slightly above the threshold: in the linear regime, the growth rate of a perturbation is a positive (possibly complex with a positive real part) constant. If the growth rate falls monotonically to zero at saturation, then the bifurcation is supercritical. In contrast, if the growth rate increases and then falls, the corresponding bifurcation is subcritical. The benefit of this method is that, once the threshold is known, only one measurement is necessary to determine the nature of the bifurcation. We focus on the growth rate represented in Figure 4.3b. The peak at the beginning is due to transient growth of the perturbation as eigenvectors combine to dramatically increase the growth. After the first stabilization at a finite value, the growth rate decays to zero. This monotonic decrease signifies that the bifurcation is supercritical. The resolution in time and the small value of the growth rate explain its high relative fluctuations.

Ways of characterizing the various branches

Once the threshold is determined, calculations are conducted for $a \geq a_c$, again with the initial condition given in (4.44). The solution will naturally evolve towards the stable branch. If several stable branches compete, the final state will depend on which basin of attraction contained the initial condition; these basins of attraction are generally complex intricate manifolds which deform when the parameters are changed, especially a. Except when initial conditions are very close to one branch, it is impossible to determine a priori to which branch an initial flow will tend. The imposed initial condition is far away from any stable branch; hence the solutions to which the initial state (4.44) evolves can be very variable and highly dependent on a. We provide an overview of the branches characterized by various symmetries in the series of examples shown in Figures 4.4 and 4.5. The preliminary calculations provide four distinct kinds of solutions

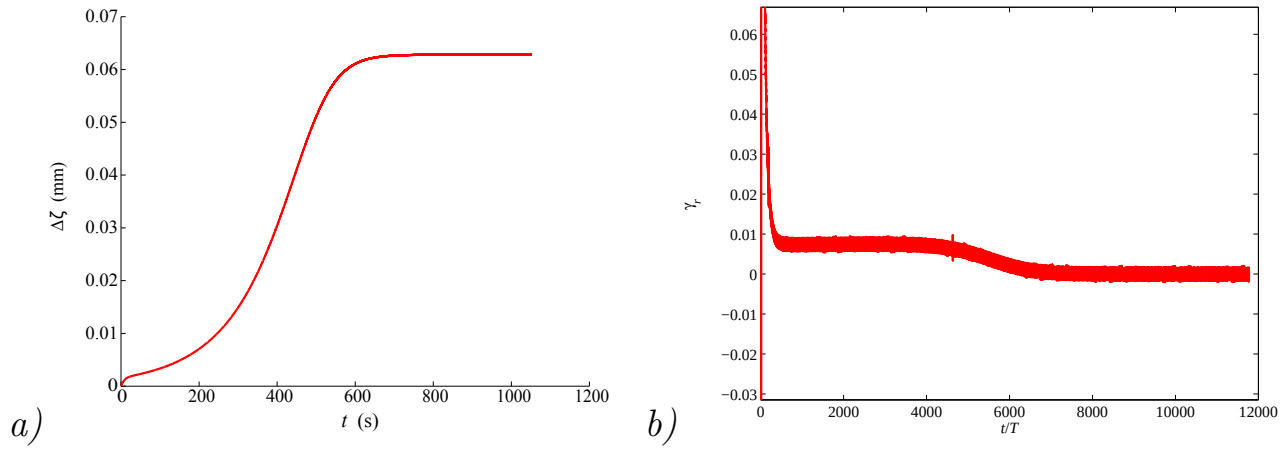

Figure 4.3: a) Growth of a small perturbation of the flat interface. Envelope of $\Delta\zeta$ as a function of time for $a = 0.0543g > a_c = 0.054186g$. b) Growth rate of $\Delta\zeta$, i.e. the time derivative of a).

at saturation starting from the state (4.44). The flow in Figure 4.4a exhibits both reflection symmetry and an approximate invariance under $\lambda/2$-translation of the mean flow. The slight imperfection in the translational invariance may be due to numerical or physical effects. The symmetries of the interface are fairly hard to define because its mean is very close to the flat interface. In Figure 4.4b, the reflection symmetry has been broken; as a consequence, streamlines have opened, pushing the fluids horizontally. On average the mean flow has $\lambda/2$-translational invariance. In Figure 4.5a, this symmetry vanishes in turn. This is not correlated in any way to the appearance of the flux. The patterns of Figures 4.4b and 4.5a exhibit a slow horizontal displacement in time. This feature constitutes the fundamental difference between the flows of Figures 4.5a and 4.5b, although it is not accessible from these graphs.

To characterize the flows with or without drift we are expecting to observe, we used several different variables. The first is the envelope of the difference $\Delta\zeta = \zeta_{\max} - \zeta_{\min}$ at saturation, which is the natural variable for describing the emergence of Faraday waves at the primary bifurcation. The second variable is used to differentiate between states with drift along the set of obtained flows. We have three alternatives. The first consists of measuring the time interval T_λ between successive maxima of the envelope of ζ_L, the height of the leftmost point of the interface. T_λ measures the time taken for the pattern to cover the distance between a crest and the next trough. These two points oscillate at the maximum amplitude and are separated from $\lambda/2$ and not λ. Then the drift velocity of the pattern at the interface must be expressed as

$$\omega_{pattern} = \frac{\pi}{T_\lambda} \tag{4.46}$$

In fact, $\omega_{pattern}$ does not a priori differentiate between solutions that vibrate horizontally from those that move at a constant speed because in both cases ζ_L has distinct extrema. Nevertheless, Figure 4.6 demonstrates that there can be differences between the horizontally oscillating patterns and the uniform drift. $\zeta_L(t)$ exhibits different behaviors between the vibration and the constant motion of the pattern if the length over which the pattern oscillates is less than $\lambda/4$. $\omega_{pattern} \neq 0$ if the pattern moves continuously. Other kinds of behaviors may be imaginable but these two are the most plausible.

Another way to quantify the drift is the calculation of the mean flux in the two fluid bulks over a time that is a multiple of a subharmonic period, $2T$. The flux in each layer is denoted by ϕ and is computed as

$$\begin{aligned}
\phi_{water} &= \frac{1}{8T\lambda}\int_0^\lambda \int_0^{<\zeta(x)>_t} \int_t^{t+8T} \mathbf{u}(x,y,t)\cdot\mathbf{e}_y \, dt\, dy\, dx \\
\phi_{air} &= \frac{1}{8T\lambda}\int_0^\lambda \int_{<\zeta(x)>_t}^{h} \int_t^{t+8T} \mathbf{u}(x,y,t)\cdot\mathbf{e}_y \, dt\, dy\, dx
\end{aligned} \tag{4.47}$$

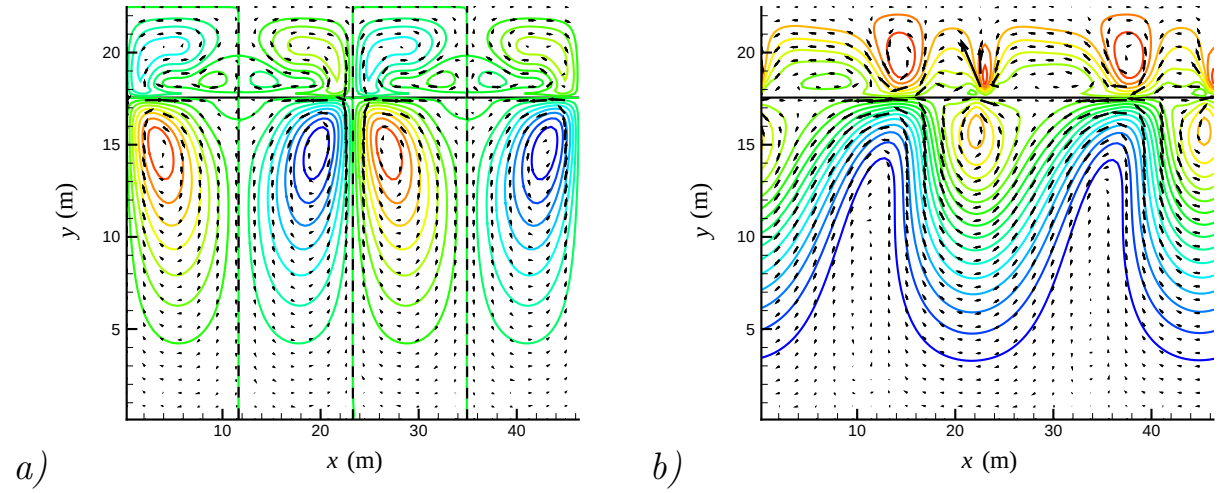

Figure 4.4: a) Mean flow over $4T$ (two subharmonic periods) of the streamfunction (colors) and the interface height ζ (solid line) for $a = 0.057g$. The solution is indicated by the black arrow in Figure 4.7. The dash-dotted lines represent the symmetry axes of the mean flow. This mean flow has both $\lambda/2$ translational symmetry and reflection symmetry. b) Mean flow over $4T$ for $a = 0.0543g$. The solution is indicated by the orange arrow in Figure 4.7. This mean flow has $\lambda/2$ translational symmetry, but no vertical axis of reflection symmetry. The streamlines extending horizontally across the domain show that there is flux.

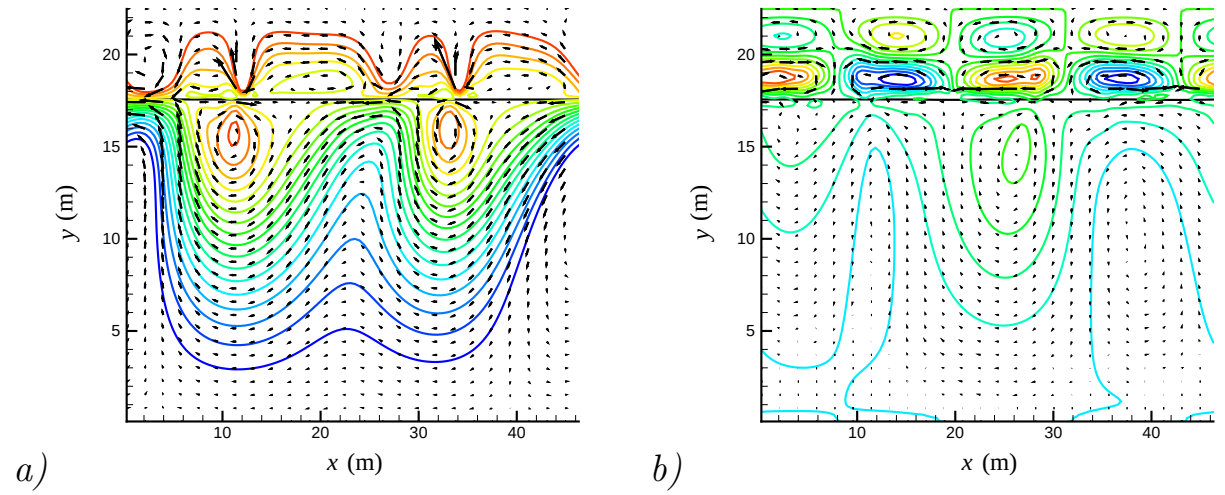

Figure 4.5: a) Mean flow over $4T$ for $a = 0.0548g$. The solution is indicated by the red arrow in Figure 4.7. This flow has neither $\lambda/2$ translational symmetry nor reflection symmetry. b) Mean flow over $4T$ for $a = 0.06g$. This flow has neither $\lambda/2$ translational symmetry nor reflection symmetry. All the streamlines in the air layer form closed loops and the patterns at the interface do not move, phenomena that are certainly related to each other.

We comment here on the order of integration in (4.47). When the time integration is carried out first, the points of the Eulerian mesh swept by the interface are sometimes in the water and sometimes in the air. This has been checked by exchanging the order of integration so as to take the fluctuations of the interface

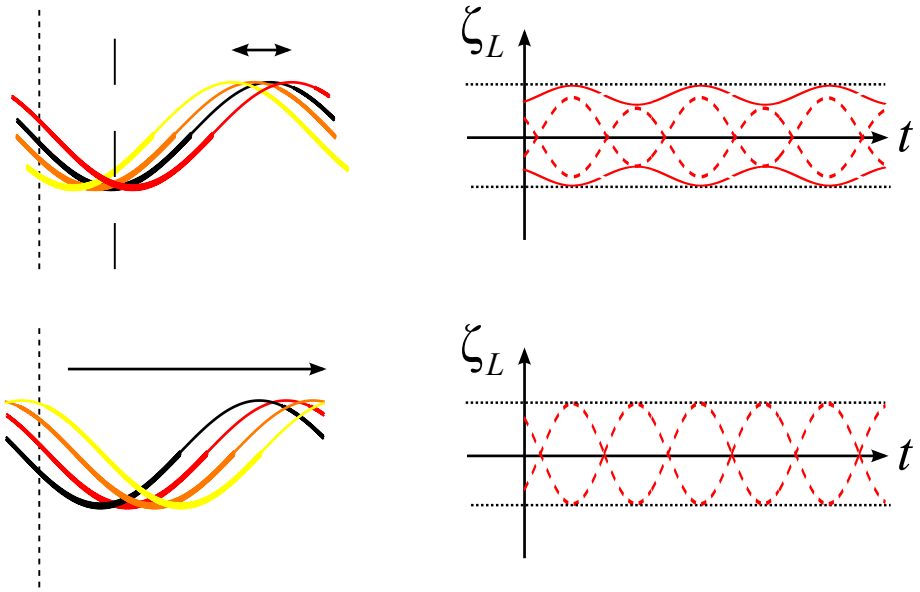

Figure 4.6: Behavior of the envelope of $\zeta_L(t)$. Left side: sine functions represent the interface at times t, $t+2T$, $t+4T$ and $t+6T$. Right side: envelope of $\zeta_L(t)$ if the pattern oscillates horizontally (top) and if it moves uniformly (bottom). The dotted lines represent the maximum and the minimum (in both space and time) of ζ. Top row, two typical scenarios for the vibration of the interface depending on the spatial phase of the pattern at the leftmost point (long or short dashed lines).

height into account:

$$\begin{cases} \phi_{water} = \dfrac{1}{8T\lambda}\displaystyle\int_0^{\lambda}\int_t^{t+8T}\int_0^{\zeta(x,t)} \mathbf{u}(x,y,t)\cdot\mathbf{e}_y \, dy\, dt\, dx \\ \phi_{air} = \dfrac{1}{8T\lambda}\displaystyle\int_0^{\lambda}\int_t^{t+8T}\int_{\zeta(x,t)}^{h} \mathbf{u}(x,y,t)\cdot\mathbf{e}_y \, dy\, dt\, dx \end{cases} \tag{4.48}$$

The two formulas led to results with negligible differences. The mean flux and the phase velocity of the patterns are not equivalent. The difference between the behavior of both quantities is related to the time-averaged velocity profile, especially at the vicinity of the interface. For example, if there is a mean mass flux only in the vicinity of the solid walls, the pattern at the interface will be stationary even if ϕ is finite. In contrast, if the main zone of mean flux surrounds the interface, then both ϕ and $\omega_{pattern}$ will be finite. In Fauve et al. (1991), the coefficient R of (4.3) is calculated as

$$R = \frac{1}{2}\ln\left|\frac{\zeta_{1,1}}{\zeta_{1,-1}}\right| \tag{4.49}$$

$R=0$ means that the pattern is symmetric, in which case there should be no drift.

Finally, the horizontal spatial periodicity of the flow averaged over durations that are multiples of $2T$ can change from one branch to another; we indeed observed averaged flows whose wavelength were either $\lambda/2$ or λ. Hence, we define a quantity measuring this departure from periodicity. The Fourier expansion in x and t of any generic vector $\mathbf{q}$ is

$$\mathbf{q}(\mathbf{x},t) = \sum_m\sum_n \hat{\mathbf{q}}_{m,n}(y)\mathrm{e}^{\mathrm{i}\left(\frac{2\pi m x}{\lambda}+\frac{\pi n t}{T}\right)} \tag{4.50}$$

We then define

$$\delta_{\lambda/2} = \frac{\overline{E}_{c_{odd}}}{\overline{E}_{c_{tot}}} \tag{4.51}$$

where $\overline{E}_{c_{odd}}$ denotes the spectral kinetic energy contained in the odd-wavenumber, time-independent modes $\hat{\mathbf{q}}_{2m+1,0}$, while $\overline{E}_{c_m}$ is the spectral kinetic energy of all time-independent modes.

$$\overline{E}_{c_{odd}} = \sum_m \left(|\hat{u}_{2m+1,0}|^2 + |\hat{v}_{2m+1,0}|^2 \right) \qquad \overline{E}_{c_{tot}} = \sum_m \left(|\hat{u}_{m,0}|^2 + |\hat{v}_{m,0}|^2 \right) \tag{4.52}$$

The quantities used to quantify the possible states of the flow all concern one particular symmetry or invariance breaking. $\Delta\zeta$ is associated with the breaking of the Euclidian symmetry along x. The resulting stable states pass from a homogeneous motionless flow to periodic flow. The flux ϕ or the pattern velocity $\omega_{pattern}$ are related to the breaking of the reflection symmetry through vertical axes of the mean flow. The difference between those two quantities lies in the fact that ϕ is a global variable whereas the pattern drift velocity is localized at the interface. However, both are consequences of the same phenomenon and are easily related to the breaking of reflection symmetry. The presence of a flux is linked with the opening of the streamlines in some parts of the domain. Because of mass conservation, if there is a nonzero net flux along some vertical axis, then this is true for any vertical axis. As a consequence, the horizontal velocity cannot be zero over an entire axis, and therefore there can be no vertical symmetry axes. Consequently, the emergence of a mean flux is a corollary of the breaking of a symmetry through vertical axes. The same kind of reasoning can be made for $\omega_{pattern}$. The variable $\delta_{\lambda/2}$ is by definition related to the breaking of an invariance: the passage from a periodicity of $\lambda/2$ to a periodicity of λ.

Bifurcation diagrams

The states described in the following figures and sections have been computed from the initial condition given in (4.44) or from saturated solutions, initially calculated with another amplitude a.

Figure 4.7a represents the evolution of $\Delta\zeta$ at saturation as a function of a/g. The transition from a motionless flow with a plane interface to Faraday waves is characterized by an increase of $\Delta\zeta$. The solutions are separated into several distinct branches, differentiated by letters from A to E. A-D, represented by circles, are obtained by simply running the code from the initial condition given by (4.44). The other solutions (branch E), shown as the black crosses, are obtained by forcing reflection symmetry at regular time intervals, the method for which is explained in detail in section 4.4.2. When the reflection is forced, $\Delta\zeta$ is a monotonic function of the acceleration. $\Delta\zeta$ undergoes a steep ascent for a/g between 0.057 and 0.0572, suggesting the presence of another bifurcation. The behavior of the unforced solutions seems more complex. Near the threshold, $\Delta\zeta$ increases strongly until it reaches a first plateau at $a/g \in]0.0542, 0.0543]$, denoted by the letter A. A second slightly higher plateau, B, follows in the interval $[0.0544, 0.0578]$ which is bistable with a third branch, C, also almost flat over $[0.055, 0.0568]$. At yet higher acceleration, $a/g = 0.057$, both the unforced and forced solutions (D and E respectively) have roughly the same amplitude $\Delta\zeta$. The unforced solution D seems to undergo the same sharp increase between 0.057 and 0.0572 and oscillate around the forced solution, E.

Figure 4.7b depicts the evolution of the horizontal flux in each fluid layer. The flux of the forced solution is invariably zero, meaning that there is no displacement of the pattern at the interface. When the reflection is not forced (branch E), the fluxes in air and water calculated by (4.47) are almost proportional. This figure exhibits quite complex behavior, with many overlapping branches. The branches behave roughly like $\Delta\zeta$ with plateaux covering the same intervals of accelerations as in Figure 4.7a. The forced and unforced states join together at 0.057 and increase for higher a/g.

Figures 4.7a-b show that the thresholds for the appearance of Faraday waves and the breaking of vertical reflection are almost simultaneous.

Figure 4.8 displays $\delta_{\lambda/2}$ as a function of a/g. The threshold for average $\lambda/2$-periodicity breaking is at slightly higher accelerations than the two other thresholds. The branch A which is characterized by $\lambda/2$-periodic time-averaged flows is stable only for $a/g \in [0.0542, 0.0543]$. Some tendencies of $\delta_{\lambda/2}$ can be related to the two other coefficients. First, the second plateau of Figure 4.7 seems to be distinguished by its high $\delta_{\lambda/2}$. Note as well that the flux-free states are all $\lambda/2$-periodic, as suggested by the set of + signs which are all on the axis $\delta_{\lambda/2} = 0$. This is confirmed by the fact that the unforced state becomes $\lambda/2$-periodic at 0.057 where the flux vanishes (see Figure 4.7b). Finally, the states of the branch D seem to be $\lambda/2$-periodic. We note that five different branches were obtained with the simulation. In contrast, we were able to characterize

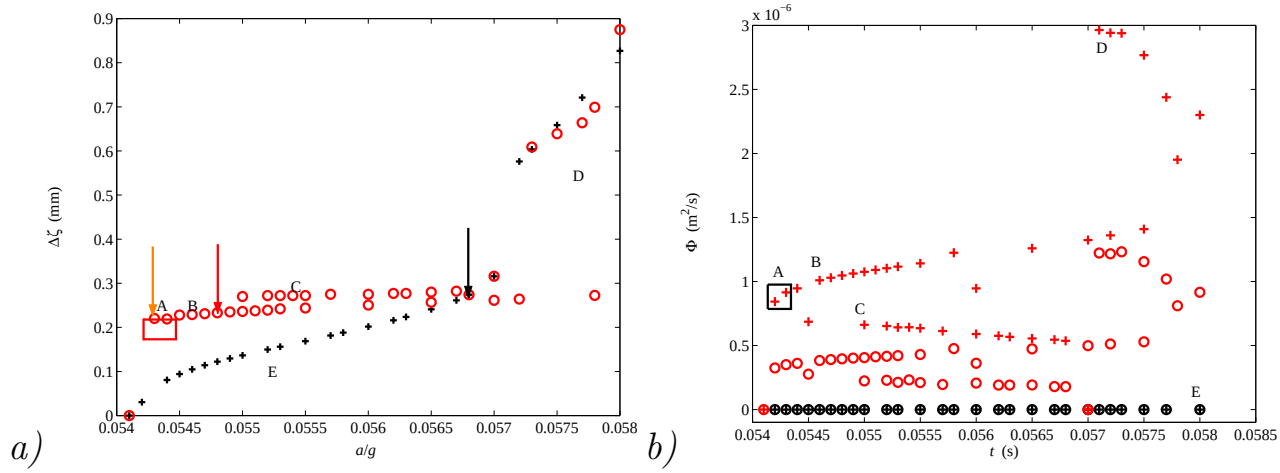

Figure 4.7: a) Evolution of the interface height amplitude $\Delta\zeta$ as a function of a/g. Red circles: states obtained without symmetry forcing. Black +: solutions observed when vertical reflection is forced. The different branches are denoted by letters from A to E. The points belonging to the branch A are surrounded for the sake of clarity. Black, orange and red arrows indicate the solutions whose mean flow has been plotted in Figures 4.4a, 4.4b and 4.5b, respectively. b) Evolution of the flux ϕ as a function of a/g. Red: when no symmetry is forced. Black: when vertical reflection is forced. In b) the circles stand for ϕ_{water} while the + stand for ϕ_{air}. The same conventions have been adopted as for Figure 4.7a.

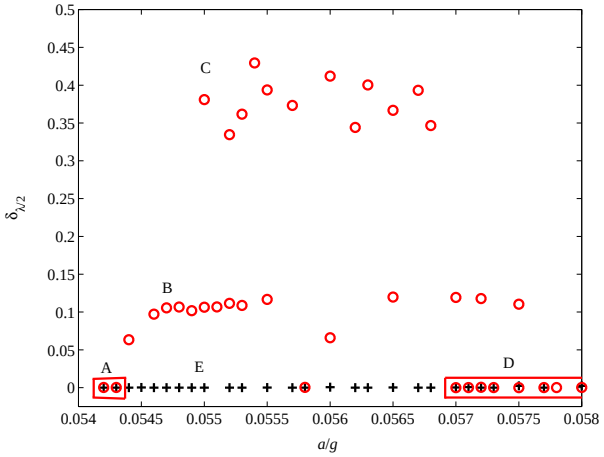

Figure 4.8: Coefficient of $\lambda/2$-nonperiodicity of the mean flow, as a function of a/g. The same conventions have been adopted as for Figure 4.7a. The circles belonging to the branches A and D have been surrounded for the sake of clarity.

these solutions by three different symmetries only.

To summarize, the Faraday waves appear via a supercritical pitchfork bifurcation, as suggested in section 4.4.2. When the primary threshold is reached, the reflection-invariant solutions (Faraday standing waves) destabilize rapidly ($0.0541 < a < 0.0542g$) in favor of drifting solutions that, over a short interval of accelerations, $a/g \in [0.0542, 0.0543]$, conserve a wavelength of $\lambda/2$. The time-averaged solutions undergo a spatial period-doubling instability. None of the aforementioned invariance is satisfied by the states for $a/g \in [0.0544, 0.0568[$. Two branches of solutions have been distinguished through the quantities involved in the bifurcation diagrams Figures 4.7a-b and 4.8. The transition between these two branches is not made through the breaking of any discernable symmetry. Bistability has been observed over the range of

a/g between 0.055 and 0.0578. This range can most likely be extended. At $a/g = 0.057$ the reflection-symmetric solution stabilizes again and also becomes $\lambda/2$-periodic on average. Further computations show no hysteresis in this transition. For $a/g \geq 0.0572$, the reflection symmetry breaks again but the averaged solutions conserve the wavelength of $\lambda/2$. Over the interval of accelerations studied, the solutions with forced reflection symmetry retain a period of $\lambda/2$.

Some interesting calculations remain to be done:

- force the mean flow to keep a wavelength of $\lambda/2$ between 0.0545 and 0.0567,
- differentiate the solutions on the branches B and C,
- hysteresis at $a/g < 0.055$.

The symmetric solutions with motionless patterns

An example of these solutions is given in Figure 4.4a. These solutions are obtained in the range of accelerations $a/g > 0.0541$. They appear to be only transient, except for accelerations between $a/g = 0.0568$ and $a/g = 0.057$. A horizontally fixed point of the interface oscillates vertically with a constant amplitude that shows that φ remains constant, or $\omega_{pattern}$ is null. After a time that depends on a, this state evolves to one in which the envelope of amplitude of the same fixed point oscillates with an amplitude equal to $\frac{1}{2}(\zeta_{max} - \zeta_{min})$, meaning that the pattern drifts in the horizontal direction, as explained in Figure 4.6.

Since the reflection-symmetric solutions are unstable, they can be calculated only if the reflection symmetry is forced. This forcing will be carried out at regular time intervals. To do this, we adopt the following method.

Let $\mathbf{q}(\mathbf{x}, t)$ be a vector field of spatial periodicity λ, with $\mathbf{q} = (u, v, \zeta)^T$ and $\mathbf{x} = (x, y)^T$. The field $\mathbf{q}(\mathbf{x})$ is reflection-symmetric across $x = x_0$ if $P_{x_0}\mathbf{q} = \mathbf{q}$, where

$$\mathbf{P}_{x_0} \begin{pmatrix} u \\ v \\ \zeta \end{pmatrix} (x, y) \equiv \begin{pmatrix} -u \\ v \\ \zeta \end{pmatrix} ((x_0 - x) \bmod \lambda, y) \tag{4.53}$$

By translating the origin via $x - x_0 \to x$, the symmetry axis is placed at $x = 0$ and we write $\mathbf{P} \equiv \mathbf{P}_0$. Because $\mathbf{q}$ is real, its Fourier decomposition in x

$$\mathbf{q}(\mathbf{x}) = \sum_m \tilde{\mathbf{q}}_m(y, t) \mathrm{e}^{\frac{\mathrm{i}2\pi mx}{\lambda}} = \sum_m \begin{pmatrix} \tilde{u}_m \\ \tilde{v}_m \\ \tilde{\zeta}_m \end{pmatrix} (y, t) \mathrm{e}^{\frac{\mathrm{i}2\pi mx}{\lambda}} \tag{4.54}$$

satisfies $\tilde{\mathbf{q}}_m(y, t) = \hat{\mathbf{q}}^*_{-m}(y, t)$. The reflection operator acts on the Fourier coefficients via:

$$\mathbf{P}\left[\sum_m \begin{pmatrix} \tilde{u}_m \\ \tilde{v}_m \\ \tilde{\zeta}_m \end{pmatrix} \mathrm{e}^{\frac{\mathrm{i}2\pi mx}{\lambda}}\right] \equiv \sum_m \begin{pmatrix} -\tilde{u}_m \\ \tilde{v}_m \\ \tilde{\zeta}_m \end{pmatrix} \mathrm{e}^{\frac{-\mathrm{i}2\pi mx}{\lambda}} = \sum_m \begin{pmatrix} -\tilde{u}_{-m} \\ \tilde{v}_{-m} \\ \tilde{\zeta}_{-m} \end{pmatrix} \mathrm{e}^{\frac{\mathrm{i}2\pi mx}{\lambda}} = \sum_m \begin{pmatrix} -\tilde{u}^*_m \\ \tilde{v}^*_m \\ \tilde{\zeta}^*_m \end{pmatrix} \mathrm{e}^{\frac{\mathrm{i}2\pi mx}{\lambda}} \tag{4.55}$$

The property of reflection symmetry $\mathbf{Pq} = \mathbf{q}$ is thus expressed for the Fourier decomposition as

$$\begin{pmatrix} \tilde{u}_m \\ \tilde{v}_m \\ \tilde{\zeta}_m \end{pmatrix} = \begin{pmatrix} -\tilde{u}^*_m \\ \tilde{v}^*_m \\ \tilde{\zeta}^*_m \end{pmatrix} \tag{4.56}$$

Thus the Fourier coefficients of a reflection-symmetric $\mathbf{q}$ must satisfy:

- $\tilde{u}_m$ is pure imaginary for all m,
- $\tilde{v}_m$ is pure real for all m,
- $\tilde{\zeta}_m$ is pure real for all m.

The forcing of the reflection symmetry $\mathbf{P}_{x_0}$ is then implemented as follows. At regular time intervals:

- Expand the fields into horizontal spatial Fourier coefficients,
- Choose a mode, usually that with largest amplitude, and compute its phase $\theta \equiv arctan\left[\frac{\mathrm{Re}(\tilde{u}_{m=1})}{\mathrm{Im}(\tilde{u}_{m=1})}\right]$,
- Multiply the mth Fourier coefficients by $\mathrm{e}^{-\mathrm{i}m\theta}$ to shift the symmetry axis to $x = 0$,
- Force u to be odd in x by making $\tilde{u}$ pure imaginary via $\tilde{u}_m \to |\tilde{u}_m|\frac{\mathrm{Im}\,(\tilde{u}_m)}{|\mathrm{Im}\,(\tilde{u}_m)\,|}$,
- Force v to be even in x by making $\tilde{v}$ pure real via $\tilde{v}_m \to |\tilde{v}_m|\frac{\mathrm{Re}\,(\tilde{v}_m)}{|\mathrm{Re}\,(\tilde{v}_m)\,|}$ and similarly for ζ,
- Reverse the phase shift to move the symmetry axis to its original position,
- Perform the inverse Fourier transform,
- Continue the calculation, repeating the above steps until convergence.

The dynamics should then tend to the symmetric solution of the lower branch, with flux suppressed.

A dynamic overview of the forced flow at $a = 0.055g$ is given in Figure 4.9. The centers of the loops formed by the streamlines and the velocity maxima are located in the air in the vicinity of the interface. In general, the velocities and their gradients have their maximum of amplitude at close to the interface, the shear stresses should be more important there. Far from the interface in the bottom fluid, the amplitudes decrease smoothly and there should not be strong forcing stemming from this part of the domain. The plots show that the streamlines form smooth closed loops and that two vertical symmetry axes cross the extrema of the interface. The following symmetry $(u, v, \zeta)(x, t + T) = (u, v, \zeta)(-x, t)$ can be noticed, which is the classical symmetry for Faraday waves. The interface describes a sine function of spatial periodicity λ. At the accelerations explored, the dynamical overviews exhibit the same qualitative properties, with variations only in the amplitudes of the interface height and velocity vectors. The loops are permanent features but become twisted as a increases; the maximal elongation of the center is locally oriented along the interface. The initial conditions from which each plot stems were flow that had already undergone possiblesymmetry breaking and therefore had reached states of drift with various velocities. This explains the differences in the position of the symmetry axes for each plot.

A more careful analysis of the flow was carried out by performing a spectral analysis of ζ and of the velocity field. We have plotted the evolution of the main modes as a function of a/g in order to have an idea of their magnitude and evolution. These modes are identified by two subscripts m and n:

$$\mathbf{q}(\mathbf{x}, t) = \sum_m \sum_n \hat{\mathbf{q}}_{m,n} \mathrm{e}^{\mathrm{i}\left(\frac{2\pi m x}{\lambda} + \frac{\pi n t}{T}\right)} \tag{4.57}$$

The dominant mode, $\hat{\zeta}_{1,1}$, is plotted versus a/g on Figure 4.10 on a linear scale and on a log-log scale in order to extract a possible power law that should emerge according to the weakly nonlinear theories. To do this, we introduce $\epsilon \equiv (a - a_c)/a_c$, for the nondimensionalized distance to the threshold a_c. We expect $\hat{\zeta}_{1,1}$ to grow as $\epsilon^{\frac{1}{2}}$ as is the classical case of pitchfork bifurcations.

Figure 4.10a corresponds to the bifurcation diagram for $\Delta\zeta$. The mode $|\hat{\zeta}_{1,-1}|$ which is identical to $|\hat{\zeta}_{1,1}|$ has not been plotted. The right and left traveling waves are then equivalent, which is characteristic of standing waves. Figure 4.10b shows that a power law exists at low ϵ but the slope of the line is only 0.40 and not 0.50 as expected. We do not know what explains this difference. When ϵ reaches 2.5% ($a/g = 0.0555$), the curve separates gradually from its linear fit and there is a gap at $\epsilon = 5.2\%$ or $a/g = 0.057$. There may be a further bifurcation at this location. More modes have been plotted in Figure 4.11 which shows that they all undergo the same abrupt change change as $|\hat{\zeta}_{1,1}|$. The modes not plotted have negligible amplitudes. Note that only the modes whose m and n have the same parity appear due to the negligible amplitude of modes with $m + n$ odd. This can be explained using results of Floquet analysis and triadic interactions and

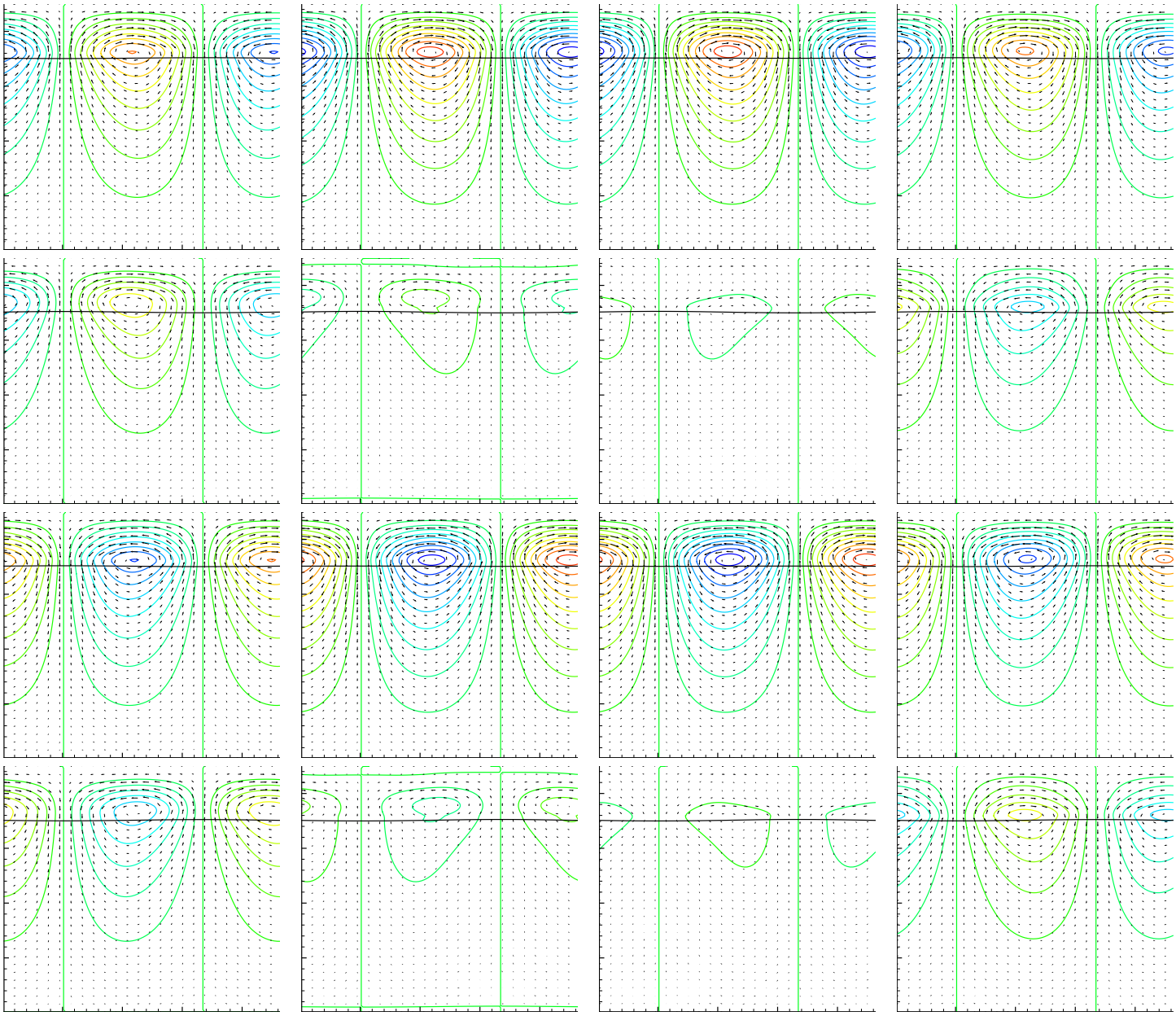

Figure 4.9: Instantaneous flow for $a/g = 0.055$ when reflection-symmetry forcing is applied. Snapshots are taken every $T/8$, starting from $(t \mod 2T) = 0$. Colors: streamfunction. Line: $\zeta(x,t)$. We recall that the interface is 17.56mm high when no forcing is applied, the total height of the box being 22.56mm. Vectors: velocity field. A uniform scale has been used throughout for both the streamfunction and the velocity field.

will be treated in section 4.4.2. At low ϵ, the slope of $\log(|\hat{\zeta}_{1,3}|)$ is estimated at 0.40, like that of $\log(|\hat{\zeta}_{1,1}|)$. The slopes associated with the modes $\log(|\hat{\zeta}_{2,0}|)$ and $\log(|\hat{\zeta}_{2,2}|)$ are 0.80 and 0.87, respectively. For $\log(|\hat{\zeta}_{3,1}|)$ and $\log(|\hat{\zeta}_{3,3}|)$, the corresponding slopes are 1.01 and 1.27. These power laws fit fairly well with those we should find by considering triadic interactions despite the unexpectedly low exponent associated with $|\hat{\zeta}_{1,1}|$.

Figure 4.12 presents the averaged fields corresponding to states like that of Figure 4.9. The averaged velocities of the flows shown on Figure 4.12 and their gradient are maximal in the vicinity of the interface. In the depths of the water, their amplitude decreases regularly. The mean stresses should, as in the

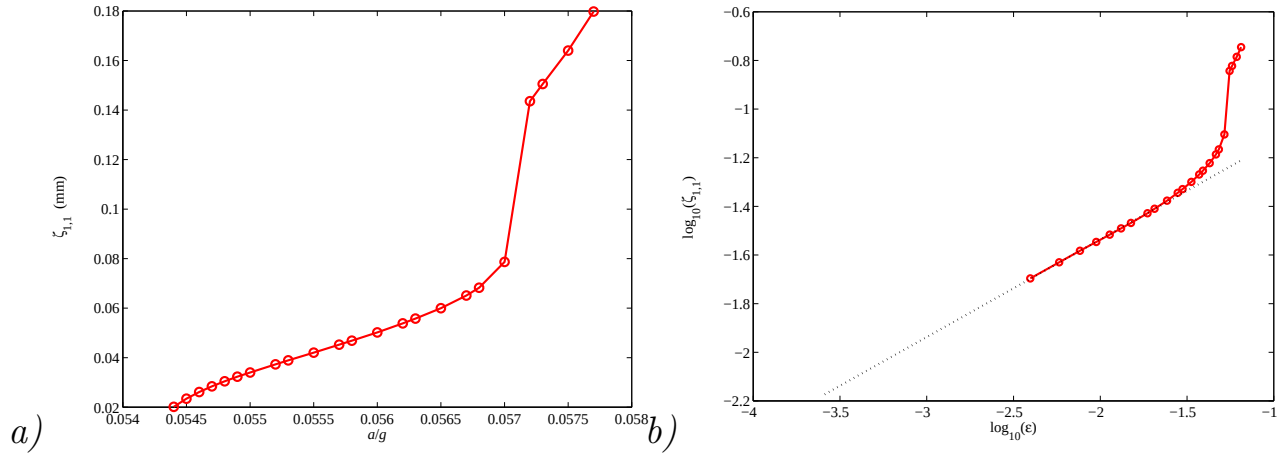

Figure 4.10: Evolution of mode $|\hat{\zeta}_{1,1}|$ as a function of acceleration. a) linear scale. b) $\log(|\hat{\zeta}_{1,1}|)$ versus $\log(\epsilon)$. The dotted black line on Figure 4.10b represents the linear interpolation of $\log(|\hat{\zeta}_{1,1}|)$ at the lower accelerations.

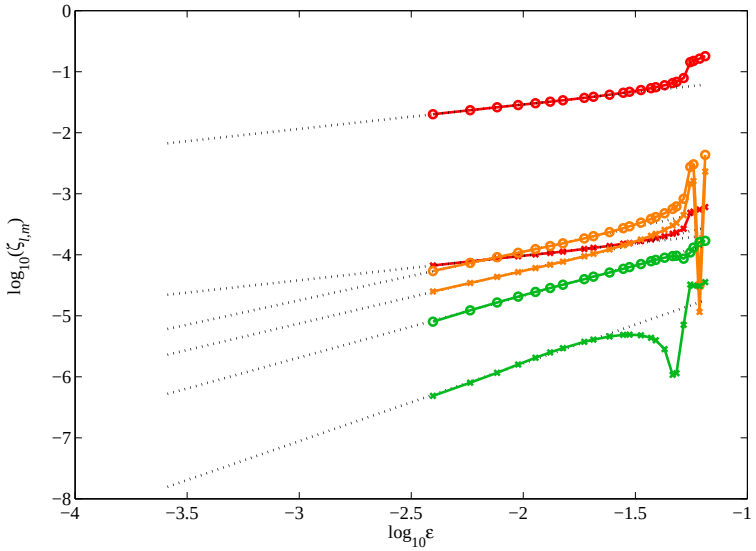

Figure 4.11: Main Fourier modes of the interface height $|\hat{\zeta}_{m,n}|$ as a function of the acceleration in a log-log graph. Red circles: $m = 1$, $n = 1$. Red crosses: $m = 1$, $n = 3$. Orange circles: $m = 2$, $n = 0$. Orange crosses: $m = 2$, $n = 2$. Green circles: $m = 3$, $n = 1$. Green crosses: $m = 3$, $n = 3$. Linear fits of each curve for the lower accelerations are represented by the dotted lines.

instantaneous snapshots, be concentrated near the interface and not just above the bottom wall. The averaged streamlines form closed loops; equivalently the velocity forms counter-rotating vortices in water and air. The sense of rotation is given by the direction of the vectors or by the coloring of the streamfunction. At $a/g = 0.0542$, there are two superposed layers of loops (one in air and one in water) that look quite symmetric. As a is increased, the centers of the vortices move jointly in water and air, such that vertical reflections are conserved (clockwise and counterclockwise vortices move in opposite directions in each layer). When a reaches $0.056g$, the loops in the air are stretched. In fact, another recirculation loop appears that is clearly visible at $a = 0.057g$. This tendency is also present in the water layer, but is less marked. Between $a = 0.057g$ and $a = 0.0572g$, the location of the abrupt transition seen in figures 4.7, 4.10 and 4.11, the

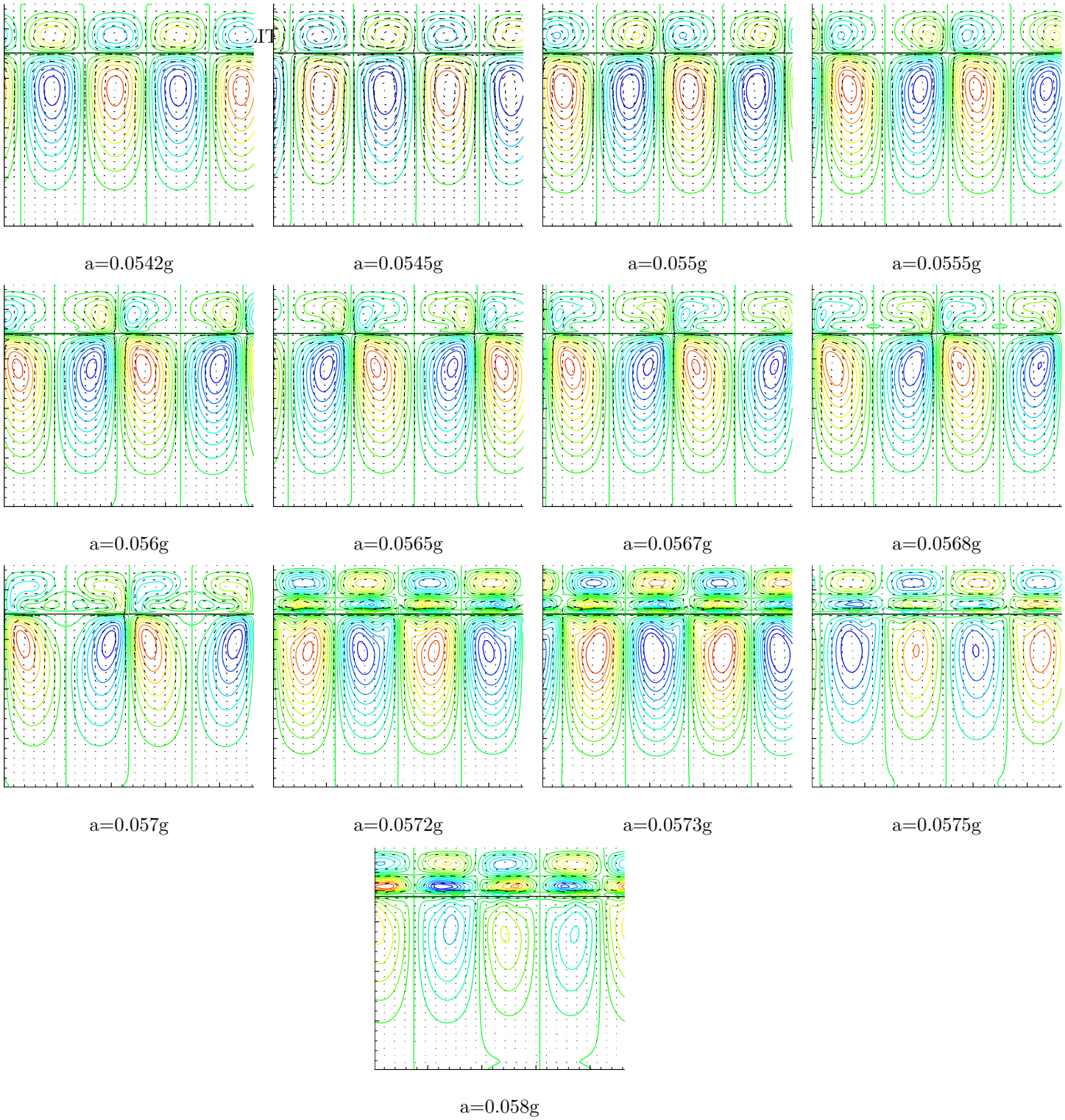

Figure 4.12: Mean flow over $4T$ at different accelerations when the vertical reflection symmetry is forced. Colors: streamfunction. Line: interface. Vectors: velocity field. The coloring and the vector fields are rescaled in each picture for the sake of clarity.

shape of the loops changes drastically. In the air, the two emerging loops have split into three superposed layers of alternating vortices. In the water, new cells have appeared near the interface. Between $0.0572g$ and $0.058g$, the intensity of the vortices seems to increase in the air relative to that in water. A departure from $\lambda/2$-periodicity can be noticed in the last two plots. The bending of one vertical border of each circulation

cell shows that the departure from $\lambda/2$-periodicity is correlated to the disappearance of two of the four initial symmetry axes. These two transformations cannot be dissociated in this framework. Finally, we assume that the jump in amplitude is related to the deformation of the streamfunction rather than to the period doubling of the mean flow which is almost imperceptible at these accelerations.

The solutions with moving pattern

As observed in section 4.4.2, the flux-free solutions are almost all unstable except at the point $a/g = 0.057$. We first intend to do as in the section 4.4.2, meaning see what the solution looks like. A dynamical overview of a drifting solution within one period of vibration of the fluid has been plotted. The acceleration is $0.055g$, the other parameters have not been changed. The set of parameters is exactly the same as on Figure 4.9 so that an objective comparison to be performed; the only thing that differs from the previous case is the fact that the periodic forcing of reflection symmetry has been relaxed.

The main feature exhibited by Figure 4.13 is that the instantaneous streamlines are no longer symmetric. They also form closed loops which divide the domain into closed recirculation cells, but these cells are curved and their boundaries, the streamlines which mark an inversion of the velocity direction, move slightly along the horizontal direction. The last two remarks are important. The fact that the instantaneous geometry of the recirculation cells changes may be responsible for the generation of a global flux. The underlying phenomenon that accounts for this global motion is called Stokes Drift. As in the case when the symmetry was forced, the stresses seem to be located close to the interface, as suggests the behavior of the velocity vectors and the streamlines.

Because of the reflection symmetry of the Navier–Stokes equations, neither the rightwards nor leftwards flux should be favored and we expect the transition to drift to occur via a pitchfork bifurcation. Hence, starting from any initial condition we should obtain solutions for which the pattern at the interface moves leftwards as well as rightwards.

At the lowest accelerations ($a/g \leq 0.0567$), the flow persists for a long time before destabilizing to solutions with drift. Our semi-Lagrangian method of front-tracking allows us to easily follow a point of the interface fixed in the x direction. We have plotted the envelope of the height of a fixed point at $a/g = 0.0545$ in Figure 4.14. Figure 4.14 shows that after the increase of the interface amplitude, both the black and the red curves are horizontal lines. As explained in section 4.4.2, the ratio of these amplitudes is constant, and hence the pattern at the interface does not move. During that time, the flow is symmetric. Afterwards, both the envelopes enlarge, and the broadness of the red one oscillates between 0 and the maximal amplitude. This signifies that the pattern has started to move; at the same time, the oscillation of the interface has begun to strengthen. The pattern motion accelerates regularly and its speed saturates, as does $\Delta\zeta$. The symmetric flow has lasted for about 500 seconds. The lifetime of the symmetric state decreases as a grows. When $a/g \leq 0.0572$, the reflection-symmetric branch no longer attracts the flow.

We first focus on the stable solutions which do not exhibit vertical reflection symmetry. We conduct a spectral study of the interface height ζ, examining the features of the few first modes in k and ω expanded as in (4.56) that we recall here:

$$\zeta(\mathbf{x}, t) = \sum_m \sum_n \hat{\zeta}_{m,n} \mathrm{e}^{\mathrm{i}\left(\frac{2\pi m x}{\lambda} + \frac{\pi n t}{T}\right)} \tag{4.58}$$

These modes are represented in Figures 4.15a-4.17d.

The behavior of modes corresponding to $n = 0$ is uninteresting and so has not been plotted. $\hat{\zeta}_{0,0}$ is constant and equal to the initial mean height of the interface, due to the integral law of mass conservation. For the same reason, the other modes $\hat{\zeta}_{0,n}$, $\forall n \neq 0$, can only be zero, independent of the vibration amplitude. The dominant mode is $\hat{\zeta}_{1,1}$, which is at least thirty times higher than its counterparts. The interface oscillates essentially with a wavelength of λ_c and at half the forcing frequency, as is typical for Faraday waves near threshold. In the entire acceleration range, the rightward $n < 0$ and leftward $n > 0$ propagating waves exhibit different behaviors which are characterized as follows

- $a/g \leq 0.0543$, branch A: the odd modes ($n + m$ odd) are zero or almost zero.
- Branch B: the odd modes are weak but non-zero; in particular, $\hat{\zeta}_{1,0}$ and $\hat{\zeta}_{3,0}$ are weaker than $\hat{\zeta}_{2,0}$. The even modes behave as for $a/g \leq 0.0544$. They vary weakly with a/g. The tendency of the odd modes is quite uncertain.

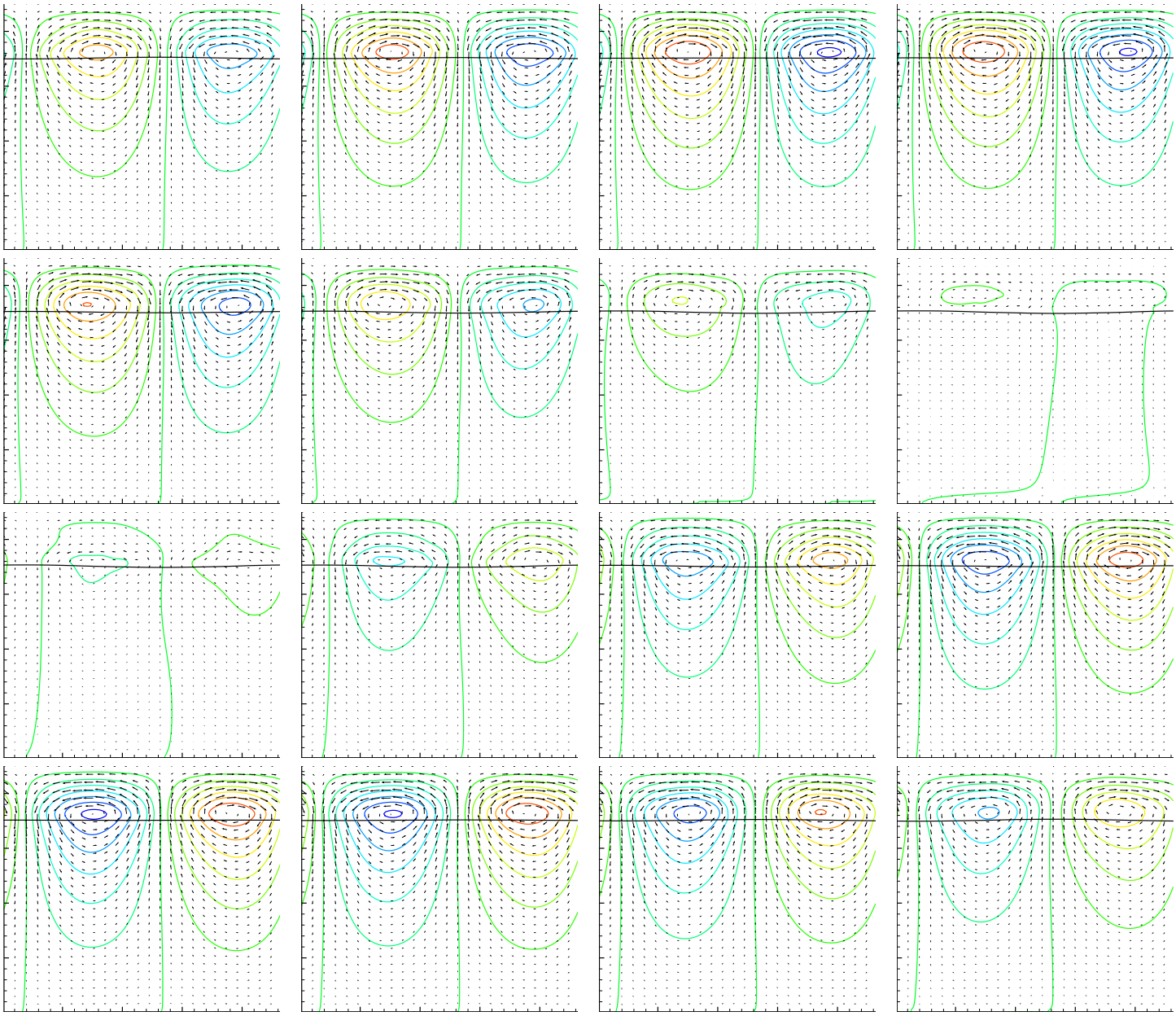

Figure 4.13: Instantaneous flow for $a/g = 0.055$ when the solution is asymmetric and exhibits a long-time pattern drift. Snapshots are taken every $T/8$, starting from $(t \mod 2T) = 0$. Colors: streamfunction. Line: $\zeta(x,t)$. The interface is 17.56mm high when no forcing is applied while the total height of the box is 22.56mm. Vectors: velocity field. A uniform scale has been used throughout for both the streamfunction and the velocity field.

- Branch C: the odd modes jump to higher values; in particular, $\hat{\zeta}_{1,0}$ and $\hat{\zeta}_{3,0}$ become stronger than $\hat{\zeta}_{2,0}$ which has been damped. The disparities between $n < 0$ and $n > 0$ are in general more significant for the odd modes. All the modes depend weakly on a/g. The hysteresis between both branches B and C is still visible here.

- Branch D: the odd modes are zero or almost zero. The even modes jump to higher values and increase with a/g.

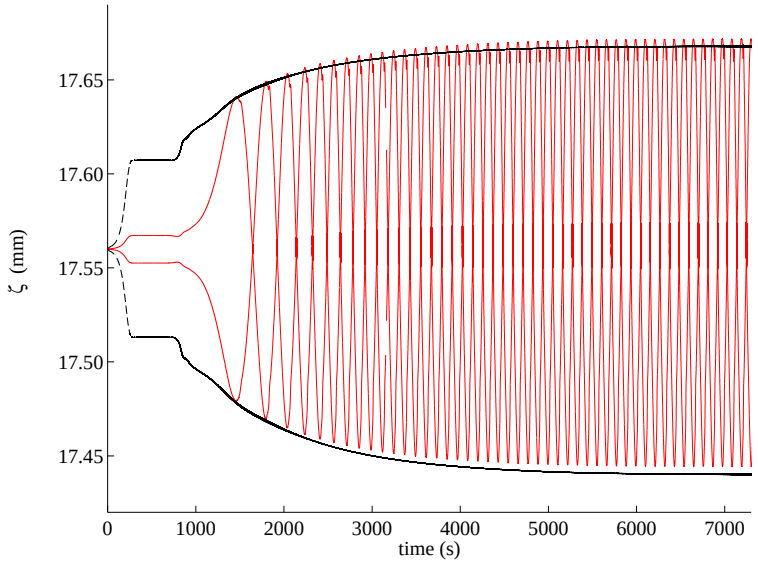

Figure 4.14: Red: Evolution in time of the envelope of $\zeta(x = 0, t)$ for $a/g = 0.0545$, as in the bottom of figure 4.6. Black: approximate envelope of $\Delta\zeta$ as in figure 4.3.

- Branch E (triangles): the odd modes are close to zero except at $a/g = 0.0575$.
- There remain some special points which do not seem to belong to any of the aforementioned branches or have behavior which is difficult to classify, for example $a = 0.0545g$, $a = 0.0558g$, $a = 0.057g$. The solution for these points might not be converged, despite long integration times.

The odd modes reveal the amplitude of the period-doubling, which is a priori the result of a tertiary bifurcation, after the rise of Faraday waves and the one of drifting states. For this reason, the underlying phenomena are more subtle and this instability can be harder to capture.

To conclude the spectral analysis of the interface, we plot the dependence on a/g of the coefficient R defined in Eq.(4.49) which measures the ratio of $\hat{\zeta}_{1,1}$ to $\hat{\zeta}_{1,-1}$, or the asymmetry of the interface height. R should be a signature of the drift and so should be strongly correlated with the flux ϕ of Figure 4.7b if the model of Fauve et al. (1991) applies. Many common features are observed in both Figures 4.7b and 4.18. The major difference lies in the variation of ϕ and R before and after the flux-free solutions found in $a/g = 0.057$. The velocity $\omega_{pattern}$ of the pattern at the interface measures more consistently the drift instability. Hence we compare the coefficient R to $\omega_{pattern}$ in Figure 4.19.

Figure 4.19 relates convincingly the drift velocity to the asymmetry coefficient. The correlation diagram (Figure 4.19b) shows that there is a strong relationship between R and $\omega_{pattern}$. Fauve et al. (1991) interpreted the drift generation as a direct consequence of the reflection symmetry breaking whose order parameter was the coefficient R. Martín et al. (2002) concluded from their study that even though a drift appeared, R would remain zero to leading order. Hence, we believe that our simulations are better described by the theory of Fauve et al. (1991) than by the analysis of Martín et al. (2002).

The mean flows of the most representative unforced solutions are displayed in Figure 4.20. The two graphs in Figure 4.20 at $a/g = 0.0542$ and $a/g = 0.0543$ show a flow which has $\lambda/2$ periodicity but no reflection symmetry. The streamlines form open paths surrounded by two peaks and closed loops near the interface. There is a global displacement of water from the right to the left of the box as suggested by the velocity vectors and the vertical gradient of coloration of the streamlines. The peaks and closed loops result from the presence of vortices in the flow. In the air, approximately the same phenomena can be seen. The motion of the air layer is in the same direction. The spatial phase difference between $a/g = 0.0542$ and $a/g = 0.0543$ is due to the drift causing the closed streamlines to occupy different positions in the two plots.

On branches B and C (these branches are indicated on Figure 4.7), the wavelength of the mean flow

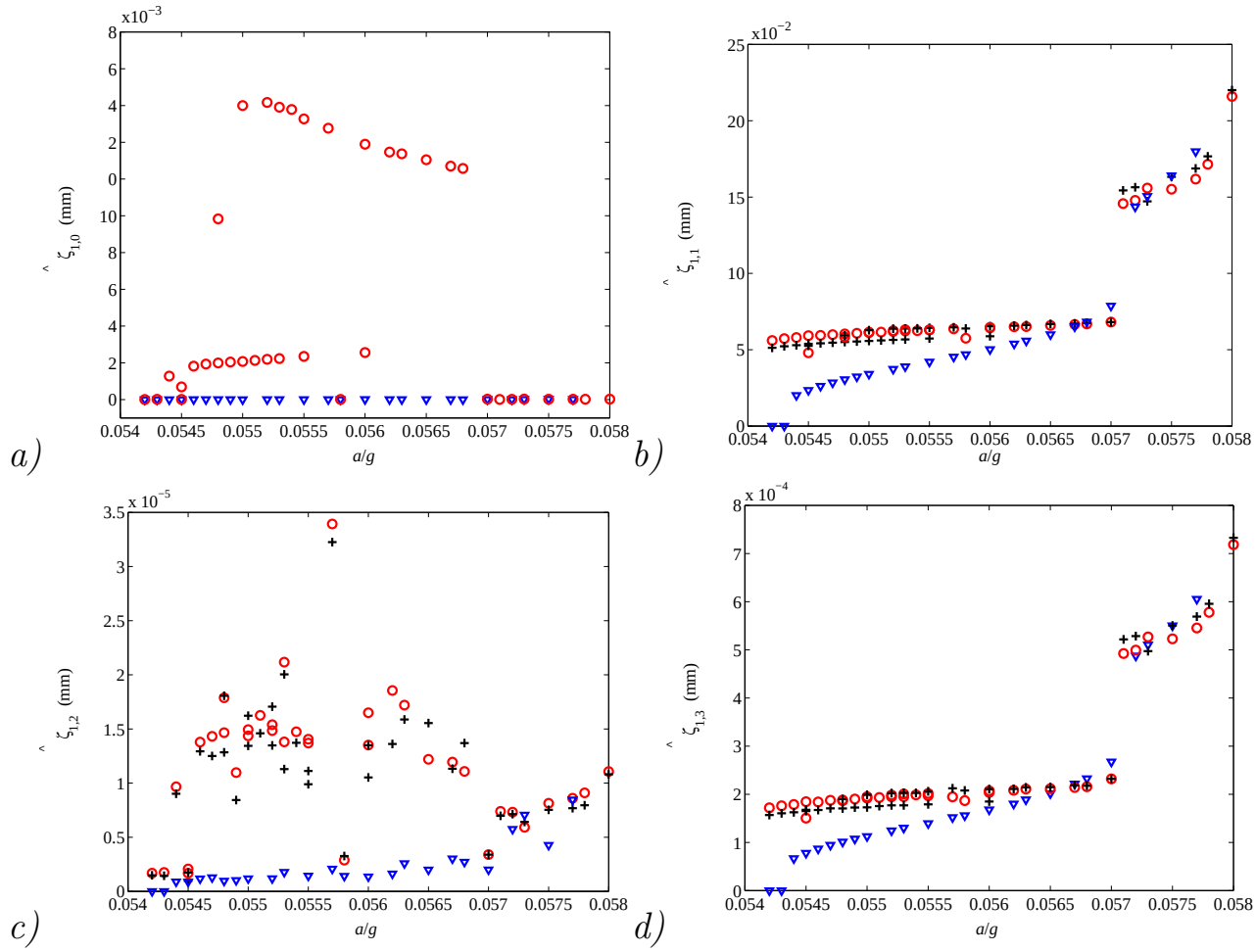

Figure 4.15: Spatiotemporal modes $k{=}k_c$ as a function of the acceleration. a) $\omega = 0$; b) $\omega = \pm\omega_0/2$; c) $\omega = \pm\omega_0$; d) $\omega = \pm 3\omega_0/2$. Red circles: leftward propagating waves ($n > 0$). Black crosses: rightward propagating waves ($n < 0$). Blue triangles: leftward and rightward propagating waves of the forced solution with reflection symmetry to make the comparison easier. The waves of zero temporal frequency do not move.

becomes λ. On branch B, the deformation is not well correlated with the acceleration, as shown in Figures 4.15a, 4.17a and the bifurcation diagram in Figure 4.8.

On branch C, the mean flows look quite similar to the previous ones. Note that the recirculations in water have almost disappeared. The color inversion results from the fact that the fluids move from left to right. It should be verified that equivalent solutions exist with drift in the other direction and that the two solutions are indeed images from each other under a vertical reflection. At the highest accelerations investigated, the streamlines are open in almost the entire water layer. In the air, the loops have reorganized into superposed layers as in section 4.4.2 in the same range of accelerations. As was the case for the symmetrized flows, the streamlines tighten near the interface, the velocities and the stresses seem then to be larger close to the interface. This contrasts with the analysis of Martín et al. (2002) which assumes that the streaming flow that comes from viscous effects and is responsible for the drift is located in the boundary layer near the bottom wall.

Forcing of the λ-periodic solutions with moving patterns

It has been seen that the branch of average-$\lambda/2$ periodic solutions destabilizes early. This branch can nevertheless be followed by forcing the average-$\lambda/2$ periodicity at regular time steps. This is not trivial

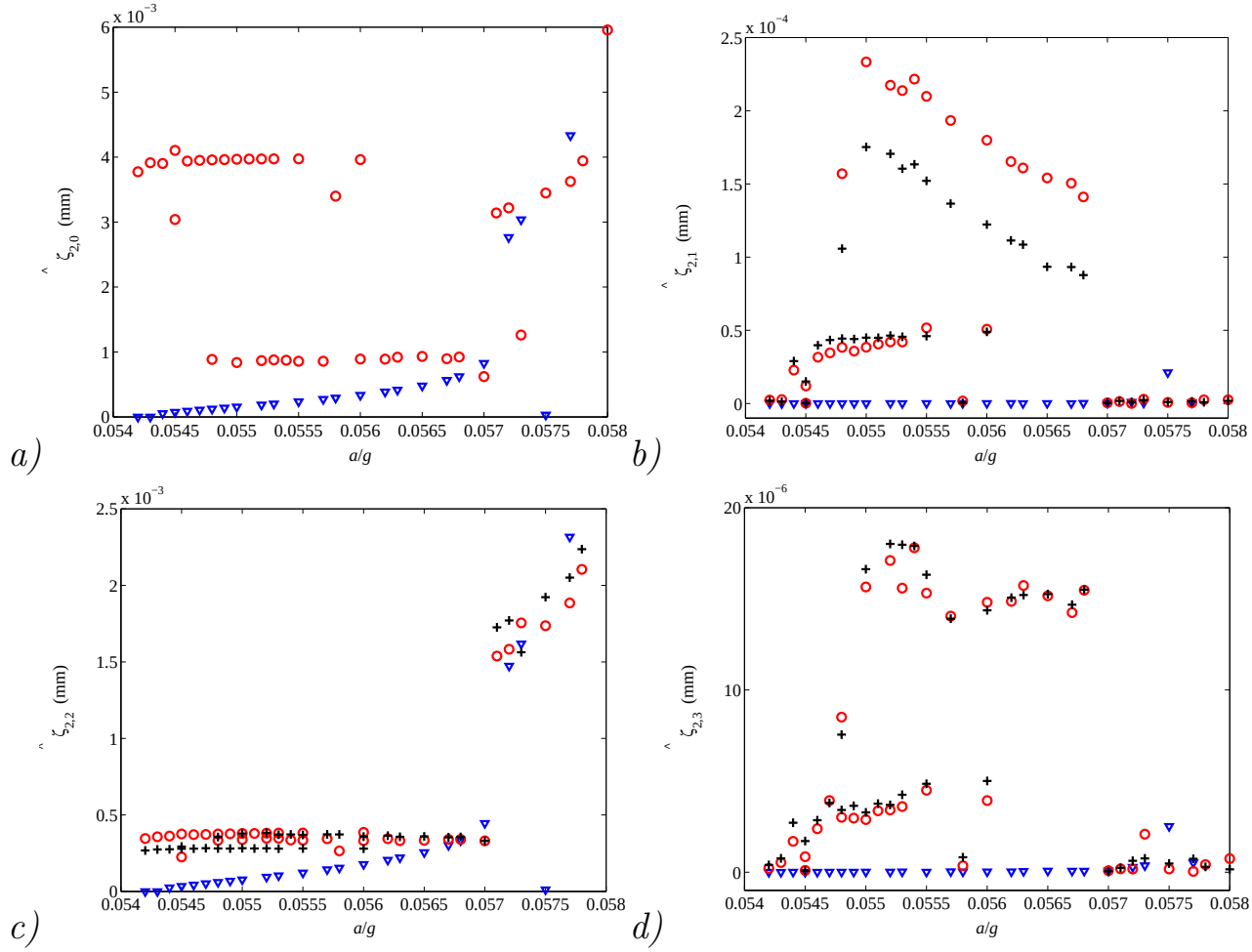

Figure 4.16: Spatiotemporal modes k=2k_c as a function of the acceleration. a) $\omega = 0$; b) $\omega = \pm\omega_0/2$; c) $\omega = \pm\omega_0$; d) $\omega = \pm 3\omega_0/2$. Same conventions as in Figure 4.15.

because the instantaneous flow does not share this property: it always has a wavelength of λ. Our method for achieving this forcing is based on the spatio-temporal Fourier transform in x and t of the instantaneous field:

$$\mathbf{q}(\mathbf{x},t) = \sum_m \sum_n \hat{\mathbf{q}}_{m,n} \mathrm{e}^{\mathrm{i}\left(\frac{2\pi m x}{\lambda} + \frac{\pi n t}{T}\right)} \tag{4.59}$$

In order for $\mathbf{q}$ to be real, the coefficients must satisfy $\hat{\mathbf{q}}_{mn} = \hat{\mathbf{q}}_{-m-n}$. The temporal mean of $\mathbf{q}(x,t)$, denoted by $\langle \mathbf{q}(x) \rangle_t$ selects the $n = 0$ temporal Fourier components:

$$\langle \mathbf{q}(x) \rangle_t = \frac{1}{2T} \int_{t=0}^{2T} \mathbf{q}(x,t)\, dt = \frac{1}{2T} \sum_m \hat{\mathbf{q}}_{m,0} \mathrm{e}^{\mathrm{i}\frac{2\pi m x}{\lambda}} \tag{4.60}$$

Periodicity in $\lambda/2$ of the mean flow is expressed by $\langle \mathbf{q}(x) \rangle_t = \langle \mathbf{q}(x + \frac{\lambda}{2}) \rangle_t$. According to (4.60), we obtain

$$\frac{1}{2T} \sum_m \hat{\mathbf{q}}_{m,0} \mathrm{e}^{\mathrm{i}\frac{2\pi m x}{\lambda}} = \frac{1}{2T} \sum_m \hat{\mathbf{q}}_{m,0} \mathrm{e}^{\mathrm{i}m\pi\left(\frac{2x}{\lambda}+1\right)} \tag{4.61}$$

The even-m terms on either side of (4.61) are necessarily equal and so (4.61) becomes

$$\Rightarrow \hat{\mathbf{q}}_{m,0} = 0 \text{ if } m \text{ is odd} \tag{4.62}$$

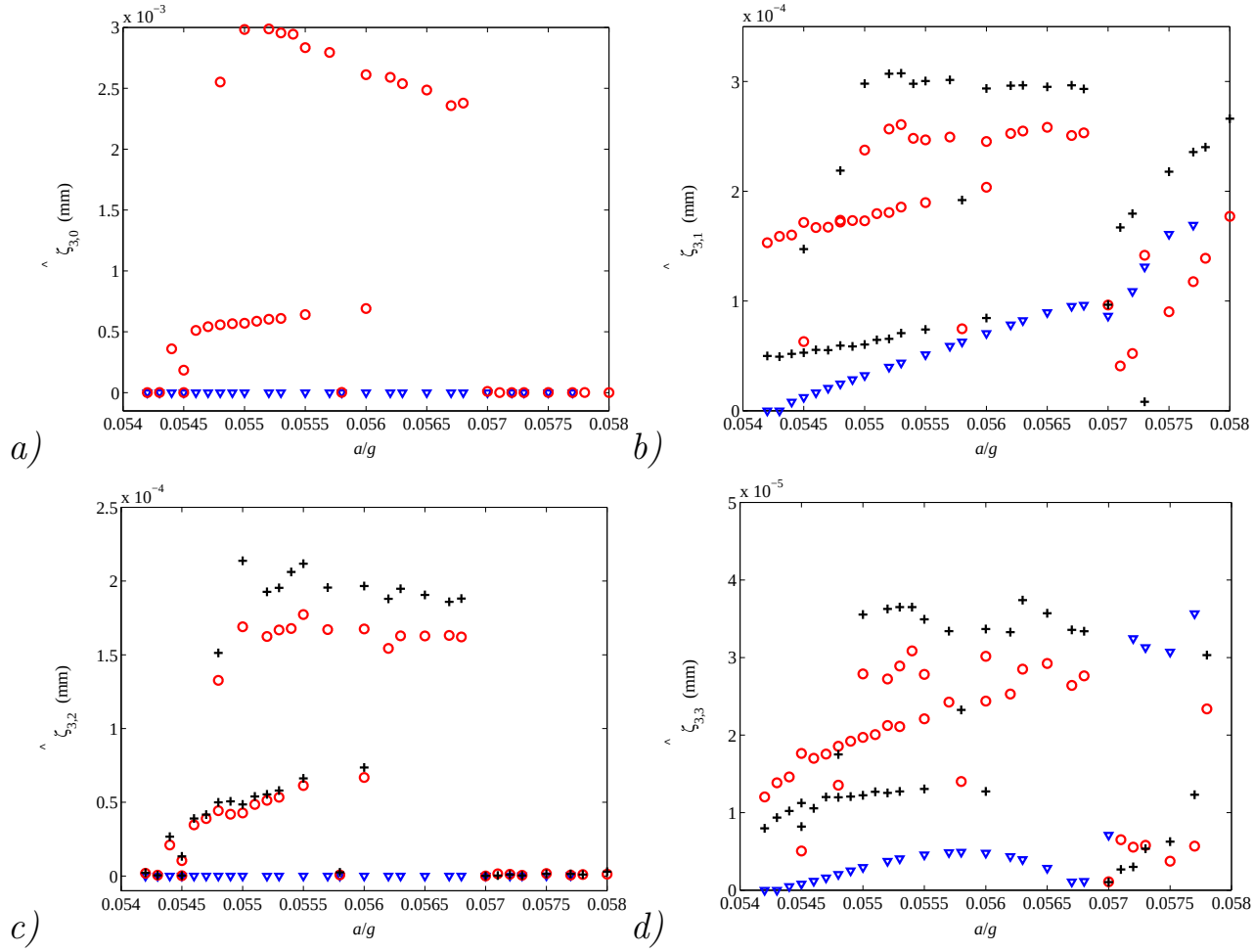

Figure 4.17: Spatiotemporal modes $k{=}3k_c$ as a function of the acceleration. a) $\omega = 0$; b) $\omega = \pm\omega_0/2$; c) $\omega = \pm\omega_0$; d) $\omega = \pm 3\omega_0/2$. Same conventions as in Figure 4.15.

This condition is both necessary and sufficient and applies to all of the velocity components. The restriction (4.62), however, does not by itself describe an invariant subspace. In particular, two modes (m, n) and $(m', -n)$, with m odd, m' even and $n \neq 0$, are not excluded by the restriction (4.62) but their quadratic nonlinear interaction yields $(m + m', n - n)$, with $m + m'$ odd and $n - n = 0$, which is forbidden by (4.62). We introduce a further restriction to a subspace which is invariant. Fields near the Faraday threshold are described by the Floquet eigenmode

$$\mathbf{Q}_1(t)\mathrm{e}^{\mathrm{i}kx} + cc = \sum_{n=-\infty}^{\infty} \mathbf{Q}_{1,n}\mathrm{e}^{\mathrm{i}kx}\mathrm{e}^{\frac{\mathrm{i}n\omega_0 t}{2}} + cc \tag{4.63}$$

with n odd when the instability is subharmonic, as is the case here. Quadratic interaction of $\mathbf{Q}_1(t)$ with itself gives rise to secondary modes

$$\left[\sum_{n=-\infty}^{\infty} \mathbf{Q}_{1,n}\mathrm{e}^{\mathrm{i}kx}\mathrm{e}^{\mathrm{i}\left(n+\frac{1}{2}\right)\omega_0 t} + cc\right]^2 = \sum_{m=-2,0,2}\ \sum_{n=-\infty}^{\infty} \mathbf{Q}_{m,n}\mathrm{e}^{\mathrm{i}mkx}\mathrm{e}^{\mathrm{i}n\omega_0 t} \tag{4.64}$$

i.e. containing spatial wavenumbers which are even multiples of k and temporal frequencies which are even multiples of $\omega_0/2$. At the next order, the interactions involve $\mathbf{Q}_1$ and $\mathbf{Q}_m(t)$, with $m \in \{-2, 0, 2\}$, and

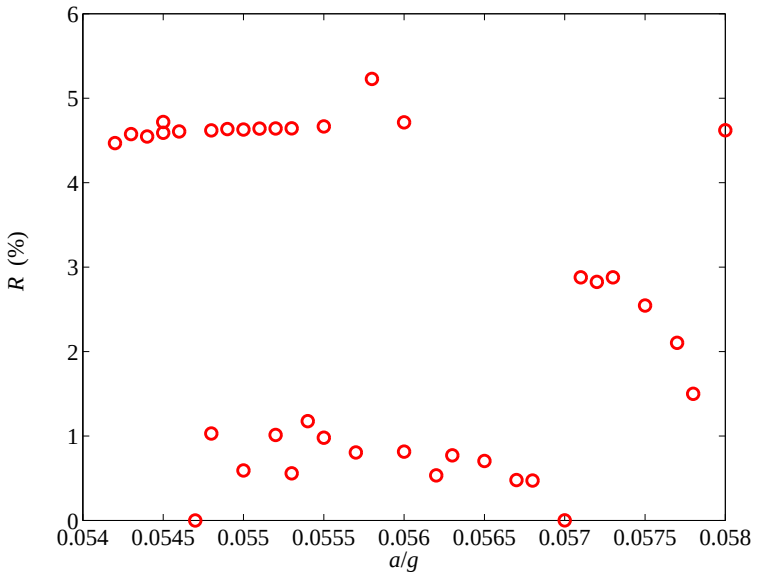

Figure 4.18: R as a function of the acceleration.

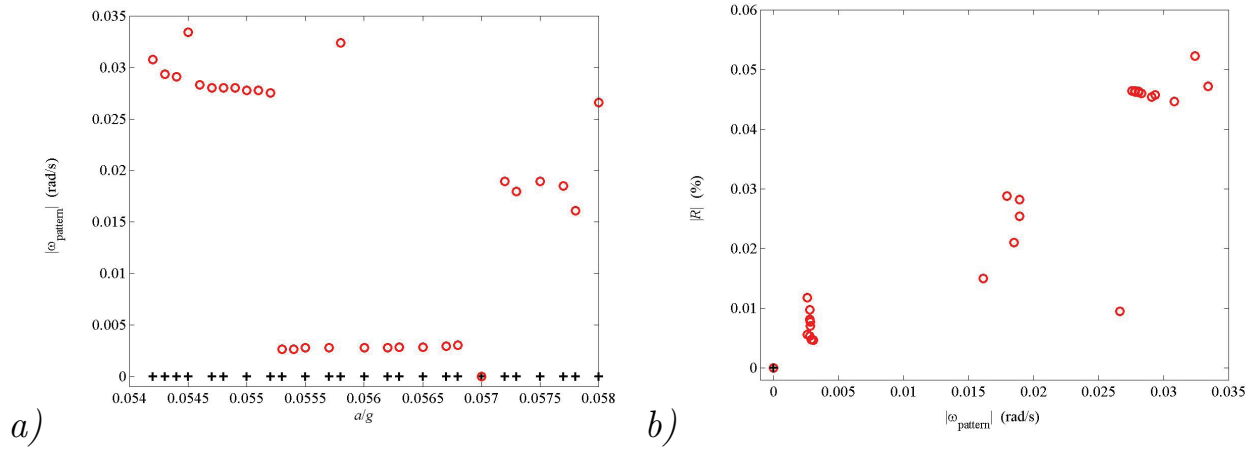

Figure 4.19: a) $\omega_{pattern}$ as a function of a/g. Circles: unforced solutions, +: Solutions whose reflection symmetry has been forced. b) Coefficient of left-right asymmetry R as a function of $\omega_{pattern}$.

produce

$$\sum_{\substack{m=-3 \\ m \text{ odd}}}^{3} \sum_{n=-\infty}^{\infty} \mathbf{Q}_{m,n} \mathrm{e}^{\mathrm{i}mkx} \mathrm{e}^{\mathrm{i}\left(n+\frac{1}{2}\right)\omega_0 t} \tag{4.65}$$

i.e. containing spatial wavenumbers which are again odd multiples of k and temporal frequencies which are odd multiples of $\omega_0/2$. This argument can be continued to higher orders to conclude that the spatio-temporal Fourier decomposition of $\mathbf{Q}$ contains spatial wavenumbers and temporal frequencies which are multiples of k, ω_0 which are either both odd or both even. This is an invariant subspace. In particular, the zero temporal frequency corresponding to the mean field (4.61) is associated only with even multiples of k, *i.e.* with a wavelength of $\lambda/2$. The appearance of fields whose means have a fundamental wavelength of λ can only be triggered by a secondary instability, at a threshold above a_c.

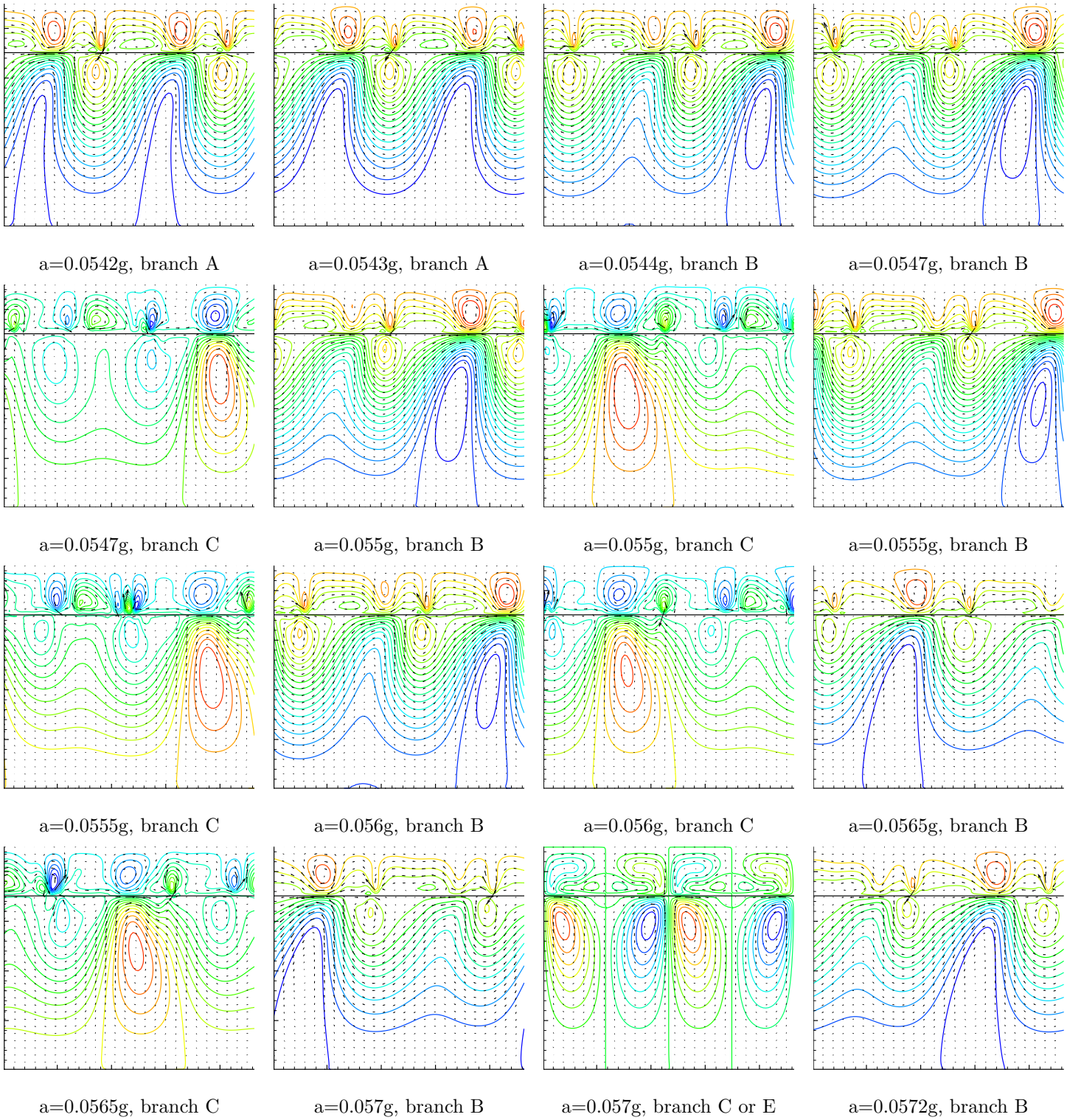

Figure 4.20: Mean flow over $4T$ at different accelerations without symmetry forcing. Colors: streamfunction. Line: interface. Vectors: velocity field. The coloring and the vector fields are rescaled in each picture for the sake of clarity. The height of the unperturbed interface is 17.56mm, the height of the box is 22.56mm.

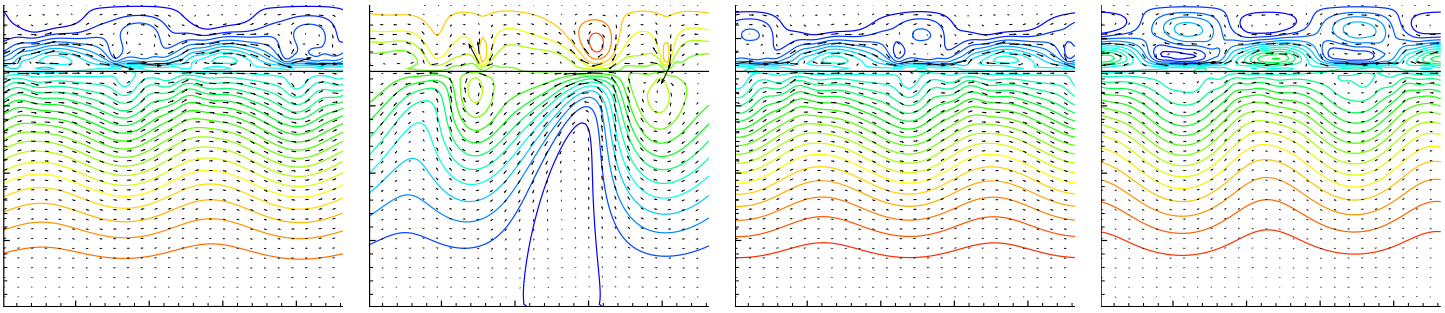

a=0.0572g, branch D a=0.0575g, branch B a=0.0575g, branch D a=0.058g, branch D

Figure 4.21: Mean flow over $4T$ at different accelerations without any forcing. Colors: streamfunction. Line: interface. Vectors: velocity field. The coloring and the vector fields are rescaled in each picture for the sake of clarity. The height of the unperturbed interface is 17.56mm, the height of the box is 22.56mm.

Our method for obtaining a mean field of wavelength $\lambda/2$, deduced from the requirement (4.62), is as follows:

- Compute the mean field, where the temporal average is taken over a multiple of the subharmonic period $2T$, and expand it into spatial Fourier modes,
- Subtract components corresponding to Fourier components $(m, 0)$, with m odd, from the instantaneous field.
- Continue integration and repeat the above steps until convergence.

4.5 Conclusion

We have simulated the drift instability of Faraday waves in a two-dimensional periodic domain. We find that drift emerges at a value of a very close to the Faraday threshold. The time required for saturation increases to infinity when a tends to a_c, preventing us from determining whether the two bifurcations are simultaneous. We compute unstable drift-free states by using an algorithm that imposes the reflection symmetry. In this way, we have been able to compare states with and without drift. It resulted from these comparisons that the emergence of the drift was correlated with an increase of the amplitude of the interface height $\Delta\zeta$. A spectral study of the interface highlighted that counter-propagating waves, initially of the same amplitude, became unequal when the drift arose. These results seem to confirm the theory of Fauve et al. (1991) and imply that the analysis of Martín et al. (2002) is not applicable to our case. We reported another difference with the theory of Martín et al. (2002), based on their hypothesis that the streaming flow which generates the drift was stronger in the neighboroud of the bottom walls rather than close to the interface. Our simulations showed that, in our case, the streaming is stronger near the free surface. This effect could be the cause of the previous disagreement and may be related to the fact that our calculations involve two fluids instead of a single one.

Following a further slight increase of the acceleration, another instability occurs, which breaks the average-$\lambda/2$ spatial periodicity of the flow. We have designed a method to force the flows to become or to remain on average $\lambda/2$ periodic; the purely drifting solutions can be tracked in this fashion. At the spatial period-doubling bifurcation, the amplitude of $\Delta\zeta$ undergoes a small increase, which we have correlated to drastic changes in the behavior of certain modes by using spatiotemporal spectral analysis. In particular, the modes $\hat{\zeta}_{mn}$ with $l+m$ odd, which were absent from the flow before the threshold, vary strongly. We have observed two types of solutions with these characteristics. These differ in the shape of their spatiotemporal spectra, and in the variables we have used to study the flows. However the transition between these two branches did not display any noticeable symmetry breaking that might account for the passage from one branch to

the other. Bistability has been seen over a range of accelerations $a/g \in [0.0545; 0.0578]$; we do not yet know the limits of this interval of bistability.

We found one value of the acceleration, $0.057g$, for which the reflection-symmetric state is stable. This symmetric state also satisfies the average-$\lambda/2$ periodicity. More generally, all reflection-symmetric solutions we have found, whether stable or unstable, are $\lambda/2$-periodic when averaged.

For higher values of a, the reflection symmetry breaks in favor of states which conserve average-$\lambda/2$ periodicity. The symmetry breaking was accompanied by a substantial increase of the interface height amplitude. Calculations performed at accelerations higher than $a = 0.058g$ indicate large number of new branches. Among these, one branch of solutions was remarkable in that no drift was observed despite their lack of reflection symmetry.

Conclusion

The work presented in this manuscript represents the first complete simulation of Faraday waves. The algorithm and code that we formulated towards this goal successfully passed all of the tests we designed. The tests of the linear regime produced an overview of the main temporal eigenvectors at the threshold of the first two instability tongues. Nonlinear three-dimensional simulations produced hexagonal patterns at the same parameter values as in the corresponding experiments. The primary difficulty in simulating these patterns is that at certain times, the bottom layer forms a very thin film, requiring high numerical resolution for sufficient accuracy. Our program also provided the first overview of the instantaneous velocity fields of a hexagonal pattern. Experimental investigations have not yet provided such a description because methods for measuring complete 3D velocity fields are quite new and perhaps too intrusive when dealing with Faraday waves, and may distort the flow.

Our simulation exhibited an exotic behaviour of the hexagons, with a change in symmetry at long times. We have discovered the existence of a probable periodic orbit containing the hexagons. The simulation showed the same qualitative results for higher resolutions and accelerations. Nevertheless, the higher the acceleration, the shorter the passage through the other symmetries. This may be because our parameters are in the transition zone between the squares and the hexagons. The spatial cohabitation encountered in the large domain of Kityk et al. (2005) would then be replaced by a temporal alternation in a domain containing only one or two hexagons. We have proposed that this orbit is homoclinic and has the hexagonal regime as a fixed point. We have begun to explore it quantitatively. This exploration has been divided into three steps: calculating the fixed point, the most unstable eigenvector around this point and the trajectory of the orbit. For the calculation of the fixed point, we have forced the hexagonal symmetry. The method designed for this purpose is new, original and can be easily adapted to many other types of pattern-forming systems such as Rayleigh-Bénard instability. The only requirements for this method are the existence of isolated fixed points and that the symmetry of the pattern be known.

Finally, we have carried out the first simulation of the drift instability in Faraday waves. We made an exhaustive study of this phenomenon, including comparisons of time-averaged patterns with and without drift, as well as comparisons of the instantaneous flows. The mean flows are interesting since they remove parasitic effects that render the observation of long-time phenomena such as the drift instability untractable. Comparisons of the spatiotemporal spectra were also made. In particular, we observed that the main modes, $\hat{\zeta}_{1,1}$ and $\hat{\zeta}_{1,-1}$ that propagate in opposite horizontal directions, lose their symmetry, which is closely connected with the generation of the drift. This led us to conclude that the analytical model proposed by Martín et al. (2002) was not applicable to our case and that the correct model was that described by Fauve et al. (1991). The drift was supplemented by a period-doubling instability.

The dynamics of the Faraday instability is extremely rich in this set of parameters. Five branches were in the small range between the primary threshold and 8% beyond it, in addition to the planar motionless flow. These include two branches whose members share the same symmetries. A method analogous to that designed to force the hexagons has been used successfully to force the reflection symmetry and to compute the branch with flux but with an average wavelength of $\lambda/2$. An increase in the acceleration seems to lead to a wide number of new branches that were not displayed here, because they contained too few points, but we mention one particular flow, which was motionless despite lacking reflection symmetry.

We hope that the work presented in this manuscript has illustrated the many open problems surrounding the Faraday instability and has demonstrated the value that numerical simulation can bring to questions that have been previously raised experimentally and theoretically.

Bibliography

Bechhoefer, J., Ego, V., Manneville, S., and Johnson, B. (1995). An experimental study of the onset of parametrically pumped surface waves in viscous fluids. *J. Fluid Mech.*, 288:325–350.

Benjamin, T. B. and Ursell, F. (1954). The stability of the plane free surface of a liquid in vertical periodic motion. *Proc. R. Soc. Lond.*, 225:505–515.

Besson, T., Edwards, W. S., and Tuckerman, L. S. (1996). Two-frequency parametric excitation of surface waves. *Phys. Rev. E*, 54:507–513.

Beyer, J. and Friedrich, R. (1995). Faraday instability: linear analysis for viscous fluids. *Phys. Rev. E*, 51:1162–1168.

Binks, D., Westra, M.-T., and van der Water, W. (1997). Effect of depth on the pattern formation of Faraday waves. *Phys. Rev. Lett.*, 79:5010–5013.

Brackbill, J. U., Kothe, D. B., and Zemach, C. (1992). A continuum method for modeling surface tension. *J. Comput. Phys.*, 100:335–354.

Cerda, E. A. and Tirapegui, E. L. (1998). Faraday's instability in viscous fluid. *J. Fluid Mech.*, 368:195–228.

Chen, P. (2002). Nonlinear wave dynamics in Faraday instabilities. *Phys. Rev. E*, 65:036308.

Chen, P. and Viñals, J. (1999). Amplitude equation and pattern selection in Faraday waves. *Phys. Rev. E*, 60:559–570.

Chen, P. and Wu, K.-A. (2000). Subcritical bifurcations and nonlinear balloons in Faraday waves. *Phys. Rev. Lett.*, 85:3813–3816.

Chorin, A. J. (1968). Numerical simulation of the Navier-Stokes equations. *Math. Comput.*, 22:745–762.

Christiansen, B., Alstrø m, P., and Levinsen, M. T. (1992). Ordered capillary-wave states: Quasicrystals, hexagons, and radial waves. *Phys. Rev. Lett.*, 68:2157–2161.

Douady, S., Fauve, S., and Thual, O. (1989). Oscillatory phase modulation of parametrically forced surface waves. *J. Phys. II*, 10:309–315.

Edwards, W. S. and Fauve, S. (1993). Parametrically excited quasicrystalline surface waves. *Phys. Rev. E*, 47:R788–R791.

Ezerskii, A. B., Korotin, P. I., and Rabinovich, M. I. (1985). Random self-modulation of two-dimensional structures on a liquid surface during parametric excitation. *Soviet Journal of Experimental and Theoretical Physics Letters*, 41:157–160.

Faraday, M. (1831). On a peculiar class of acoustical figures; and on certain forms assumed by groups of particles upon vibrating elastic surfaces. *Philos. Trans. R. Soc. London*, 121:299–340.

Fauve, S., Douady, S., and Thual, O. (1991). Drift instabilities of cellular patterns. *J. Phys. II*, 1:311–322.

Goda, K. (1979). A multistep technique with implicit difference schemes for calculating two- or three-dimensional cavity flows. *J. Comput. Phys.*, 30:76–95.

Guermond, J.-L., Minev, P., and Shen, J. (2006). An overview of projection methods for incompressible flows. *Comp. Meth. Appl. Mech. Eng.*, 195:6011–6045.

Harlow, F. H. and Welch, J. E. (1965). Numerical calculation of time dependent viscous incompressible flow of fluid with free surface. *Phys. Fluids*, 8:2182.

Henderson, R. D. and Barkley, D. (1996). Secondary instability in the wake of a circular cylinder. *Phys. Fluids*, 8:1683–1685.

Huepe, C., Ding, Y., Umbanhowar, P., and Silber, M. (2006). Forcing function control of Faraday wave instabilities in viscous fluids. *Phys. Rev. E*, 73:16310.

Kakutani, T. and Matsuuchi, K. (1975). Effect of viscosity on long gravity waves. *J. Phys. Soc. of Jpn.*, 39:237–246.

Kityk, A. V., Embs, J., Mekhonoshin, V. V., and Wagner, C. (2005). Spatiotemporal characterization of interfacial Faraday waves by means of a light absorption technique. *Phys. Rev. E*, 72:036209.

Kityk, A. V., Embs, J., Mekhonoshin, V. V., and Wagner, C. (2009). Erratum: Spatiotemporal characterization of interfacial Faraday waves by means of a light absorption technique. *Phys. Rev. E*, 79:029902.

Kudrolli, A. and Gollub, J. P. (1996). Patterns and spatiotemporal chaos in parametrically forced surface waves: a systematic survey at large aspect ratio. *Physica D*, 97:133–154.

Kudrolli, A., Pier, B., and Gollub, J. P. (1998). Superlattice patterns in surface waves. *Physica D*, 123:99–111.

Kumar, K. (1996). Linear theory of Faraday instability in viscous fluids. *Proc. R. Soc. Lond.*, 452:1113–1126.

Kumar, K. and Tuckerman, L. S. (1994). Parametric instability of the interface between two fluids. *J. Fluid Mech.*, 279:49–68.

Lamb, S. H. (1930). *Hydrodynamics*. Dover Publications, New York.

Lioubashevski, O., Arbell, H., and Fineberg, J. (1996). Dissipative solitary states in driven surface waves. *Phys. Rev. Lett.*, 76:3959–3962.

Malomed, B. A. and Tribelsky, M. I. (1984). Bifurcations in distributive kinetic systems with aperiodic instability. *Physica D*, 14:67–87.

Martel, C. and Knobloch, E. (1997). Damping of nearly inviscid water waves. *Phys. Rev. E*, 56:5544–5548.

Martín, E., Martel, C., and Vega, J. M. (2002). Drift instability of standing Faraday waves. *J. Fluid Mech.*, 467:57–79.

Moisy, F., Rabaud, M., and Salsac, K. (1984). A synthetic Schlieren method for the measurement of the topography of a liquid interface. *Exp. Fluids*, 46:1021–1036.

Müller, H. W. (1993). Periodic triangular patterns in the Faraday experiment. *Phys. Rev. Lett.*, 71:3287–3290.

Müller, H. W., Wittmer, H., Wagner, C., Albers, J., and Knorr, K. (1997). Analytic stability theory for Faraday waves and the observation of the harmonic surface response. *Phys. Rev. Lett.*, 78:2357–2360.

Murakami, Y. and Chikano, K. (2001). Two-dimensional direct numerical simulation of parametrically excited surface waves in viscous fluid. *Phys. Fluids*, 13:65–74.

Mutabazi, I., Hegseth, J. J., Andereck, C. D., and Wesfreid, J. E. (1988). Pattern formation in the flow between two horizontal coaxial cylinders with a partially filled gap. *Phys. Rev. A*, 38:4752–4760.

O'Connor, N. L. (2008). *The complex spatiotemporal dynamics of a shallow fluid layer*. PhD thesis, Virginia Polytechnic Institute and State University, Blacksburg, VA.

Périnet, N., Juric, D., and Tuckerman, L. S. (2009). Numerical simulation of Faraday waves. *J. Fluid Mech.*, 635:1–26.

Peskin, C. S. (1977). Numerical analysis of blood flow in the heart. *J. Comput. Phys.*, 25:220–252.

Porter, J., Topaz, C., and Silber, M. (2004). Pattern control via multi-frequency parametric forcing. *Phys. Rev. Lett.*, 93:034502.

Rabaud, M., Michalland, S., and Couder, Y. (1990). Dynamical regime of directional viscous fingering: spatiotemporal chaos and wave propagation. *Phys. Rev. Lett.*, 64:184–187.

Rayleigh, L. (1883a). On maintained vibrations. *Philos. Mag.*, 15:229–235.

Rayleigh, L. (1883b). On the crispations of fluid resting upon a vibrating support. *Philos. Mag.*, 16:50–58.

Rucklidge, A. M. and Silber, M. (2009). Design of parametrically forced patterns and quasipatterns. *SIAM J. Appl. Dyn. Syst.*, 8:298–347.

Saad, Y. (1996). *Iterative methods for sparse linear systems*. SIAM, Philadelphia.

Shu, C. W. and Osher, S. (1989). Efficient implementation of essentially non-oscillatory shock capturing schemes, ii. *J. Comput. Phys.*, 83:32–78.

Simon, A. J., Bechhoefer, J., and Libchaber, A. (1988). Solitary modes and the eckhaus instability in directional solidification. *Phys. Rev. Lett.*, 61:2574–2577.

Skeldon, A. C. and Guidoboni, G. (2007). Pattern selection for Faraday waves in an incompressible viscous fluid. *SIAM J. Appl. Math.*, 67:1064–1100.

Sussman, M., Fatemi, E., Smereka, P., and Osher, S. (1998). An improved level set method for incompressible two-phase flows. *Computers & Fluids*, 27:663–680.

Temam, R. (1984). *Navier-Stokes Equations, Theory and Numerical Analysis*. North-Holland, Amsterdam.

Tryggvason, G., Bunner, B., Esmaeeli, A., Juric, D., Al-Rawahi, N., Tauber, W., Han, J., and Jan, Y.-J. (2001). A front-tracking method for the computations of multiphase flow. *J. Comput. Phys.*, 169:708–759.

Ubal, S., Giavedoni, M. D., and Saita, F. A. (2003). A numerical analysis of the influence of the liquid depth on two-dimensional Faraday waves. *Phys. Fluids*, 15:3099–3113.

Umbanhowar, P. B., Melo, F., and L., S. H. (1996). Localized excitations in a vertically vibrated granular layer. *Nature*, 382:793–796.

Valha, J., Lewis, J. S., and Kubie, J. (2002). A numerical study of the behaviour of a gas–liquid interface subjected to periodic vertical motion. *Int. J. Numer. Methods Fluids*, 40:697–721.

Vega, J. M., Knobloch, E., and Martel, C. (2001). Nearly inviscid Faraday waves in annular containers of moderately large aspect ratio. *Physica D*, 154:313–336.

Walden, R. W., Kolodner, P., Passner, A., and Surko, C. M. (1985). A front-tracking method for the computations of multiphase flow. *Phys. Rev. Lett.*, 55:496–499.

Wehausen, J. V. and Laitone, E. V. (1960). *Encyclopedia of Physics*. Springer-Verlag, Berlin.

Zhang, W. and Viñals, J. (1997). Pattern formation in weakly damped parametric surface waves. *J. Fluid Mech.*, 336:301–330.